"STUDY OF CRYSTAL STRUCTURE AND ELECTRICAL PROPERTIES ON LEAD TITANATE AND LEAD ZIRCONATE TITANATE BASED CERAMIC OXIDES"

A THESIS

Submitted by

NIRANJAN SAHU

(Roll. No: 50710003)

For the award of the degree

of

DOCTOR OF PHILOSOPHY

DEPARTMENT OF PHYSICS

NATIONAL INSTITUTE OF TECHNOLOGY,

ROURKELA, ODISHA-INDIA-769008

OCTOBER-2011

DECLARATION

I here by declare that thesis entitled **"STUDY OF CRYSTAL STRUCTURE AND ELECTRICAL PROPERTIES ON LEAD TITANATE AND LEAD ZIRCONATE TITANATE BASED CERAMIC OXIDES"** which is being submitted by me to National Institute of Technology for the award of degree of **Doctor of Philosophy** is original and authentic work conducted by me in the Department of Physics, National Institute of Technology, Rourkela under the supervision of **Prof. S. Panigrahi**, Department of Physics, National Institute of Technology, Rourkela. No part or full form of this thesis work has been submitted elsewhere for a similar or any other degree.

Date:

Niranjan Sahu

Department of Physics,

National Institute of Technology,

Rourkela, Odisha-769008

CERTIFICATE

This is to certify that the thesis entitled **"STUDY OF CRYSTAL STRUCTURE AND ELECTRICAL PROPERTIES ON LEAD TITANATE AND LEAD ZIRCONATE TITANATE BASED CERAMIC OXIDES"** submitted by **Mr. Niranjan Sahu (Roll No. 50710003)**, to the National Institute of Technology, Rourkela for the award of the degree of ***Doctor of Philosophy*** is a bonafide record of research work carried out by him under my supervision. In my opinion, the work fulfills the requirements for which it is being submitted. The contents of the thesis, in full or in parts, have not been submitted to any other Institute or University for the award of any degree or diploma.

Date:

Prof. S. Panigrahi

Department of Physics,

National Institute of Technology,

Rourkela, Odisha – 769008

Dedicated to my Parents:

LATE BHAGABAN SAHU

&

Mrs.Sabitri Sahu

ACKNOWLEDGEMENTS

The five years valuable time, I've spent at National Institute of Technology, Rourkela have given me the source of the most precious experience in my life. I take the opportunity to acknowledge all those who directly or indirectly helped me throughout this difficult journey. With deep regards and profound respect, I avail this opportunity to express my deep sense of gratitude and indebtedness to my Ph.D. supervisor **Dr. S. Panigrahi** Department of Physics, National Institute of Technology, Rourkela, for introducing the present research topic and for inspiring guidance, constructive criticism and valuable suggestions throughout this research work. I would like to thank him for his encouragement and, introducing me to different subjects, such as experimental techniques, solid state physics, ceramic materials and many other advanced physics subjects. I am happy to carry out my Ph.D. Thesis work under such a kind hearted person. I will never forget his company and suggestions throughout my life. I will remain ever grateful to him for teaching physics to me till my thesis submission.

I would like to express my deep sense of gratitude to **Dr. Manoranjan Kar**, Asst. Professor, department of physics, Indian Institute of Technology Patna whose vast knowledge in the field of science and technology has enlightened me in different area of materials science and physics. His deep sense of appreciation, unparalleled moral support, constructive and honest criticism has been a constant source of inspiration to me.

I would like to extend my thanks to **Dr. S. Jena,** my doctoral committee chairman and head of the department of physics, NIT Rourkela for his constant support and valuable suggestions. Also I am grateful to my doctoral committee members **Dr. D. Behera**, Department of Physics, and **Dr. H. B. Sahu**, Department of Mining Engineering, National Institute of Technology, Rourkela, for their time to time suggestions whenever I approached to them.

I would like to thank my course coordinator **Dr. S. C. Mishra**, Professor in the Metallurgy and Material Science Engineering, N.I.T, Rourkela, for teaching me the advanced topics in X-ray diffraction technique during my course work.

I would like to express my deep sense of gratitude to **Dr. Pawan Kumar**, Associate professor in the department of Physics, N.I.T, Rourkela to extend his lab facility for my experimental work.

I extend my heart-felt thanks to **Dr. A. K. Thakur**, Asst. Professor in the department of Physics and Materiology, Indian Institute of Technology, Kharagpur to extend electrical measurement facility in his solid state ionic laboratory at IIT Kharagpur and, his valuable suggestions and discussions.

I am grateful to President **Er. K. C. Sahoo**, Vice President (P & E) **Er. S. K. Sahu** and Secretary **Er. R. N. Dash** of Purushottam Institute of Engineering and Technology, Rourkela for providing me financial support to complete my research work at NIT, Rourkela as a sponsored candidate.

I also must acknowledge **Dr. S. K. Sarangi,** Director, National institute of Technology, Rourkela for providing me a platform to carry out my research work at NIT Rourkela.

I am grateful to technical staff Mr. Sushil Kumar Sahoo of ceramic engineering department, Mr U. K. Sahoo and Mr. Rajesh pattnaik of Metallurgy and Material Science Engineering Department, NIT, Rourkela for their help for XRD and SEM-EDS measurements.

I am thankful to Professor. S. N. Dash, Dr. T. Badapanda, Miss. Sasmita Das and other faculty members of Purushottam Institute of Engineering and Technology, Rourkela, for their help, co-operation and suggestions.

I feel a deep sense of gratitude for my father, late Bhagaban Sahu, and mother, Mrs. Sabitri Sahu, who formed a part of my vision and taught me the good things that really matter in my life.

I am grateful to my brothers, sisters, relatives and friends for their constant encouragement and moral support.

I want to thank my wife **Mrs. Bijaylaxmi Sahu (Luni)** for giving moral support, throughout this long difficult journey. She gives me many reasons to smile everyday and to pursue my research work happiness. I am happy to dedicate my thanks to my little **Son Nucleon (Bunu/Poogo)** who came to me with God grace with his beautiful smile which has supported me in difficulties during my Ph.D. Also I am grateful to my in-laws (**Mr. B. N. Padhiary & Mrs. Pabitra Padhiary**) for giving me constant encouragement.

It is difficult to express my thanks to all of the people who ever helped me during my Ph.D. Hence at last but not in the list, I am grateful to my all friends and teachers for their advice and valuable discussions.

Above all, I thank our saving **Durga Mata** for giving me all these people to help and encourage me, and for the skills and opportunity to complete this thesis.

Date: **Niranjan Sahu**

ABSTARCT

The lead based perovskite material (PT, PZT) has so many technological applications such as: multilayer capacitor, dielectric resonator, thin film resistor, piezoelectric transducers, elecrostrictive actuators, hydrogen sensor, electro optical modulator, laser host, switch magnetic bubble memory etc. The property of the lead based material can also be enhanced by substituting different transition materials within the perovskite. Again there is a very less report on the detailed crystal structure study (Employing the Rietveld Method) of the modified lead based perovskite ceramics. There were no detailed study on crystal structure and physical properties of $Pb_{1-x}La_xTiO_3$ (PLT) at high concentration of La content. The introduction of an optimized amount of lanthanum (La) not only increases the stability but also softens the ferroelectric properties of the material. Also there was not much report on the detailed crystal structure (Employing the Rietveld method) and physical properties of B site modification of PLT with general formula $(Pb_{0.70}La_{0.30})(Ti_{1-x}A_x)O_3$, (A = Mn and Al). The main objective to study this material was to explore the structural and electrical properties of both iso (Mn^{3+}) and aliovant (Al^{3+}) substitution on the B site of $Pb_{0.7}La_{0.3}TiO_3$ cubic perovskite. Manganese (Mn^{3+}) as an acceptor ion may replace Ti^{4+} site and the addition segregates at grain boundaries. Mn doping in lead titanate is also a good candidate for fabricating piezoelectric devices. Mn belongs to valence unstable ions; it can affect the stability of the material. Aluminium does not have a bonding d-orbit or d-electrons, and has a stable valence and solely displays a valence of 3^+, different from the isovalent substitutions for Ti^{4+}. So the aliovalent substitutions of Al^{3+} for Ti^{4+} in $Pb_{0.7}La_{0.3}TiO_3$ would be interesting for studying the doping effect on the crystal structure, lattice dynamics and electrical properties. The oxygen ion vacancy concentration in rare earth (La^{3+}) and manganese modified lead titanate could have an important contribution to the electrical response of these materials.

There are lots of reports on the structural and electrical properties of modified lead zirconate titanate ceramics in the MPB region. But there is hardly found few reports on the detailed crystal

structure (Employing the Rietveld method) of lead zirconate titanate in and around the MPB region which overcomes the existence of two phases. The doping substituent can either occupy A-site, B-site or both as donor or acceptor based on chemical valance with respect to the original ions. The substitution of the transition elements of the B-site will modify the electrical properties of the ferroelectric materials. It is also well known that the fluctuation of the oxidation state of the transition metal ions (Fe^{3+}, Mn^{3+}) results in the formation of oxygen ion vacancies to reserve the local electrical neutrality and causes thermally activated conduction.

The main objectives of the present thesis are to understand the crystal structure and electrical transport properties of modified PT and PZT ceramics. The following materials have prepared to study the properties in this thesis: (i) $Pb_{1-x}La_xTiO_3$ (x = 0.00, 0.10, 0.25, 0.30 and 0.50), (ii) $(Pb_{0.70}La_{0.30})(Ti_{1-x}Mn_x)O_3$ (x = 0.00, 0.05, 0.10, 0.15 and 0.20), (iii) $Pb_{0.70}La_{0.30})(Ti_{1-x}Al_x)O_3$, x = 0.00, 0.05, 0.10, 0.15 and 0.20, (iv) $Pb(Zr_{1-x}Ti_x)O_3$ (x =1, 0.35 and 0.65), (v) $Pb(Zr_{0.65-x}Mn_xTi_{0.35})O_3$ (x = 0.00, 0.05, 0.10 and 0.15) and (vi) $Pb(Zr_{0.65-x}Fe_xTi_{0.35})O_3$ (x = 0.00, 0.05, 0.10 and 0.15). The detailed crystal structure has been studied by analyzing XRD patterns (Employing the Rietveld method). The Morphological study by scanning electron microscope (SEM) and the elemental analysis of energy dispersive spectrum has been carried out using SEM-EDS. Electrical properties by the Impedance analyzer/Gain phase analyzer/ and or LCR meter have been studied in detail.

The present thesis has been divided into 8 Chapters. The Chapters are, **Chapter 1:** Introduction, **Chapter 2**: Literature review, **Chapter 3:** Experimental techniques, **Chapter 4**: Structural analysis and electrical behavior of $Pb_{1-x}La_xTiO_3$ ceramics, **Chapter 5**: Structural analysis and electrical behavior of $Pb_{0.70}La_{0.30}Ti_{1-x}A_xO_3$ (A = Al & Mn) ceramics, **Chapter 6**: Structural analysis and electrical properties of Mn ion modified PZT ceramics, **Chapter 7**: Structural analysis and electrical properties of Fe^{3+} ion modified PZT ceramics and **Chapter 8**: Conclusions and future work.

In Chapter 1 (Introduction) describes the history of ferroelectric materials. Also details about crystal structure and physical properties have been discussed. Chapter 2 (Literature review)

has been unlighted about a literature survey on PT, PZT and modified PT & PZT. Also motivation and objectives of the present thesis work have been discussed.

Chapter 3 (experimental technique) presented details about the method of preparation and experimental methods used for characterization of the present samples. All the samples were prepared by following solid state route at high temperature. Phase purity has been studied by X-ray diffraction (XRD) technique. All the XRD patterns were analyzed by employing the Rietveld method. Crystal structure parameters (Cell parameters, cell volume, bond length, bond angle, etc.) were obtained from the analysis. A microstructure study was carried out by scanning electron microscope (SEM). Elemental analysis has been done by using the energy dispersive spectrum with the help of SEM-EDS measurement. Frequency variation of dielectric properties at different temperatures has been carried out by using computer controlled LCR and/or an impedance analyzer. Also the electrical properties of all the samples have been studied by using an impedance analyzer. Finally P-E loop has been taken from some selected samples with the help of P-E Loop tracer.

Chapter 4 discussed the detailed crystal structure, microstructure, dielectric and electrical properties of the $Pb_{1-x}La_xTiO_3$ (PLT) (x = 0.0, 0.10, 0.25, 0.30 and 0.50) samples. X-ray diffraction (XRD) studies at room temperature reveal that, the parent compound $PbTiO_3$ crystallize to tetragonal structure with *P4mm* space group and the samples for $x \geq 0.10$ crystallize to cubic perovskite phase with space group $Pm\bar{3}m$. The micrograph has been suggested that the grains are distributed homogeneously throughout the surface and the grain size increases with increase in La content. A broad and diffused phase transition with a decrease in transition temperature has been observed in the temperature and frequency dependent dielectric measurement of the La doped $PbTiO_3$. From AC conductivity analysis we have observed that the activation energy decreases with the La concentration. The ferroelectric behavior of La doped $PbTiO_3$ is also confirmed by the hysteresis loop. The bulk resistance of the material decreases with the rise in temperatures. This exhibits a typical negative temperature coefficient of resistance (NTCR) behavior of the material.

The temperature dependent bulk conductivity indicates that the electrical conduction in the material is a thermally activated process.

Chapter 5 gives the information about manganese/aluminium modified lead lanthanum titanate ceramics with a general formula $(Pb_{0.70}La_{0.30})(Ti_{1-x}A_x)O_3$, (A = Mn, Al) (where x = 0.0, 0.05, 0.10, 0.15 and 0.20) have been synthesized by solid-state reaction route at high temperature. The observed peaks in the XRD patterns have been indexed to $Pm\bar{3}m$ space group with cubic symmetry and all the XRD patterns have been analyzed by employing the Rietveld method. Highly dense microstructure can be obtained with a decrease in grain size on increasing the value of both Mn and Al concentration. Nyquist plot of Mn doped $Pb_{0.70}La_{0.30}TiO_3$ comprises two semicircular arcs, whose centers lie below the real axis. The semicircle at higher frequencies attributed to transport phenomena in the bulk and another at lower frequencies, are related to transport phenomena at grain boundaries. The experimental plots are fitted with a suitable equivalent circuit by using commercially available software *ZSIMP WIN Version 2*. The theoretical data are in good agreement with the experimental data.

Mn ion modified $Pb(Zr_{0.65-x}Mn_xTi_{0.35})O_3$ perovskite has been discussed in Chapter 6. All the materials crystallize to *R3c* space group with rhombohedral symmetry and exhibits ferroelectric to paraelectric transition. The lattice parameters, unit cell volumes and crystallite size are found to decrease with the increase of Mn concentration. The Curie temperature (T_c) decreases with the Mn concentration. We have observed that dielectric constant decreases and AC conductivity increases with the increase in Mn concentration of all frequencies. All the compositions show dispersion of AC conductivity in both the low and high frequency regions. The existence of low frequency dispersion indicates that the charge carriers may be either ionic or electronic nature.

Chapter 7 discussed the properties of $Pb(Zr_{0.65-x}Fe_xTi_{0.35})O_3$ (x = 0.00, 0.05, 0.10 and 0.15) materials. All the materials crystallize to *R3c* space groups in rhombohedral symmetry. The Rietveld refinement study shows that the lattice parameters, cell volume and crystallite size decreases with increase in Fe contents. The temperature and frequency dependence dielectric study shows that the transition temperature decreases with an increase in the dielectric constant. It is also

observed that above T_c there is a sharp increase in conductivity, below T_c the ac conductivity decreases linearly with decrease in temperature. The sharp increase in conductivity is attributed to the increase in polarizability of a material around T_c. It is observed that the activation energy decreases with the Fe^{3+} ion concentration. The complex impedance, electric modulus formalism and dielectric loss analysis are used to analyze the data. The impedance analysis indicates that the material exhibits negative temperature coefficients of resistance behavior with grain conduction and temperature dependent relaxation phenomena. The activation energies calculated from the temperature dependence of conductive pattern and the relaxation time variation pattern is almost same. This indicates that the conductivity and relaxation species are identical and the conduction process may be attributed to the same type of charge carriers.

Chapter 8 is focused on the conclusions of the present thesis. Structural transition from *P4mm* (tetragonal symmetry) to $Pm\bar{3}m$ (cubic symmetry) has been observed at x~0.10 for $Pb_{1-x}La_xTiO_3$ samples. Diffuse phase transition behavior is observed in the dielectric study with decrease in dielectric constant. From the Nyquist plot analysis the grain resistance decreases with an increase in temperature which shows negative temperature coefficient of resistance (NTCR) of the material. The existence of grain and grain boundary phenomena of the material is more clearly separated in complex impedance formalism. Impedance spectroscopy shows the existence of non-Debye type relaxation phenomena in $(Pb_{0.70}La_{0.30})(Ti_{1-x}A_x)O_3$ (where A = Mn, Al and x = 0.0, 0.05, 0.10, 0.15 and 0.20) samples. The Mn modified lead zirconate titanate is crystallize to *R3c* space group and, lattice parameters, unit cell volumes and crystallite size decrease with the increase in Mn concentration. The lattice parameters, cell volume, bond lengths and crystallite size decrease with the doping of Fe^{3+} ions in Zr sites of $Pb(Zr_{0.65-x}Fe_xTi_{0.35})O_3$ materials. The doping of Fe^{3+} ion creates a vacancy on B-site of ABO_3 perovskite structure of PZT which leads to create free space charge in the materials. It leads to increase the activation energy which causes the increase in conductivity with the Fe^{3+} ion concentration.

CONTENTS

LIST OF TABLES

LIST OF FIGURES

ABBREVIATIONS

AFE	Antiferroelectric
CIS	Complex impedance spectroscopy
CPE	Constant phase element
DPT	Diffused phase transition
DRAM	Dynamic random access memory
EDS	Energy dispersive spectroscopy
FE	Ferroelectric
FDPT	Ferroelectric diffused phase transition
FERAM	Ferroelectric random access memory
FWHM	Full width at half maximum
MPB	Morphotrpic phase boundary
NTE	Negative thermal expansion
NTCR	Negative temperature co-efficient of resistance
PE	Paraelectric
PT	$PbTiO_3$
PLT	$Pb_{1-x}La_xTiO_3$

PLMT	$(Pb_{0.70}La_{0.30})\ (Mn_xTi_{1-x})O_3$
PLAT	$(Pb_{0.70}La_{0.30})\ (Al_xTi_{1-x})O_3$
PZT	$Pb(Zr_{1-x}Ti_x)O_3$
PZMT	$Pb(Zr_{0.65-x}Mn_x)Ti_{0.35}O_3$
PZFT	$Pb(Zr_{0.65-x}Fe_x)Ti0_{.35}O_3$
PVA	Polyvinyl alcohol
PV	Pseudo voight
RS	Rochelle salt
SEM	Scanning electron microscope
WH	Williamson Hall
XRD	X-ray diffraction

NOTATIONS

ENGLISH SYMBOLS

a, b, c	Lattice parameters
A	Electrode area of the sample
E_a	Activation energy
E_c	Coercive field
f	Frequency
k_B	Boltzmann constant
M'	Real part of modulus
M''	Imaginary part of Modulus
P_r	Remnant polarization
P_s	Saturation polarization
R_g, R_{gb}	Grain resistance and grain boundary resistance
R_p	Profile factor
R_{wp}	Weighted profile factor
R_{exp}	Expected weight factor
R_{Bragg}	Bragg factor
R_f	Crystallographic factor
t	Tolerance factor
T	Temperature
T_c	Curie temperature
T_m	Temperature corresponding to ε_m
V	Unit cell volume
Z'	Real part of impedance

Z''	Imaginary part of impedance
tanδ	Dielectric loss tangent

GREEK SYMBOLS

ε_r	Relative dielectric constant
ε_m	Maximum value of dielectric constant
ω	Relaxation frequency
ω_{max}	Maximum relaxation frequency
θ	Bragg's angle
λ	X-ray wavelength
γ	Diffuseness exponent
τ	Relaxation time
σ	Conductivity
σ_{ac}	AC conductivity
σ_{dc}	DC conductivity
σ_b	Bulk conductivity
$\sigma_{o,}\ \tau_o$	Pre exponential factor
Φ	Phase angle
χ^2	Reduced chi-square

CHAPTER 1

INTRODUCTION

CHAPTER 1

INTRODUCTION

1.1 Ferroelectricity

There has been a continuous interest in the fabrication of new ferroelectric materials since the discovery of ferroelectricity in single crystals of Rochelle salt ($NaKC_4H_4O_6.4H_2O$) (*Valasek*,1921) [1] and its subsequent extension into the domain of polycrystalline ceramics of barium titanate ($BaTiO_3$) during mid-1940s (*Haertling*,1999) [2]. Ferroelectricity has also been called Seignette electricity, as Seignette or Rochelle Salt (RS) was the first material found to show ferroelectric properties such as a spontaneous polarization on cooling below the Curie point, ferroelectric domains and a ferroelectric hysteresis loop. A huge leap in the research on ferroelectric materials came in the 1950's, leading to the widespread use of many other ferroelectric ceramics including lead titanate ($PbTiO_3$ or PT), lead zirconate titanate ($PbZr_{1-x}Ti_xO_3$ or PZT), lead lanthanum zirconate titanate ($Pb_{1-x}La_xZr_{1-y}Ti_yO_3$ or PLZT), and relaxor ferroelectrics like lead magnesium niobate (PMN). These ferroelectric materials have been developed and utilized for a variety of applications. Ferroelectricity is a spontaneous electric polarization of a material that can be reversed by the application of an external electric field. Ferroelectricity is the phenomenon, by virtue of which some materials exhibit spontaneous electric polarization, even in the absence of any externally applied field. Ferroelectric crystals possess regions with uniform polarization called ferroelectric domains. Within a domain, all the electric dipoles are aligned in the same direction. There may be many domains in a crystal separated by interfaces called domain walls. A ferroelectric single crystal, when grown, has multiple ferroelectric domains. A single domain can be obtained by domain wall motion made possible by the application of an appropriate electric field. A very strong field could lead to the reversal of the polarization in the domain, known as domain switching [3]. The name refers to certain magnetic analogies, though it is somewhat

misleading as it has no connection with iron (ferrum) at all. The development of new ceramic processing and thin film technology lead the materials to a wide range of industrial and commercial applications. Application of these materials includes high dielectric constant capacitors, piezoelectric sonar, ultrasonic transducers, medical diagnostic transducers, buzzers, gas igniters, positive coefficient sensors and switches, ultrasonic motors, electro optic valves, thin film capacitors and ferroelectric thin film memories (*Lines and Glass*, 1977) [4]. The biggest uses of ferroelectric ceramics is in the areas such as dielectric ceramics for capacitor applications, ferroelectric thin films for non volatile memories, piezoelectric materials for medical ultrasound imaging and actuators, and electro-optic materials for data storage and displays.

The historical roots leading to the discovery of ferroelectricity can be traced back to the last century and the work of the famous crystal physicists Weiss, Pasteur, Pockels, Hooke, Growth, Voigt and the brothers Curie. Beginning with the pioneering work on Rochelle salt and potassium dihydrogen phosphate, the study of ferroelectrics accelerated rapidly during World War II with the discovery of barium titanate. Then came a period of rapid proliferation with more than 100 new ferroelectrics identified in the next decade, including lead zirconate titanate, the most widely used piezoelectric transducers.

1.2 Crystallographic signature of ferroelectricity

The lattice structure described by the Bravais unit cell of the crystal governs the crystal symmetry. Though there are thousands of crystals in nature, they all can be grouped together into 230 microscopic symmetry types or space groups based on the symmetry elements [5]. Most of the crystals possess symmetry elements in addition to the repetitions expressed by the crystal lattice. The operation of any single symmetry element of the group leaves the pattern of symmetry unchanged. In studying the physical properties of crystals, only the orientations of the symmetry elements and not their relative positions are important. Hence, if only the orientations of the symmetry elements are taken into account, then the macroscopic symmetry elements in crystals reduce to a center of symmetry, mirror plane, 1, 2, 3, 4 or 6 fold rotation axes and 1, 2, 3, 4 or 6

fold inversion axes. A combination of these symmetry elements gives us the macroscopic symmetry also called as point groups. It can be shown by the inspection of the 230 space groups that there are just 32 point groups. The seven crystal systems can be divided into these point groups according to the point group symmetry it possess. Out of 32 point groups, 21 are non-centrosymmetric; however 20 non-centrosymmetric point groups are piezoelectric [6]. Among these 20 piezoelectric, 10 have a unique polar axis and possess spontaneous polarization (which is in general temperature dependent), are called pyroelectric. Similar to pyroelectric materials, ferroelectrics possess spontaneous polarization but the magnitude and direction of the polarization can be reversed by an external electric field. Thus the conditions necessary to classify materials as ferroelectric are: (i) the existence of spontaneous polarization and (ii) reversible spontaneous polarization. Fig. 1.1 shows the inter-relationship of piezoelectric and subgroups on the basis of symmetry.

These point groups do not show polarity. The remaining 21 point groups do not have a center of symmetry (i.e. non-centro symmetric). A crystal having no center of symmetry possesses one or more crystallographically unique directional axis. All non-centro symmetric point groups, except the 32 point groups, show the piezoelectric effect along unique directional axes.

The ferroelectric materials can be classified into four subgroups based on the unit cell structure such as: (a) the tungsten-bronze group, (b) oxygen octahedral (ABO_3) group, (c) the pyrochlore group and (d) the bismuth-layer structure group [7]. Out of these four, ABO_3 perovskites have attracted much attention due to various factors, which will be discussed in the following sections.

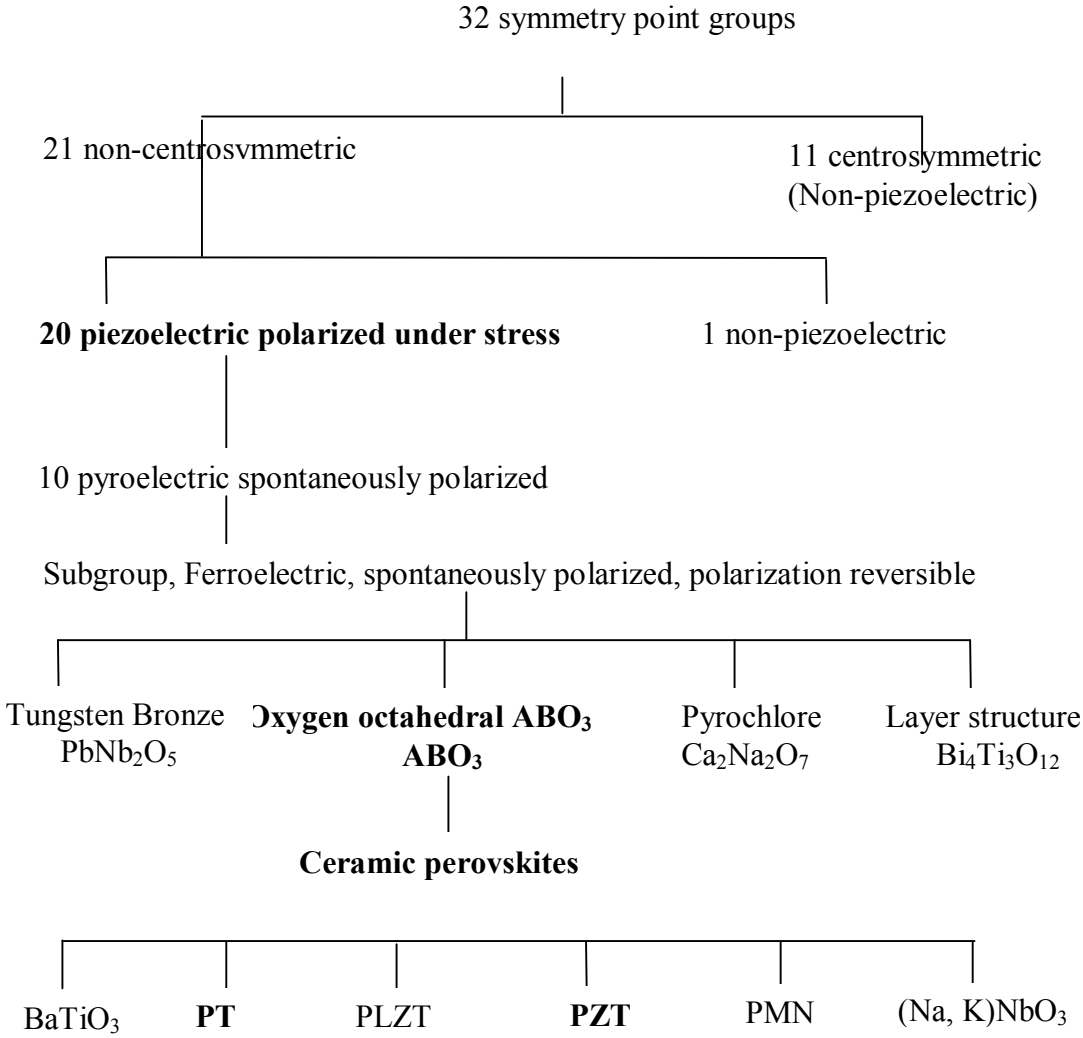

Fig. 1.1: Flow chart of inter-relationship of piezoelectric and subgroups on the basis of symmetry.

1.3 Perovskite structure

In Ural Mountains Gustav Rose discovered $CaTiO_3$ in 1839 and named it Perovskite after an eminent Russian mineralogist, Count Lev Alexevich Von Perovski. Perovskite is a family name of a group of materials and the mineral name of calcium titanate ($CaTiO_3$) having a structure of the type ABO_3. The ideal perovskite structure is simple cubic, and this is what we generally imply when we refer to the perovskite structure. The mineral perovskite is $CaTiO_3$ and is actually orthorhombic at room temperature, becoming cubic at temperatures above 900°C [8]. The simple cubic structure (space symmetry $Pm\bar{3}m$) consists of corner sharing oxygen octahedra (BO_6) arranged in three dimensions with smaller, highly charged cations (B: Ti^{4+}, Zr^{4+}, Sn^{4+}, Nb^{5+}, Ta^{5+}, W^{6+} etc.) located in the middle of the octahedral, and lower charged, larger cations (A: Na^{+1},

K^{+1}, Ca^{2+}, Ba^{2+}, Pb^{2+} etc.) in between the octahedral. The coordination number of A-site cation is 8 to 12 whereas the coordination number of B-site cation is 6. Its simplest structure is cubic, which is the highest temperature form of many mixed oxides of the ABO_3 type. The ideal ABO_3 structure is shown in Fig. 1.2. Most perovskite type ferroelectrics are compounds with either $A^{2+}B^{4+}O_3^{2-}$ or $A^{1+}B^{5+}O_3^{2-}$ type formulation.

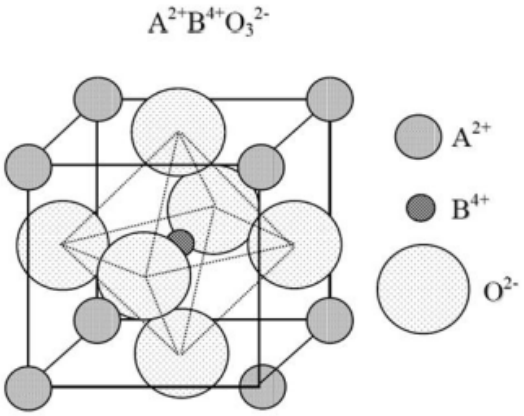

Fig. 1.2: An ideal cubic ABO_3 perovskite unit cell.

The ideal cubic perovskite structure is distorted by cation substitutions (either A site or B site) and/or oxygen off-stoichiometry. It is mainly due to cation size mismatch, John-Teller effect and the electron instability. The ideal cubic structure is modified into a lower symmetry structure such as orthorhombic, rhombohedral, etc. due to the following three mechanisms, i.e. (i) cooperative tilting of BO_6 octahedra, (ii) displacement of the cations, and (iii) distortions of the BO_6 octahedra. The tilting of the BO_6 octahedra is most relevant in deciding the overall space group symmetry of the particular PT perovskite (*Knight* 1994; *Yang et al* 1999) [9, 10]. This distortion is characterized by the Goldsmith tolerance factor,

$$t = d_{A\text{-}O} \Big/ \sqrt{2}(d_{B\text{-}O}) \tag{1.1a}$$

Or

$$t = \frac{(R_A + R_O)}{\sqrt{2}(R_B + R_O)} \tag{1.1b}$$

Where, d_{A-O} and d_{B-O} is the average A cation-oxygen and B cation-oxygen distances respectively. R_A and R_B are the ionic radii of A and B-site cations and, R_O for the O-site anions. In the case of a cubic perovskite t = 1. Stable perovskite structure is found for "t" values in the range of 0.88 to about 1.09. A perovskites structure containing small cations will lead to t < 1, while large cations will give rise to t > 1. The displacement of the cations and the distortion of the octahedra are usually correlated and driven by electronic instability of the metal cations. The John-Teller distortion in KCuF (*Okazaki et al*, 1961) [11] and the cation displacement in $PbZrO_3$ (*Corker et al*, 1997) [12] are the typical examples. Octahedral tilting is a more common distortion mechanism that can be realized by tilting the rigid BO_6 octahedra while maintaining their corner sharing connectivity (Glazer 1972) [13]. This type of distortion is generally observed when the A-site cation is too small for the cubic structure. Very few ion combinations fulfill these strict relative size criteria. The perovskite structure is particularly important for several reasons: i. many perovskites are ferroelectric, ii. many perovskites are piezoelectric and iii. many perovskites have a high dielectric constant.

Many piezoelectric (including ferroelectric) ceramics such as Barium Titanate ($BaTiO_3$), Lead Titanate ($PbTiO_3$), Lead Zirconate Titanate (PZT), Lead Lanthanum Zirconate Titanate (PLZT), Lead Magnesium Niobate (PMN), $SrTiO_3$, Potassium Niobate ($KNbO_3$), Potassium Sodium Niobate ($K_xNa_{1-x}NbO_3$), and Potassium Tantalate Niobate ($K(Ta_xNb_{1-x})O_3$) have a perovskite type structure. The size of an atom or ion, and how well it fits into its crystallographic site is one of the most important aspects in determining the stability of an ionic structure. The O^{2-} anion and the larger cation (A^{2+}) have similar radii, so that the structure is not just determined by O^{2-}. The larger cation and the anion combine to form a "close-packed" arrangement with the smaller cation, B^{4+}, sitting in the oxygen octahedral interstices.

By the 1950s the solid solution system $Pb(Zr,Ti)O_3$ (PZT), which also possess the perovskite structure, was found to be ferroelectric. PZT compositions are now the most widely exploited of all

piezoelectric ceramics both in research and industry. An up to date brief description of PT and PZT systems can be found in *Moulson* (1990) [14]. A great attention has been given to the perovskite oxides due to their excellent physico-chemical properties and wide range of applications. A few of them are listed in Table 1.1. Nevertheless, the perovskite structure is extremely common. This is because the perovskite structure can distort in a number of ways to accommodate ions with non-ideal sizes. This leads to a rich array of phase transitions, which makes perovskites one of the most technologically and geologically important structure types.

Table 1.1: Properties and applications [15] of perovskite materials.

Property	Applications
Dielectric property	Multilayer capacitor, dielectric resonator, thin film resistor
Optical property	Electro optic modulator, laser host, switch
Ferroelectric/piezoelectric property	Piezoelectric transducers, PTC thermistor, electrostrictive actuators.
Magnetic property	Magnetic bubble memory, ferromagnet
Ionic/proton conducting property	Solid electrolyte, SOFC electrolyte, hydrogen sensor

1.4 Curie point and phase transitions

All ferroelectric materials have a transition temperature called the Curie point (T_c). At a temperature $T > T_c$ the crystal does not exhibit ferroelectricity, while for $T < T_c$ it is ferroelectric. On decreasing the temperature through the Curie point, a ferroelectric crystal undergoes a phase transition from a non-ferroelectric phase to a ferroelectric phase. If there is more than one ferroelectric phases, the temperature at which the crystal transforms from one ferroelectric phase to another is called the transition temperature. Early research works on ferroelectric transitions have

been summarized by *Nettleton et al* [16, 17]. Near the Curie point or transition temperatures, thermodynamic properties including dielectric, elastic, optical and thermal constants show an anomalous behavior. This is due to a distortion in the crystal as the phase structure changes. One distinctive characteristic of ferroelectrics is the hysteresis loop in the polarization versus electric field curve. A net spontaneous polarization exists even at zero electric field and the loop disappears at the Curie temperature Tc, where the material undergoes a phase transition from high temperature paraelectric and low temperature ferroelectric state. The temperature dependence of the dielectric constant above the Curie point ($T > T_c$) in ferroelectric crystals is governed by the Curie-Weiss law [18]:

$$\varepsilon_r = \varepsilon_0 + \frac{C}{T - T_c} \qquad (1.2)$$

Where ε_r the relative permittivity of the material, ε_0 is the permittivity of vacuum; C is the Curie constant and T_c is the Curie temperature, and it is the actual temperature where the crystal structure changes. The sharp anomaly corresponds to the phase transition at T_c is shown in Fig.1.3. A phase transition occurs at the temperature T_c. Above the transition temperature the substance is in the paraelectric phase, in which the elementary dipoles of the various unit cells in the crystal are oriented randomly and, below the transition temperature, the substance is in the ferroelectric phase.

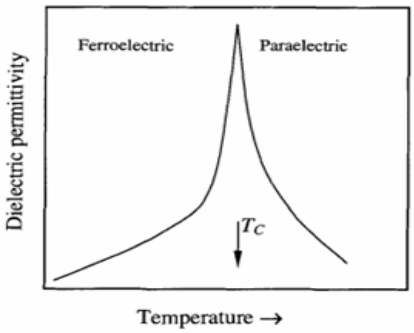

Fig.1.3: An illustration of dielectric permittivity as a function of temperature for normal ferroelectrics.

1.4.1 Diffuse phase transition

Many phase transitions in macroscopic homogeneous materials are characterized by the fact that the transition temperature is not sharply defined. Of these, so-called diffuse phase transition temperature (DPT) [19], the transition is smeared out over a certain temperature interval, resulting in a gradual change of physical properties in this temperature region. Though this phenomenon is observed in several types of materials, however, the most remarkable examples of DPT are found in ferroelectric materials. Ferroelectrics diffuse phase transitions (FDPT) are first mentioned in the literature in the early 1950's. Some characteristics of the DPT are: (a) broadened maxima in the permittivity versus temperature curve, (b) gradual decrease of spontaneous and remnant polarizations with rising temperature, (c) transition temperatures obtained by different techniques which do not coincide, (d) relaxation character of the dielectric properties in transition region and (e) no Curie-Weiss behavior in certain temperature intervals above the transition temperature. The diffuseness of the phase transition is assumed to be due to the occurrence of fluctuations in a relatively large temperature interval around the transition. Usually two kinds of fluctuations are considered: (a) compositional fluctuation and (b) polarization (structural) fluctuation. From the thermodynamic point of view, it is clear that the compositional fluctuation is present in ferroelectric solids-solutions and polarization fluctuation is due to the small energy difference between high and low temperature phases around the transition. This small entropy difference between ferroelectric and paraelectric phase will cause a large probability of fluctuation. *Kanzing* (1957) [20] has been observed from X-ray diffraction that in a narrow temperature range around the transition $PbTiO_3$ single crystal splits up into FE (ferroelectric) and paraelectric (PE) micro regions. Complex perovskite type ferroelectrics with distorted cation arrangements show DPT which is characterized by a broad maximum for the temperature dependence of dielectric constant ε_r and dielectric dispersion in the transition region. For DPT, ε_r follows modified temperature dependence [21],

$$\frac{1}{\varepsilon_r} - \frac{1}{\varepsilon_m} = \frac{(T - T_m)^{\gamma}}{C'} \tag{1.3}$$

where T_m is the temperature at which ε_r reaches maximum, ε_m is the value of ε_r at T_m, C′ is the modified Curie Weiss constant and is the critical exponent, explains the diffusivity of the materials, which lies in the range $1< \gamma < 2$ (*Tiwari*, 1994) [22]. The smeared out ε_r versus T response has generally been attributed (*Kirillov et al*, 1973) [23] to the presence of micro regions with local compositions vary from the average composition over a length scale of 100 to 1000 Å. Different micro regions in a macroscopic sample are assumed to transfer at different temperature, so-called Curie range, leading DPT which is due to compositional fluctuations. The dielectric and mechanical properties of the FE system below their T_C are functions of the state of polarization and stress. So ferroelectrics have major application today because of their characteristic electro-optic, dielectric and hysteresis properties. For many practical applications, it is desired to use the very large property maxima in the vicinity of the ferroelectric phase transition, to move the transition into the temperature range of interest and to broaden the very large sharp peak values. In DPT the dielectric maxima is now much rounder and polarization persists for a short range of temperature above T_m.

1.4.2 Polarization mechanism in ferroelectric materials

Basically, polarizability is a consequence of the fact that the molecules, which are the building blocks of all substances, are composed of both positive charges (nuclei) and negative charges (electrons). When a field acts on a molecule, the positive charges are displayed in a direction of the field. The effect is therefore to pull the opposite charges apart, i.e., to polarize the molecule [24]. There are different types of polarization processes, depending on the structure of the molecules which constitute the solid. Basically, there are three types polarization mechanisms contribute to the total polarizability. In general, therefore, we may write for the total polarizability:

$$\alpha = \alpha_e + \alpha_i + \alpha_d \tag{1.4}$$

which is the sum of the various contributions; α_e , α_i , and α_d are the electronic, ionic, and dipolar polarizabilities, respectively. The different polarizabilities are active in different frequencies as shown in Fig. 1.4. The electronic contribution is present in any type of substances, but the presence of the other two terms depends on the material under consideration. Thus the term α_i is present in ionic covalent crystals such as Si and Ge, which are non-ionic and non-dipolar, the polarizability is entirely electronic in nature. The relative magnitudes of the various contributions in above equation are such that, in non-dipolar, ionic substances the electronic part is often of the same order as the ionic. In dipolar substances, however, the greatest contribution comes from the dipolar part. The various polarizabilities may be segregated from each other because each contribution has its own characteristic features which distinguish it from the others. Dipolar polarizability, for instance, exhibits strong dependence on temperature, while the other two contributions are essentially temperature independent. The behavior of different type polarization is shown in Fig. 1.4.

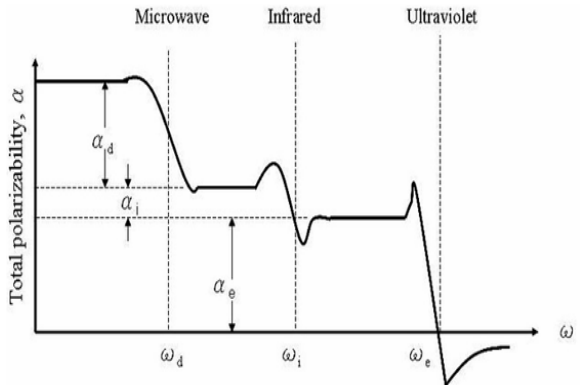

Fig. 1.4: The behavior of different type of polarization.

1.5 Lead based perovskite materials

1.5.1 Lead titanate ($PbTiO_3$, PT)

Technological development has been a key to meeting the new demands of the evolving society. Therefore, there is a constant need for new and improved materials. The perovskite

structure has and continues to attract interest, because of its suitability for applications in telecommunication. Lead titanate ($PbTiO_3$), or simply PT, is one of the most important members in the ferroelectric and piezoelectric families. PT is a classic example of ferroelectric perovskites with a high lattice strain or tetragonality (c/a = 1.064). Its temperature-driven cubic to tetragonal phase transition at T_C = 763 K is taken as an example of a purely displacive transition [25]. PT exhibits a unique negative thermal expansion (NTE) in the perovskite family. Lead titanate ($PbTiO_3$) has strong ferroelectric behavior because of the Pb-O and Ti-O covalent bonds as compared to $BaTiO_3$ where covalent bonding exists only between Ti and oxygen atoms. Lead titanate is a ferroelectric material having a structure similar to $BaTiO_3$ with a high Curie point 490°C. On decreasing the temperature through the Curie point a phase transition from the ferroelectric tetragonal phase to paraelectric cubic phase takes place. Lead titanate ceramics are difficult to fabricate in the bulk form as they undergo a large volume change on cooling below the Curie point. It is the result of a tetragonal (c/a =1.064) to cubic (c/a =1.00) phase transformation leading to a strain of > 6%. Hence, pure $PbTiO_3$ ceramics crack and fracture during fabrication. The spontaneous strain developed during cooling can be reduced by modifying the lead titanate with lanthanum (La) dopants and also other dopants such as Ca, Sr, Ba, Sn, and W to obtain a crack free ceramic. During the selection of doping element one has to consider the ionic radius of ions (listed in Table 1.2) to get a tolerance factor of stable structure. One representative modified lead titanate composition that has been extensively investigated recently is $(Pb_{0.76}\ Ca_{0.24}\ )\ ((Co_{0.50}\ W_{0.50}\ )_{0.04}\ Ti_{0.96})O_3$ with 2 mol. % MnO added to it. This composition has a decreased c/a ratio and Curie point of 255^{o}C [23, 24]. As an example, PLT unit cell consists of a corner linked network of oxygen octahedral with Ti^{4+} ions occupying the B sites and Pb^{2+} and La^{3+} ions situated at the A site created by linking octahedra. As a result of different oxidation states between Pb^{2+} and La^{3+}, some of the A sites and B sites are vacant to maintain electrical neutrality in the structure [26]. The atomic radii of pure and doped PT, PZT are given in Table 1.2.

Table 1.2: The atomic radii of component ions in PT and modified PT, PZT and some doped PZT.

Ions	Ionic radius (Å)
Pb^{2+}	1.20
Zr^{4+}	0.79
Ti^{4+}	0.68
O^{2-}	1.32
La^{3+}	1.01
Al^{3+}	0.51
Mn^{3+}, Mn^{4+}	0.66; 0.60
Fe^{2+}, Fe^{3+}	0.74; 0.64

Ferroelectricity is a spontaneous electric polarization of a material that can be reversed by the application of an external electric field. Ferroelectricity is the phenomenon, by virtue of which some materials exhibit spontaneous electric polarization, even in the absence of any externally applied field. Ferroelectric crystals possess regions with uniform polarization called ferroelectric domains. Within a domain, all the electric dipoles are aligned in the same direction. There may be many domains in a crystal separated by interfaces called domain walls. A ferroelectric single crystal, when grown, has multiple ferroelectric domains. A single domain can be obtained by domain wall motion made possible by the application of an appropriate electric field. A very strong field could lead to the reversal of the polarization in the domain, known as domain switching. The spontaneous polarisation depends on temperature in PT. A typical curve of polarzation versus temperature is shown Fig. 1.5.

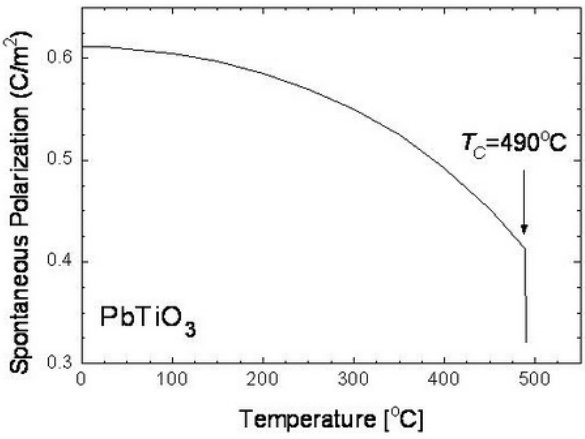

Fig. 1.5: The spontaneous polarization versus temperature plot of the "$PbTiO_3$".

1.5.2 Lead zirconate titanate [$Pb(Zr_{1-x}Ti_x)O_3$, PZT]

Lead zirconate titanate (PZT) is a binary solid solution of $PbZrO_3$ an antiferroelectric (orthorhombic structure) and $PbTiO_3$ a ferroelectric (tetragonal perovskite structure). It may exist in either phase; cubic, orthorhombic, rhombohedral, or tetragonal, depending on composition (Zr/Ti ratio) and temperature. PZT has a perovskite type structure with the Ti^{4+} and Zr^{4+} ions occupying the B site at random, Pb ions the corners and oxygen the face centers. The ratio of $PbZrO_3$ to $PbTiO_3$ affects the properties. At high temperatures PZT has the cubic perovskite structure which is paraelectric. On cooling below the Curie point line, the structure undergoes a phase transition to form a ferroelectric tetragonal or rhombohedral phase. In the tetragonal phase, the spontaneous polarization is along the <100> set of directions while in the rhombohedral phase the polarization is along the <111> set of directions. Most physical properties such as dielectric and piezoelectric constants show an anomalous behavior at the morphotropic phase boundary (MPB). The MPB separating the two ferroelectric tetragonal and orthorhombic phases has a room temperature composition with a Zr/Ti ratio of ~ 52/48. PZT ceramics with the MPB composition show excellent piezoelectric properties. The poling of the PZT ceramic is also easy at this composition because the spontaneous polarization within each grain can be switched to one of the 14 possible orientations (eight [111] directions for the rhombohedral phase and six [100] directions for the tetragonal

phase). Below the Zr/Ti ratio of 95/5 the solid solution is antiferroelectric (AFE) with an orthorhombic phase. On the application of an electric field to this composition a double hysteresis loop is obtained. This is because of the strong influence of the antiferroelectric $PbZrO_3$ phase [27].

In order to suit some specific requirements for certain applications, piezoelectric ceramics can be modified by doping them with ions which have a valence different than the ions in the lattice. Piezoelectric PZT ceramics having the composition at the MPB can be doped with ions to form "hard" and "soft" PZT's. Hard PZT's are doped with acceptor ions such as K^+, Na^+ (for A site) and Fe^{3+}, Al^{3+}, Mn^{3+} (for B site), creating oxygen vacancies in the lattice [28]. Hard PZT's usually have lower permittivities, smaller electrical losses and lower piezoelectric coefficients. On the other hand, soft PZT's are doped with donor ions such as La^{3+} (for A site) and Nb^{5+}, Sb^{5+} (for B site) leading to the creation of A site vacancies in the lattice. The soft PZTs have a higher permittivity, larger losses, higher piezoelectric coefficient and are easy to pole and dipole. It can be used for applications requiring very high piezoelectric properties. The direction in PZT structure is shown in Fig.1.6 (a-c).

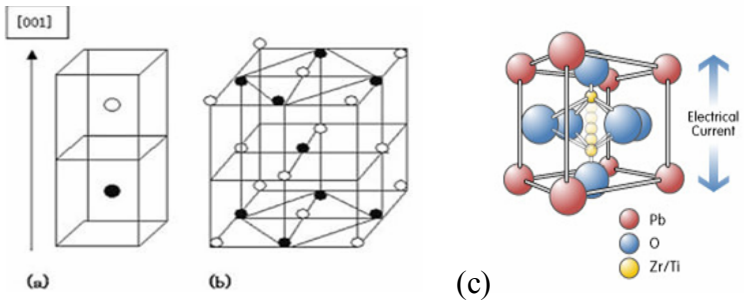

Fig. 1.6: (a-c) At high temperatures PZT has the cubic perovskite structure which is paraelectric. On cooling below the Curie point line, the structure undergoes a phase transition to form a ferroelectric tetragonal or rhombohedral phase. In the tetragonal phase, the spontaneous polarization is along the <100> set of directions while in the rhombohedral phase the polarization is along the <111> set of directions.

The uses of PZT ceramics in electronic appliances are manifold, depending on whether the device employs the direct piezoelectric effect, the converse piezoelectric effect or both. This phenomenon is benefited in numerous device applications as given in Table 1.3.

Table 1.3: Applications and devices of piezoelectric ceramics [29].

Classification	Applications
High voltage generators	Gas appliances, cigarette lighter, fuse (igniters) for explosive, flash bulbs
High power ultrasonic generators	Ultrasonic cleaner, sonar, echo sounding, ultrasonic machining, atomization, polarization
Transducers for sound and ultrasound in air	Microphones (e.g. for telephone), burglar alarm system, remote control, loud speaker, buzzers, medical ultrasonic equipment
Resonators and filters	Ratio and televisions, remote control, electronic instrumentation
Delay lines	Color televisions, computers, electronic instrumentation, telephones
Keyboards	Computers, printers, desk calculators, slot machines, telephones

CHAPTER 2

LITERATURE REVIEW

CHAPTER 2

LITERATURE REVIEW

2.1 Introduction

In this chapter, an attempt is made to provide a review on the synthesis of $PbTiO_3$, $Pb(Zr,Ti)O_3$ perovskites. Also the effect of substitutions and sintering temperatures on the physical and chemical properties of these ceramic oxides will be discussed.

2.2 Survey of previous work

Lead titanate ($PbTiO_3$) is one of the important ferroelectric materials having perovskite structure with excellent dielectric, ferroelectric and electro-optic properties [30-34]. Physical properties of $PbTiO_3$ (PT) can be significantly modified by substitutions in both the cationic sites by other metal ions with suitable valency and ionic size [35, 36]. The perovskite type oxides have attracted a considerable attention of researchers since it has many excellent physical properties and suitable for practical applications in electronic industries. In recent times, a significant interest has been arisen in the area of ferroelectric field due infrared sensors [37], capacitors [38], dynamic random access memories (DRAMs) [39], non-volatile RAMs [40], un-cooled infrared detectors [41], piezoelectric actuators [42], Shutters [43], optical modulators [44], microwave [45], colossal magnetoresistance [46], magneto-electric and electro-optic devices [47-50], etc. The PT undergoes a phase transition at a temperature of 490˚C from tetragonal (*P4mm*) ferroelectric phase to centrosymmetric cubic ($Pm\bar{3}m$) paraelectric phase [51]. An appropriate incorporation of La into lead titanate tunes the phase transition temperature and consequently makes the PLT material suitable for a wide range of device applications at room temperature. There are several methods to prepare $PbTiO_3$, and $Pb(Zr,Ti)O_3$ (PZT) solid solutions in the solid state reaction method, co-precipitation and sol-gel method. The solid state reaction method has been studied since 1973-1974 by *Okazaki and Nagata et al* [52] and *Martirena and Burfest et al* [53]. During 1981-1983, *Chandratreya* [54] and

Hiremath et al [55] proposed the reaction mechanisms involved in the formation of PZT and PLZT solid solutions prepared via the solid state reaction method. *Patil et al* [56], *Rahaman et al* (1995) [57], *Rahaman et al* (2008) [58], and *Kang et al* [59] reported that solid state process requires calcination temperature more then 750°C for phase formation and sintering temperature more than 1000°C to achieve better densification. Later on, the PT and PZT preparation methods have been continuously developed. In 1991, *Ichinose and Kimura et al* [60] reported the use of 0.3 mm diameter zirconia ball in grinding $PbTiO_3Pb(Ni_{1/3}Nb_{1/3})O_3$ ceramics after high temperature annealing, which yielded ultra fine powder. Furthermore, they found that the piezoelectric properties of the sintered sample depend on the grain size and mechanical properties such as hardness. *A. P. Barranco et al* [61] studied PT based ceramics and observed that doping of PT-based ceramics is very important to reduce its high tetragonality and maintain the optimal piezoelectric characteristics for practical applications. *Z. Zhang et al* [62], *K. Ramam et al* [63] and *T. Young Kim et al* [64] studied the lead titanate ceramics and they had reported the ferroelectric properties of lead titanate are controlled by a suitable substitution at the A site and/or B site. *H. Ihrig* [65] studied lead titanate ceramic and had observed the aliovalent cation dopants have been undertaken to improve electrical properties. *Smolensky et al* (1984) [66], *Keizer, K et al* [67] reported that the isomorphic substitution of lead by lanthanum atoms induces some interesting changes in the physical properties of $PbTiO_3$ material. When the lanthanum content is higher than 25 atom%, a diffuse character of the ferroelectric paraelectric phase transition (DPT) is observed. *X. Dai et al* [68], *D. Hennings,* [69], *K. Keizer et al* [70] and *M. Kuwabara et al* [71] reported that the lanthanum induced modification concerning $PbTiO_3$ results in structural changes that can be directly related to the nature of the phase transition. R. D. S*hannon,* [72] reported that in La^{3+} modified $PbTiO_3$ materials, La^{3+} replaces Pb^{2+} rather than Ti^{4+} in Pb-based perovskites. To keep the neutrality of the charge, since that replacement is aliovalent, site vacancies are created. *E. C. S. Tavares et al* [73] observed that in La modified PT ceramics for temperatures higher than T_c, a residual short-range structural disorder has been found, which is not to be compatible with the

centrosymmetric cubic structure usually observed in the paraelectric phase. It has been suggested that the lanthanum-induced modification concerning $PbTiO_3$ results in structural changes that can be directly related to the nature of the phase transition [74-77].

The $PbTiO_3$ and La doped PT crystal structure has been exhaustively studied [78-80]. *Teslic et al* [81] and *Egami et al* [82] also found a discrepancy between structural results obtained by XRD and neutron scattering data when they studied the local atomic structure of $PbZr_{1-x}Ti_xO_3$ (PZT), $Pb(Mg_{1/3}\ Nb_{2/3})O_3$ (PMN) and $Pb_{1-x}\ La_x\ Zr_yTi_{1-y}O_3$ (PLZT) systems. *P. P. Neves et al* [83] studied the structure of the La modified PT ceramic samples by XRD-Rietveld refinements and reported that the tetragonality of the structure gradually diminishes with the increase of La content until a structural phase transition from tetragonal-to-cubic structure, which takes place in the range between 25 and 30 atom % of La samples. In fact, the samples with x ranging from 0 to 25 atom % crystallize in the *P4mm* space group, whereas the sample with 30 atom % of La crystallizes in the $Pm\bar{3}m$ spacegroup. The refinement of XRD data also confirmed the existence of only A-site vacancies, which are introduced to the perovskite structure by the aliovalente replacement of Pb^{2+} by La^{3+} cations. *M. Kellati et al* [84] studied that La modified PT ceramics by sol-gel method and reported that grain size and density increases with the increase of La concentration. Annealing temperature and duration of the annealing process have a great influence on the microstructure and dielectric properties. *W. Ren et al* [85] studied La modified PT and observed that the Curie temperature T_c of PT reduces linearly with the molar % incorporation of La-content. *Yao et al* [86], *P. Venkateswarlu. et al* [87] observed from lanthanum-doped lead titanate (PLT) thin films, a universal power law relation was brought into picture to explain the frequency dependence of AC conductivity. The temperature dependence of AC conductivity was analyzed in detail. The activation energy obtained from the temperature dependence of AC conductivity was attributed to the shallow trap-controlled space charge conduction in the bulk of the sample. The impedance analysis combined with modulus spectroscopy was also performed to get an insight of the microscopic features like grain, grain boundary and film–electrode interfaces and their effects in

the film. *R. Emerson et al* [88] studied the isomorphic substitution of lead by lanthanum atoms and reported some changes in the structural properties of $PbTiO_3$ host material. For instance, when lanthanum content is higher than 25% in mol, a diffuse character of the ferroelectric-to-paraelectric phase transition (DPT), which is a tetragonal-to-cubic transition, is observed. It has been reported that the lanthanum-induced modification concerning $PbTiO_3$ results in structural changes that can be directly related to the nature of the phase transition.

Doping has also been proved to be an effective way in controlling the ferroelectric behavior of lead titanate. The doping substituent can either occupy A-site, B-site or both as donor or acceptor based on chemical valance with respect to the original ions. Manganese (Mn^{3+}) as an acceptor ion may replace Ti^{4+} site and as addition segregates at grain boundaries [89]. Mn doping in lead titanate is also a good candidate for fabricating piezoelectric devices [90]. Mn belongs to valence unstable ions; it can affect the stability of the material. The introduction of an optimized amount of lanthanum (La) not only increases the stability but also softens the ferroelectric properties of materials. It also enhances the dielectric property and remnant polarization, as well as reducing the coercive field which is favored in ferroelectric random access mermory (FERAM) applications [91].

A. Shukla et al [92] studied that Mn^{4+} ion modified PLT and reported the detailed studies of dielectric and electrical properties. Their studies indicate that the material exhibits: (a) shifting of Curie temperature towards the lower temperature side on increasing Mn concentration, (b) increase in dielectric constant and electrical conductivity on increasing manganese concentration and (c) follow Arrhenius relation in the high temperature region. *M. Savinov et al* [93] studied that Mn doped $SrTiO_3$ ceramics and reveal strongly pronounced Arrhenius-type dielectric relaxation with activation energy 59–68 meV depending on the Mn concentration. Complex impedance spectroscopy (CIS) is a useful technique with enormous potential and possibilities for characterization of the electrical and electro-chemical properties of materials [94, 95]. Complex

impedance spectroscopy is normally used to distinguish between grain and grain boundary contributions and also been widely used in order to study the dielectric behaviors of crystalline and polycrystalline materials, especially ferroelectric materials [96]. The transformation of the arcs with temperature variation indicates the occurrence of a single relaxation process characterized by a distribution of relaxation times with a mean relaxation time. The most considered approach to interpret the depression of the semicircle is the statistical distribution of relaxation times [97]. The peaks are asymmetric and broader than the ideal Debye curve. The frequency range where the peaks occur is indicative of transition from long range to short range mobility [98].

Ce Sun et al [99] studied Al doped PT ceramics and reported the lattice dynamics and the crystal structure of $PbTi_{1-x}Al_xO_3$ with enhanced spontaneous polarization. The Al-doping reinforced the covalence of Pb–O (II), which indicated that the Pb–O hybridization was strengthened. The dopant Al without a d-orbit and d-electrons reinforced the covalence of Pb–O (II) in the $PbTi_{1-x}Al_xO_3$ system. *G. V. Lewis et al* [100] studied Al modified PT ceramics and investigated the series of trivalent dopants in titanate by using simulation and conductivity measurements. Their results indicated that Al^{3+} behaves as acceptors in most cases (B-site occupancy). *T. Iijima et al* [101,102] studied that the substitution of Al for Ti in $PbTiO_3$ and found to improve the dielectric constant effectively; also, Al-doped $PbTiO_3$ thin films showed a lower leakage current compared with that of a normal $PbTiO_3$ thin film. Therefore doping Al in $PbTiO_3$ might play an important role in crystal structure, lattice dynamics, and ferroelectricity. Aluminium does not have a bonding d-orbit or d-electrons, and has a stable valence and solely displays a valence of 3^+, different from the isovalent substitutions of Zr^{4+}, Hf^{4+}, Mn^{4+} for Ti^{4+}, so the aliovalent substitutions of Al^{3+} for Ti^{4+} in $PbTiO_3$ would be interesting for studying the doping effect on the structure, lattice dynamics, and ferroelectric properties [103-106].

$Pb(Zr,Ti)O_3$ or PZT is an important ferroelectric material with excellent dielectric and piezoelectric properties in compositions at the morphotropic phase boundary (MPB) region, where tetragonal and rhombohedral phases meet. The origins of the high properties are still being debated.

A recent interpretation is based on the discovery of a third, monoclinic phase in the MPB region [107-109]. *T. Ikeda et al* [110] reported lead zirconate titanate [$Pb(Zr,Ti)O_3$, PZT] a solid solution of ferroelectric $PbTiO_3$ ($T_c = 490^oC$) and anti-ferroelectric PbZrO3 ($T_c = 230^oC$). P. *Roychoudhary et al* [111], *S. L. Fu et al* [112], *R. Lal et al* [113], *W. Jackson et al* [114] and *T. B. Weston et al* [115] reported that due to high dielectric constant, piezoelectric and pyroelectric coefficients, spontaneous polarization and Curie temperature much above the room temperature, with different Zr/Ti ratios it has widely been used for various kinds of piezoelectric, pyroelectric and ferroelectric devices. *B. Jaffe et al* [116] and *Edson et al* [117] studied the mechanism of phase formation in PZT prepared by the partial oxalate method. They found that the $PbZr_xTi_{1-x}O_3$ (PZT) phase reacted with PbO forming the PZT phase without intermediate phase, and the XRD patterns showed coexistence of rhombohedral and tetragonal phases for $0.40 \leq x \leq 0.60$. In addition, low calcination temperature resulted in the rhombohedral phase. *Joseph and co-workers* [118] investigated the structure of $Pb(Zr_xTi_{1-x})O_3$ solid solution by the X-ray Rietveld method. The study showed that tetragonal and rhombohedral phase coexist even when Zr/Ti is 40/60.

Percira et al [119] reported on the effect of Nb^{5+} doping in PZT(65/35) that Nb_2O_5 was a good sintering aid for PZT based materials (high density, small grain size). Furthermore, the addition of Nb^{5+} decreased the dielectric constant. *Chandraprakash et al* [120] studied the structural and dielectric properties of $Pb_{0.925-x}Sm_xLa_{0.075}(Zr_{0.2}Ti_{0.8})_{0.95}O_3$; x = 0, 0.02 prepared by the double sintering ceramic method. They found that all compositions showed a single tetragonal phase and the dielectric constant increased with increasing Sm^{3+} concentration. The literature survey reveals that a considerable amount of work has been carried out on $Pb(Zr_{1-x}Ti_x)O_3$, at different compositions [121-123]. Depending upon the specific requirement of piezoelectric ceramics, suitable compositions of the PZT system may be chosen [124]. Also the crystal structure and novel physical properties can be tuned by replacing Pb and/or Zr and/or Ti with the substitution of smaller cations. In recent years, a lot of attention has been given to the substitution of suitable ions either at A or B-site in the perovskite lattice. In this context, a large number of ferroelectric

oxides of the perovskite structure have been fabricated and characterized [125, 126] It has been observed that the mode of phase transition in these compounds depends on the variation of the composition. Lots of work has been done on different kinds of modifications of PZT [127-130] both in forms of thin films and bulk, including modifications of PZT by substitution of Mn at B sites. *Guiffard et al* [131] have reported conductivity mechanisms of doubly doped (Mn with Nb/F) PZT ($Pb_{0.89}(Ba,Sr)_{0.11}(Zr_{0.52}Ti_{0.48})O_3$). *Klimov et al* [132] Studied the structural and piezoelectric properties of $(Pb_{0.960}Sr_{0.040})(Zr_{0.527}Ti_{0.467}Mn_{0.005})O_3$ system. *Hall and Cherdhirunkorn* [133] studied the effects of sintering on the phase and microstructures of $Pb(Zr_{0.52}Ti_{0.48})_{1-x}Mn_xO_3yF_y$ complex system. *Park et al*. [134] reported the piezoelectric properties of Nb and Nb/Mn co-doped $Pb(Zr_{0.53}Ti_{0.47})O_3$ ceramics. *B.Tiwari et al* [135] studied the effect of Mn-substitution on structural and dielectric properties of $Pb(Zr_{0.65-x}Mn_xTi_{0.35})O_3$ ceramics and reported the dielectric properties of PZMT, change in dielectric constant, and ac conductivity. *S. K. Pandey et al* [136] studied the Samarium (Sm) modified lead zirconate titanate (PSZT: $Pb_{1-x}Sm_x(Zr_{0.65}Ti_{0.35})O_3$ ceramics were synthesized by solid state ceramic route and reported the rhombohedral structure up to x = 0.04. with Sm substitution, the grain size first increases up to x = 0.02 and then decreases. *Balgovind Tiwari et al* [137] studied the polycrystalline samples of $Pb(Zr_{0.65-x}\ Mn_xTi_{0.35})O_3$ (PZMT) were prepared by a high-temperature solid-state reaction technique and reported the effect of compositional variation of manganese (Mn) on the electrical behavior of the PZMT systems have been carried out by a nondestructive complex impedance spectroscopy (CIS) technique at 400˚C. The Nyquist plots suggest that the grains only are responsible in the conduction mechanism of the materials. The occurrence of single arc in the complex modulus spectrum of all the compositions of Mn confirms the single-phase characteristics of the PZMT compounds, and also confirms the presence of non-Debye type of relaxation in the material. *Rajiv Ranjan et al* [138] studied the solid solutions of $Pb_{1-x}Sm_x(Zr_{0.55}Ti_{0.45})_{1-x/4}O_3$ (PSZT) were synthesized by mixed oxide method at high temperature and reported that dielectric properties of PSZT materials were made at various temperatures and frequencies which reveal that the compounds have transition temperature well

above the room temperature. The temperature dependence of AC conductivity indicated that the conduction process is due to singly ionized (in ferroelectric region). *S. R. Shannigrahi el al* [139] studied the Ferroelectric $Pb_{1-z}Nd_z(Zr_{0.60}Ti_{0.40})_{1-z/4}O_3$ (PNZT) powders have been prepared through the acetate alkoxide sol-gel techniques. X-ray diffraction (XRD) and Transmission electron microscope (TEM) studies indicate that the PNZT powders can be formed at 550°C in the perovskite structure. The pellet samples (sintered at 1300°C for 7 h) prepared from the above powders has high density. The SEM study shows the uniform distribution of spherical grains throughout the sample surface. Studies of dielectric and electrical properties show that PNZT has a diffuse phase transition of second order.

In addition, the results show that the parabolic scaling between grain and domain size is broken in Fe^{3+} doped PZT. Oxygen vacancies are expected to disrupt the continuity of the oxygen octahedral network and spontaneous polarization. The homogeneous region of polarization, which define ferroelectric domains should be of the same scale as the regions undisturbed by the defects [140-142]. Thus, despite the presence of nanodomains and a higher concentration of rhombohedral phase, Fe^{3+} ion doped ceramics exhibit lower properties than undoped samples. This suggests that the hardening effect of acceptor dopants is stronger than properties enhancement related to a finer domain wall structure [143-146]. *Moure et al* [147] reported the microstructure and piezoelectric properties of PZT doped with Fe^{3+} and Sb^{3+}.

2.3 Motivation of the present thesis work

The lead based perovskite material (PT, PZT) has so many technological applications such as: multilayer capacitor, dielectric resonator, thin film resistor, piezoelectric transducers, electrostrictive actuators, hydrogen sensor, electro optical modulator, laser host, switch magnetic bubble memory etc. The property of the lead based material can also be enhanced by substituting different transition materials within the perovskite. Again there is a very less report on the detailed crystal structure study (employing the Rietveld method) of the modified lead based perovskite

ceramics. There were no detailed study on crystal structure and physical properties of $Pb_{1-x}La_xTiO_3$ (PLT) at high concentration of La content. The introduction of an optimized amount of lanthanum (La) not only increases the stability but also softens the ferroelectric properties of the material. Also there was not much report on the detailed crystal structure (Employing the Rietveld method) and physical properties of B site modification of PLT with general formula $(Pb_{0.70}La_{0.30})(Ti_{1-x}A_x)O_3$, (A = Mn and Al). The main objective to study this material was to explore the structural and electrical properties of both iso (Mn^{3+}) and aliovalent (Al^{3+}) substitution on the B site of $Pb_{0.7}La_{0.3}TiO_3$ cubic perovskite. Manganese (Mn^{3+}) as an acceptor ion may replace Ti^{4+} site and an addition segregates at grain boundaries. Mn doping in lead titanate is also a good candidate for fabricating piezoelectric devices. Mn belongs to valence unstable ions; it can affect the stability of the material. Aluminium does not have a bonding d-orbit or d-electrons, and has a stable valence and solely displays a valence of +3, different from the isovalent substitutions for Ti^{4+}. So the aliovalent substitutions of Al^{3+} for Ti^{4+} in $Pb_{0.7}La_{0.3}TiO_3$ would be interesting for studying the doping effect on the crystal structure, lattice dynamics and electrical properties. The oxygen ion vacancy concentration in rare earth (La) and manganese modified lead titanate could have an important contribution to the electrical response of these materials.

There are lots of reports on the structural and electrical properties of modified lead zirconate titanate ceramics in the MPB region. But there is hardly found few reports on the detailed crystal structure (Employing the Rietveld method) of lead zirconate titanate in and around the MPB region which overcomes the existence of two phases. The doping substituent can either occupy A-site, B-site or both as donor or acceptor based on chemical valance with respect to the original ions. The substitution of the transition elements of the B-site will modify the electrical properties of the ferroelectric materials. It is also well known that the fluctuation of the oxidation state of the transition metal ions (Fe^{3+}, Mn^{3+}) results in the formation of oxygen ion vacancies to reserve the local electrical neutrality and causes thermally activated conduction.

2.4 Objective of the present thesis work

The main objective is to understand the crystal structure and electrical transport properties of modified PT and PZT ceramics. The followings are the objectives of the present thesis work:

1. To prepare the following single phase materials by ceramic route:

i. $(Pb_{1-x}La_x)TiO_3$ x = 0.00, 0.10, 0.25, 0.30 and 0.50

ii. $(Pb_{0.70}La_{0.30})(Ti_{1-x}Mn_x)O_3$ x = 0.00, 0.05, 0.10, 0.15 and 0.20

iii. $(Pb_{0.70}La_{0.30})(Ti_{1-x}Al_x)O_3$ x = 0.00, 0.05, 0.10, 0.15 and 0.20

iv. $Pb(Zr_{1-x}Ti_x)O_3$ x = 1, 0.35 and 0.65

v. $Pb(Zr_{0.65-x}Mn_xTi_{0.35})O_3$ x = 0.00, 0.05,0.10 and 0.15

vi. $Pb(Zr_{0.65-x}Fe_xTi_{0.35})O_3$ x = 0.00, 0.05, 0.10 and 0.15

2. The detailed crystal structure study by analyzing XRD patterns by employing the Rietveld refinement method with the help of FullProf program.

3. The morphological study by scanning electron microscope (SEM) and the elemental analysis of energy dispersive spectrum by using SEM-EDS.

4. The study of the electrical properties by the Impedance analyzer/Gain phase analyzer/ and or LCR meter.

An overview of the selection of the materials and various experimental techniques employed to characterize these materials is shown in the form of a flow chart given below.

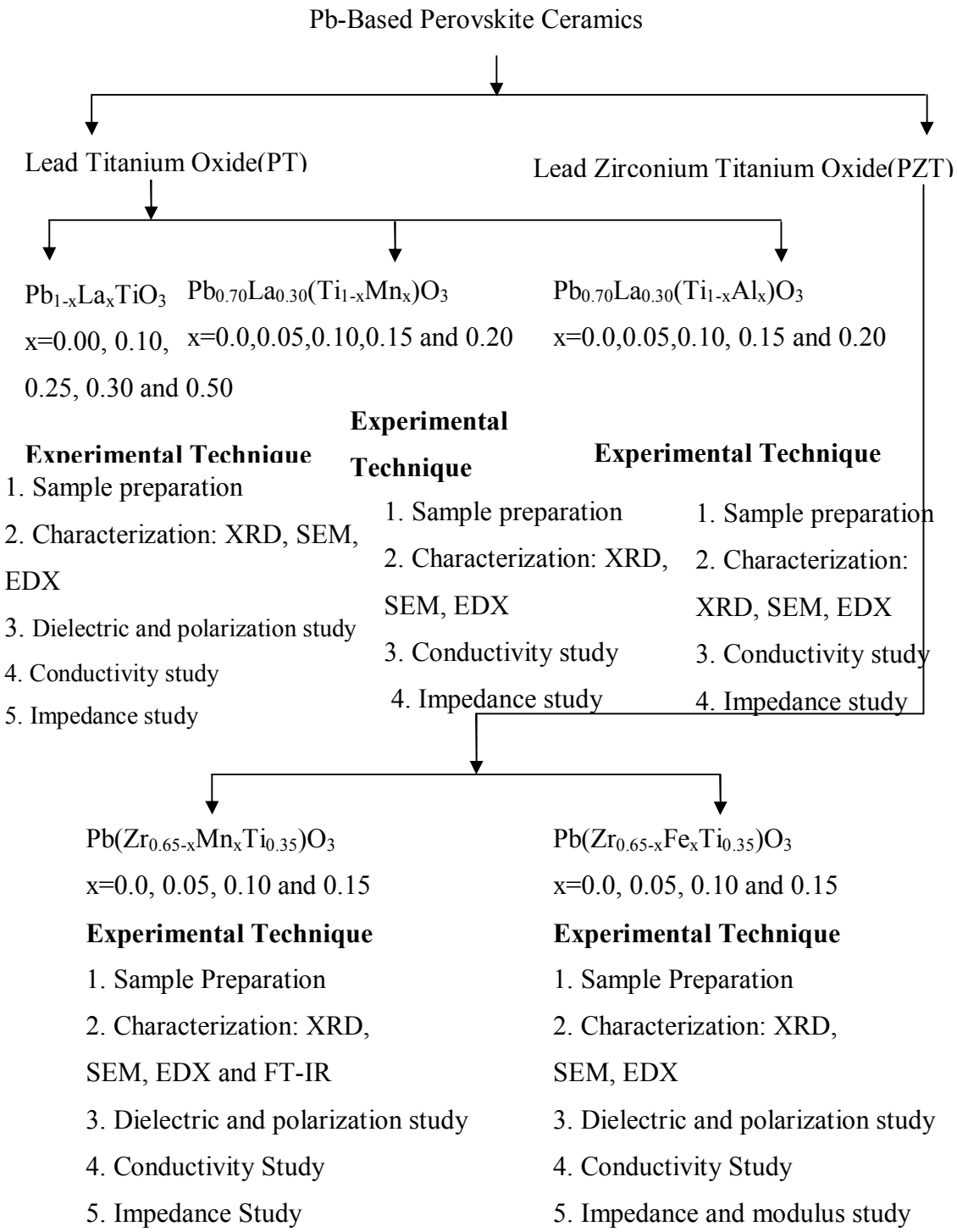
Pb-Based Perovskite Ceramics
Lead Titanium Oxide(PT)
Lead Zirconium Titanium Oxide(PZT)
$Pb_{1-x}La_xTiO_3$
x=0.00, 0.10, 0.25, 0.30 and 0.50
$Pb_{0.70}La_{0.30}(Ti_{1-x}Mn_x)O_3$
x=0.0,0.05,0.10,0.15 and 0.20
$Pb_{0.70}La_{0.30}(Ti_{1-x}Al_x)O_3$
x=0.0,0.05,0.10, 0.15 and 0.20
Experimental Technique
1. Sample preparation
2. Characterization: XRD, SEM, EDX
3. Dielectric and polarization study
4. Conductivity study
5. Impedance study
Experimental Technique
1. Sample preparation
2. Characterization: XRD, SEM, EDX
3. Conductivity study
4. Impedance study
Experimental Technique
1. Sample preparation
2. Characterization: XRD, SEM, EDX
3. Conductivity study
4. Impedance study
$Pb(Zr_{0.65-x}Mn_xTi_{0.35})O_3$
x=0.0, 0.05, 0.10 and 0.15
Experimental Technique
1. Sample Preparation
2. Characterization: XRD, SEM, EDX and FT-IR
3. Dielectric and polarization study
4. Conductivity Study
5. Impedance Study
$Pb(Zr_{0.65-x}Fe_xTi_{0.35})O_3$
x=0.0, 0.05, 0.10 and 0.15
Experimental Technique
1. Sample Preparation
2. Characterization: XRD, SEM, EDX
3. Dielectric and polarization study
4. Conductivity Study
5. Impedance and modulus study

CHAPTER 3

EXPERIMENTAL TECHNIQUES

CHAPTER 3

EXPERIMENTAL TECHNIQUES

In this chapter, the synthesis of the materials selected for present thesis work and the experimental techniques employed to characterize the samples are briefly discussed.

3.1 Synthesis

Nowadays, many studies have been carried out on the different synthesis methods, phase development, electrical and dielectric behavior of various perovskites structured ferroelectric ceramics. Ceramic materials are one of the major groups in the materials science because of their direct and indirect applications in day to day life. It is well known that the properties of materials are mostly dependent on the method of synthesis. Hence the synthesis of new ceramic powders is of great importance in the field of research work. There are several methods of preparation such as mechanical method, which includes solid-state reaction, and ball milling etc., and the chemical method, which includes sol-gel, wet-dry and polymer-sol-gel etc. To achieve a quality product with respect to purity, homogeneity, reactivity, particle size etc., each method finds its own advantages and disadvantages. In this contest, the solid-state reaction found to be the easiest, convenient and low cost technique among other available methods by means of performance, reliability, reproducibility and economy.

3.1.1 Solid state reaction method

The various steps in the solid-state reaction process are represented as a flow chart shown in Fig. 3.1. In the present work, raw powders with high purity are used for the material preparation. The constituents of the required specimen are taken in a stoichiometric ratio and dry mixed followed by wet mixing with acetone as a medium. The mixing is accomplished using agate mortar and pestle. The amount of acetone used is just enough to form slurry to prevent the selective sedimentation of the reagents. After proper mixing, mixed powders were annealed at different

temperatures by an indigenous programmable furnace with intermediate grinding to avoid agglomeration of the particles. The calcined powders were used for the study of their phase formation as well as their reaction mechanism. After studying the phase formation, the powders are again grounded and are mixed with poly vinyl alcohol (PVA) (which acts as a binder) to reduce the brittleness, and to have better compactness amongst the granules of the materials. The green pellets of dimension 10 mm diameter and 1 mm thickness are made using a uniaxial press with the help of a tungsten carbide dye. The pellets were kept at 600˚C for 2h to remove the binder and the process of heating should be slow enough to avoid the formation of cracks and blistering in the ceramics. Then the pellets are sintered to increase the density toughness of the sample with higher temperature with soaking time as minimum as possible. Heat treatment is different for different composition materials. Hence the detailed heat treatment is described in respective chapters.

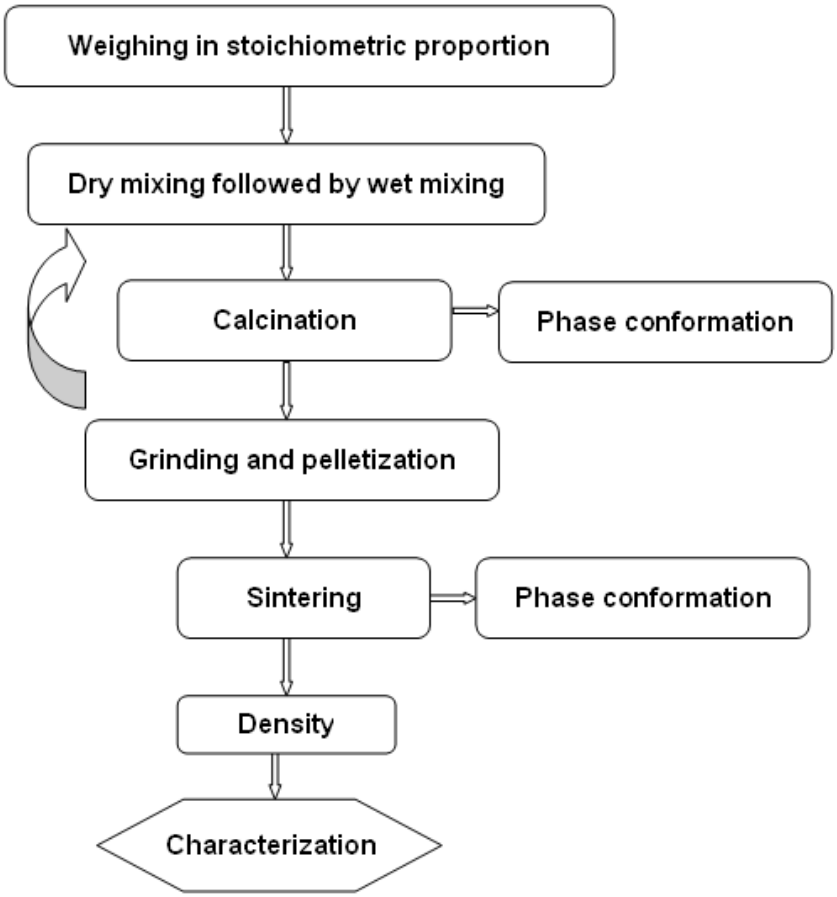

Fig. 3.1: Flow chart describing the various steps involved in solid-state reaction route.

To synthesize a lead based perovskite, one has to aware of certain important parameters: (i) toxic nature of lead oxide needs to careful handling to avoid health hazard and (ii) the volatile nature of PbO (as it starts evaporating at 750˚C) which creates vacancies at Pb and O sites [148,149] (*Smyth et al,* 1989; *Cho et al,* 1997). In the present case the calcinations and sintering were done within a special arrangement suggested by *Kingon* and *Clark* [150] in the presence of packing powder ($PbZrO_3$) to avoid PbO loss.

3.1.2 Sintering

The density of the electronic ceramic is a very sensitive parameter and that directly affects their properties. Therefore, proper sintering of the pellets is essential for electrical measurement. All the pellets were taken on an alumina plate and sintered at different temperature in a programmable furnace at a heating rate of 5^oC per minute with an intermediate shocking of 2 hours at 600^oC for organic binder removal in the initial heat treatment. A lead rich atmosphere was maintained to minimize lead loss during sintering.

3.2 Characterization

3.2.1 X-ray diffraction

The X- ray diffraction technique has been used to study the phase purity and crystal structure of the prepared compounds. Powder X-ray diffraction (XRD) measurements were carried out at room temperature using a commercial X-ray diffractometer supplied by X-pert MPD, Philips, UK by employing CuK_α radiation (1.5418Å). In the present investigation, all the XRD data were collected with the setting of 30mA current and 40kV voltage for X-ray generator. The instrument is based on the Bragg-Brentano geometry as shown in Fig. 3.2. In this geometry, the source to sample distance and the sample to detector distance are kept equal. A perspex sheet with a rectangular groove was used for sample mount where the powder sample was filled uniformly in the groove. The data were collected in an usual θ-2θ scan with an angular speed $1\text{-}2^0$/minute and a step size of $0.01\text{-}0.05^0$.

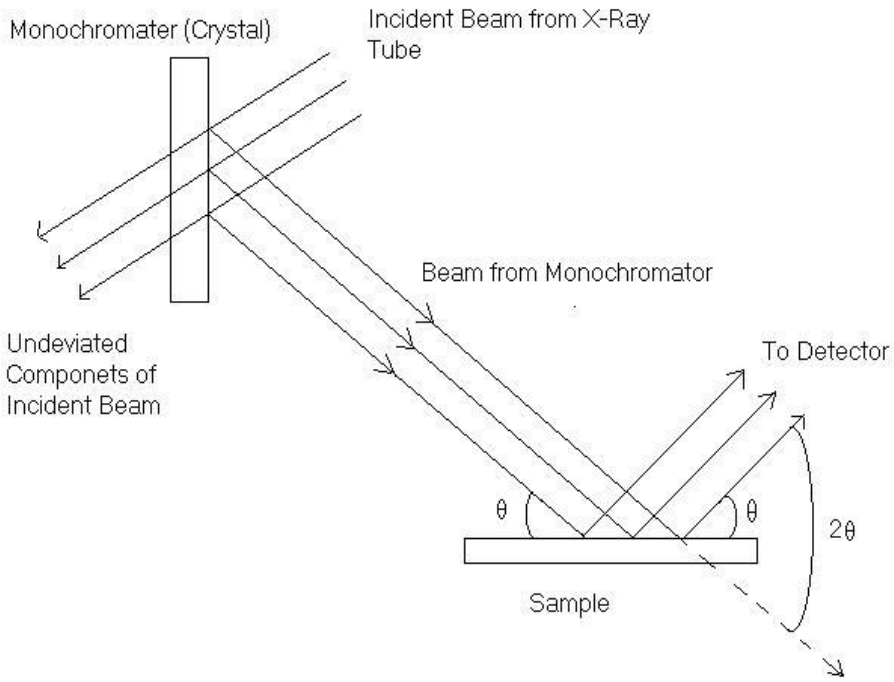

Fig. 3.2: Ray diagram of X- ray diffractometer.

All the XRD patterns were analyzed by employing the Rietveld profile refinement [151] with the help of Fullprof program to determine the crystal structure parameters. The lattice parameters, occupancy, atomic positions, scale factor, half-width parameters etc. were varied at the time of refinement.

Inter atomic distances (bond length) and bond angles were calculated using the refined fractional coordinates and lattice parameters as follows. Let us consider two position vectors A (x_1,y_1,z_1) and B (x_2,y_2,z_2), referred to the same base system consisting of three non-coplanar vectors r_1, r_2 and r_3, and they can be written as,

$$A \cdot B = \left(x_1 r_1 + y_1 r_2 + z_1 r_3\right) \cdot \left(x_2 r_1 + y_2 r_2 + z_2 r_3\right) \tag{3.1}$$

Equation 3.1 can be written as,

$$A \cdot B = \begin{bmatrix} x_1 & y_1 & z_1 \end{bmatrix} \begin{bmatrix} r_1 \cdot r_1 & r_1 \cdot r_2 & r_1 \cdot r_3 \\ r_2 \cdot r_1 & r_2 \cdot r_2 & r_2 \cdot r_3 \\ r_3 \cdot r_1 & r_3 \cdot r_2 & r_3 \cdot r_3 \end{bmatrix} \begin{bmatrix} x_2 \\ y_2 \\ z_2 \end{bmatrix} \tag{3.2}$$

The above equation can be written in simple form as,

$$A \cdot B = A^{/} GB \tag{3.3}$$

Here $A^{/}$ is a transpose matrix of A, and G is a matrix tensor. The elements $g_{ij} = r_i \cdot r_j$ are the scalar product of the base vectors. Let us assume that A = B, so that the equation 3.3 will be,

$$A \cdot A = |A| \cdot |A| = A^{/} GA \tag{3.4}$$

$$\Rightarrow |A| = \sqrt{A^{/} GA} \tag{3.5}$$

The scalar product of two vectors can be written as,

$$A \cdot B = |A||B|\cos(\theta) \tag{3.6}$$

Where, θ is the angle between the vectors A and B. Using Equations 3.5 and 3.6, we can get,

$$\cos(\theta) = \frac{A^{/} GB}{\sqrt{A^{/} GA} \cdot \sqrt{B^{/} GB}} \tag{3.7}$$

Eqns. 3.5 and 3.7 are generally used to obtain the vector lengths and the angles between the vectors. In crystallography, the vectors r_1, r_2, r_3 can be replaced by lattice parameters a, b and c (translation vectors). The inter atomic bond length'd' can be obtained using the following matrix product,

$$d^2 = \begin{bmatrix} \Delta x & \Delta y & \Delta z \end{bmatrix} \begin{bmatrix} a \cdot a & a \cdot b & a \cdot c \\ b \cdot a & b \cdot b & b \cdot c \\ c \cdot a & c \cdot b & c \cdot c \end{bmatrix} \begin{bmatrix} \Delta x \\ \Delta y \\ \Delta z \end{bmatrix} \tag{3.8}$$

Here x, y, z and x+Δx, y+Δy and z+Δz are the positions of two atoms forming the bonds in fractional coordinates. For an orthorhombic system ($a \neq b \neq c$ and $\alpha = \beta = \gamma = \pi/2$), the bond length is found to be,

$$d = \sqrt{a^2\Delta x^2 + b^2\Delta y^2 + c^2\Delta z^2} \tag{3.9}$$

Similarly for a hexagonal system ($a = b \neq c$, $\alpha = \beta = \pi/2 \neq \gamma = 2\pi/3$),

$$d = \sqrt{a^2\Delta x^2 + b^2\Delta y^2 + c^2\Delta z^2 - ab\Delta x\Delta y} \tag{3.10}$$

3.2.1.1 Bragg-Brentano geometry

Sample height variations can cause peak shift when using Bragg-Brentano geometry shown in Fig. 3.3. The sample height effects are cancelled out when using a parallel beam. Resolution is not as good as for Bragg-Brentano geometry and analyses can take slightly longer as the scintillation detector must be used instead of the position sensitive detector. Bragg-Brentano geometry is definitely the best choice for indexing, structure solution and Rietveld analysis of powder samples.

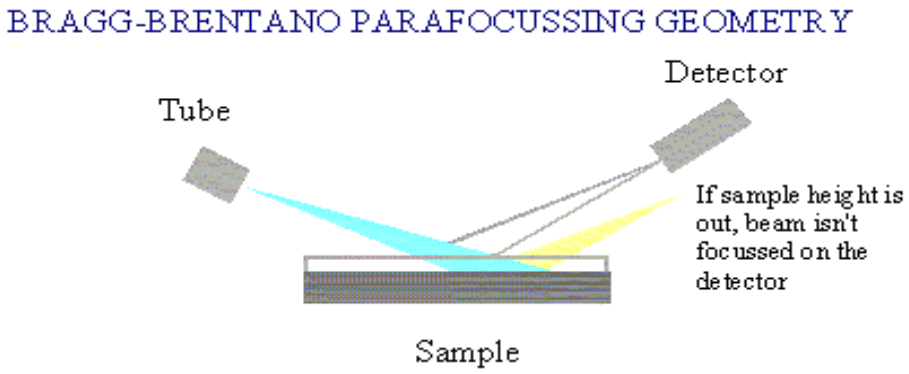

Fig. 3.3: "Bragg-Brentano geometry".

3.2.2 Rietveld refinement technique

Rietveld refinement is a technique devised by Hugo Rietveld [151] which is used to characterize the crystalline materials. The neutron and X-ray diffraction of powder samples results in a pattern characterized by reflexes (peaks) in intensity at certain positions. The height, width and position of these reflections can be used to determine many aspects of the materials structure. The Rietveld method uses a least squares approach to refine a theoretical line profile until it matches the measured profile. The introduction of this technique was a significant step forward in the diffraction analysis of powder samples. The method was first reported for the diffraction of monochromatic neutrons where the reflection-position is reported in terms of the Bragg angle 2θ. This terminology will be used here although the technique is equally applicable to alternative scales such as X-ray energy or neutron time-of-flight. The only wavelength and technique independent

scale is in reciprocal space units or momentum transfer Q, which is historically rarely used in powder diffraction but very common in all other diffraction and optics techniques. The relation is

$$Q = \frac{4\pi \sin(\theta)}{\lambda} \tag{3.11}$$

The shape of a powder diffraction reflection is influenced by the characteristics of the beam, the experimental arrangement, and the sample size and shape. In the case of monochromatic neutron sources the convolution of the various effects has been found to result in a reflex almost exactly Gaussian in shape. If this distribution is assumed then the contribution of a given reflection to the profile y_i at position $2\theta_i$ is:

$$y_i = I_k exp\left[-4ln\left(\frac{2}{H_k^2}\right)(2\theta_i - 2\theta_k)^2\right] \tag{3.12}$$

Where H_k is the full width at half peak height (full-width at half-maximum), $2\theta_k$ is the centre of the reflex, and I_k is the calculated intensity of the reflex (determined from the structure factor, the Lorentz factor, and multiplicity of the reflection). At very low diffraction angles the reflections may acquire an asymmetry due to the vertical divergence of the beam. Rietveld used a semi-empirical correction factor, A_s to account for this asymmetry

$$A_s = 1 - \left[\frac{sP(2\theta_i - 2\theta_k)^2}{tan\theta_k}\right] \tag{3.13}$$

Where P is the asymmetry factor and s is +1, 0, -1 depending on the difference $2\theta_i$-$2\theta_k$ being positive, zero or negative respectively. At a given position more than one diffraction peak may contribute to the profile. The intensity is simply the sum of all reflections contributing at the point $2\theta_i$. The width of the diffraction peaks are found to broaden at higher Bragg angles. This angular dependency was originally represented by

$$H_k^2 = U \tan^2 \theta_k + V \tan \theta_k + W \quad (3.14)$$

Where U, V and W are the half width parameters and may be refined during the fit. In powder samples there is a tendency for plate or rod-like crystallites to align themselves along the axis of a cylindrical sample holder. In solid polycrystalline samples the production of the material may result in a greater volume fraction of certain crystal orientations. In such cases the reflex intensities will vary from that predicted for a completely random distribution. The Rietveld method allowed for moderate cases of the former by introducing a correction factor [152],

$$I_{corr} = I_{obs} \exp\left(-G\alpha^2\right) \quad (3.15)$$

Where I_{obs} is the intensity expected for a random sample, G is the preferred orientation parameter and α is the acute angle between the scattering vector and the normal of the crystallites. The principle of the Rietveld method is to minimize a function M which analyzes the difference between a calculated profile y (calc) and the observed data y (obs). Hugo Rietveld defined such an equation with W_i is the statistical weight and c is an overall scale factor such that $y^{cal} = Cy^{obs}$ is given by

$$M = \sum_i W_i \left\{ y_i^{obs} - \frac{1}{c} y_i^{calc} \right\}^2 \quad (3.16)$$

The quality of the agreement between observed and calculated profiles is measured by set conventional factors. In FullProf program two sets of indices are calculated, according to the meaning of the integer n. In the first set n is the total number of points used in the refinement (n =*NPTS-NEXC* = total number of points in the pattern minus total number of excluded points). Structure and microstructure refinements were carried out simultaneously by refining, scale factors, lattice parameters, occupancy factors, variable fractional atomic coordinates, particle size, r.m.s. lattice strain, preferred orientation factors, background, shift lattice constants, isotropic

thermal parameters, strain anisotropy factor, atomic functional positions, bond lengths and bond angles etc. of individual phases. Considering the integrated intensity of the peaks as a function of structure/microstructure parameters only, the Marquardt least-squares procedures were adopted for minimizing the difference between the observed and simulated powder diffraction patterns.

The quality of the refinements are known based on the values of reliability factors such as, R_p, R_{wp}, R_{exp}, R_{Bragg}, R_F and χ^2 and they are defined as follows.

$$\text{Profile factor, } R_p = 100\frac{\sum_{i=1,n}\left|y_i - y_{c,i}\right|}{\sum_{i=1,n} y_i} \tag{3.17}$$

Here 'y_i' is the observed point (experimental) and '$y_{c,i}$' is the calculated point and n represents the number of data points.

$$\text{Weighted profile factor, } R_{wp} = 100\left[\frac{\sum_{i=1,n}\omega_i\left|y_i - y_{c,i}\right|^2}{\sum_{i=1,n}\omega_i y_i^2}\right]^{1/2} \tag{3.18}$$

Here $\omega_i = \frac{1}{\sigma_i^2}$, σ_i^2 is the variance of observation y_i.

$$\text{Expected weight factor, } R_{\exp} = 100\left[\frac{n-p}{\sum_{i=1,n}\omega_i y_i^2}\right]^{1/2} \tag{3.19}$$

Here *(n – p)* is the number of degrees of freedom. '*n*' is the total number of experimental points and '*p*' is the number of refined parameters.

$$\text{Reduced chi-square, } \chi^2 = \left[\frac{R_{wp}}{R_{\exp}}\right]^2 \tag{3.20}$$

$$\text{Bragg factor, } R_B = 100\frac{\sum_h\left|I_{obs,h} - I_{calc,h}\right|}{\sum_h I_{obs,h}} \tag{3.21}$$

Here '*h*' is the vector which levels the Bragg reflections. The $I_{obs,h}$ is the observed integrated intensities and $I_{calc,h}$ is the calculated intensities.

$$\text{Crystallographic } R_F \text{ factor, } R_F = 100\frac{\sum_h\left|F_{obs,h} - F_{calc,h}\right|}{\sum_h F_{obs,h}} \tag{3.22}$$

Here $F_{obs,h}$ and $F_{calc,h}$ are the observed and calculated structural factors respectively. The goodness of fit (GoF) is established by comparing $R_{wp}$with the expected error, R_{exp}. The background was corrected using a Chebyschev polynomial of the first kind. The diffraction peak profiles were better fitted by the Thompson-Cox-Hastings pseudo-Voigt (*PV-TCH*) function and by the asymmetry function described by *Finger et al* (1994) [153]. The pseudo-voight function was chosen for the profile shape refinement because it is used to resolve strain and size contribution to peak broadening. The *PV(x)* (Pseudo Voigt) function is a linear combination of a Lorentzian L' and a Gaussian G' of the same FWHM. So there are two parameters characterizing the peak shape: $PV(x) = PV(x, \eta, H)$. If the $L'(x)$ and $G'(x)$ are normalized, *PV(x)* is also normalized. The integral breadth of a normalized Pseudo-Voigt function is just the inverse of the maximum value. The FWHM is the same for *L(x)*, *G(x)* and *PV(x)*. The strain anisotropy was corrected by the phenomenological model described by *Stephens et al* (1999**)** [154]**.**

3.2.3 Estimation of crystallite size

The studies on crystalline materials require an accurate determination of crystallite size as well as the microstrain induced in the material. X-ray diffraction (XRD) and transmission electron microscopy (TEM) are the two well known techniques for this purpose. Based on XRD principles, numerous approaches such as the use of Scherrer equation, integral breadth analysis, single line approximation, Hall Williamson method, Rietveld refinement method etc. have been developed for the crystallite size determination.

An accurate estimation of crystallite size becomes essential when such materials are produced with their crystallite size of the order of less then 100nm. Though TEM is one of the powerful techniques for crystallite size measurement, it has certain limitations. Since TEM images represent only a local region, many samples and images are required to provide average information for the entire sample. Not only this, the TEM sample preparation method is an involved and time consuming one. The XRD technique is free from these limitations. XRD is, for other hand, a simpler and easier approach for the determination of the crystallite size for powder samples.

The reduced crystallite size, the lattice strain and instrumental effects accounts for the total broadening of XRD peaks. When the crystallites of a material are smaller (less than 100nm) they have too small a number of parallel diffraction planes and eventually they produce broadened diffraction peaks instead of sharp peaks. Lastly, instrumental factors such as unresolved α_1 and α_2 peaks for imperfect focusing also lead to line broadening. The observed peak broadening β_0 may be represented as

$$\beta_0 = \beta_i + \beta_r \tag{3.23}$$

Here β_0 is the observed peak broadening in radians; β_i= broadening due instrumental factors, in radians and β_r =broadening due crystallite size and lattice strain. The above equation holds good if the diffraction peaks exhibit purely Cauchy profile. However, when the diffraction peaks show a mixed behavior (i.e. partly Cauchy and partly Gaussian) for their profiles, the following equation holds well,

$$\beta_r = \left[(\beta_o - \beta_i)(\beta_o^2 - \beta_i^2)^{1/2}\right]^{1/2} \tag{3.24}$$

Now according to Scherrer equation, the broadening due to small crystallite size can be written as [155-157],

$$\beta_c = k\lambda / S_c cos\theta \tag{3.25}$$

Here β_c= broadening solely due to small crystallite size, k = constant whose value depends on particle shape and usually taken as 1.0; S_c is the small crystallite size in nanometers; θ is the Bragg's angle; λ is the wavelength of X-ray beam in nm.

According to Wilson the broadening due to lattice strain may be expressed by the relation [158],

$$\beta_s = e \tan\theta \tag{3.26}$$

Here β_s= Peak broadening due to lattice strain, 'e' is the strain distribution within the material.

Using the equation 3.25 and equation 3.26, the total peak broadening

$$\beta_r = k\lambda / S_c cos\theta \ + e \tan\theta \tag{3.27}$$

Multiplying cosθ on both sides of the above equation [159], then one can get

$$\beta_r \cos\theta = k\lambda/S_c + e \sin\theta \quad (3.28)$$

Further it may be clarified that the error in evaluating the crystallite size turns out to be quite high due to scattering of data and also instrumental broadening factor is not taken into account. So it is not very meaningful to estimate the error in determination of crystallite size using Hall-Williamson method [159].

The effect of the synthesis and processing conditions are reflected in the structural strain of the samples. The broadening of reflections due to microstrains was considered to have angular dependence of the form

$$FWHM^2_{STRAIN} = D^2_{ST} tan^2\theta \quad (3.29)$$

Where FWHM = Full Width Half Maximum, D_{ST} = Coefficient related to strain, θ = Bragg diffraction angle. The Scherrer's formula is given as [157],

$$FWHM^2_{size} = \frac{IG}{(cos\theta)^2} \quad (3.30)$$

Where IG is a measure of the isotropic size effect. The size is related to IG as

$$S_C = \frac{180K\lambda}{\left(\pi(IG)^{1/2}\right)} \quad (3.31)$$

Where λ is the CuK_α wavelength and K is the Scherrer's crystal shape, generally close to unit for circular shape.

Finally, the Rietveld refinement method [152] is developed for the estimation of crystallite size, which may be written as

$$FWHM^2 = \left(U + D^2_{ST}\right)\left(tan^2\theta\right) + V\left(tan\theta\right) + W + \frac{IG}{cos^2\theta} \quad (3.32)$$

Where U, V and W are the usual peak shape parameters, IG is a measure of the isotropic size effect, D_{ST} = Coefficient related to strain. IG & D_{ST} can be refined in Rietveld method.

Rietveld method is the more accurate method than W.H method and Scherer method for crystallite size estimation of powder samples in view of the ability of the former approach to measure the pure breadth of the diffraction peaks i.e. solely due to smaller crystallite size.

3.2.4 Scanning electron microscopy (SEM)

The scanning electron microscopy (SEM) is a useful technique to study the topography, morphology and composition of the materials with much higher resolution. When a beam of highly energetic electrons strikes the sample, the secondary electrons, x-rays and back-scattered electrons are ejected from the sample as shown in Fig. 3.4(a). The X-ray photon may be absorbed by an atom resulting in the ejection of one of the bound electrons of that atom. The energy distribution of emitted X-rays and electrons is shown in Fig. 3.4(b) and Fig. 3.4(c) respectively. These electrons are then collected by the detector and convert into a signal that displays on a screen. In the present study, the SEM micrograph was taken on the fractured surface of the sample using scanning electron microscope (SEM: JSM-840 Scanning electron microscope JEOL).

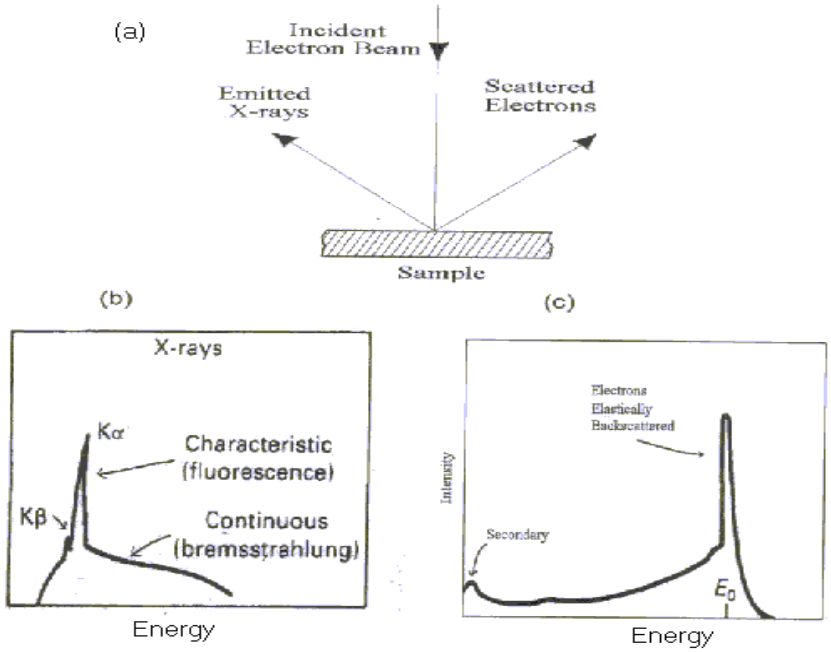

Fig.3.4 (a-c): (a) The scattering process of an electron beam in SEM. The energy distribution of (b) X-rays and (c) electrons, after emission from the sample surface.

As some of the samples are non-conducting, a thin layer of platinum is coated using a sputter coater. For measurement of the grain size, some lines of known length were drawn to the micrograph. The number of grains cut by the lines was counted. Then the average grain sizes were

calculated by dividing the length of the line by the no of grain coming under that line. Minimum 10 lines, each having the length not less than 200 micrometers were drawn on the different places of a single micrograph and average grain sizes were calculated to minimize the error.

3.2.4.1 Energy-dispersive X-ray spectroscopy (EDS)

Energy dispersive X-ray spectroscopy (EDS) is an analytical technique used for the elemental analysis or chemical characterization of a sample. It is one of the variants of X-ray fluorescence spectroscopy which relies on the investigation of a sample through interactions between electromagnetic radiation and matter, analyzing X-rays emitted by the matter in response to being hit with charged particles. Its characterization capabilities are due in large part to the fundamental principle that each element has a unique atomic structure allowing X-rays that are characteristic of an element's atomic structure to be identified uniquely from one another. There are four primary components of the EDS setup: the beam source; the X-ray detector; the pulse processor; and the analyzer. A number of free-standing EDS systems exist. However, EDS systems are most commonly found on scanning electron microscopes (SEM-EDS) and electron microprobes. Scanning electron microscopes are equipped with a cathode and magnetic lenses to create and focus a beam of electrons, and since the 1960s [160,161] they have been equipped with elemental analysis capabilities. A detector is used to convert X-ray energy into voltage signals; this information is sent to a pulse processor, which measures the signals and passes them onto an analyzer for data display and analysis.

3.2.5 Electroding

The selection of suitable electrode for the test materials is important. In the present thesis work contacting, conducting thin film electrode method is adopted because (i) it causes a minimum error caused by an air gap between the electrode and the surface of the test material, which is more in case of contacting rigid metal electrode method, and (ii) procedure to measure dielectric

constant are simple, which are relatively complex in non-contacting electrode method. In our case, all the ceramic bodies after sintering were polished well and coated on both sides with conducting silver paste.

3.2.6 Dielectric measurement

To measure the relative dielectric constant and dielectric loss, LCR meter can be used. In this work (few of the samples), the relative dielectric constant and dielectric loss measurements were carried out at an AC input signal level of 1.3 V peak to peak over a wide temperature (40C–500^0C) and frequency (100Hz–1MHz) range using a computer-controlled Solartron *IMPEDANCE/GAIN-PHASE ANALYZER SI 1260* (Model) in the department of ceramic engineering, NIT, Rourkela and the rest of the samples have been measured in the dielectric (capacitance and dissipation) and impedance parameters (i.e. and phase angle) were obtained at an input signal level of 1.3V in a wide temperature and frequency using a computer-controlled *LCR HiTESTER/Impedance analyzer(HIOKI 3522-50)* which was also attached with high temperature microwave furnace *(Model:DPI-1200)* in the department of physics and meteorology (solid state ionic Laboratory) in Indian Institute of Technology, Kharagpur. The electrode samples were used to make the measurements. The LCR meter, was interfaced with the computer and the data (capacitance and D factor) was collected as a function of temperature at different frequencies.

When a dielectric material is subjected to an electric field, polarization takes place due to induced dipole moment or rotation of permanent electric dipoles present in the material. The macroscopic behavior of a dielectric can be understood by considering the dielectric in between the parallel plate capacitor. Fig. 3.5 (a, b) shows the AC voltage and current with a dielectric.

The measured capacitance was then converted into dielectric constant using the following formula [162-165],

$$C = \frac{\varepsilon_r \varepsilon_0 A}{d} \tag{3.33}$$

$$\varepsilon_r = \frac{Cxd}{\varepsilon_0 xA} \tag{3.34}$$

Where, C: Capacitance in farad (F),

ε_0 : Permittivity of free space in farad per meter (8.85 x 10^{-12} F/m),

ε_r : Dielectric constant or relative permittivity of the sample,

A : Area of each plane electrode in square meters (m^2), d: Separation between the electrodes in meters (m).

When an alternative potential $V=Voei\omega t$ is applied, the total current in the dielectric is given by $I=j\omega\varepsilon_r c_o V$ (3.35)

As ε_r is the complex quantity i.e. $\varepsilon_r = \varepsilon_r^{'} - j\varepsilon_r^{''}$, I can be written as

$$I = J\omega\varepsilon_r^{'} - j\varepsilon_r^{''} c_0 V \tag{3.36}$$

The value of $\varepsilon_r^{'}$ determines the out-of phase component of the current and the value of $\varepsilon_r^{''}$ determines the in-phase component of the current.

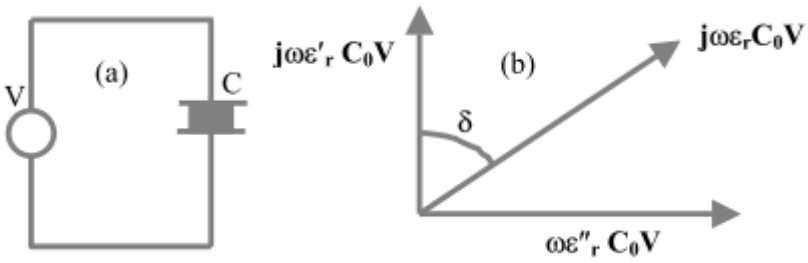

Fig.3.5 (a, b): (a) AC voltage applied to capacitor with a dielectric between the plates and (b) The current leads the applied voltage by (90°-δ).

$\tan\delta = \frac{\varepsilon_r^{''}}{\varepsilon_r^{'}}$, tan δ is called the loss factor or dielectric loss or dissipation.

The ac conductivity can determine by the relation

$$\sigma_{ac} = \varepsilon_0 \varepsilon_r \omega \tan\delta \tag{3.37}$$

$$\sigma_{ac} = \varepsilon_0 \varepsilon_r 2\pi f \tan\delta \tag{3.38}$$

3.2.7 Polarization measurement

Polarisation measurement has been carried out by using P-E loop tracer supplied by M/s. Marine India PE loop tracer. All the samples were pooled at 5kV. Experimental conditions are discussed in respective chapters. The temperature variation of remnant polarization (P_r), spontaneous polarization (P_s) and coercive field (E_c) of the samples were recorded.

3.2.8 Complex impedance spectroscopy (CIS) analysis

The complex impedance spectroscopy [166] is a powerful tool to investigate the electrical properties of the complex perovskite oxides. The main advantages of the techniques include: i) it involves relatively simple electrical measurements that can readily be automated, ii) the measurements can be implemented by using arbitrary electrodes, iii) the results can be often correlated with the properties such as composition, microstructure, defects, dielectric properties, chemical reaction etc. of the sample, iv) the resistance of the grain boundaries and that of grains can be easily separated in most of the polycrystalline samples. AC measurements are often made with a Wheatstone bridge type of apparatus (LCR HiTESTER/Impedance analyzer (HIOKI 3522-50)/ Solartron *IMPEDANCE/GAIN-PHASE ANALYZER SI 1260* (Model) in which the resistance R and capacitance C of the sample are measured and balanced against variable resistors and capacitors. The impedance $|Z|$ and the phase difference (θ) between the voltage and current are measured as a function of frequency for the given sample and the technique is called impedance spectroscopy. Analysis of the data is carried out by plotting the imaginary part of the impedance $Z''=|Z|\cos\theta$ against the real part $Z'=|Z|\sin\theta$ on a complex plane called the impedance plot. An impedance plot with linear scale is used to analyze the equivalent circuit as follows. Impedance plot of a pure resistor is a point on real axis and that of pure capacitor is a straight line coinciding with the imaginary axis. The impedance of a parallel RC combination is expressed by the following relation,

$$Z^* = Z' - jZ'' = \frac{R}{1 + j\omega RC} \tag{3.39}$$

After simplification, one gets

$$(Z' - \frac{R}{2})^2 + Z''^2 = (\frac{R}{2})^2 \tag{3.40}$$

$$Z' = \frac{R}{1 + (\omega RC)^2} \tag{3.41}$$

$$Z'' = \frac{R(\omega RC)}{(1 + \omega RC)^2} \tag{3.42}$$

ω is the angular frequency, which represents the equation of a circle with radius R/2 and center at (R/2,0). Thus, a plot of Z' vs. Z″ (as parametric function of) will result in a semicircle of radius R/2 as shown in Fig. 3.6(a) and the equivalent circuit is shown in Fig. 3.6 (b). (This plot is often called a Nyquist plot). The time constant of the simple circuit is defined as

$$\tau = R_g C_g = \frac{1}{\omega_m} \tag{3.44}$$

This corresponds to the relaxation time of the sample and the characteristic frequency lies at the peak of the semi-circle. In an ideal polycrystalline sample, the impedance plot exhibits an arc at high frequency corresponds to the bulk property of the sample, an arc at low frequency corresponds to the grain boundary behavior and a spike at the lowest frequency corresponds to the electrode effect. Fig. 3.7 (a) shows a typical impedance plot for a polycrystalline sample and Fig 3.7 (b) represented the equivalent circuit. The Fig. 3.8 shows the photograph of the arrangement used for the dielectric and impedance measurement.

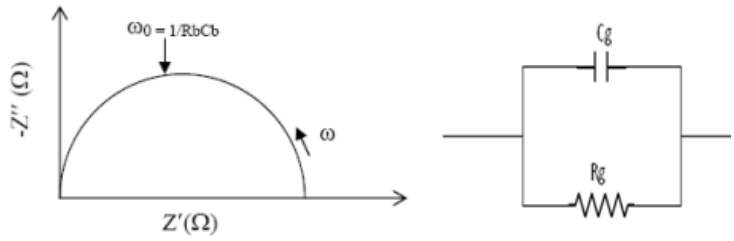

(a) (b)

Fig. 3.6 (a, b): (a) The impedance plot for a circuit of a resistor and a capacitor in parallel and (b) the corresponding equivalent circuit

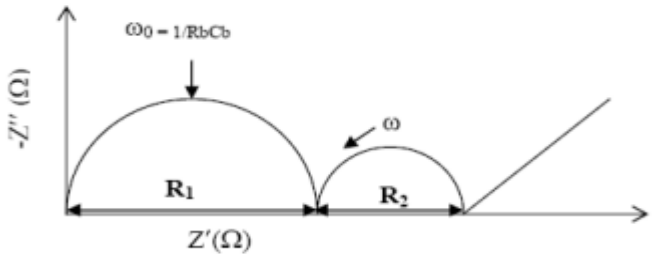

(a)

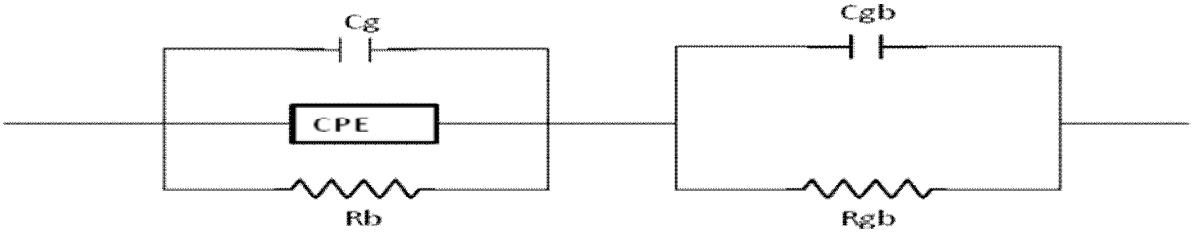

(b)

Fig. 3.7 (a, b): (a) The impedance plot for an ideal polycrystalline sample and (b) the corresponding equivalent circuit

Fig. 3.8: The photograph of the arrangement used for the dielectric and impedance measurement.

CHAPTER 4

STRUCTURAL ANALYSIS AND ELECTRICAL BEHAVIOR OF $Pb_{1-x}La_xTiO_3$ CERAMICS

CHAPTER 4

STRUCTURAL ANALYSIS AND ELECTRICAL BEHAVIOR OF $Pb_{1-x}La_xTiO_3$ CERAMICS

This chapter aims to study various physical properties of La free and lanthanum modified lead titanate ceramic. The chapter starts with the synthesis followed by characterization of the materials. The sample is synthesized by solid state reaction route and then characterized by XRD, SEM, EDS, dielectric and complex impedance techniques. The Rietveld refinement method was employed for structural analysis. The diffused phase transition was analyzed by dielectric measurements. The electrical properties are studied by complex impedance spectroscopy (CIS) technique.

4.1 Sample preparation

The $Pb_{1-x}La_xTiO_3$ (x = 0.0, 0.10, 0.25, 0.30 and 0.50) compounds were prepared by conventional solid state route as discussed in chapter 3. The stoichiometric ratio of starting compounds such as lead oxide (PbO, 99%), lanthanum oxide (La_2O_3, 99.9%) and titanium oxide (TiO_2, 99%) were weighed by using a high precision electronic balance. The above compounds were mixed and grinded under acetone using agate mortar and pestle. The grinding was carried out under acetone till the acetone evaporates from the mortar. The mixture was ball milled for 8h to make homogeneous mixture and calcined at 900^0C for 6h. The fine powders of the above samples were pressed into cylindrical pellets of 6 mm diameter and 1 mm thickness under a uni-axial pressure of 6 ton using a hydraulic press. Finally the pellets were sintered at 1100^0C for over 4h with 5% extra lead oxide to compensate the lead loss at high temperature and then cooled to room temperature at the rate of 2^0C min^{-1}. All the above sintering processes were carried out in the air.

4.2 Results and discussion

4.2.1. X-ray diffraction analysis by employing the Rietveld method

The XRD patterns of all the samples were recorded by using Philips PANalytical X'pert-MPD X-ray diffractometer (XRD) (Model- PW3020). The CuKα radiation was used as an X-ray source. The machine was operated at 35kV and 30mA. The data were collected with step size of 0.02^0 and time constant of 1 second. The XRD patterns of $Pb_{1-x}La_xTiO_3$ (PLT) for x = 0, 0.10, 0.25, 0.30 and 0.50 calcined at 900^0C for 6 h are shown in Fig. 4.1. All the samples are in the single phase form. The XRD patterns of x = 0 (La free sample) could be indexed to *P4mm* space group in tetragonal symmetry. However, the La doped samples (x = 0.10, 0.25, 0.30 and 0.50) could be indexed using $Pm\bar{3}m$ space group in cubic symmetry. The overlap of the three tetragonal reflections (102), (201) and (210) confirms the tetragonal-to-cubic phase transition. We have not observed any peak corresponds to *P4mm* space group in the XRD pattern of x = 0.10 sample. Hence, it has been found that a phase transition from tetragonal to cubic symmetry with increase of La concentration. Similar behavior has been observed by other research groups [83] on $Pb_{1-x}La_xTiO_3$ materials.

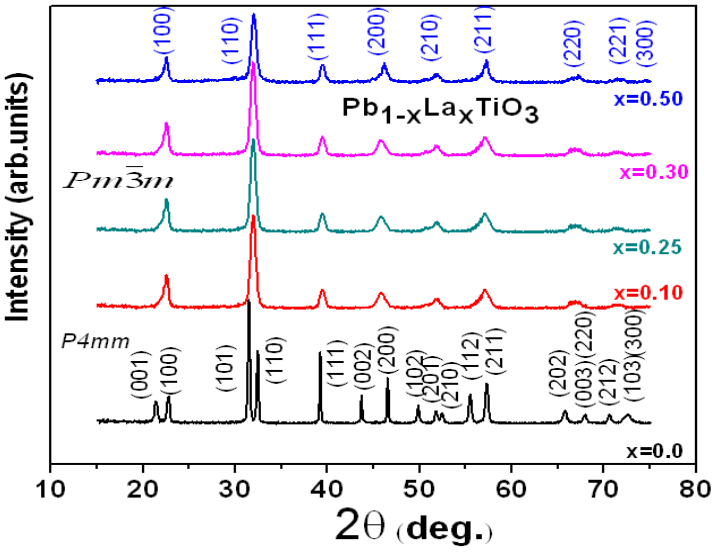

Fig. 4.1: XRD patterns of $Pb_{1-x}La_xTiO_3$ (PLT) compound for x = 0, 0.10, 0.25, 0.30 and 0.50 calcined at 900˚C for 6h.

The XRD patterns of the samples sintered at 1100^0C for 4h are shown in the Fig. 4.2. We have observed that, the broadening of XRD peaks has been reduced in 1100^0C sintered samples compare to that of 900^0C calcined samples. We have not observed any additional peak in 1100^0C sintered samples compare to that of 900^0C calcined sample. It reveals that, the structure does not change with the increasing of annealing temperature. However, the crystallite size increases with the increasing of annealing temperature which is discussed in next section.

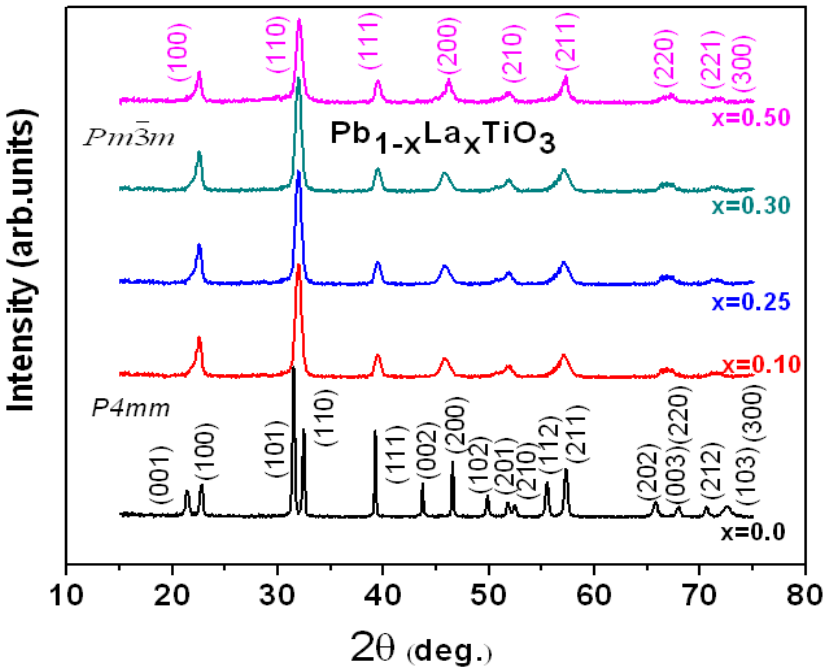

Fig. 4.2: XRD patterns of $Pb_{1-x}La_xTiO_3$ (PLT) compound for x = 0, 0.10, 0.25, 0.30 and 0.50 sintered at 1100^0C for 4h.

X-ray diffraction is a simpler and easier approach for the determination of crystallite size of powder samples. The underlying principle for such a determination involves precise quantification of the broadening of the diffraction peaks. There are a few techniques involving to calculate the crystallite size such as, Scherrer's method [157], Williamson- Hall method [159], and Rietveld refinement method [152]. The Crystallite size obtained from above three different methods (as described in chapter 3) is listed in Table 4.1. We have observed that the crystallite size obtained by Rietveld method is less than that of WH method. It is due to the correction of peak broadening factor taking into account of all instrumental factors. Also the crystallite size obtained by WH

method is less than those obtained by Scherrer's formulae. It is because, the strain correction factor has been taken into account in case of WH method whereas it has not taken into account in Scherrer's method. From the above discussion, we conclude that, Rietveld method is the best method among the above three methods to calculate crystallite size for XRD peak broadening. Hence, the crystallite size for all other materials studied in this thesis has been calculated using only Rietveld method. It is observed that crystallite size decreases with increase in La concentration for both the annealed samples. Also the crystallite size increases with increase of sintering temperature for both La free and La substituted samples. The average crystallite sizes (obtained from above three methods) versus La concentration of $Pb_{1-x}La_xTiO_3$, x = 0.0, 0.10, 0.25, 0.30 and 0.50 samples are shown Fig. 4.3 (a) and Fig. 4.3 (b) for the samples calcined at 900˚C and sintered at 1100˚C respectively.

Table 4.1: Average crystallite size (nm) calculated by various methods for the samples $Pb_{1-x}La_xTiO_3$ (x = 0.0, 0.10, 0.25, 0.30 and 0.50) calcined at 900˚C for 6h and sintered at 1100˚C for 4h.

Sample composition	crystallite size (nm)		
	Scherrer's Method	W. H. Method	Rietveld Method
$PbTiO_3$ (900˚C)	21.1(5)	16.3(11)	15.9(8)
$PbTiO_3$ (1100˚C)	44.2(5)	43.8(3)	43.2(2)
$Pb_{0.90}La_{0.10}TiO_3$ (900˚C)	19.8(3)	16.0(3)	15.3(11)
$Pb_{0.90}La_{0.10}TiO_3$ (1100˚C)	40.6(12)	40.1(11)	39.1(8)
$Pb_{0.75}La_{0.25}TiO_3$ (900˚C)	19.1(10)	15.1(4)	13.4(8)
$Pb_{0.75}La_{0.25}TiO_3$ (1100˚C)	38.5(7)	37.8(7)	36.1(2)
$Pb_{0.70}La_{0.30}TiO_3$ (900˚C)	17.8(6)	13.8(3)	12.2(9)
$Pb_{0.70}La_{0.30}TiO_3$ (1100˚C)	36.6(17)	35.3(13)	34.7(3)
$Pb_{0.50}La_{0.50}TiO_3$ (900˚C)	15.4(3)	12.4(5)	11.2(8)
$Pb_{0.50}La_{0.50}TiO_3$ (1100˚C)	34.0(4)	30.3(9)	29.3(5)

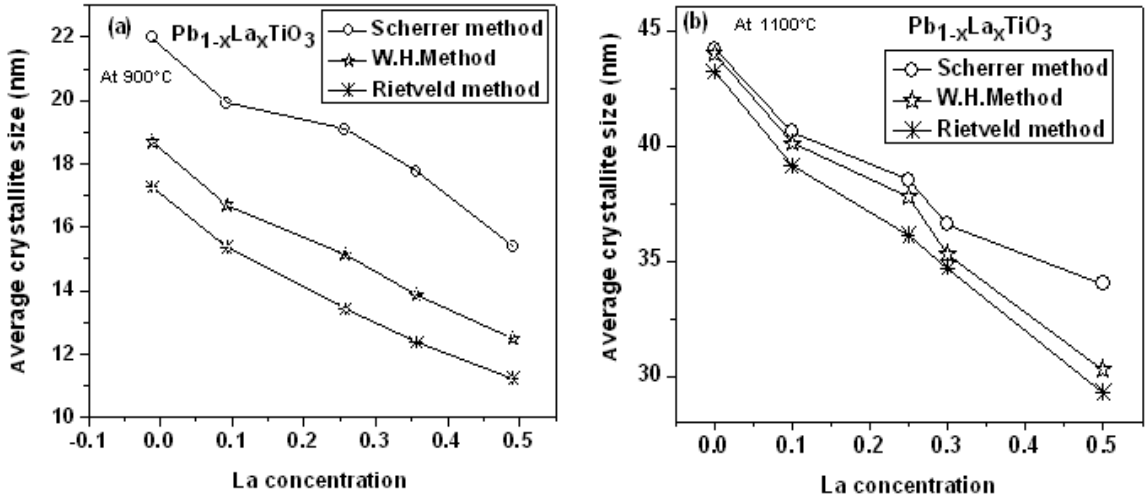

Fig. 4.3 (a, b): The average crystallite size versus La concentration (a) calcined at 900˚C for 6h and (b) sintered at 1100˚C for 4h of $Pb_{1-x}La_xTiO_3$ (PLT) powders with (x=0, 0.10, 0.25, 0.30 and 0.50).

The XRD patterns were analyzed by employing the Rietveld refinement technique [152] with the help of the FullProf program [167]. In the La free sample ($PbTiO_3$), the Ti, O_1 and O_2 are positively shifted along c direction, whereas in the La doped sample (space group $Pm\bar{3}m$), these atoms occupy exactly the corners (A site), the face centers (Oxygen's sites), and the body center (B site) of the unit cell, which means the ideal perovskite cubic structure. For all La-containing $PbTiO_3$ samples, the A-site occupancy was shared between Pb and La. Considering A-site vacancies only, the refinements of the sample containing unrealistic values for the atomic occupancies and worse statistical compatible parameters, even for the samples with high La content. Nevertheless, it is important to emphasize that realistic occupancy results depend on the atomic number difference between the atoms involved in the site occupancy refinements. In this case, the Pb (82) and La (57) atomic numbers are significantly different, which usually permits a suitable occupancy refinement.

The refined XRD patterns of the La free sample (PT) and a typical doped sample $Pb_{1-x}La_xTiO_3$, x = 0.10 (PLT10) calcined at 900^0C are shown in Fig. 4.4 and Fig. 4.5 respectively. Also for La free sample (PT) and a typical doped sample $Pb_{1-x}La_xTiO_3$, x = 0.10 (PLT10) calcined at

1100^0C are shown in Fig. 4.6 and Fig. 4.7 respectively. All the observed peaks could be refined using *P4mm* space group in tetragonal symmetry for La free sample ($PbTiO_3$, x=0.00). However, XRD patterns for La modified samples have been refined using $Pm\bar{3}m$ space group in cubic symmetry.

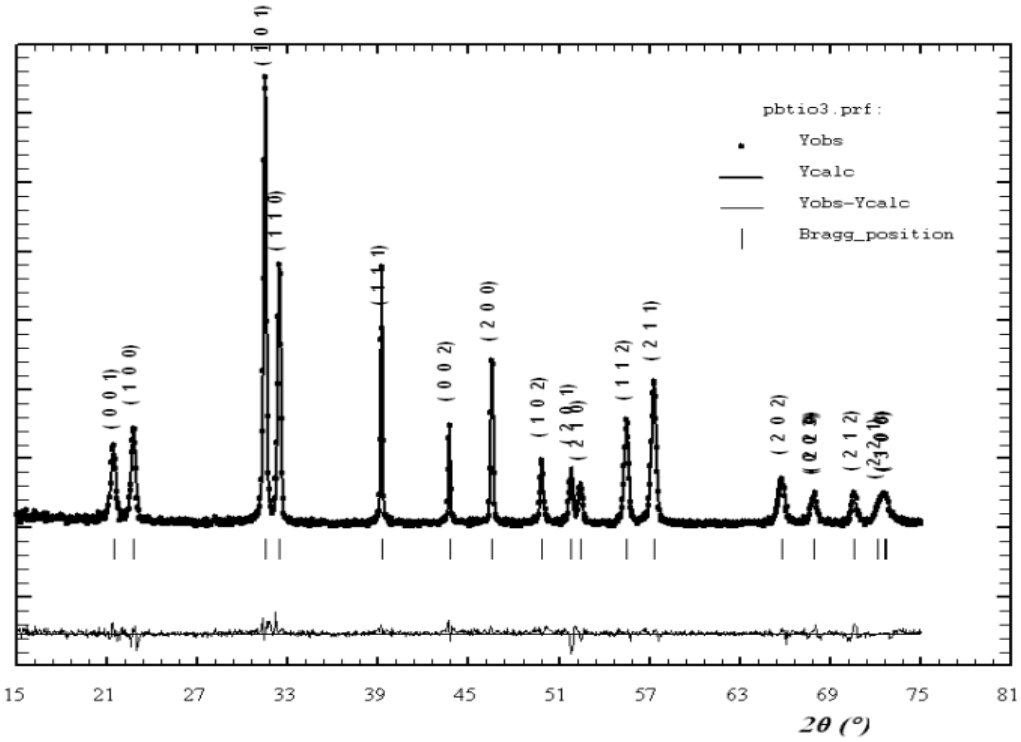

Fig. 4.4: XRD pattern for $PbTiO_3$ calcined at 900˚C for 6h with refined data obtained by Rietveld method. The experimental points are given as dot (·) and theoretical data are shown as solid lines. The difference between theoretical and experimental data is shown as a bottom line. The vertical lines represent the Bragg's allowed peaks.

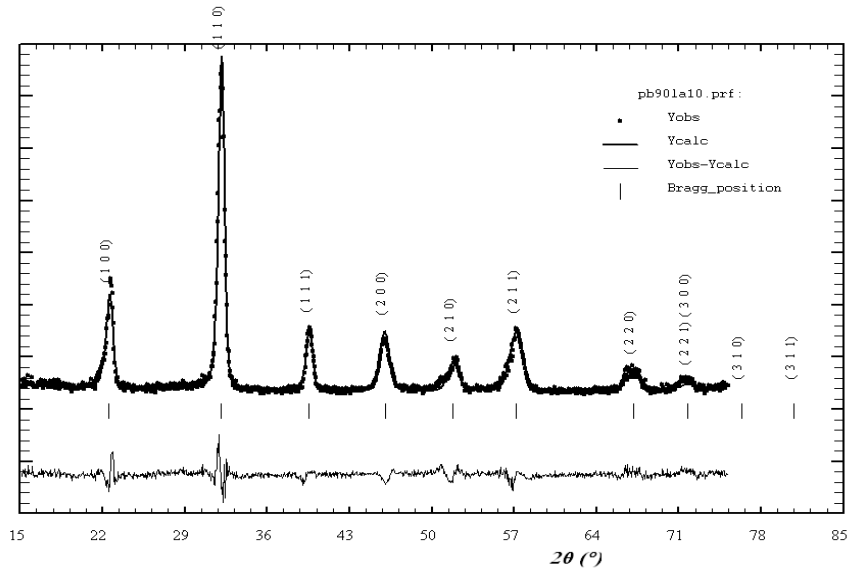

Fig. 4.5: XRD pattern for the sample $Pb_{0.90}La_{0.10}TiO_3$ calcined at 900˚C for 6h with refined data obtained by the Rietveld method. The experimental points are given as plus (+) and theoretical data are shown as solid lines. The difference between theoretical and experimental data is shown as a bottom line. The vertical lines represent the Bragg's allowed peaks.

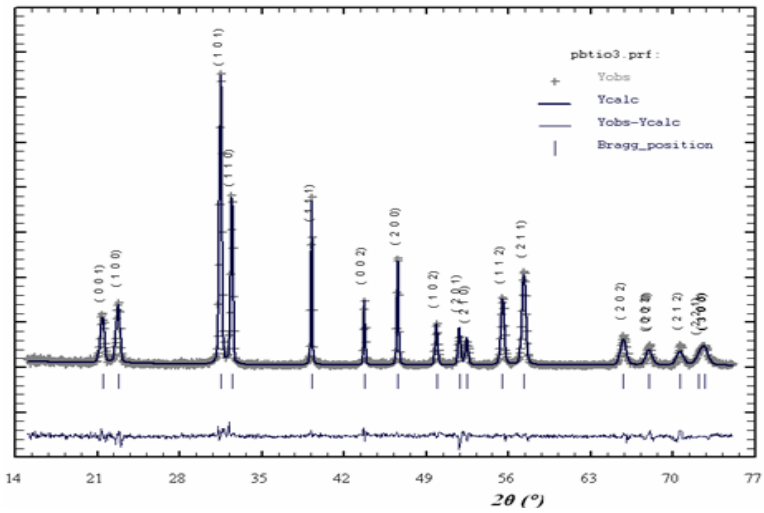

Fig. 4.6: XRD pattern of $PbTiO_3$ sintered at 1100˚C for 4h with refined data obtained by the Rietveld method. The experimental points are given as plus (+) and theoretical data are shown as solid lines. The difference between theoretical and experimental data is shown as a bottom line. The vertical lines represent the Bragg's allowed peaks.

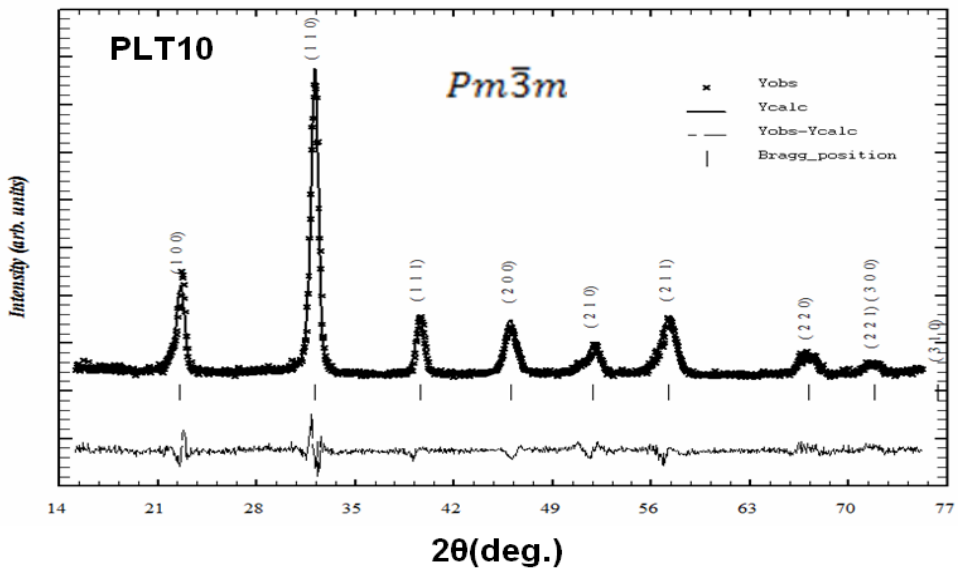

Fig. 4.7: XRD pattern for $Pb_{0.90}La_{0.10}TiO_3$ with refined data obtained by Rietveld method. The experimental points are given as plus (+) and theoretical data are shown as solid lines. The difference between theoretical and experimental data is shown as a bottom line. The vertical lines represent the Bragg's allowed peaks.

The Lattice parameters, occupancy, fractional atomic positions etc. were taken as the free parameters during the fitting. The lattice parameters and unit cell volume were found to be decreased with the La concentration; it could be due to the smaller ionic size of La^{3+} (1.06 Å) comparing to that of Pb^{2+} (1.20 Å). The fractional atomic positions and isothermal parameter for 1100^0C sintered sample $PbTiO_3$ and $Pb_{0.90}La_{0.10}TiO_3$ (PLT10) are shown in Table 4.2 and Table 4.3 respectively. The A-site occupancy, lattice parameters, cell volume, the goodness of the fitting parameter is listed in Table 4.4 and Table 4.5 for the samples annealed at 900^0C and 1100^0C respectively. The bond lengths and bond angles have been calculated by using the refined parameter with the help of powder cell program. Also we have observed that, the Pb-Ti, Ti-O_1, Ti-O_2, Pb-O_1 and Pb-O_2 bond lengths decreased with the increase in La concentration. The variations of the Ti-O and Pb-O distances with lanthanum are shown in Fig. 4.8 (a) and Fig. 4.8 (b) for the samples annealed at 900^0C and 1100^0C respectively. It has been observed that Ti-O_2 and Pb-O_1 bond lengths remain almost constant for all the samples. This behavior was expected since Ti-O_2

and Pb-O_1 lie on the perpendicular plane to the ferro-distortive axis, which is unaffected by the c-axis distortion. On the other hand, it is observed that increasing La content, Ti-O_1, and Pb-O_2 distances are statistically different from La free and La doped samples due to its structural changes and symmetry dependence. The values of bond lengths and bond angles are capitalized for the sample $Pb_{0.90}La_{0.10}TiO_3$ calcined at 900^0C and 1100^0C in Table 4.4 and Table 4.5 respectively. Using the refined parameters the suggested stable crystal structure of $PbTiO_3$ and $Pb_{0.90}La_{0.10}TiO_3$ are shown in Fig. 4.9 and Fig. 4.10 (a-c) respectively.

Table 4.2: Fractional atomic positions and isothermal parameters of the sample $PbTiO_3$ sintered at 1100˚C for 4h.

Atom	X	Y	Z	B_{iso}
Pb	0.0000	0.0000	0.0000	0.9921
Ti	0.5000	0.5000	0.5377	0.9843
O_1	0.5000	0.5000	0.1118	1.0000
O_2	0.0000	0.5000	0.6174	0.9713

Table 4.3: Fractional atomic positions and isothermal parameters of the sample $Pb_{0.90}La_{0.10}TiO_3$ sintered at 1100˚C for 4h.

Atom	X	Y	Z	B_{iso}
Pb	0.0000	0.0000	0.0000	0.9921
La	0.0000	0.0000	0.0000	0.9921
Ti	0.5000	0.5000	0.5000	0.9843
O_1	0.5000	0.5000	0.0000	1.0000
O_2	0.0000	0.5000	0.5000	0.9713

Table 4.4: Parameters obtained from Rietveld analysis of $Pb_{1-x}La_xTiO_3$ (PLT) powders with (x = 0, 0.10, 0.25, 0.30 and 0.50) annealed at 900ºC for 6 h.

Sample Parameter	x=0.0	0.10	0.25	0.30	0.50
Space group	P4mm	$Pm\bar{3}m$	$Pm\bar{3}m$	$Pm\bar{3}m$	$Pm\bar{3}m$
Pb(Occup.)	0.9923(11)	0.8974(8)	0.7415(10)	0.6978(4)	0.4981(2)
La(Occup.)	0.0000	0.1075(1)	0.2494(10)	0.3015(5)	0.5014(2)
Ti(Occup.)	0.9840(7)	0.9840(2)	0.9840(3)	0.9956(7)	0.9840(11)
a = b (Å)	3.9871(8)	3.9602(3)	3.9521(1)	3.9504(6)	3.9324(5)
c (Å)	4.1384(9)	3.9602(3)	3.9521(1)	3.9504(6)	3.9324(5)
Volume ($Å^3$)	62.9 (2)	62.7 (9)	62.5(3)	62.3(7)	62.2(3)
χ^2 (chi^2)	1.32	2.44	4.62	2.12	4.96
R_p	3.70	19.9	14.7	13.5	12.8
R_{wp}	4.20	24.8	21.3	23.7	18.9
R_{exp}	3.91	8.47	8.59	7.34	6.89
R_{Bragg}	5.63	14.4	4.75	13.7	11.8
R_f	3.21	5.99	3.90	7.09	6.32
Pb-Ti (Å)	3.52(14)	3.48(11)	3.42(21)	3.40(10)	3.38(22)
Ti-O_1 (Å)	2.50(6)	2.46(8)	2.33(7)	2.23(3)	2.05(3)
Ti-O_2 (Å)	2.08(2)	2.07(4)	2.06(3)	2.06(8)	2.05(9)
Pb-O_1 (Å)	2.81(4)	2.80(2)	2.79(5)	2.78(4)	2.78(2)
Pb-O_2 (Å)	3.21(3)	3.14(4)	3.10(9)	3.00(5)	2.79(9)
∠Pb-Ti-O_1	51.49	54.73	54.73	54.73	54.73
∠Pb-Ti-O_2	46.01	125.5	125.5	125.5	125.5
∠Pb-Ti-Pb	67.19	70.52	70.52	70.52	70.52
∠O_2-Ti-O_2	103.24	180	180	180	180

Table 4.5: Parameters obtained from Rietveld analysis of $Pb_{1-x}La_xTiO_3$ (PLT) powders for x = 0, 0.10, 0.20, 0.25 and 0.50 sintered at 1100ºC for 4 h.

Sample Parameter	x=0.0	0.10	0.25	0.30	0.50
Space group	P4mm	$Pm\bar{3}m$	$Pm\bar{3}m$	$Pm\bar{3}m$	$Pm\bar{3}m$
Pb(Occup.)	0.9976(17)	0.8874(12)	0.7315(11)	0.6878(1)	0.4981(12)
La(Occup.)	0.0000	0.1095(11)	0.2324(10)	0.3040(4)	0.5084(7)
Ti(Occup.)	0.9965(22)	0.9720(2)	0.9720(2)	0.9956(7)	0.9720(2)
a = b (Å)	3.9887(3)	3.9402(8)	3.9385(11)	3.9383(7)	3.9321(5)
c (Å)	4.1380(9)	3.9402(8)	3.9385(11)	3.9383(7)	3.9321(5)
Volume ($Å^3$)	62.8(2)	62.1(4)	61.8(13)	61.1(3)	60.2(4)
χ^2 (chi^2)	2.04	4.53	4.53	3.62	2.37
R_p	18.7	22.1	22.1	19.9	18.4
R_{wp}	24.8	28.8	20.6	21.8	24.1
R_{exp}	12.2	12.4	10.4	9.56	15.6
R_{Bragg}	13.3	12.4	11.4	12.7	12.4
R_f	8.2	10.1	5.1	8.52	7.7
Pb-Ti (Å)	3.55(14)	3.47(11)	3.45(11)	3.41(14)	3.39(2)
Ti-O_1 (Å)	2.55(7)	2.53(3)	2.51(9)	2.48(6)	2.45(7)
Ti-O_2 (Å)	2.18(5)	2.17(6)	2.15(7)	2.14(9)	2.12(5)
Pb-O_1 (Å)	3.41(5)	3.40(2)	3.38(8)	3.36(8)	3.34(3)
Pb-O_2 (Å)	4.58(3)	4.47(7)	4.43(6)	3.96(4)	3.85(7)
∠Pb-Ti-O_1	71.96(2)	102.13(1)	102.73(1)	102.73(1)	102.73(1)
∠Pb-Ti-O_2	84.01(2)	145.55(2)	145.55(2)	145.55(2)	145.55(2)
∠Pb-Ti-Pb	77.19(3)	71.52(4)	71.52(4)	71.52(3)	71.52(4)
∠O_2-Ti-O_2	107.14(6)	149.11(3)	149.11(3)	149.11(2)	149.11(1)

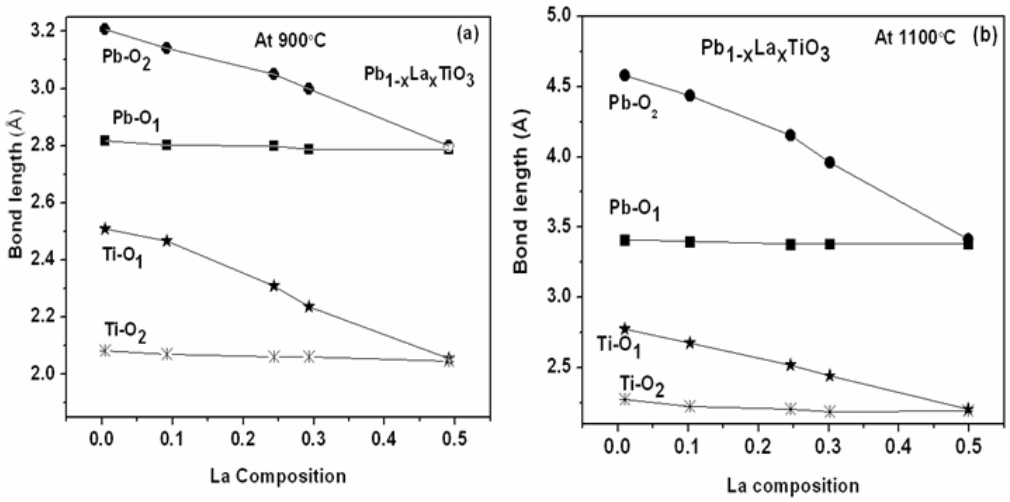

Fig. 4.8 (a, b): The dependence of the Ti-O and Pb-O bond lengths with the La content of $Pb_{1-x}La_xTiO_3$ samples of x = 0, 0.10, 0.25, 0.30 and 0.50 (a) calcined at 900ºC for 6 h and (b) sintered at 1100˚C for 4h.

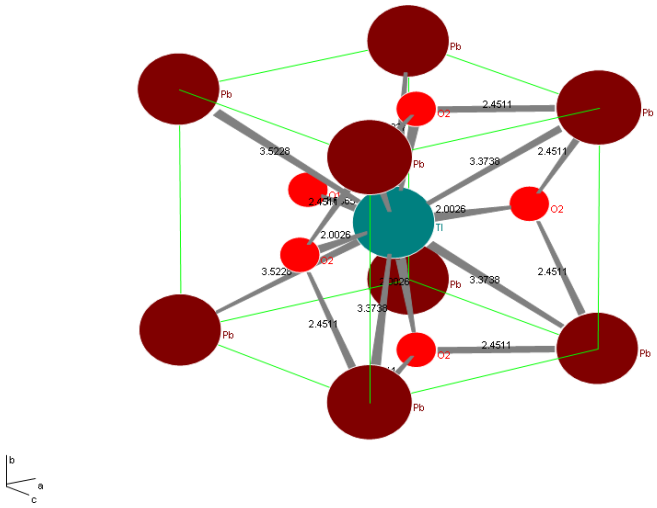

Fig. 4.9: Structure of $PbTiO_3$ obtained from the Rietveld analysis parameters.

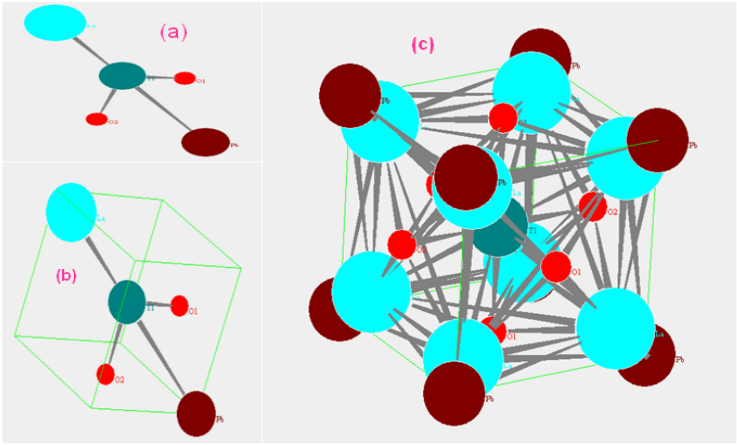

Fig. 4.10 (a-c): (a) Positions of the atoms, (b) position of the atoms in crystal co-ordinate and (c) crystal structure of a typical sample $Pb_{0.90}La_{0.10}TiO_3$ obtained from the Rietveld analysis parameters.

4.2.2 Microstructural and compositional analysis

The scanning electron micrographs were recorded using a JEOL Scanning electron microscope (SEM) (JEOL T-330) at room temperature. SEM photographs of the undoped and La modified samples sintered at 1100ºC are shown in the Fig. 4.11 (a-e). It is observed that the samples are uniform and the grains are in the order of micrometers. The average grain sizes are found to be 1 to 4.5µm. It is found that the grain size increases with increase of La concentration.

The compositional analysis was carried out by SEM-energy dispersive spectroscopy (EDS). The energy dispersive X-ray spectroscopy (EDS) is shown in the Fig. 4.12 (a-e) for the samples x = 0.0, 0.10, 0.25, 0.30 and 0.50 respectively. The EDS analysis reveals that, all the compositions are

as per the prepared sample. The experimental and theoretical EDS values are compared in Table 4.6. We have observed that, both values are close to each other.

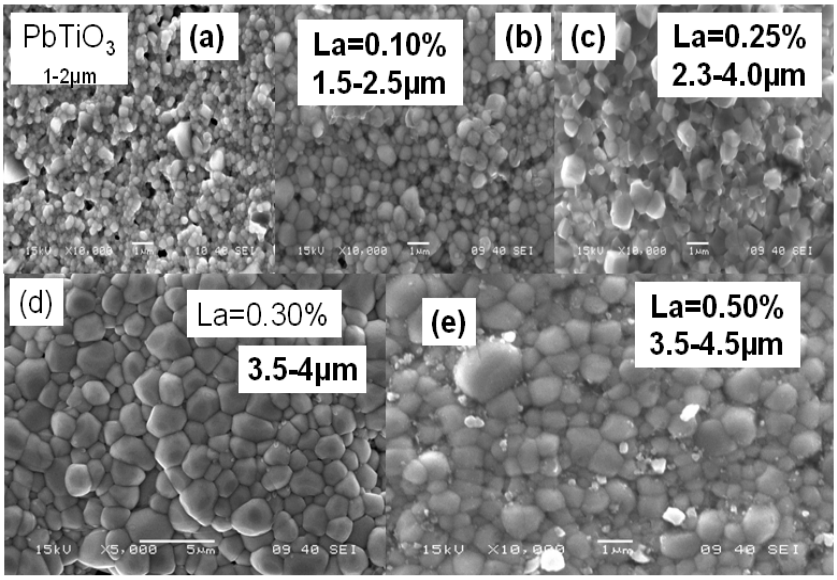

Fig.4.11 (a-e): SEM micrographs of sintered $Pb_{1-x}La_xTiO_3$ ceramic with (a) x=0.00, (b) x=0.10, (c) x=0.25, (d) x=0.30, and (e) x=0.50.

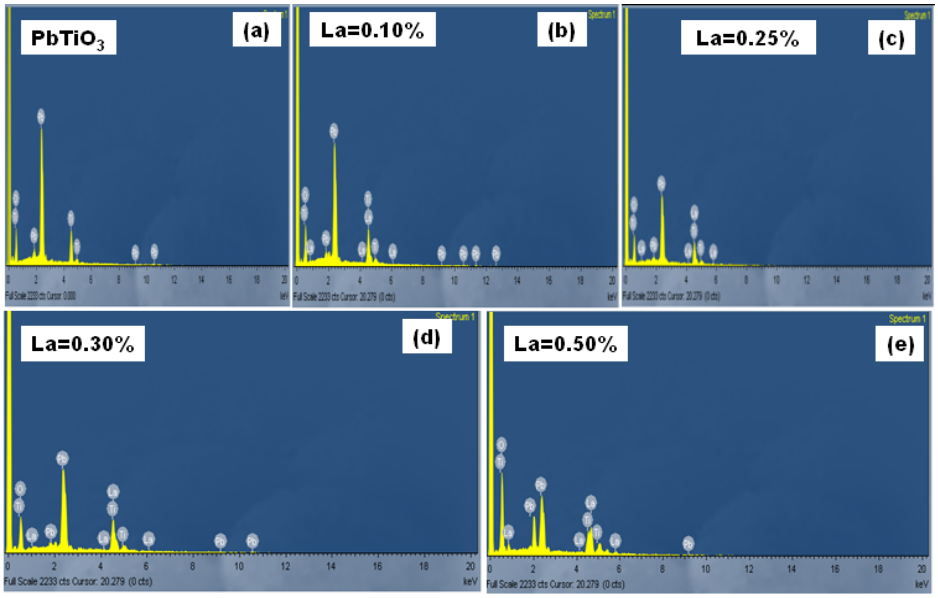

Fig. 4.12 (a-e): EDS micrographs of sintered $Pb_{1-x}La_xTiO_3$ ceramic with (a) x = 0.00, (b) x = 0.10, (c) x = 0.25, (d) x = 0.30, and (e) x = 0.50.

Table 4.6: Elemental analysis of pure and La modified PT annealed at 1100°C for 4h.

Composition	Element	Wt % Calculated	Wt% from EDS
$Pb_{1-x}La_xTiO_3$ X=0.00	Pb	63.60	62.65
	La	0.0	0.0
	Ti	22.77	24.01
	O	13.62	14.34
$Pb_{1-x}La_xTiO_3$ X=0.10	Pb	53.99	53.05
	La	11.63	11.85
	Ti	21.47	22.45
	O	12.90	12.65
$Pb_{1-x}La_xTiO_3$ X=0.25	Pb	48.99	48.05
	La	20.63	20.85
	Ti	21.47	22.45
	O	8.90	8.65
$Pb_{1-x}La_xTiO_3$ X=0.30	Pb	41.48	42.06
	La	26.82	25.35
	Ti	19.79	20.74
	O	14.90	11.05
$Pb_{1-x}La_xTiO_3$ X=0.50	Pb	34.17	35.73
	La	30.69	30.98
	Ti	18.82	18.98
	O	17.31	14.37

4.2.3 Dielectric analysis

Temperature variation of dielectric constants (ε_r) at different frequencies are shown in the Fig. 4.13(a-e) for the samples x = 0.00, 0.10, 0.25, 0.30 and 0.50 sintered at 1100˚C for 4h respectively. It is observed that the dielectric constant increases with the temperature and reach to a maximum value and, then decreases with the temperature. It suggests that the material goes transition from ferroelectric to paraelectric phase with the temperature. This is the behavior of a normal ferroelectric material. The temperature at which dielectric constant is maximum has been denoted as T_c. The T_c was calculated from the temperature versus $\left|\frac{d\epsilon_r}{dT}\right|$ plot and it was taken the temperature at $\left|\frac{d\epsilon_r}{dT}\right|$ is zero. The maximum ε_m and T_c values are given in Table 4.7. It is observed that, the maximum dielectric constant decreases with the frequency. The higher value of ε_r of low frequency suggests that, the contribution comes from a different type of polarizations i.e. space

charge, ionic, electronic etc. However at high frequency the contribution does not come from the polarization having large relaxation time. Mostly the large relaxation time is observed due to space charge polarization. The similar behavior of dielectric response to frequency is observed in other ferroelectric materials [167-169]. The space charge polarization arises from the charge accumulation at grain boundaries and at electrode interfaces.It is mainly due to lead and mobile oxygen vacancies [170].

Again from the Fig. 4.13 (a-e), it is observed that, the T_c and maximum dielectric constant (ε_m) decrease with the La concentration. It could be due to the diffusion of dielectric with the La concentration. The maximum dielectric constant (ε_m) decreases with the increase of frequency, which is characteristic of a relaxation phenomenon [171]. For lead titanate type materials, the stability of long range interaction is believed to be suppressed by decoupling effects caused by the incorporation of ions at the A site of the perovskite structure. Similar behavior has been observed in La doped samples [172-174]. We have calculated the Full Width Half Maximum (FWHM) at the transition temperature from the dielectric constant versus temperature curve. The values are found to be 76.43, 118.12, 153.42, 194.84 and 224.45 for x = 0.0, 0.10, 0.25, 0.30 and 0.50 samples respectively. Hence the sample x = 0.00, 0.10 behaves like a normal ferroelectric material. However the large FWHM suggests the samples x = 0.25, 0.30 and 0.50 are diffused type ferroelectric material. Also from the Fig. 4.13 (a-e), depending on the La content, the first case, for temperatures higher than T_c, a centrosymmetric cubic structure $Pm\bar{3}m$ is expected since the material undergoes a phase transition to a paraelectric material. In the second case, for temperatures lower than T_c, a residual short-range structural disorder has been found [175] not to be compatible with the centrosymmetric cubic structure usually observed in the ferroelectric phase. At x ~ 0.30, the dielectric constant shows the similar behavior with the frequency in both paraelectric and ferroelectric regions. Hence, we have taken PLT30 as a parent material in which we have doped transition elements in B site (Ti site) to study the electrical behavior and it has been discussed in Chapter 5.

The temperature variation of dielectric loss (tan (δ) is shown in Fig. 4.14 (a-e) for the samples x = 0.00, 0.10, 0.25, 0.30 and 0.50 respectively at different frequencies (1kHz-1MHz). It has been observed that, the dielectric loss almost constant below T_c and it increases when approach to T_m. It is found that dielectric loss decreases with increase of La concentration. It could be due to increase of space charge polarization [170].

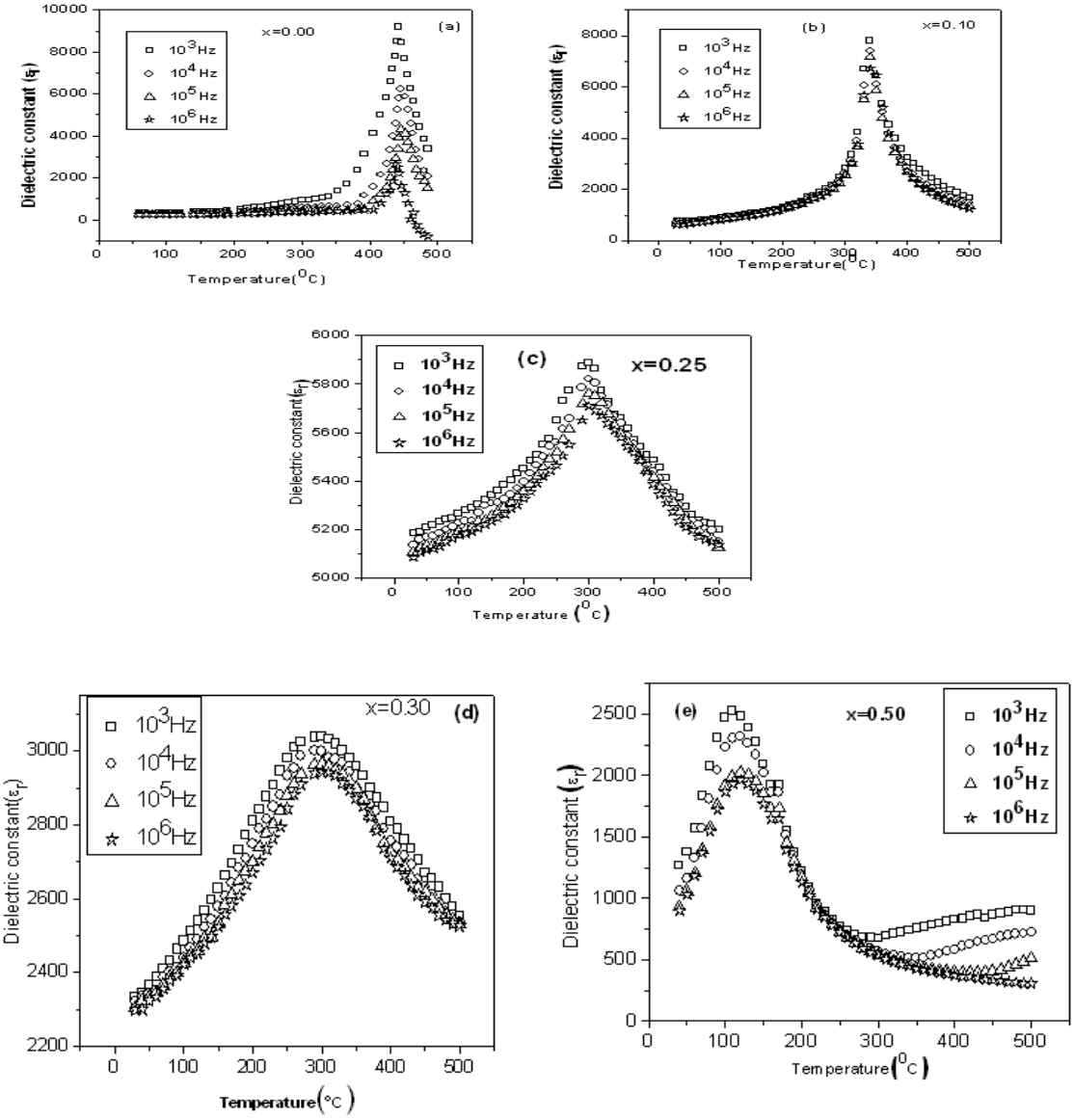

Fig. 4.13 (a-e): The dielectric constants versus temperature of $Pb_{1-x}La_xTiO_3$, (a) x = 0.0, (b) x = 0.10, (c) x = 0.25, (d) x = 0.30, and (e) x = 0.50.

Table 4.7: The observed T_c and ε_m obtained from dielectric measurements at different frequencies of $Pb_{1-x}La_xTiO_3$, x = 0.0, 0.10, 0.25, 0.30 and 0.50.

Composition	Frequency (Hz)	T_c	ε_m
x = 0.00	10^3	445	9193
	10^4	445	6290
	10^5	445	4475
	10^6	445	2764
x = 0.10	10^3	340	7790
	10^4	340	7402
	10^5	340	7151
	10^6	340	6724
x = 0.25	10^3	301	5883
	10^4	301	5824
	10^5	301	5764
	10^6	301	5715
x = 0.30	10^3	293	3045
	10^4	295	3010
	10^5	297	2971
	10^6	299	2944
x = 0.50	10^3	110	2527
	10^4	113	2339
	10^5	116	2042
	10^6	118	1954

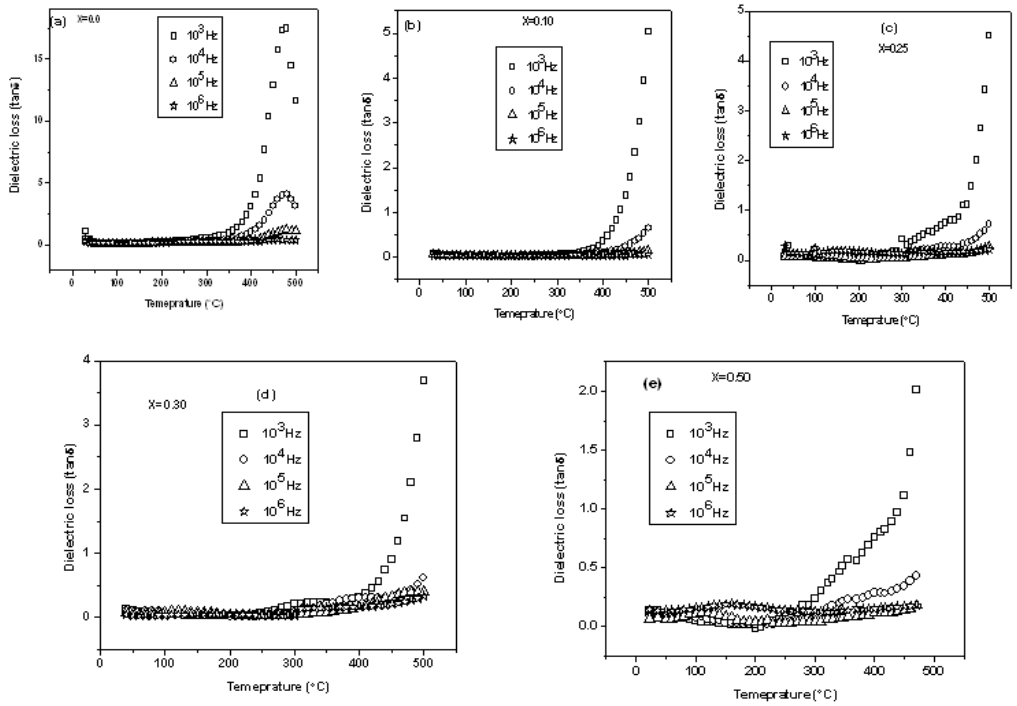

Fig. 4.14 (a-e): The dielectric loss versus temperature of $Pb_{1-x}La_xTiO_3$, (a) x = 0.0, (b) x = 0.10, (c) x = 0.25, (d) x = 0.30, and (e) x = 0.50.

4.2.4 Polarization study

P-E hysteresis loop is shown in Fig. 4.15 (a-e) for all the samples. All the compositions of the sintered sample at room temperature showed well defined ferroelectric behaviour. The coercive field (E_c), remnant polarization (P_r), saturation polarization (P_s) and remnance ratio (P_r/P_s) determined from the hysteresis loops are listed in Table 4.8. P_r was found to increase with La concentration from which one can predict that material gets ferroelectrically soften. Domain switching becomes easier because La^{3+} ions substitutes Pb^{2+} ions at A site and the presence of multiple ions (Pb^{2+} and La^{3+}) resulted in higher multi-domain polarization as evidenced by increase in P_r and P_s. The remnance ratio (P_r/P_s) was found to decrease with increase of La concentration. The P_r and E_c values are comparable to that reported in the literature for the polycrystalline materials [176, 177]. The high remnant polarization samples can be used as memory application in electronic industry.

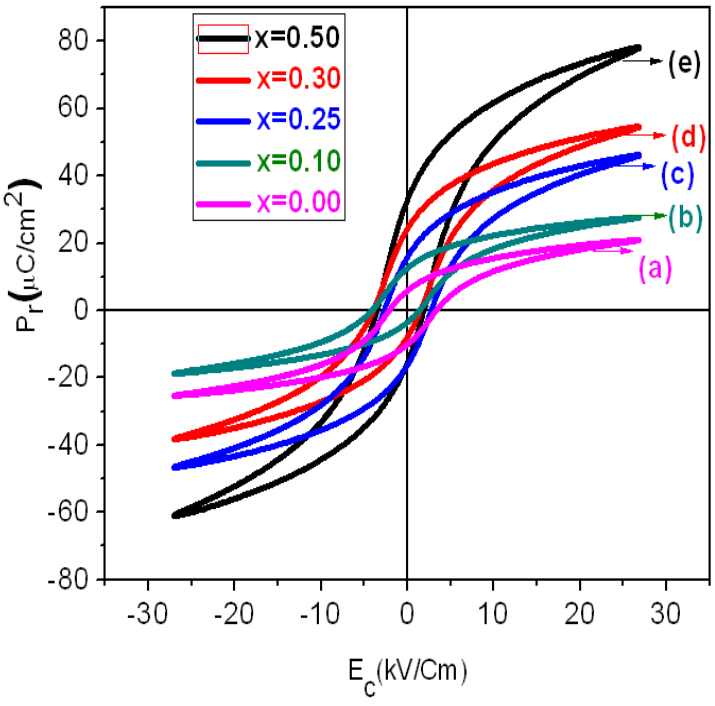

Fig. 4.15 (a-e): Ferroelectric hysteresis loop of the samples (a) $PbTiO_3$, (b) $Pb_{0.9}La_{0.1}TiO_3$, (c) $Pb_{0.75}La_{0.25}TiO_3$, (d) $Pb_{0.70}La_{0.30}TiO_3$, and (e) $Pb_{0.5}La_{0.5}TiO_3$ sintered at 1100˚C for 4h.

Table 4.8: Observed values of P_r, E_c, P_s and P_r/P_s for $Pb_{1-x}La_xTiO_3$, x = 0.0, 0.10, 0.25, 0.30 and 0.50 at room temperature.

x	P_r (μC/cm^2)	E_c(kV/cm)	P_s(μC/cm^2)	(P_r/P_s)
0.00	16.14	4.18	18.30	0.881
0.10	19.77	3.43	25.34	0.780
0.25	20.29	3.18	43.01	0.471
0.30	27.51	1.87	52.84	0.520
0.50	35.56	1.81	75.81	0.469

4.2.5 Electrical conductivity studies

4.2.5.1 Impedance analysis

Generally, the impedance properties of materials arise due to intragrain, intergrain and electrode processes. The motion of charges could occur in a number of ways: (i) dipole reorientation, (ii) space charge formalism and (iii) charge displacement. Thus, the complex impedance formalism allows for a direct separation of the bulk, grain boundary and the electrode phenomena. The complex impedance of the electrode/ceramic/ electrode capacitor can be demonstrated as the sum of the single RC circuit with parallel combination, which can be written as

$$Z^*(T) = Z_0 \int \frac{y(\tau,T)d(\tau)}{1+j\omega\tau} \tag{4.1}$$

$$Z'(\omega,T) = Z_0(T) \int \frac{y(\tau,T)d(\tau)}{1+\omega^2\tau^2} \tag{4.2}$$

$$Z''(\omega,T) = Z_0(T) \int \frac{(\omega\tau)^* y(\tau,T)d(\tau)}{1+\omega^2\tau^2} \tag{4.3}$$

Here τ =RC represents the relaxation time, T the time period and y(τ, T) the distribution of relaxation times. The variation of the imaginary part of complex impedance Z″ (ω, T) provides information about the distribution function y (τ, T) [178].

4.2.5.2 Real part of impedance study

Fig. 4.16 (a-e) shows the real part of impedance (Z′) versus frequency at different temperatures of the sample $Pb_{1-x}La_xTiO_3$ for x = 0.0, 0.10, 0.25, 0.30 and 0.50 respectively. From this figure it is observed that the Z′ has higher values at lower frequencies and it decreases monotonically with increase in frequency and attains a constant value at higher frequencies irrespective of temperatures. The magnitude of Z′ decreases with increase in temperature and its value for all temperatures merge in the high frequency domain. The decrease in the real part of impedance (Z′) with a rise in the value of temperature and frequency may be due to increase in AC conductivity. The merger of the real parts of the impedance (Z′) for all temperatures in the high frequency domain indicates a possibility of the release of space charge as a result of lowering in the barrier properties of the materials [179].

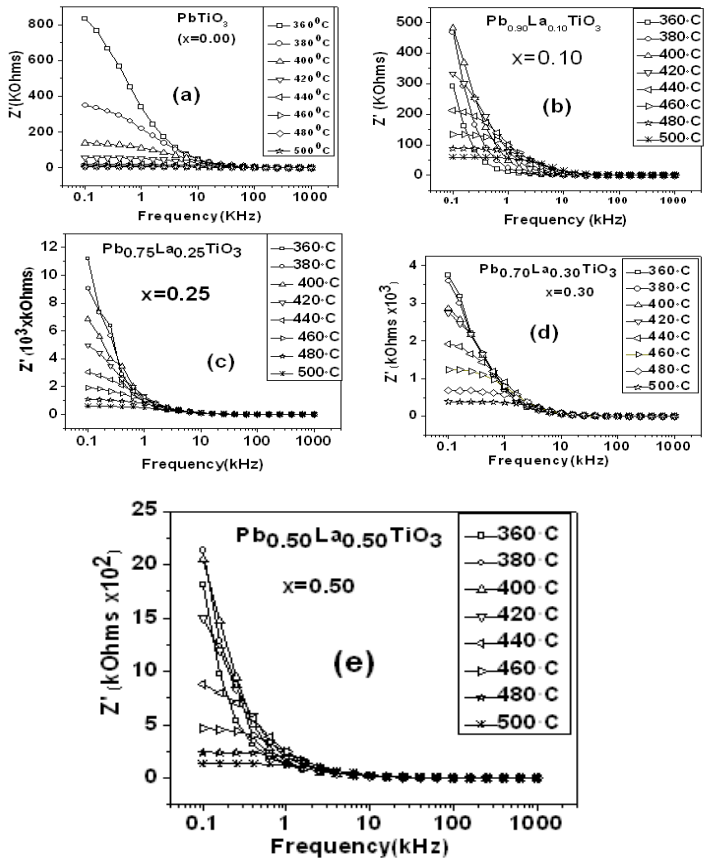

Fig. 4.16 (a-e): Variations of the real part of the impedance (Z′) versus frequency at some selected temperatures of the sample $Pb_{1-x}La_xTiO_3$ for (a) x = 0.0, (b) x = 0.10, (c) x = 0.25, (d) x = 0.30 and (e) x = 0.50.

4.2.5.3 Imaginary part of impedance study

Fig. 4.17 (a-e) shows the variation of the imaginary part of impedance (Z″) with frequency at different temperatures of the sample $Pb_{1-x}La_xTiO_3$ for x = 0.0, 0.10, 0.25, 0.30 and 0.50 respectively. It is observed that, Z″ monotonously decrease with a rise in frequency (without any peak) at low temperatures. However, at higher temperature peaks are observed and the observed peak frequency is known as relaxation frequency. The decrease in the magnitude of Z″ and a clear shift in the peak frequency towards the higher frequency with the increasing temperature have been observed. The asymmetric peaks shift towards the high frequency side indicates a correlation between the motions of mobile ion charges. The asymmetry in the peak broadening with a rise in temperature shows the spread of relaxation times with different time constants and hence the

relaxation is of non-Debye type. The peak location gives the relaxation time from the relation ω_{max} τ =1, Here ω_{max} is the angular frequency at the maximum of Z″-frequency pattern.

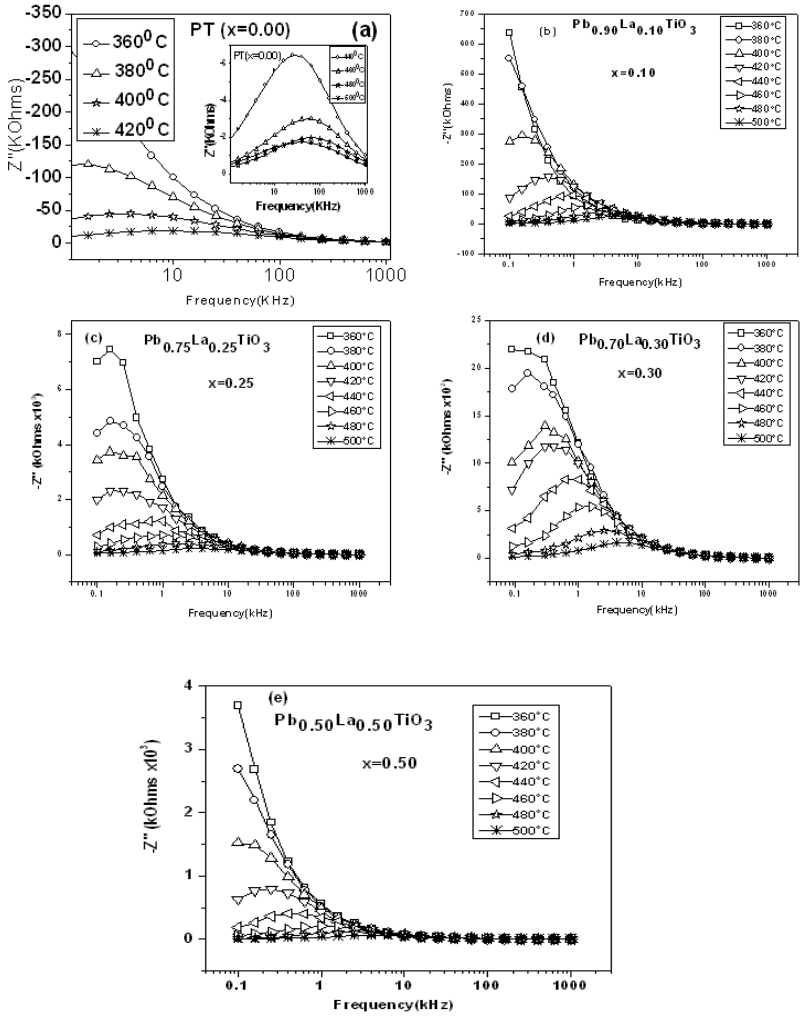

Fig. 4.17 (a-e): Variations of the imaginary part of the impedance Z″ versus frequency at some selected temperatures of the sample $Pb_{1-x}La_xTiO_3$ for (a) x = 0.0, (b) x = 0.10, (c) x = 0.25, (d) x = 0.30 and (e) x = 0.50.

4.2.5.4 Nyquist plot analysis

Fig. 4.18 (a-e) shows the Nyquist plot allowing theoretical fitting at a different temperatures of the sample $Pb_{1-x}La_xTiO_3$ for x = 0.0, 0.10, 0.25, 0.30 and 0.50 respectively. The high-frequency curves attribute to the bulk properties of the material and arise due to parallel combination of the grain resistance (R_g) and grain capacitance (C_g) as shown inset of Fig. 4.18(a-e), whereas the low frequency semicircles are attributed to the grain boundary effects. The diameter of the

semicircle increases with decreasing temperature. This trend indicates the insulating behavior of the sample at lower temperatures. The grain resistance (R_g) is found to decrease with a rise in temperature indicated by the shift in the radius of the semicircular arcs towards the left side on the real (Z′) axis. This provides convincing evidence that the electrical properties of PLT are dependent on microstructural as well as temperature. To evaluate the resistance-capacitance response of grains (R_gC_g) the impedance spectra were analyzed by means of the complex nonlinear least square method which fits the equivalent circuits, consisting two parallel R and C to the Nyquist plot. Excellent agreement between the experimental points and the theoretical curves (generated from commercially available software *ZSIMP WIN Version 2*) was obtained. The points on the plot represent the experimental data, while the solid line represents the theoretical curve. The value of the circuit elements obviously depends on the volume fraction of the individual components. The bulk conductivity or apparent conductivity or DC conductivity (σ_b) of the sample can be determined using the relation [180],

$$\sigma_b = \frac{t}{R_g A} \tag{4.4}$$

Here t is the thickness, A is the electrode area of the sample and R_g is the grain resistance. A single non-degenerate process involves a single non-degenerate relaxation time for the given set of R_g and C_g at a temperature. The relaxation time(τ) is given as,

$$\tau = C_gR_g = \frac{1}{\omega} \tag{4.5}$$

The best fitted values for R_g, C_g, R_gC_g obtained for all the sample is presented in Table 4.9. The value of σ_b and τ calculated by using the equation (4.4) and (4.5) at different temperatures for all the samples and those values are listed in the Table 4.9.The nature of variation of τ and σ_b with the inverse of temperature as shown in Fig. 4.18 (a-e) implies that the relaxation process is temperature dependent.

Also from the Nyquist plots and the data obtained after fitting confirms that the values of bulk resistances decrease with increase in temperature, which is an effect analogous to the negative

temperature co-efficient of resistance (NTCR) in the conventional semiconductors. So, the result indicates semiconducting behaviors of the materials. It is observed that the electrical properties and impedance behavior of a ceramic oxide are phase sensitive parameter. The nature of variation of τ with temperature for all the compounds is shown in Fig. 4.19. They appear to follow the Arrhenius relations [181],

$$\tau = \tau_0 e^{-\frac{E_a}{k_B T}} \qquad (4.6)$$

where τ_0, σ_0 are the pre-exponential factors, E_a is the activation energy, k_B is the Boltzmann constant and T is absolute temperature.

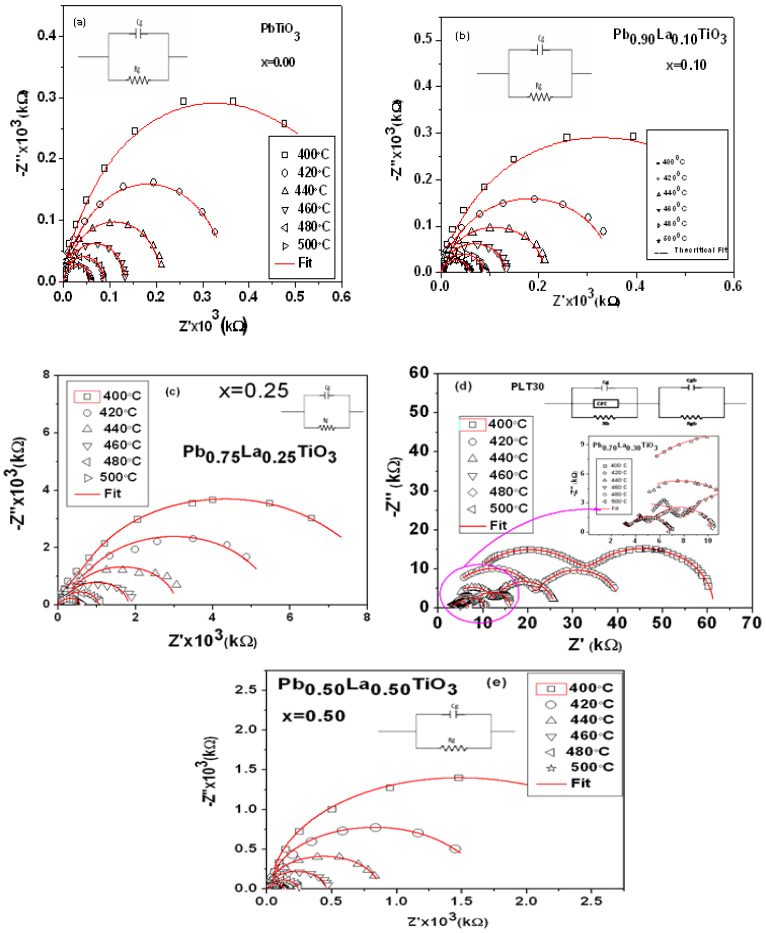

Fig. 4.18 (a-e): (Color online) Nyquist plot (symbol), fitted data (solid line) and equivalent circuit (inset) at different temperatures of the sample $Pb_{1-x}La_xTiO_3$ for (a) x = 0.0, (b) x = 0.10, (c) x = 0.25, (d) x = 0.30, and (e) x = 0.50.

Table 4.9: The observed values of Cg, R_g, relaxation time ($\tau=C_gR_g$) and bulk conductivity ($\sigma_b= t/R_gA$) obtained from the theoretical fitting of the Nyquist plot at different temperatures of the sample $Pb_{1-x}La_xTiO_3$, x = 0.0, 0.10, 0.25, 0.30 and 0.50.

Sample	T(°C)	C_g(nF)	R_g(kΩ)	τ (s)	σ_b $(\Omega m)^{-1}$
x = 0.00	400	1.355	$5.93x10^5$	$0.80x10^{-3}$	$3.9x10^{-7}$
	420	0.729	$1.56x10^5$	$1.14x10^{-4}$	$1.5x10^{-6}$
	440	0.611	$9.98x10^4$	$6.10x10^{-5}$	$2.3x10^{-6}$
	460	0.524	$6.14x10^4$	$3.22x10^{-5}$	$3.8x10^{-6}$
	480	0.458	$3.85x10^4$	$1.75x10^{-5}$	$6.1x10^{-6}$
	500	0.408	$2.53x10^3$	$0.30x10^{-6}$	$1.57x10^{-5}$
x = 0.10	400	1.335	$5.94x10^5$	$0.81x10^{-3}$	$4.0x10^{-7}$
	420	1.144	$3.24x10^5$	$0.46x10^{-3}$	$7.4x10^{-7}$
	440	0.889	$1.91x10^5$	$1.76x10^{-4}$	$1.2x10^{-6}$
	460	0.702	$1.27x10^5$	$0.89x10^{-4}$	$1.8x10^{-6}$
	480	0.588	$8.40x10^4$	$0.49x10^{-4}$	$2.8x10^{-6}$
	500	0.197	$1.53x10^3$	$1.03x10^{-5}$	$9.3x10^{-5}$
x = 0.25	400	0.736	$7.55x10^6$	$0.55x10^{-2}$	$3.1x10^{-4}$
	420	0.716	$4.83x10^6$	$0.49x10^{-2}$	$4.9x10^{-4}$
	440	0.559	$3.50x10^5$	$1.96x10^{-3}$	$6.87x10^{-4}$
	460	0.538	$2.60x10^5$	$0.23x10^{-3}$	$1.50x10^{-4}$
	480	0.447	$9.04x10^4$	$0.81x10^{-3}$	$2.66x10^{-3}$
	500	0.324	$7.30x10^4$	$0.41x10^{-4}$	$3.29x10^{-2}$
x = 0.30	400	0.116	$2.65x10^6$	$0.31x10^{-3}$	$2.23\ x10^{-6}$
	420	0.115	$2.60x10^6$	$0.30x10^{-3}$	$9.98\ x10^{-5}$
	440	0.114	$3.50x10^5$	$0.76x10^{-5}$	$3.55\ x10^{-5}$
	460	0.107	$6.63x10^4$	$0.29x10^{-5}$	$1.08\ x10^{-4}$
	480	0.101	$6.02x10^4$	$0.60x10^{-5}$	$3.91\ x10^{-3}$
	500	0.087	$3.53x10^4$	$0.31x10^{-4}$	$6.68\ x10^{-2}$
x = 0.50	400	0.329	$2.03x10^6$	$0.66x10^{-3}$	$1.18\ x10^{-7}$
	420	0.309	$1.60x10^6$	$0.49x10^{-3}$	$1.51x10^{-7}$
	440	0.291	$8.48x10^5$	$0.24x10^{-3}$	$2.84x10^{-7}$
	460	0.283	$4.44x10^5$	$0.12x10^{-3}$	$5.41x10^{-7}$
	480	0.275	$1.28x10^5$	$0.35x10^{-4}$	$1.87x10^{-7}$
	500	0.228	$5.64x10^3$	$0.35x10^{-5}$	$4.26x10^{-5}$

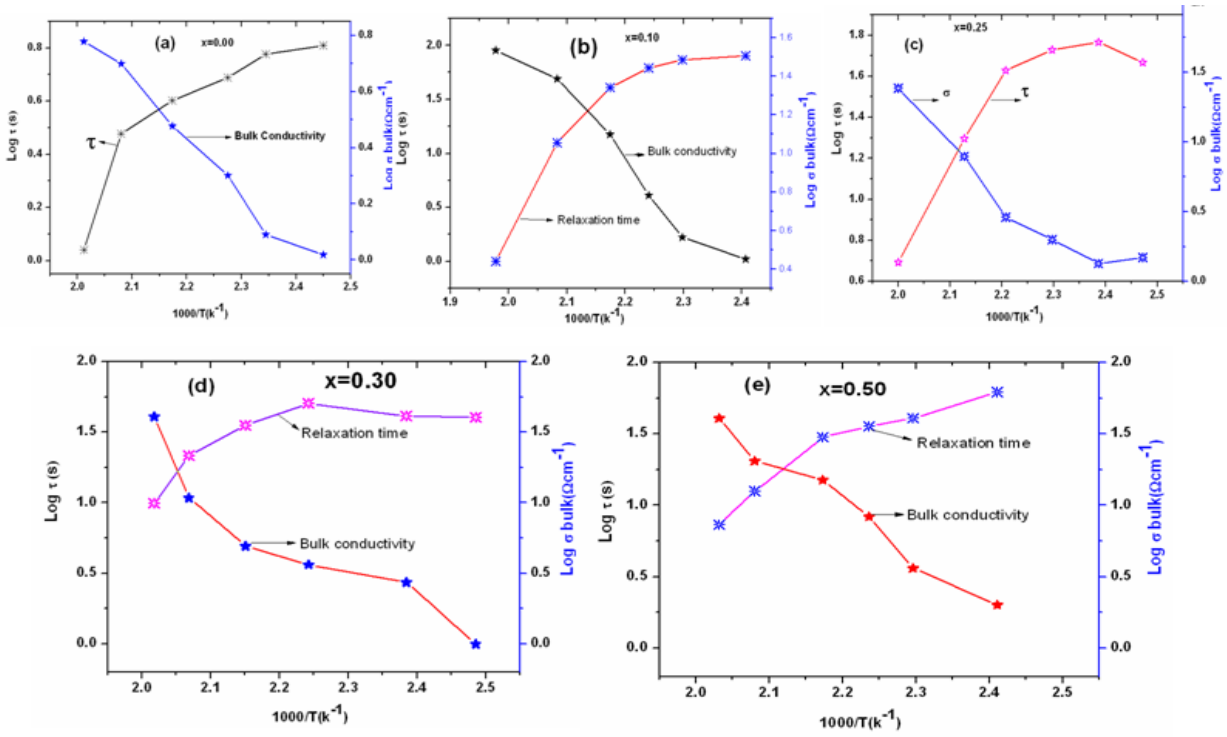

Fig. 4.19 (a-e): The bulk conductivity and relaxation time with the inverse of the temperature of the sample $Pb_{1-x}La_xTiO_3$ for (a) x = 0.0, (b) x = 0.10, (c) x = 0.25, (d) x = 0.30 and (e) x = 0.50.

4.2.5.5 AC and DC conductivity analysis

The AC conductivity can be calculated using the relation (discussed in chapter-3),

$$\sigma_{ac} = 2\pi f \varepsilon_0 \varepsilon_r \tan\delta \qquad (4.7)$$

Where $2\pi f = \omega$, f is the frequency. ε_o is the permittivity of free space, ε_r is the relative dielectric constant, tanδ is the dissipation factor. Fig. 4.20 (a-e) shows the variation of AC conductivity with frequency for x = 0.00, 0.10, 0.25, 0.30 and 0.50 samples respectively. Temperature below 400^0C, σ_{ac} is linearly varies with frequency and above that (with increase of temperature) nonlinearity occurred in the low frequency region. This behavior reveals that hopping mechanism plays an important role in the conduction process in the low temperature region. Generally, the frequency dispersion of σ_{ac} follows universal power law [181],

$$\sigma(\omega) = \sigma(0) + A\omega^n \quad (0<n<1) \qquad (4.8)$$

Where σ(ω) is the total conductivity, σ(0) is the frequency independent conductivity, the coefficient A and exponent n are temperature and material intrinsic property dependent constants, and the term

$A\omega^n$ associated with the AC dependence and it characterizes all dispersion phenomena. Equation 4.8 corresponds to the short range hopping conduction of charge carriers. The hopping takes place by charge carriers through trap sites separated by energy barriers of variable heights. The number of charge carriers (which have high relaxation time due to the higher energy barrier) might be less in number. These charge carriers respond in the low frequency region only. Hence, the conductivity is lower at low frequency region. The number of charge carriers with low barrier height is more and it responds easily with higher frequency. Hence it showed high conductivity at higher frequencies. At higher temperatures the thermal energy of the charge carriers is increased and consequently the relative potential barrier height is also reduced. At low temperatures, the electronic hopping conduction dominates the conductivity and ionic hopping makes little contribution.

The DC conductivity at different temperatures has been extracted from the extrapolation of the frequency independent plateau region from the log σ_{ac} versus log ω plot. Fig. 4.21 shows the temperature dependence of DC conductivity and slopes obey Arrhenius relation.

A frequency independent relation between AC conductivity and temperature is defined as [181],

$$\sigma = \sigma_0 e^{-\frac{E_a}{k_B T}} \qquad (4.9)$$

Where σ_o is the pre-exponential factor, k_B is the Boltzmann constant and E_a is the activation energy for conduction. Activation energy (E_a) is listed for all the samples in Table 4.10. These values are compared with the Pb based polycrystalline ceramic materials [135,137,139]. It is found that the activation energy decreases with the increase of La concentration.

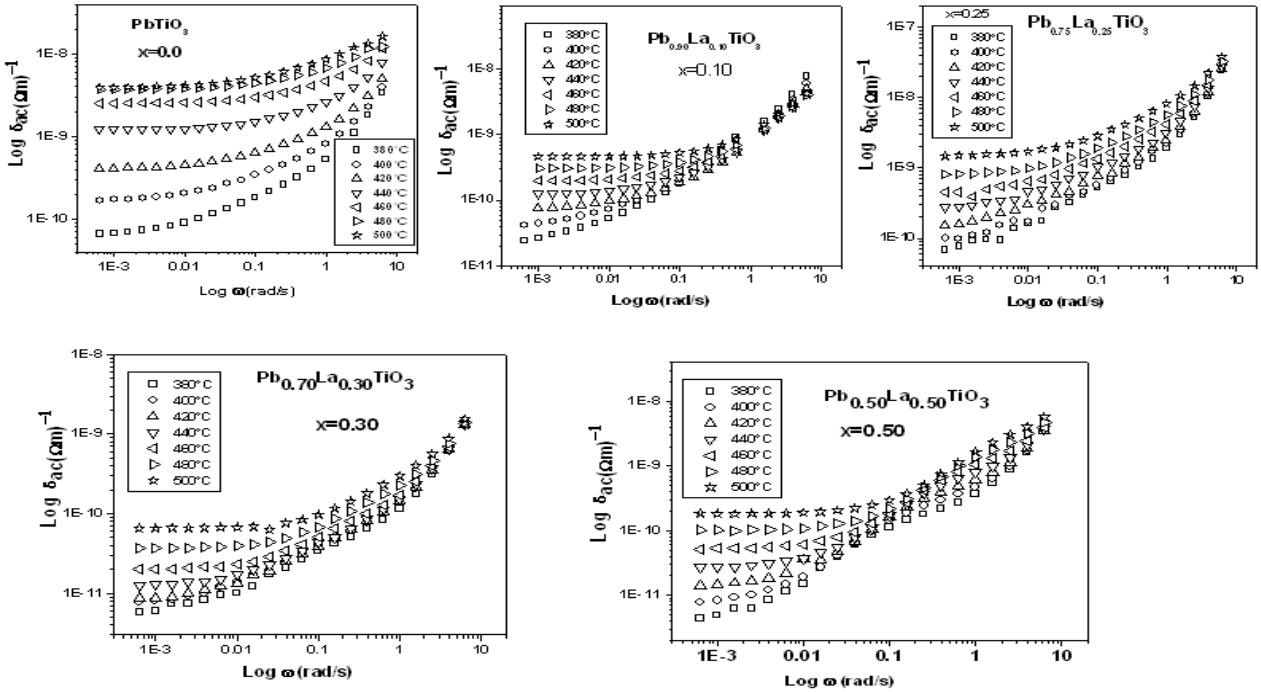

Fig. 4.20 (a-e): The variation of AC conductivity with the frequency of the sample (sintered at 1100^0C for 4h) $Pb_{1-x}La_xTiO_3$ for (a) x = 0.0, (b) x = 0.10, (c) x = 0.25, (d) x = 0.30 and (e) x = 0.50.

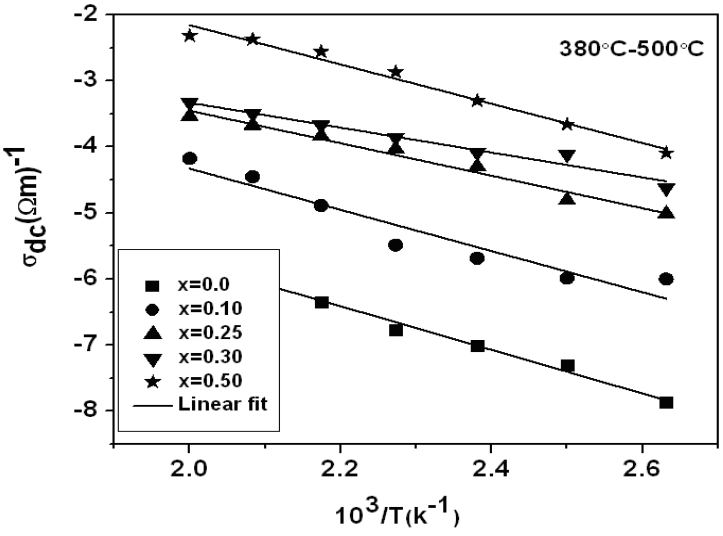

Fig. 4.21: The variation of DC conductivity with the inverse of the temperature of the sample $Pb_{1-x}La_xTiO_3$ for x = 0.0, 0.10, 0.25, 0.30, and 0.50.

4.2.5.6 Electrical modulus analysis

The modulus analysis has an advantage that it suppresses the information about electrode effects [182-185]. This can also be used to study conductivity relaxation times [186]. The complex modulus is defined as the inverse of the complex permittivity and in the present work, the impedance data were converted into electrical modulus using the relations M′ (real part) =

$\omega C_0 Z''$ and M'' (imaginary part) = $\omega C_0 Z'$, where $C_0 = \varepsilon_0 A/t$, A is the area of the sample, t is the thickness of the sample and $\varepsilon_o = 8.854 \times 10^{-12}$F/m is the permittivity of the free space [187].

Fig. 4.22 (a-e) shows the variation of the real part of the electric modulus as a function of frequency at different temperatures. At lower frequencies, M' tends to be very small, confirming that the contribution from the electrode effect is negligible and hence can be ignored when the data are analyzed in modulus formalism. The observed dispersion in M' at higher frequencies may be attributed to conductivity relaxation due to short range mobility of charge carriers.

Fig. 4.23 (a-e) shows the variation of the imaginary part of the electric modulus as a function of frequency at different temperatures. The asymmetric nature of M'' plot is suggestive of the stretched exponential character of relaxation times of the material. Each peak attains a maximum value (M''_{max}) at frequency ω_{max} called conductivity relaxation frequency and it obeys the Arrhenius relation.

Fig. 4.24 shows the plot of log ω_{max} versus $10^3/T$ at different temperatures of all the compounds which shows Arrhenius behavior. The calculated activation energy from M'' spectra is given in Table 4.10. The activation energy from M''_{max} spectra represents non-localized conduction (long range conduction). The variation of M' and M'' with frequency over a wide range of temperature, the appearance of a peak in the spectrum that changes its position with temperature confirms the presence of temperature dependent relaxation in good agreement with the CIS results. The peaks undergo a systematic shift towards higher frequency with increase in temperature. The broadening of the peak also occurs with rise in temperature and it indicates the spread of relaxation with different mean time constant. The results definitely suggest non-Debye type of relaxation in the materials.

Fig. 4.25 shows the Cole Cole plot of the sample $Pb_{1-x}La_xTiO_3$ for x = 0.0, 0.10, 0.25, 0.30 and 0.50. The asymmetric semicircular arc is observed in this plot and confirms the presence of an electrical relaxation phenomenon in the material. A comparison of activation energy obtained from

different (i) σ_{dc} (380-500˚C) (ii) Relaxation time (τ) (iii) apparent bulk conductivity (σ_b) (iii) Z''_{max} and (iv) M''_{max} spectra of PLT compound is given in Table 4.10.

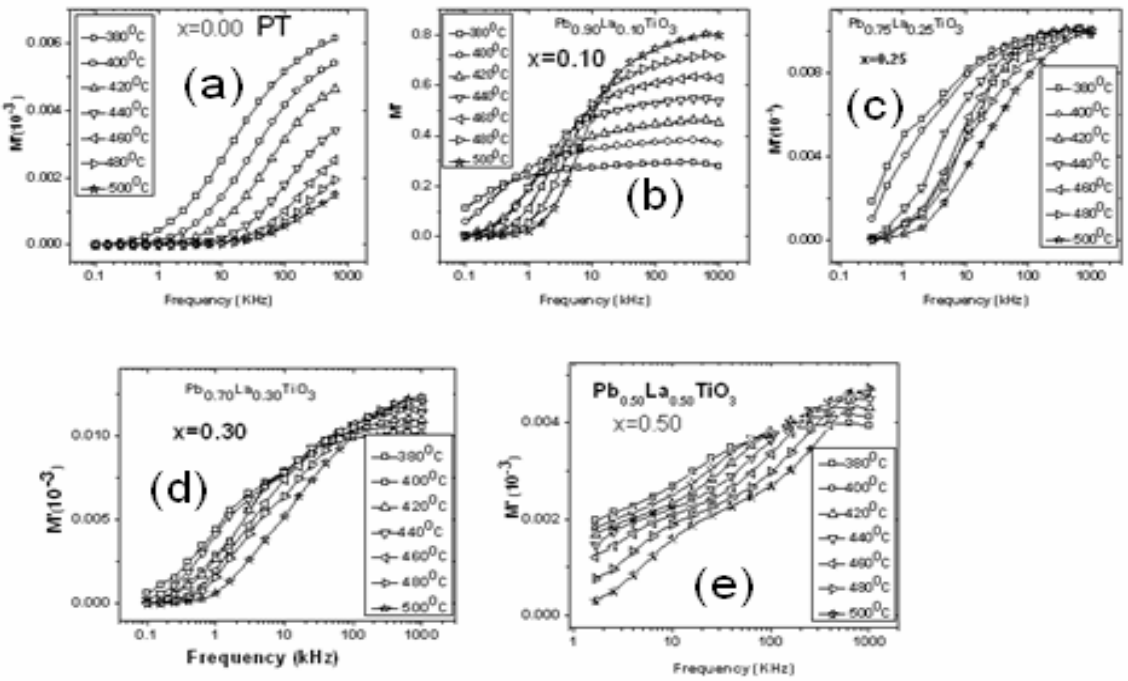

Fig. 4.22 (a-e): The real part of modulus versus frequency at some selected temperature of the sample $Pb_{1-x}La_xTiO_3$ for (a) x = 0.0, (b) x = 0.10, (c) x = 0.25, (d) x = 0.30, and (e) x = 0.50.

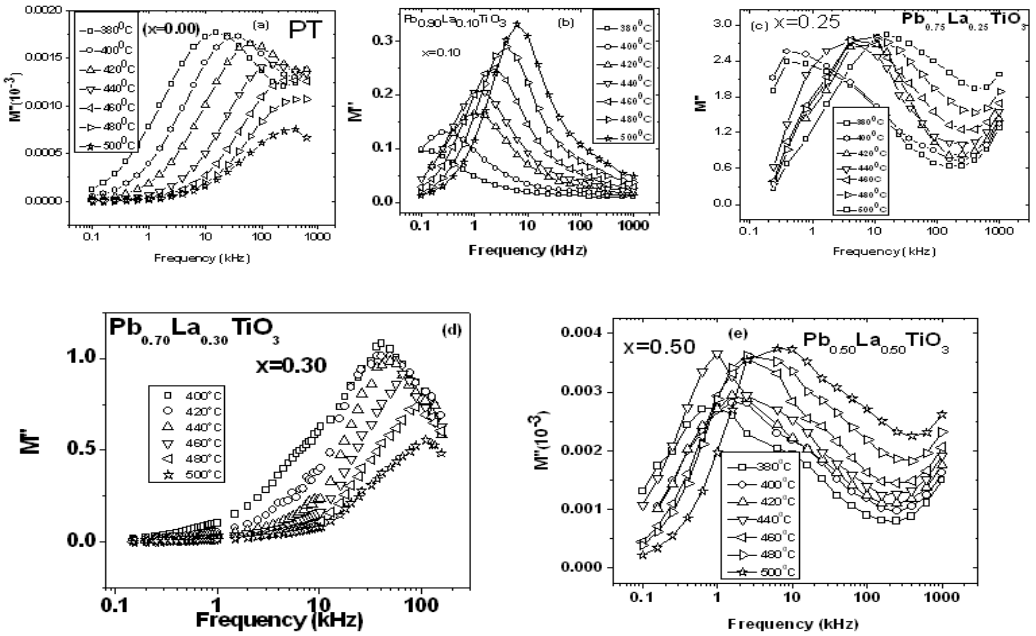

Fig. 4.23 (a-e): The imaginary part of modulus versus frequency at some selected temperature of the sample $Pb_{1-x}La_xTiO_3$ for (a) x = 0.0, (b) x = 0.10, (c) x = 0.25, (d) x = 0.30, and (e) x = 0.50.

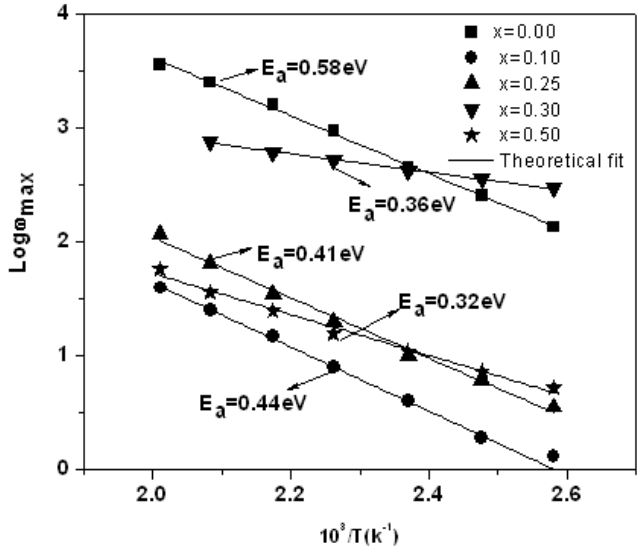

Fig. 4.24: Log ω_{max} versus $10^3/T$ (obtained from M″spectra) at different temperatures of the sample $Pb_{1-x}La_xTiO_3$ for x = 0.0, 0.10, 0.25, 0.30, and 0.50.

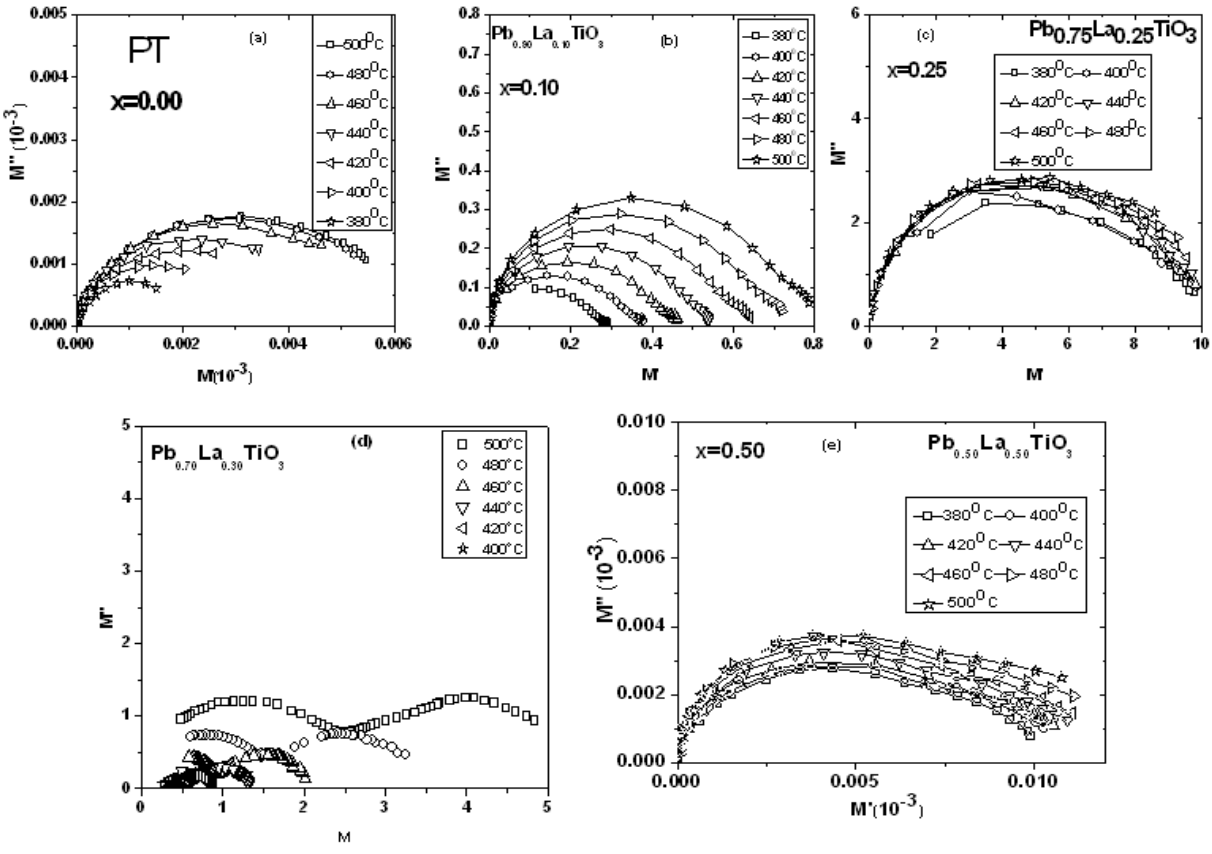

Fig. 4.25 (a-e): The real part of impedance versus imaginary part of impedance at some selected temperature of the sample $Pb_{1-x}La_xTiO_3$ for (a) x = 0.0, (b) x = 0.10, (c) x = 0.25, (d) x = 0.30, and (e) x = 0.50.

Table 4.10: Activation energy in eV obtained from (i) σ_{dc} (380-500˚C) (ii) relaxation time (τ) (iii) apparent bulk conductivity (σ_b) (iii) Z''_{max} and (iv) M''_{max} spectra of PLT compound.

Sample	$E_a(\sigma_{dc})$	$E_a(\tau)$	$E_a(\sigma_b)$	$E_a(Z''_{max})$	$E_a(M''_{max})$
x = 0.00	0.53	0.53	0.51	0.59	0.58
x = 0.10	0.49	0.41	0.42	0.46	0.44
x = 0.25	0.41	0.37	0.33	0.42	0.41
x = 0.30	0.37	0.32	0.31	0.35	0.36
x = 0.50	0.29	0.29	0.30	0.31	0.32

4.3 Summary

PT and PLT samples prepared by solid state reaction route crystallize in a pure perovskite phase. The structure of the $Pb_{1-x}La_x\ TiO_3$ ceramic samples was studied by XRD-Rietveld refinement technique. The tetragonality of the structure gradually diminishes with the increase of La content until a structural phase transition from tetragonal-to-cubic structure, which takes place in the range between 10% atom of La samples. In fact, the samples with x = 0.0 crystallize in the *P4mm* space group, whereas the sample with ranged 10% to 50% atom of La crystallizes in the $Pm\bar{3}m$ space group. The refinement of XRD data also confirmed the existence of only A-site vacancies, which are introduced to the perovskite structure by the aliovalent replacement of Pb^{2+} by La^{3+} cations. From SEM analysis it is observed that the grains are uniformly distributed throughout the surface. Grain size increases with increase of La concentration.

Ferroelectric to paraelectric transition has been observed in all the materials. Ferroelectric property diffuses with high La concentrations. A room temperature P-E loop reavels the ferroelectric ordering in the sample. AC conductivity increases and activation energy decreases with the La concentrations. A slow dynamic relaxation phenomenon is observed at and around the ferroelectric transition temperature. The variation of the imaginary part of impedance and modulus

with frequency shows asymmetric peaks and the peak maximum shifts towards higher frequencies with increase in temperature. These features lead to a non-Debye type of relaxation behavior in the investigated system. From the Nyquist plot analysis the grain resistance decreases with an increase in temperature which shows negative temperature coefficient of resistance (NTCR) of the material which is the behavior of a typical semiconductor [188].

CHAPTER 5

STRUCTURAL AND ELECTRICAL BEHAVIOR OF $(Pb_{0.70}La_{0.30})(Ti_{1-x}A_x)O_3$, (A = Mn or Al and $0.0 \leq x \leq 0.20$) CERAMICS

CHAPTER 5

STRUCTURAL AND ELECTRICAL BEHAVIOR OF $(Pb_{0.70}La_{0.30})(Ti_{1-x}A_x)O_3$, (A = Mn or Al and $0.0 \leq x \leq 0.20$) CERAMICS

As discussed in Chapter 4, the sample $Pb_{0.70}La_{0.30}TiO_3$ exhibit diffuse type of ferroelectric behavior. Hence, this chapter aims to study the influence of Mn and Al ion substituted on B-site (Ti site) of $Pb_{0.70}La_{0.30}TiO_3$ ceramic. In the first part, the influence of Mn in $(Pb_{0.70}La_{0.30})(Ti_{1-x}Mn_x)O_3$ on structural and electrical behavior was studied. In the second part the effect of Al in $(Pb_{0.70}La_{0.30})(Ti_{1-x}Al_x)O_3$ on structural and electrical properties was discussed. The chapter starts with synthesis and followed by characterizations with results and discussion. The samples were synthesized by solid state reaction route and then characterized by X-ray diffraction, scanning electron microscopy, energy dispersive X-ray spectroscopy and complex impedance spectroscopy.

5.1 Sample preparation

Perovskite $(Pb_{0.70}La_{0.30})(Ti_{1-x}A_x)O_3$ where (A = Mn, Al) for x = 0.0, 0.05, 0.10, 0.15 and 0.20) ceramics have been prepared by the solid state method at high temperature. Stoichiometric ratios of PbO, La_2O_3, Mn_2O_3/Al_2O_3 and TiO_2 with 99.9% purity were weighed by using a high precision electronic balance. The flow chart for the preparation of the sample has already discussed in Chapter 3. The Mn and Al doped samples were fired at 900^oC for 8h. The fine powders of the above compounds were pressed into cylindrical pellets of 6 mm diameter and 1 mm thickness under a uni-axial pressure of 6 ton using a hydraulic press. Finally the pellets of both Mn and Al doped

samples sintered at 1100°C for over 4h with 5% extra lead oxide to compensate the lead loss at high temperature and then cooled to room temperature at the rate of 2°C min^{-1}.

5.2 Structural and electrical behavior of $(Pb_{0.70}La_{0.30})(Ti_{1-x}Mn_x)O_3$, ($0.0 \leq x \leq 0.20$) ceramics.

5.2.1 Structural analysis by employing the Rietveld method

The XRD patterns of $(Pb_{0.70}La_{0.30})(Ti_{1-x}Mn_x)O_3$, (x=0.0, 0.05, 0.10, 0.15 and 0.20) samples annealed at 900ºC for 8h and 1100ºC for 4h were shown in Fig. 5.1 and Fig. 5.2 respectively. The peaks of the single phase materials could be indexed using space group $Pm\bar{3}m$ with cubic symmetry. The average crystallite size calculated by using Rietveld method (discussed in Chapter 3 and 4) are listed in Table 5.1 for both 900ºC and 1100ºC annealed samples. The crystallite size decreases with increase of Mn concentration. Crystallite size increases with increase of annealed temperature. It is due to the formation of larger crystals at high temperature.

The XRD patterns for all the samples were analyzed by employing the Rietveld refinement technique [152] with the help of the Fullprof program. The refined XRD patterns of the sample calcined at 900ºC for 8h and sintered at 1100^0C for 4h is shown in Fig. 5.3 (a-e) and Fig. 5.4 (a-e) respectively. It is observed that all the peaks could be well refined to $Pm\bar{3}m$ space group. Lattice parameters, occupancy, fractional atomic positions etc. were taken as the free parameter during the fitting. The lattice parameters, cell volume and the goodness of the fitting parameters are listed in Table 5.2 and Table 5.3 for both the annealed samples. The site occupancy factors for each atom was refined separately and then fixed at the refined value. In the final refinement, the isotropic thermal parameters and the oxygen occupancy factor were refined. The lattice parameters and unit cell volumes are found to be decreased with the increase of Mn concentration, it could be due to the smaller ionic size of Mn^{3+} (0.66Å) to that of ionic size of Ti^{4+} (0.68Å). The lattice parameters, cell volume versus Mn compositions for different annealing temperatures is shown in Fig. 5.5 (a, b). The bond lengths and angles were calculated with the help of a powder cell program of both the

annealed samples and the values were listed in Table 5.2 and Table 5.3. Using the refined parameter the stable crystal structure is suggested which is shown in Fig. 5.6 (a) and Fig. 5.6 (b) for the Mn free and a typical Mn doped sample respectively. The splitting of Wyckoff positions after refinement of $(Pb_{0.70}La_{0.30})(Ti_{1-x}Mn_x)O_3$ for x = 0.0, 0.05, 0.10, 0.15, 0.20 samples annealed at 1100ºC is cited in Table 5.4.

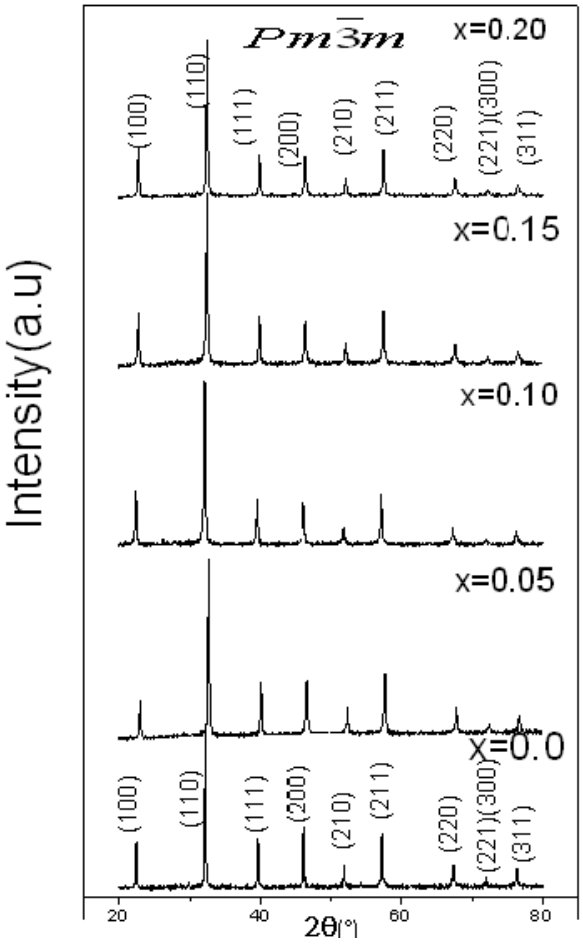

Fig. 5.1: XRD patterns of $(Pb_{0.70}La_{0.30})(Ti_{1-x}Mn_x)O_3$ for x = 0.0, 0.05 ,0.10, 0.15, and 0.20 samples annealed at 900ºC for 8h.

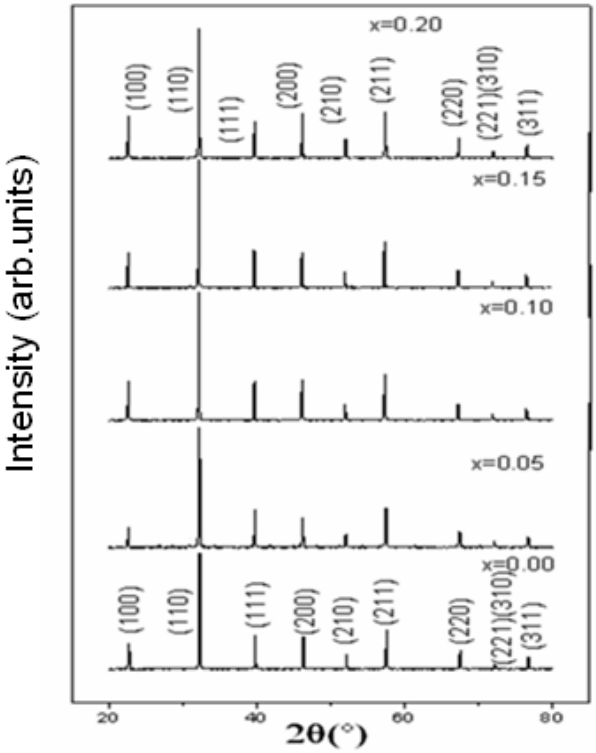

Fig. 5.2: XRD patterns of $(Pb_{0.70}La_{0.30})(Ti_{1-x}Mn_x)O_3$ for x = 0.0, 0.05, 0.10, 0.15, and 0.20 samples annealed at 1100ºC.

Table 5.1: Crystallite size of the sample $(Pb_{0.70}La_{0.30})(Ti_{1-x}Mn_x)O_3$ for x = 0.0, 0.05, 0.10, 0.15, and 0.20 samples annealed at 900ºC for 8h and 1100ºC.

Sample	Rietveld method (crystallite size (nm))	
	900^0C	1100^0C
$Pb_{0.70}La_{0.30}TiO_3$	12.2(9)	34.7(3)
$Pb_{0.70}La_{0.30}(Ti_{0.95}Mn_{0.05})O_3$	11.4(12)	34.2(10)
$Pb_{0.70}La_{0.30}(Ti_{0.90}Mn_{0.10})O_3$	10.9(3)	33.3(6)
$Pb_{0.70}La_{0.30}(Ti_{0.85}Mn_{0.15})O_3$	10.5(4)	33.0(10)
$Pb_{0.70}La_{0.30}(Ti_{0.80}Mn_{0.20})O_3$	10.0(11)	32.1(10)

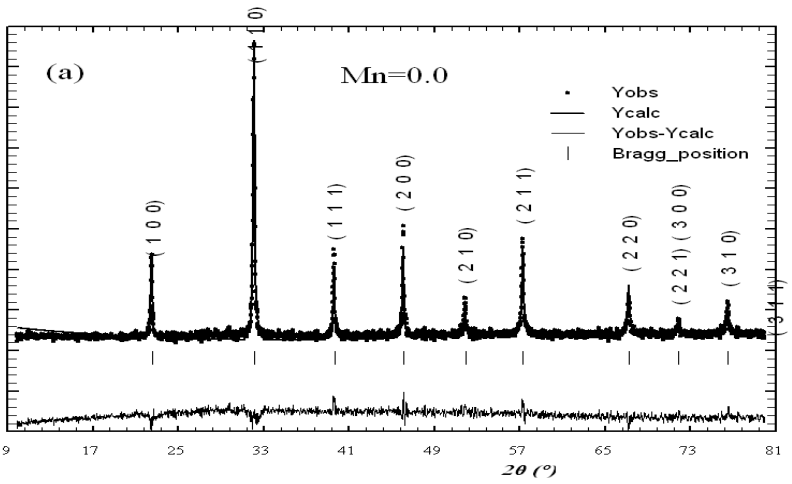
(a)
Mn=0.0
Yobs
Ycalc
Yobs-Ycalc
Bragg_position
(1 0 0)
(1 1 0)
(1 1 1)
(2 0 0)
(2 1 0)
(2 1 1)
(2 2 0)
(2 2 1) (3 0 0)
(3 1 0)
(3 1 1)
9
17
25
33
41
49
57
65
73
81
2θ (°)

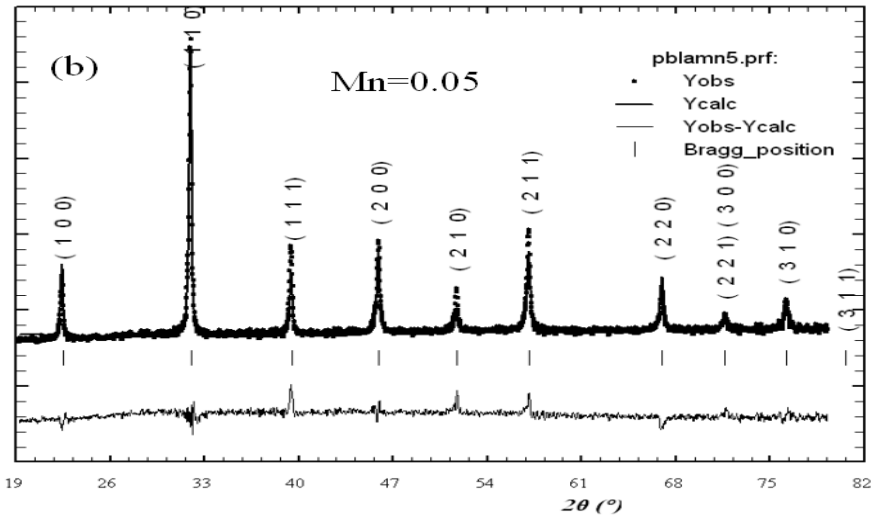
(b)
Mn=0.05
pblamn5.prf:
Yobs
Ycalc
Yobs-Ycalc
Bragg_position
(1 0 0)
(1 1 0)
(1 1 1)
(2 0 0)
(2 1 0)
(2 1 1)
(2 2 0)
(2 2 1) (3 0 0)
(3 1 0)
(3 1 1)
19
26
33
40
47
54
61
68
75
82
2θ (°)

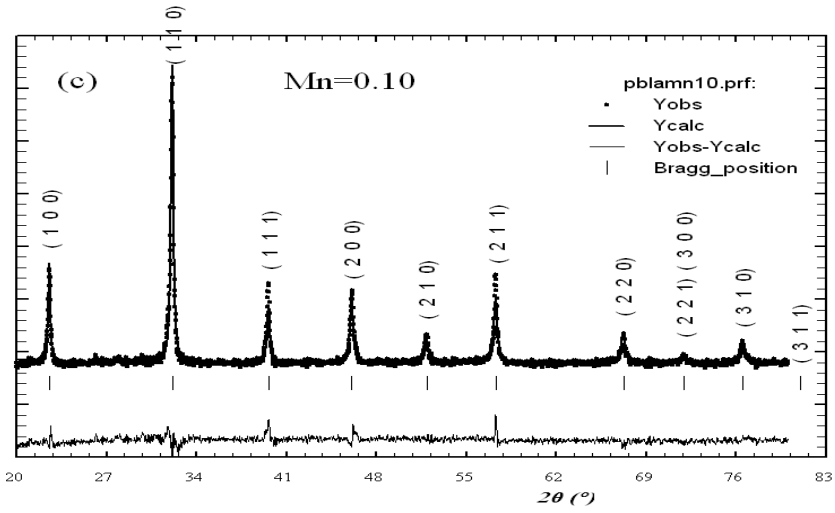
(c)
Mn=0.10
pblamn10.prf:
Yobs
Ycalc
Yobs-Ycalc
Bragg_position
(1 0 0)
(1 1 0)
(1 1 1)
(2 0 0)
(2 1 0)
(2 1 1)
(2 2 0)
(2 2 1) (3 0 0)
(3 1 0)
(3 1 1)
20
27
34
41
48
55
62
69
76
83
2θ (°)

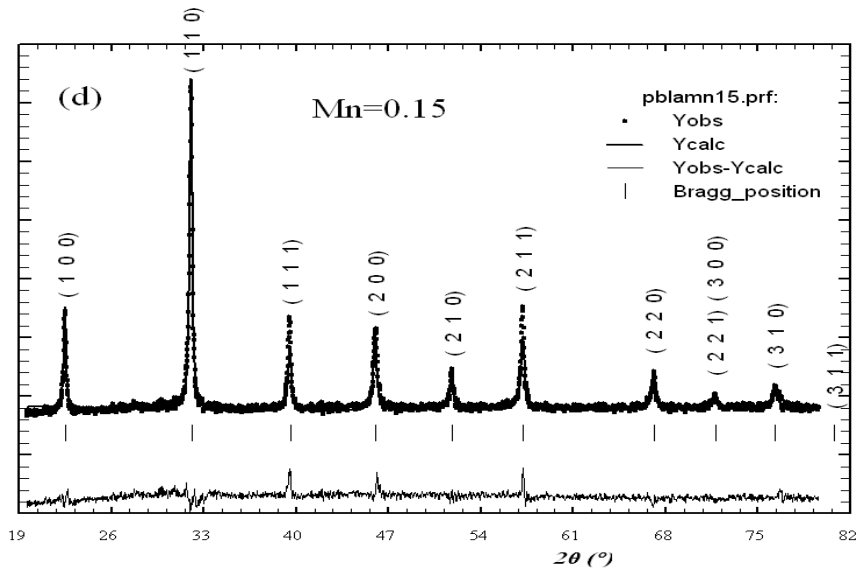

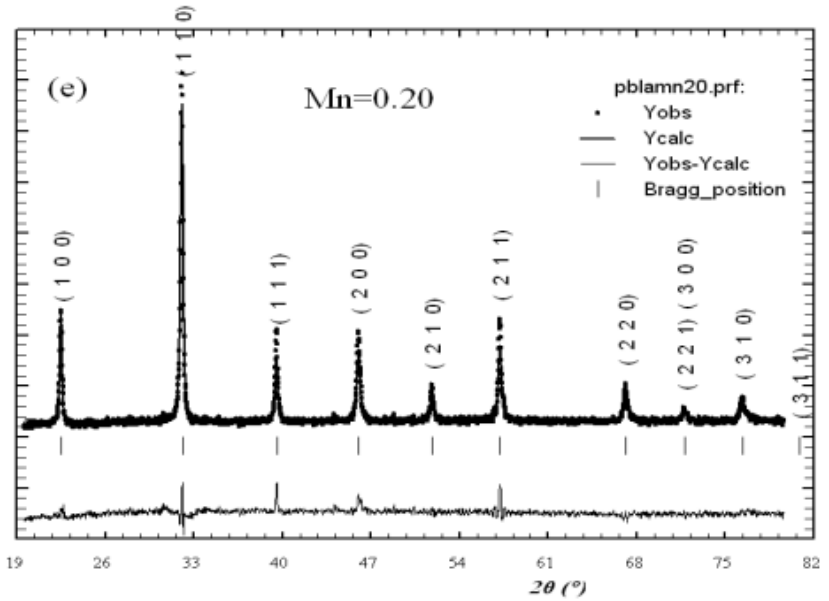

Fig. 5.3 (a-e): Refined patterns of $(Pb_{0.70}La_{0.30})(Ti_{1-x}Mn_x)O_3$ samples (a) x = 0.0, (b) x = 0.05, (c) x = 0.10, (d) x = 0.15, and (e) x = 0.20 annealed at 900ºC for 8h respectively. The experimental points are given as dot (**.**) and theoretical data are shown as solid lines. The difference between theoretical and experimental data is shown as a bottom line. The vertical lines represent the Bragg's allowed peaks.

Table 5.2: Parameters obtained from Rietveld analysis of $(Pb_{0.70}La_{0.30})(Ti_{1-x}Mn_x)O_3$, samples for x = 0.0, 0.05, 0.10, 0.15, 0.20 annealed at 900ºC for 4 h.

Sample → / Parameters ↓	x = 0.00	x = 0.05	x = 0.10	x = 0.15	x = 0.20
Space group	$Pm\bar{3}m$	$Pm\bar{3}m$	$Pm\bar{3}m$	$Pm\bar{3}m$	$Pm\bar{3}m$
Pb(Occup.)	0.6978(4)	0.5867(8)	0.6676(4)	0.6670(6)	0.6870(7)
La(Occup.)	0.3015(5)	0.1867(8)	0.2676(4)	0.2670(6)	0.2870(7)
Ti(Occup.)	0.9956(7)	0.9500(8)	0.9606(9)	0.8500(4)	0.8000(1)
Mn(Occup)	--	0.0500(8)	0.1006(9)	0.1505(2)	0.2010(3)
a=b=c(Å)	3.9504(6)	3.9492(9)	3.9476(8)	3.9440(2)	3.9401(2)
Volume ($Å^3$)	62.3(7)	61.4(1)	61.2(6)	60.9(4)	60.5(1)
χ^2 (chi^2)	2.12	2.02	2.38	3.04	2.73
R_p	13.5	37.3	26.1	33.6	25.4
R_{wp}	23.7	33.3	25.0	30.2	23.9
R_{Bragg}	13.7	26.5	11.7	20.1	16.0
R_f	7.09	14.3	9.96	12.1	10.3
R_{exp}	7.34	12.0	10.3	10.2	9.91
Pb-Ti/La (Å)	3.405(10)	3.412(6)	3.134(6)	3.058(2)	3.010(2)
Pb-Mn-La (Å)	-	3.141(7)	3.251(7)	4.021(8)	4.275(5)
Ti/La-O_1 (Å)	2.235(3)	1.982(5)	1.774(4)	1.784(3)	1.999(2)
Ti/La-O_2 (Å)	2.068(8)	2.125(3)	1.754(3)	1.805(2)	1.801(8)
$\angle Pb-Ti/La-Pb$	16.86(3)	19.22(6)	17.65(1)	16.85(6)	16.52(14)
$\angle Pb-Ti/Mn-O_1$	102.32(3)	96.29(2)	105.14(7)	107.61(3)	111.35(4)
$\angle Pb-Ti/La-O_2$	45.51(6)	104.12(9)	108.86(6)	112.21(4)	112.99(4)
$\angle Pb-La-Mn$	-	125.32(4)	121.62(4)	121.10(8)	119.84(4)
$\angle La-O_2-Mn$	-	113.41(2)	113.59(2)	109.42(2)	109.78(3)
$\angle La-O_1-Mn$	-	84.10(6)	83.95(5)	82.32(4)	80.87(5)

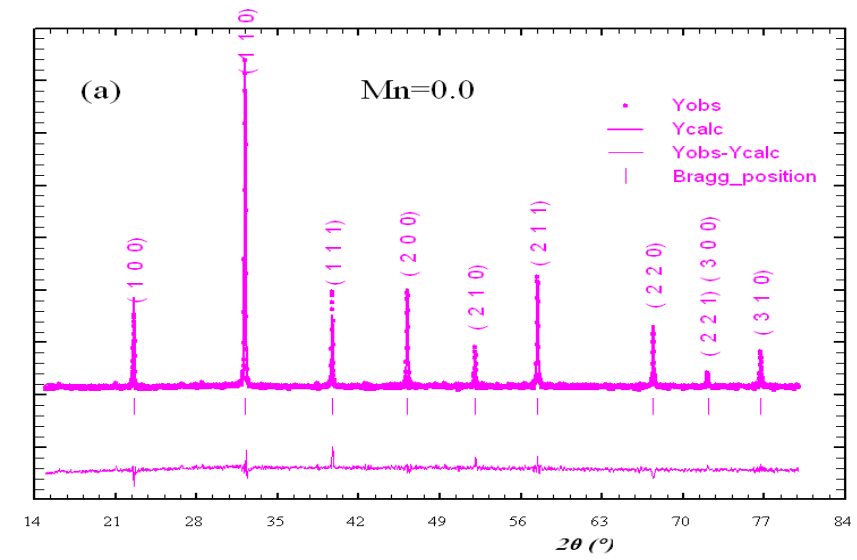
(a)
Mn=0.0
Yobs
Ycalc
Yobs-Ycalc
Bragg_position
(1 0 0)
(1 1 0)
(1 1 1)
(2 0 0)
(2 1 0)
(2 1 1)
(2 2 0)
(2 2 1) (3 0 0)
(3 1 0)
14 21 28 35 42 49 56 63 70 77 84
2θ (°)

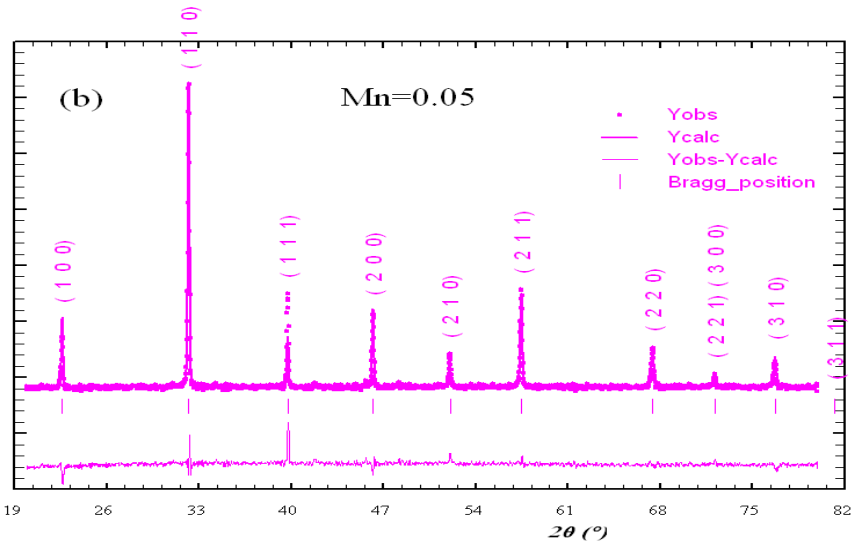
(b)
Mn=0.05
Yobs
Ycalc
Yobs-Ycalc
Bragg_position
(1 0 0)
(1 1 0)
(1 1 1)
(2 0 0)
(2 1 0)
(2 1 1)
(2 2 0)
(2 2 1) (3 0 0)
(3 1 0)
(3 1 1)
19 26 33 40 47 54 61 68 75 82
2θ (°)

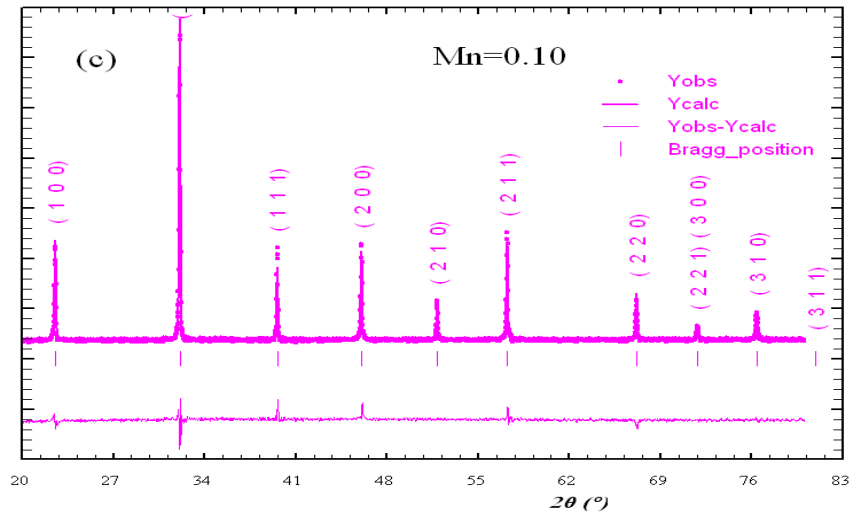
(c)
Mn=0.10
Yobs
Ycalc
Yobs-Ycalc
Bragg_position
(1 0 0)
(1 1 1)
(2 0 0)
(2 1 0)
(2 1 1)
(2 2 0)
(2 2 1) (3 0 0)
(3 1 0)
(3 1 1)
20 27 34 41 48 55 62 69 76 83
2θ (°)

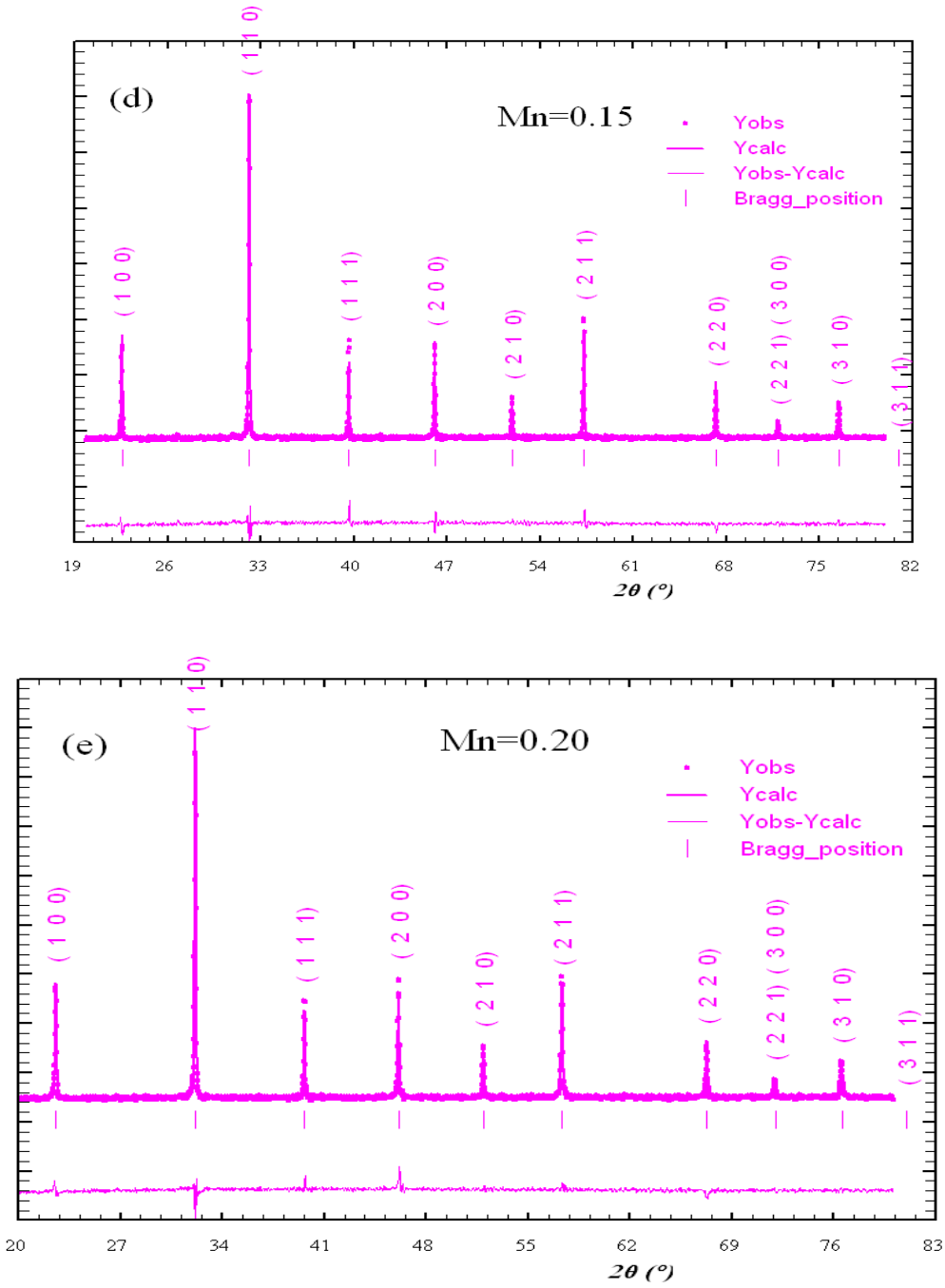

Fig. 5.4 (a-e): Refined patterns of $(Pb_{0.70}La_{0.30})(Ti_{1-x}Mn_x)O_3$ samples (a) x = 0.0, (b) x = 0.05, (c) x = 0.10, (d) x = 0.15, and (e) x = 0.20 annealed at 1100ºC for 4h. The experimental points are given as dot (**.**) and theoretical data are shown as solid lines. The difference between theoretical and experimental data is shown as a bottom line. The vertical lines represent the Bragg's allowed peaks.

Table 5.3: Parameters obtained from Rietveld analysis of $(Pb_{0.70}La_{0.30})(Ti_{1-x}Mn_x)O_3$ powders for x = 0.0, 0.05, 0.10, 0.15, 0.20 annealed at 1100ºC for 4 h.

Sample → / Parameters ↓	x = 0.00	x = 0.05	x = 0.10	x = 0.15	x = 0.20
Space group	$Pm\bar{3}m$	$Pm\bar{3}m$	$Pm\bar{3}m$	$Pm\bar{3}m$	$Pm\bar{3}m$
Pb(Occup.)	0.6878(1)	0.5882(3)	0.6808(3)	0.6676(7)	0.6870(5)
La(Occup.)	0.3040(4)	0.1882(3)	0.2808(3)	0.2670(6)	0.2870(5)
Ti(Occup.)	0.9956(7)	0.9500(1)	0.9080(6)	0.8501(5)	0.8030(3)
Mn(Occup)	--	0.0507(2)	0.1090(5)	0.1506(5)	0.2071(4)
a=b=c (Å)	3.9383(7)	3.9362(6)	3.9330(5)	3.9292(3)	3.9250(2)
Volume ($Å^3$)	61.1(3)	60.9(6)	60.8(3)	60.5(2)	60.4(8)
χ^2 (chi^2)	3.62	2.84	2.47	2.53	2.37
R_p	19.9	26.6	18.3	18.6	16.7
R_{wp}	21.8	27.3	20.4	19.6	18.7
R_{Bragg}	12.7	15.5	10.8	9.26	11.1
R_f	8.52	13.1	7.90	6.15	7.42
R_{exp}	9.56	10.3	8.64	8.80	9.02
Pb-Ti/La (Å)	3.417(14)	3.469(3)	3.333(3)	3.251(5)	3.201(2)
Pb-Mn-La (Å)	-	3.138(1)	3.198(5)	4.136(5)	4.251(5)
Ti/La-O_1 (Å)	2.484(6)	1.789(8)	1.674(3)	1.774(5)	1.986(5)
Ti/La-O_2(Å)	2.142(9)	2.074(5)	1.886(5)	1.845(2)	1.802(3)
$\angle Pb-Ti/La-Pb$	15.85(2)	18.29(6)	16.67(5)	16.53(8)	16.52(5)
$\angle Pb-Ti/La-O_1$	101.23(5)	92.29(11)	103.56(3)	103.69(8)	104.35(3)
$\angle Pb-Ti/La-O_2$	47.41(5)	109.93(6)	111.32(7)	114.23(4)	114.96(5)
$\angle Pb-La-Mn$	-	127.29(5)	120.56(3)	120.30(5)	119.95(2)
$\angle La-O_2-Mn$	-	114.58(2)	112.32(4)	111.98(3)	111.86(2)
$\angle La-O_1-Mn$	-	86.25(4)	83.52(3)	82.96(2)	81.35(5)

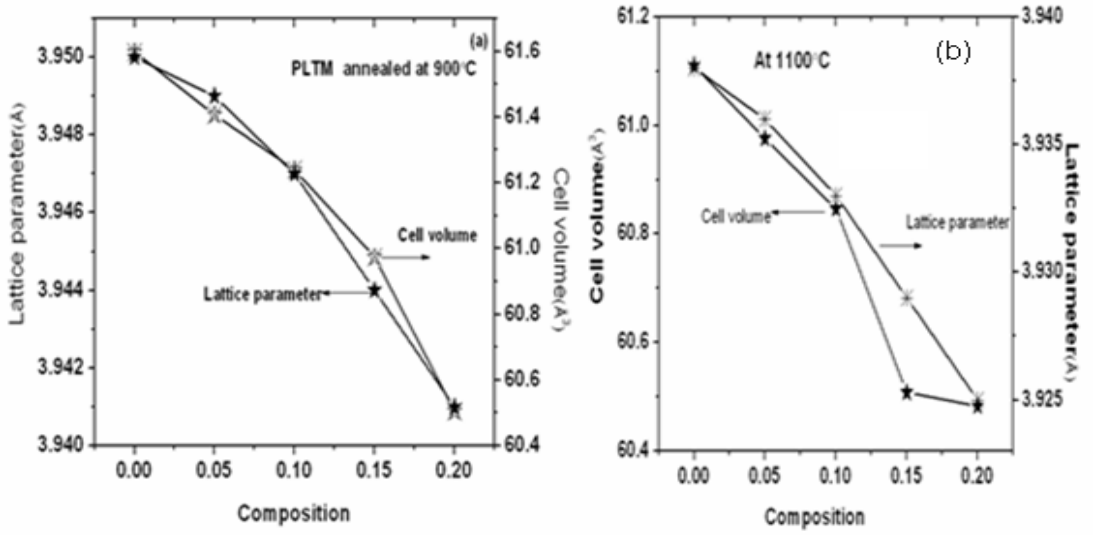

Fig. 5.5 (a, b): Lattice parameter, cell volume versus Mn concentration of $(Pb_{0.70}La_{0.30})(Ti_{1-x}Mn_x)O_3$ for x = 0.0, 0.05, 0.10, 0.15, 0.20, and 0.25 samples: (a) annealed at 900ºC for 8h and (b) sintered at 1100 ºC for 4h.

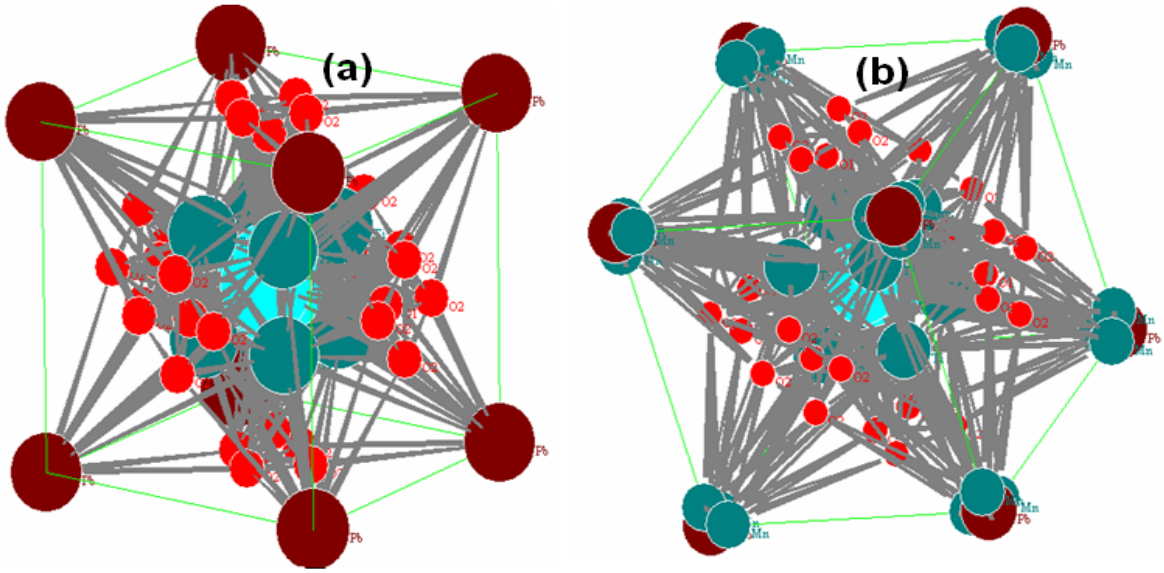

Fig. 5.6 (a, b): Crystal structure of (a) $(Pb_{0.70}La_{0.30})TiO_3$ and a typical sample of (b) $(Pb_{0.70}La_{0.30})(Ti_{0.85}Mn_{0.15})O_3$ annealed at 1100˚C for 4h.

Table 5.4: Splitting of Wyckoff positions after refinement of $(Pb_{0.70}La_{0.30})(Ti_{1-x}Mn_x)O_3$ for x = 0.0, 0.05, 0.10, 0.15, 0.20 samples annealed at 1100ºC for 4h.

Sample → / Wyckoff Positions ↓	x = 0.00	x = 0.05	x = 0.10	x = 0.15	x = 0.20
Pb	1a	1a	1a	1a	1a
La	6b	6b	6b	6b	6b
Ti	8c	8c	8c	8c	8c
Mn	---	8d	6d	1d	1d
O	12e	6e	6e	6e	6e

5.2.2 Microstructural and compositional analysis

The scanning electron micrograph of the $(Pb_{0.70}La_{0.30})(Ti_{1-x}Mn_x)O_3$ for x = 0.05, 0.10, 0.15 and 0.20 samples annealed at 1100ºC for 4h is shown in the Fig. 5.7(a-d). It can be noticed that the samples are uniform and the grains are in order of micron size. These micrographs revealed that the grain structure of the samples is dense, crack free and smooth [189].The grain size decreases with increase of Mn concentration. The average grain sizes of the samples are found to be 2.5-3.5µm. The SEM-EDS spectrums are shown in Fig. 5.8 (a-d). The energy dispersive spectrum (EDS) analysis reveals that, all the compositions present in the samples are close to as prepared. The experimental EDS wt% and theoretical EDS wt% of all the samples have been given in Table 5.5.

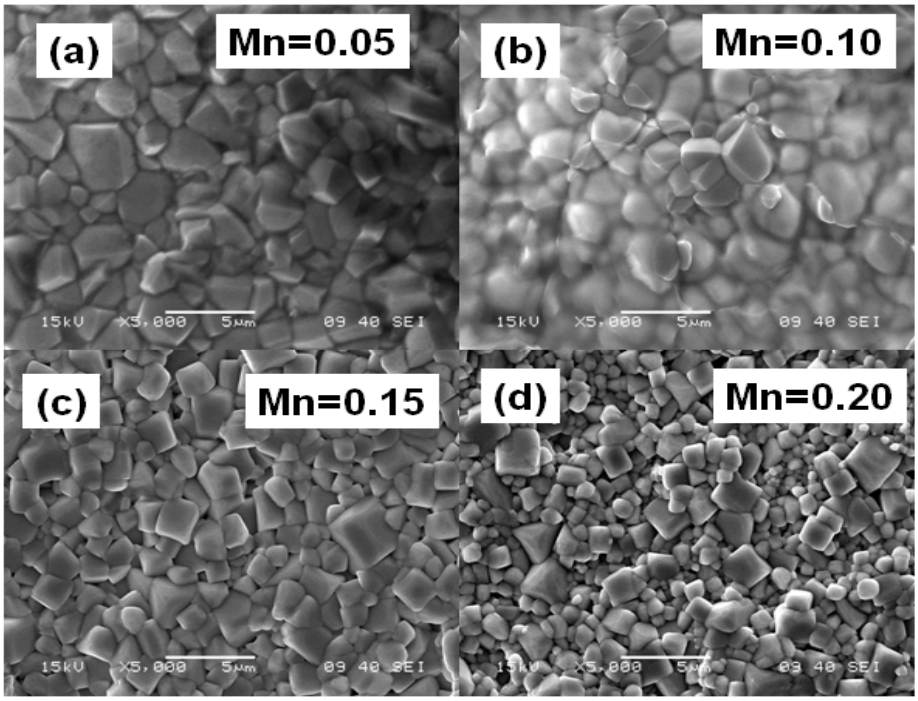

Fig. 5.7 (a-d): The SEM of $(Pb_{0.70}La_{0.30})(Ti_{1-x}Mn_x)O_3$ for (a) x = 0.05, (b) x = 0.10, (c) x = 0.15, and (d) x = 0.20 samples annealed at 1100ºC for 4h.

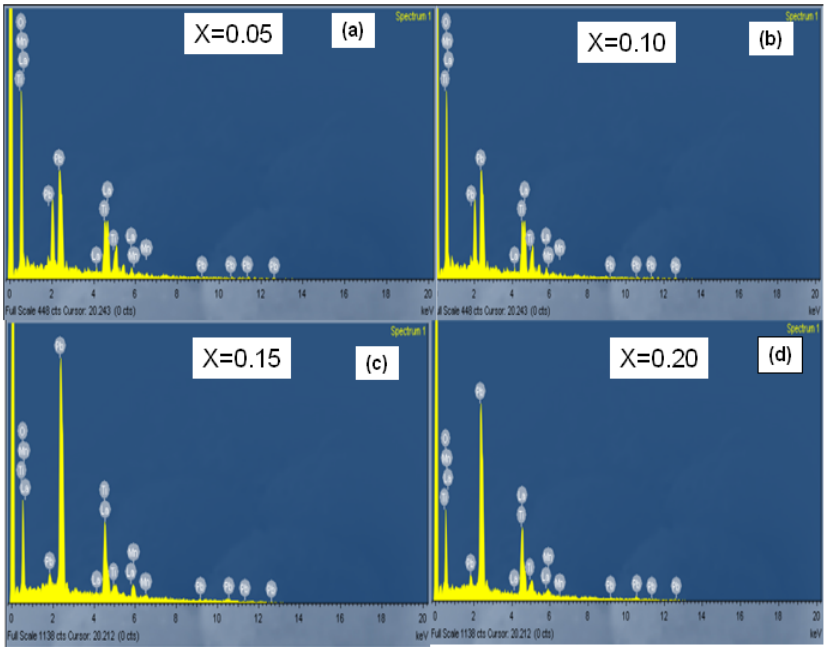

Fig. 5.8 (a-d): The EDS of $(Pb_{0.70}La_{0.30})(Ti_{1-x}Mn_x)O_3$ for x = 0.05, (b) x = 0.10, (c) x = 0.15, and (d) x = 0.20 samples annealed at 1100ºC for 4h.

Table 5.5: Elemental analysis of $(Pb_{0.70}La_{0.30})(Ti_{1-x}Mn_x)O_3$, for (a) x = 0.05, (b) x = 0.10, (c) x = 0.15, and (d) x = 0.20 samples annealed at 1100ºC for 4h.

Composition	Element	Wt% calculated	Wt% EDX
x = 0.05	Pb	47.31	47.09
	La	26.51	26.31
	Ti	15.49	16.94
	O	9.80	9.81
	Mn	0.88	0.85
x = 0.10	Pb	47.28	47.59
	La	26.49	26.81
	Ti	14.66	13.44
	O	9.90	10.49
	Mn	1.77	1.67
x = 0.15	Pb	47.24	47.55
	La	26.47	28.93
	Ti	13.84	14.67
	O	9.73	7.72
	Mn	2.71	2.33
x = 0.20	Pb	47.21	47.06
	La	26.45	26.93
	Ti	13.01	13.19
	O	9.78	9.63
	Mn	3.54	3.19

5.2.3 Electrical conductivity studies

5.2.3.1 Impedance analysis

Fig. 5.9 (a) shows the variation of real part of impedance (Z′) with frequency of $(Pb_{0.70}La_{0.30})(Ti_{1-x}Mn_x)O_3$, (x = 0.15, PLTM15) at different temperatures. It is observed that the magnitude of Z′ decreases with the increase in both frequency as well as temperature for all the samples which indicate an increase in AC conductivity. The Z′ values for all temperatures merge above 100 kHz.

This may be due to the release of space charges as a result of reduction in the barrier properties of the material with the rise in temperature and may be a responsible factor in the enhancement of AC conductivity of the material with temperature at higher frequencies. Further, at low frequencies the Z' values decrease with the rise in temperature which reveals the negative temperature coefficient of resistance (NTCR) type behavior. It is the typical behavior of semiconductors.

Fig. 5.9 (b) shows the variation of the imaginary part of impedance (Z'') with frequency at different temperatures of PLTM15 sample. The Z'' values reach a maximum peak (Z''_{max}) and the value of Z''_{max} shifts to higher frequencies with increasing temperature for all the samples. A peak broadening which is slightly asymmetrical in nature can be observed with the rise in temperature. The broadening of peaks in frequency suggests that there is a spread of relaxation times, i.e., the existence of a temperature dependent electrical relaxation phenomenon in the material (Hosono et al, 2001) [190]. The value of maximum frequency and relaxation time of $(Pb_{0.70}La_{0.30})(Ti_{1-x}Mn_x)O_3$, (x = 0.15) (PLTM15) ceramic is capitalized in Table 5.6. The Arrhenius behavior of maximum frequency and temperature of a typical sample PLTM15 is shown in Fig. 5.9 (c).

Table 5.6: The values of log of maximum frequency and relaxation time (τ) of a typical sample $(Pb_{0.70}La_{0.30})(Ti_{1-x}Mn_x)O_3$, (x = 0.15) ceramic.

Temperature(^oC)	Logω_{max}	τ (rad/s)
400	0.69932	0.19984
420	0.84859	0.14171
440	0.96587	0.10818
460	1.08448	0.10818
480	1.2764	0.08232
500	1.42567	0.03753

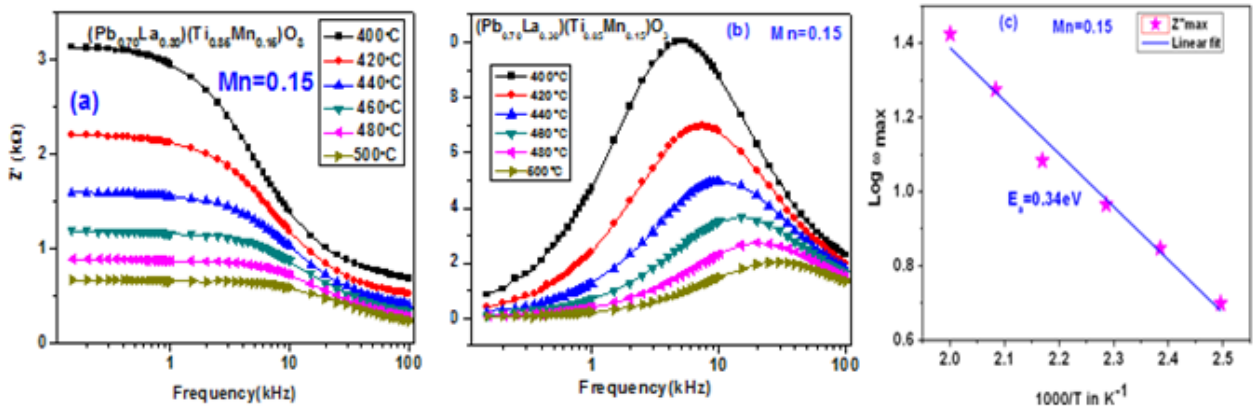

Fig. 5.9 (a-c): The typical plot of the frequencies versus (a) real and (b) imaginary part of impedance spectra at different temperatures of $(Pb_{0.70}La_{0.30})(Ti_{1-x}Mn_x)O_3$, (x = 0.15) ceramic and, (c) $Log\omega_{max}$ versus 1000/T plot.

Nyquist plots of Complex impedance spectrum of $(Pb_{0.70}La_{0.30})(Ti_{1-x}Mn_x)O_3$ for x = 0.05, 0.10, 0.15 and 0.20 samples annealed at 1100˚C are shown in Fig. 5.10 (a-d) respectively. It shows depressed semicircular arcs with their centers lying below the real axis. The angle by which the semicircle is depressed below the real axis and the amount of inclination of the straight line are related to the width of the distribution of the relaxation time. This suggests the poly-dispersive nature of the sample. Using commercially available software *ZSIMP WIN Version 2,* the impedance data were analyzed in order to obtain the bulk resistance (R_g) and grain boundary resistance (R_{gb}). The observed feature can be modeled by equivalent circuits as shown in inset of Fig. 5.10. The impedance plot comprises two semicircular arcs. The assignment of the two semicircular arcs to the electrical response is due to grain interior and grain boundary (*MacDonald*, 1987) [166]. As the temperature increases, the radius of the arc corresponding to the bulk resistance of the sample decreases indicating an activated conduction mechanism. Fig. 5.11 (a-e) shows the variation of grain and grain boundary resistance of $(Pb_{0.70}La_{0.30})(Ti_{1-x}Mn_x)O_3$ for x = 0.0, 0.05, 0.10, 0.15, 0.20 ceramics respectively. The grain and grain boundary resistance decreases with an increase in temperature with the Arrhenius dependence of the form [181],

$$R = \beta e^{-\frac{E_a}{k_B T}} \tag{5.1}$$

Where, R is the resistance, β is the exponential component, E_a is the activation energy, k_B is the Boltzmann constant and T is the absolute temperature. The experimental data of R_g and R_{gb} were fitted to Equation 5.1. The fitted parameters are enlisted in Table 5.7.

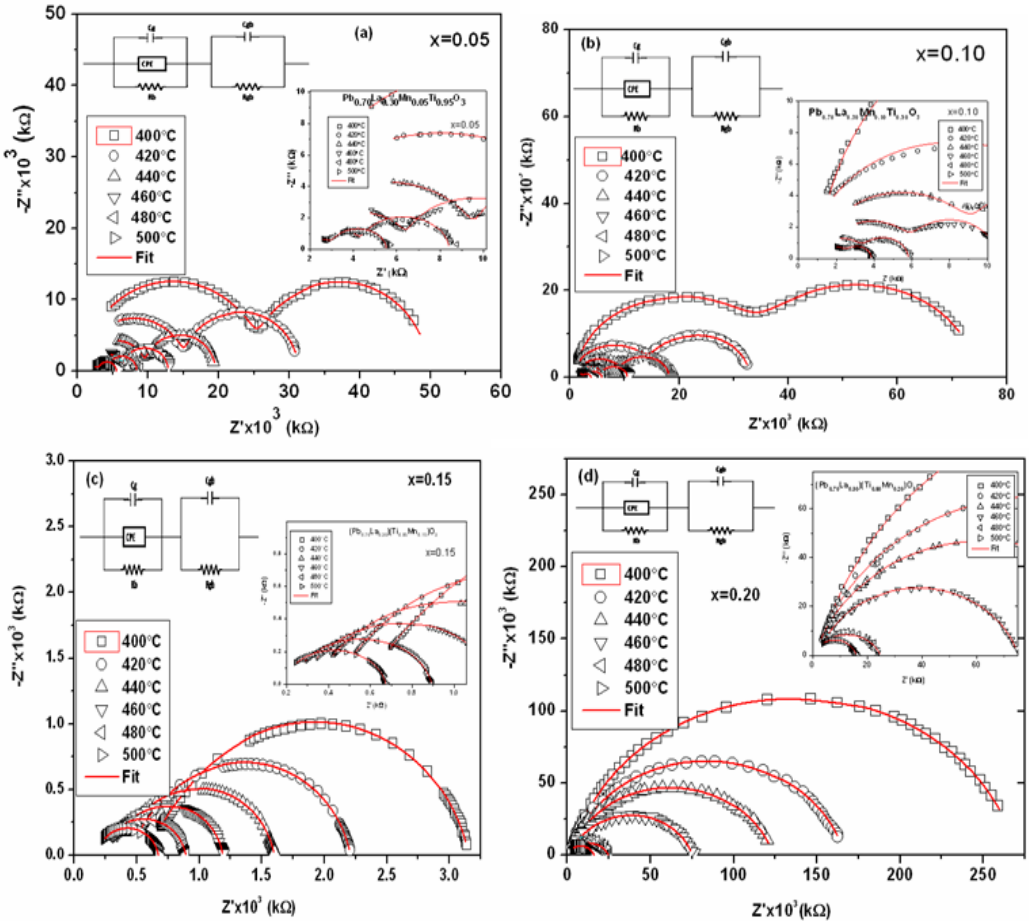

Fig.5.10 (a-d): Nyquist plot of complex impedance spectrum of $Pb_{0.70}La_{0.30})(Ti_{1-x}Mn_x)O_3$ samples annealed at 1100˚C for (a) x = 0.05, (b) x = 0.10, (c) x = 0.15, and (d) x = 0.20. Inset shows the equivalent circuit diagram.

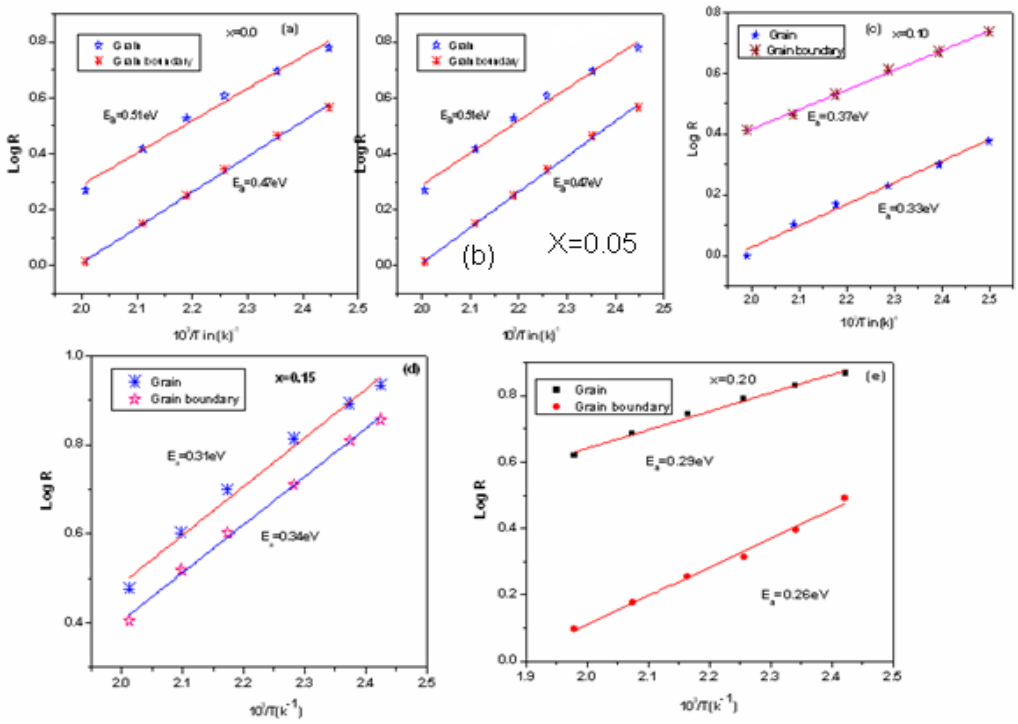

Fig. 5.11 (a-e): The variation of grain and grain boundary resistance of $(Pb_{0.70}La_{0.30})(Ti_{1-x}Mn_x)O_3$ samples annealed at 1100˚C for (a) x = 0.00, (b) x = 0.05, (c) x = 0.10, (d) x = 0.15, and (e) x = 0.25.

5.2.3.2 AC and DC conductivity analysis

Fig. 5.12 (a-d) shows the variation of AC conductivity as a function of frequency at various temperatures for $(Pb_{0.70}La_{0.30})(Ti_{1-x}Mn_x)O_3$ for x = 0.05, 0.10, 0.15, 0.20 ceramics. We have observed that conductivity increases with increase of temperature. The frequency independent behavior of the conductivity in the low frequency region is observed but that become sensitive at high frequency region, which generally known as hopping frequency, shifted towards higher frequency side with the increase of temperature. In the high frequency region where the conductivity increases are caused due to the hopping of charge carrier in finite clusters. Frequency independent AC conductivity has been observed in the high temperature indicates the long range movement of mobile charge carriers. The AC conductivity pattern indicates a progressive rise in conductivity with an increase of temperature. The activation energy obtained from this conductivity is given in Table 5.8. The activation energy corresponds to the energy required for the polaron to

jump over the grain boundaries. As the temperature increases, the polarons have sufficient thermal energy to get activated and jumped over the barrier. Thus it is clear that AC conductivity of the present materials is governed by the polaron hopping mechanism and is influenced by both frequency and temperature.

Table 5.7: Grain and grain boundary resistance and capacitance from Nyquist plot of $Pb_{0.70}La_{0.30})(Ti_{1-x}Mn_x)O_3$, (x = 0.0, 0.05, 0.10, 0.15, 0.20) ceramics.

Sample	T ˚C	CPE_g nF	R_g k Ω	CPE_{gb} nF	R_{gb} k Ω
x = 0.0	400	0.038	$3.13x10^4$	1.24	$3.65x\ 10^4$
	420	0.171	$3.06x\ 10^4$	1.29	$2.11x\ 10^4$
	440	0.218	$5.02x\ 10^3$	1.40	$9.31x10^3$
	460	0.248	$4.23x\ 10^3$	2.92	$4.48x\ 10^3$
	480	0.350	$7.23x\ 10^2$	3.34	$5.67x\ 10^2$
	500	0.795	$1.98x\ 10^2$	4.24	$2.69x10^2$
x = 0.05	400	0.152	$2.85x\ 10^4$	9.75	$2.76x\ 10^4$
	420	0.147	$1.96x\ 10^4$	10.6	$1.88x\ 10^4$
	440	0.142	$1.02x\ 10^4$	13.0	$1.33x10^4$
	460	0.133	$8.06x\ 10^3$	16.8	$5.47x\ 10^3$
	480	0.122	$3.23x\ 10^3$	17.5	$5.04x\ 10^3$
	500	0.133	$1.52x\ 10^3$	18.9	$3.19x10^3$
x = 0.10	400	0.404	$3.34x\ 10^4$	7.42	$3.94x\ 10^4$
	420	0.388	$1.36x\ 10^4$	9.17	$1.85x\ 10^4$
	440	0.385	$7.86x\ 10^3$	11.2	$9.04x\ 10^3$
	460	0.377	$4.97x\ 10^3$	12.7	$4.60x\ 10^3$
	480	0.344	$1.44x\ 10^3$	16.0	$4.10x\ 10^3$
	500	0.285	$1.28x\ 10^3$	18.2	$1.36x\ 10^3$
x = 0.15	400	0.254	$1.50x\ 10^3$	4.31	$1.04x\ 10^3$
	420	0.235	$1.17x\ 10^3$	4.37	$5.82x\ 10^2$
	440	0.216	$8.95x\ 10^2$	4.76	$3.54x\ 10^2$
	460	0.209	$6.99x\ 10^2$	5.30	$2.12x\ 10^2$
	480	0.204	$6.67x\ 10^2$	5.37	$2.10x\ 10^2$
	500	0.199	$4.90x\ 10^2$	6.34	$1.36x\ 10^2$
x = 0.20	400	0.214	$3.66x\ 10^5$	2.37	$3.09x\ 10^5$
	420	0.211	$1.65x\ 10^5$	3.71	$1.82x\ 10^5$
	440	0.146	$1.23x\ 10^5$	4.24	$1.04x\ 10^5$
	460	0.130	$7.31x\ 10^4$	5.90	$7.18x\ 10^4$
	480	0.124	$2.47x\ 10^4$	6.39	$2.40x\ 10^4$
	500	0.115	$3.31x\ 10^3$	8.44	$3.33x\ 10^3$

Fig. 4.13 shows the variation of DC conductivity (σ_{dc}) with the inverse of temperature. The nature of conductivity variation (linear dependence of σ_{dc} with 10^3/T) indicates an increase in conductivity with rise in temperature which is a typical Arrhenius-type behavior. This suggests that electrical conduction in the material is a thermally activated process which is governed by the relation [181],

$$\sigma_{dc} = \sigma_0 e^{-\frac{E_a}{k_B T}} \qquad (5.2)$$

Here the symbols bear the usual meanings (described in previous chapters). The comparison of E_a (in eV) obtained from (i) σ_{ac}, (ii) σ_{dc}, (iii) relaxation time, (iv) R_g, (v) R_{gb} and (vi) Z''_{max} of PLTM ceramic is cited in Table 5.8.

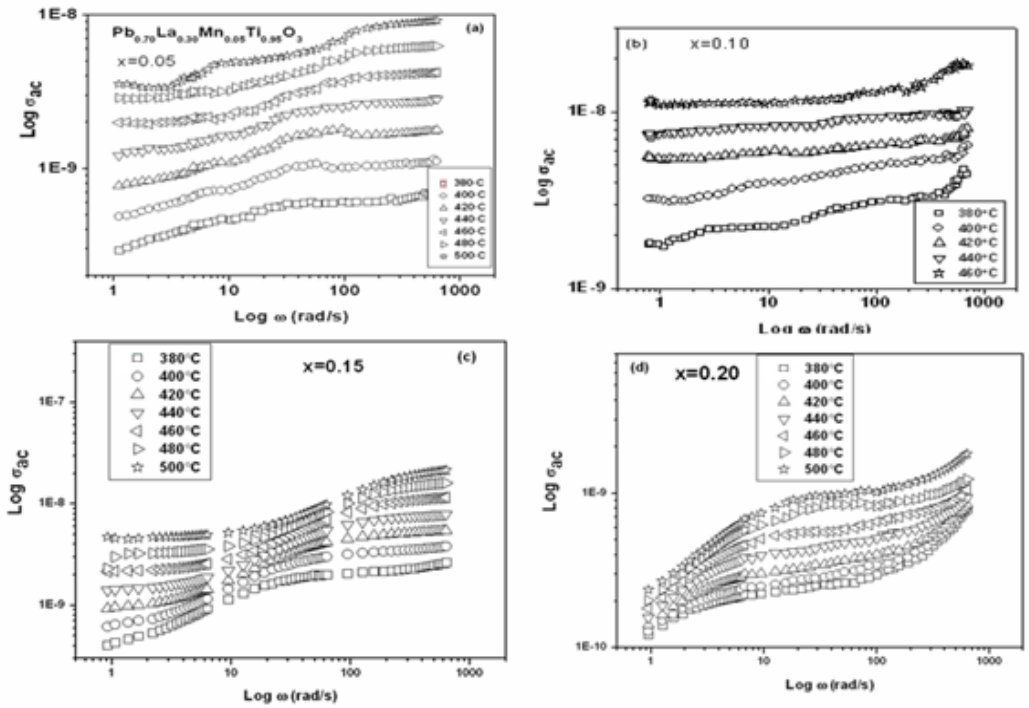

Fig. 5.12 (a-d): The variation of AC conductivity as a function of frequency at different temperatures of $(Pb_{0.70}La_{0.30})(Ti_{1-x}Mn_x)O_3$ for (a) x = 0.05, (b) x = 0.10, (c) x = 0.15, and (d) x = 0.20 ceramics.

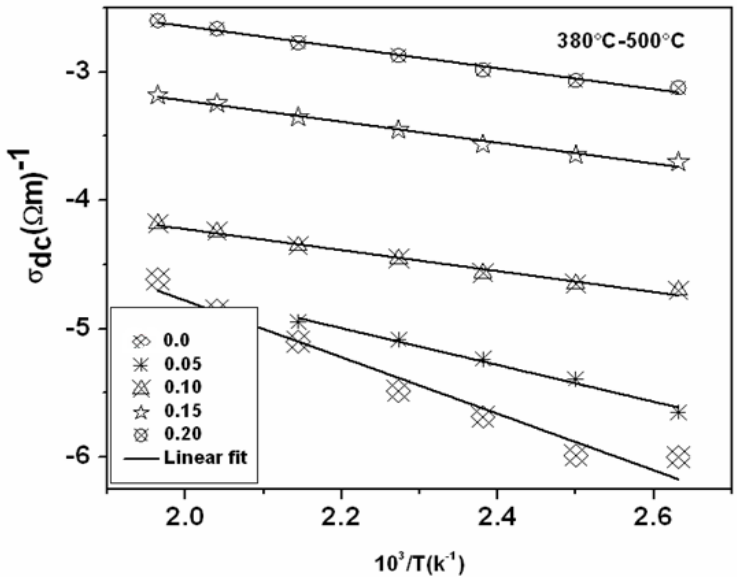

Fig. 5.13: Variation of DC conductivity of $Pb_{0.70}La_{0.30})(Ti_{1-x}Mn_x)O_3$ for x = 0.05, 0.10, 0.15, 0.20 ceramics with the inverse of temperature.

Table 5.8: Comparison of E_a (in eV) obtained from (i) $\sigma_{ac,}$ (ii) $\sigma_{dc,}$ (iii) relaxation time, (iv) $R_{g,}$ (v) $R_{gb,}$ and (vi) Z''_{max} of PLTM ceramic.

Sample	$E_a(\sigma_{ac})$	$E_a(\sigma_{dc})$	$E_a(\tau)$	$E_a(R_g)$	$E_a(R_{gb})$	$E_a(Z'')$
x = 0.00	0.37	0.31	0.35	0.47	0.51	0.41
x = 0.05	0.35	0.34	0.33	0.39	0.41	0.42
x = 0.10	0.32	0.31	0.31	0.33	0.37	0.38
x = 0.15	0.29	0.27	0.29	0.31	0.34	0.34
x = 0.20	0.26	0.28	0.26	0.29	0.26	0.28

5.2.4 Summary

The materials PLTM has been successfully prepared by ceramic route and no structural change was found with Mn concentration. Structural analysis was done by employing the Rietveld method and was found that, lattice parameters and cell volume decrease with increase in Mn concentration. Impedance spectroscopy shows the existence of a non-Debye type relaxation phenomenon in the materials and it has been used to establish a relation between microstructure and electrical properties of the materials. The reduction of grain and grain boundary resistances (R_g and R_{gb}) of

materials to increase in temperature shows the negative temperature co-efficient of resistance (NTCR) which is typical behavior of conventional semiconductors. So, the results indicate a typical semiconducting behavior of the materials. Activation energy decreases with an increase in Mn concentration. This change in behavior indicates the participation of Mn ions in the conduction, thermally activated and relaxation process.

5.3 Structural and electrical behavior of $(Pb_{0.70}La_{0.30})(Ti_{1-x}Al_x)O_3$, $(0.0 \leq x \leq 0.20)$ ceramics

5.3.1 Structural analysis by employing the Rietveld method

XRD patterns of $(Pb_{0.70}La_{0.30})(Ti_{1-x}Al_x)O_3$ (PLTA) for x = 0.0, 0.05, 0.10, 0.15, 0.20 calcined at 900ºC for 8h are shown in Fig. 5.14. It is observed that, the samples are in single-phase form and all observed peaks could be indexed using $Pm\bar{3}m$ space groups with cubic symmetry. Fig. 5.15 shows the X-ray diffraction patterns of $(Pb_{0.70}La_{0.30})(Ti_{1-x}Al_x)O_3$ (x = 0.0, 0.05, 0.10, 0.15, 0.20) sintered at 1100ºC for 4h. All the XRD patterns were analyzed by employing the Rietveld refinement technique with the help of Fullprof program. The refined XRD patterns for the samples annealed at 900ºC and 1100^0C are shown in Fig. 5.16 (a-d) and Fig. 5.17 (a-d) respectively. All the patterns could be refined using $Pm\bar{3}m$ space groups with cubic symmetry. Average crystallite size has been calculated by using the Rietveld method [152] is listed in Table 5.9 for both 900ºC and 1100ºC annealed samples. It is observed that the average crystallite size increases with annealing temperatures which is due to the formation of larger crystals during the time of annealing at high temperatures. The crystallite size decreases with increase of Al concentration for the samples annealed at a particular temperature. It could be due to the strain effect which develops due to the size mismatch of different cations. The crystallite size, lattice parameters, occupancy, fractional atomic positions, thermal parameters etc. were taken as the free parameter during the fitting. All the refined parameters, goodness of fitting parameters, position of occupancies, bond lengths and bond angles calculated from the refined parameters are listed in Table 5.10 and Table 5.11 for the samples annealed at 900^0C and 1100^0C respectively. The lattice parameters and unit cell volumes

are found to be decreased with the increase of Al concentrations, it could be due to the smaller ionic size of Al^{3+} (0.51Å) to that of ionic size of Ti^{4+} (0.68Å). From bond lengths it is confirmed that Al-doping reinforced the co-valance of Pb-O, Which indicated that the Pb-O hybridization was strengthened [99]. The Rietveld refinement treatment was done to reduce the overlapping position in the same place between Ti and Al. Therefore the crystal structure becomes more stable. The lattice parameters and cell volume versus Al compositions for different annealing temperatures are shown in Fig. 5.18 (a) and Fig. 5.18 (b) respectively. Using the refined parameters the crystal structure was suggested, which is shown in Fig. 5.19. In crystallography a Wyckoff position is a point belonging to a set of points for which site symmetry groups are conjugate subgroups of the space group. Wyckoff positions are used in calculations of crystal properties. The splitting of the Wyckoff position of the atoms for all the compositions after refinement is capitalized in Table 5.12.

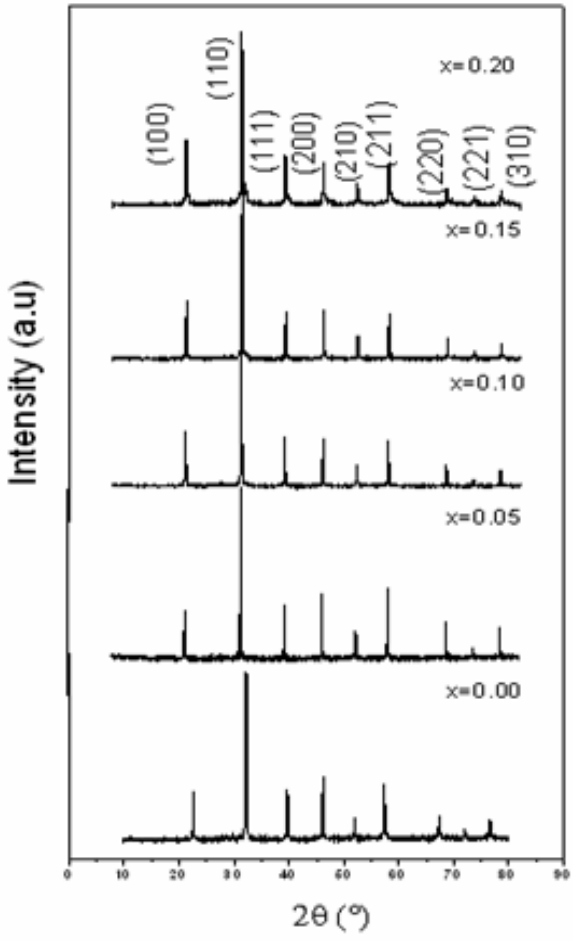

Fig. 5.14: XRD patterns of $(Pb_{0.70}La_{0.30})$ $(Ti_{1-x}Al_x)O_3$ for x = 0.0, 0.05, 0.10, 0.15, and 0.20 samples annealed at 900ºC for 8h.

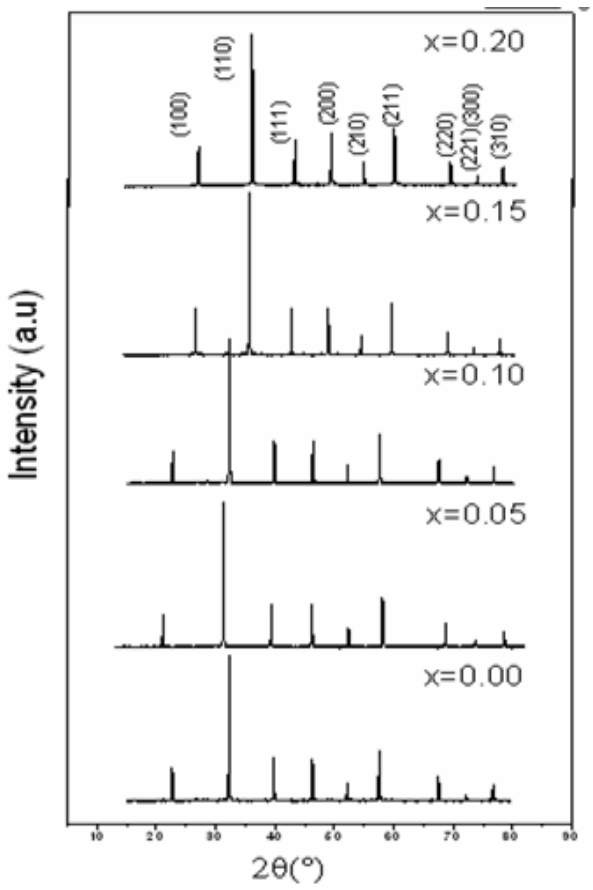

Fig. 5.15: XRD patterns of $(Pb_{0.70}La_{0.30})$ $(Ti_{1-x}Al_x)O_3$ for x = 0.0, 0.05, 0.10, 0.15, and 0.20 samples annealed at 1100ºC for 4h.

Table 5.9: Crystallite size of the sample $(Pb_{0.70}La_{0.30})(Ti_{1-x}Al_x)O_3$ for x = 0.0, 0.05, 0.10, 0.15, and 0.20 samples annealed at 900ºC for 8h and 1100ºC for 4h.

Sample	Rietveld method (crystallite size (nm))	
	900^0C	1100^0C
$Pb_{0.70}La_{0.30}(Ti_{0.95}Al_{0.05})O_3$	18.1(1)	36.1(11)
$Pb_{0.70}La_{0.30}(Ti_{0.90}Al_{0.10})O_3$	17.2(2)	35.2(3)
$Pb_{0.70}La_{0.30}(Ti_{0.85}Al_{0.15})O_3$	16.4(8)	33.0(1)
$Pb_{0.70}La_{0.30}(Ti_{0.80}Al_{0.20})O_3$	15.7(5)	32.1(1)

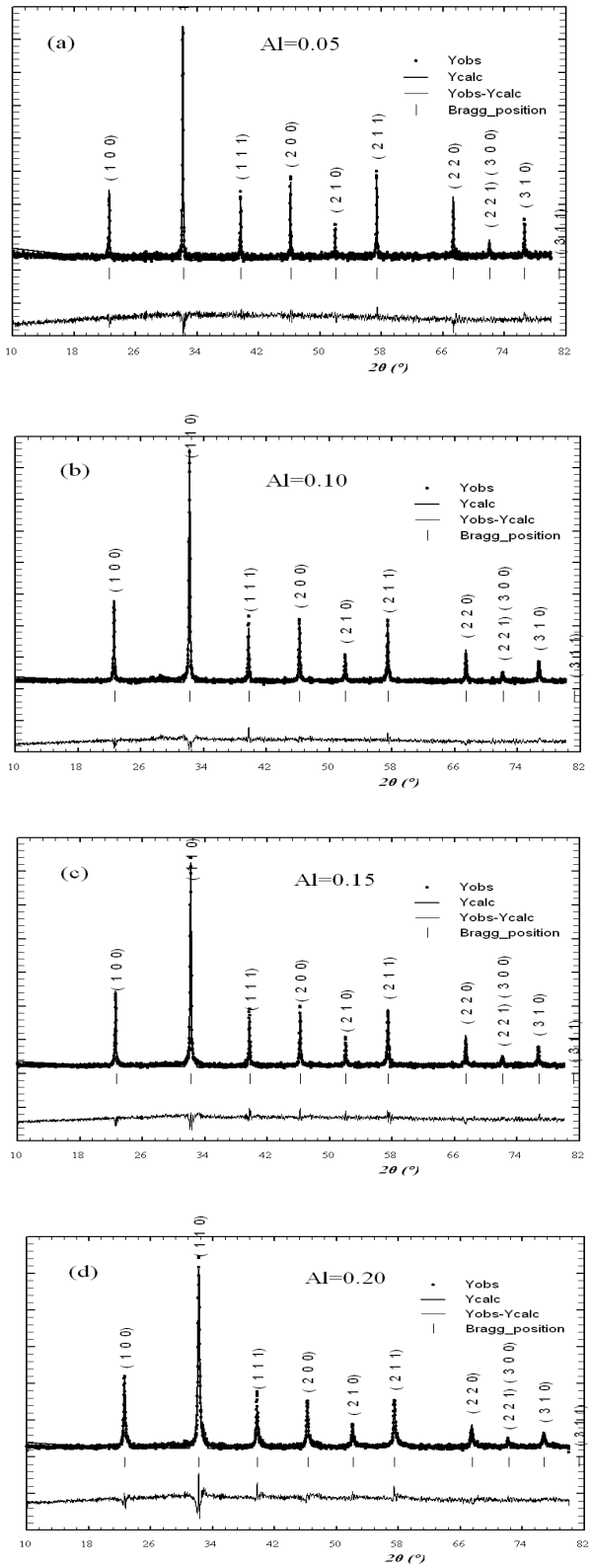

Fig. 5.16 (a-d): Refined patterns of $(Pb_{0.70}La_{0.30})(Ti_{1-x}Al_x)O_3$ for x = 0.05, 0.10, 0.15, and 0.20 samples annealed at 900ºC for 8h. The experimental points are given as dot (**.**) and theoretical data are shown as solid lines. The difference between theoretical and experimental data is shown as a bottom line. The vertical lines represent the Bragg's allowed peaks.

Table 5.10: Parameters obtained from Rietveld analysis of $(Pb_{0.70}La_{0.30})(Ti_{1-x}Al_x)O_3$ for x = 0.0, 0.05, 0.10, 0.15,0.20 samples annealed at 900ºC for 8h.

Samples → / Parameters ↓	x = 0.05	x = 0.10	x = 0.15	x = 0.20
Space group	$Pm\bar{3}m$	$Pm\bar{3}m$	$Pm\bar{3}m$	$Pm\bar{3}m$
Pb (Occup.)	0.631(7)	0.682(2)	0.674(3)	0.665(4)
La (Occup.)	0.231(8)	0.282(4)	0.270(7)	0.265(7)
Ti (Occup.)	0.950(8)	0.906(5)	0.849(7)	0.807(8)
Al (Occup.)	0.051(8)	0.106(5)	0.158(3)	0.198(10)
a=b=c (Å)	3.929(9)	3.925(12)	3.924(19)	3.922(8)
Volume ($Å^3$)	60.688(11)	60.486(6)	60.457(6)	60.341(4)
χ^2 (chi^2)	1.74	1.40	1.88	1.73
R_p	20.2	16.9	21.0	23.2
R_{wp}	22.1	18.3	22.7	20.5
R_{Bragg}	14.3	10.8	11.7	12.2
R_f	12.9	8.8	10.7	13.3
R_{exp}	13.6	9.79	10.2	10.3
Pb-Ti/La (Å)	3.41(4)	3.13(3)	3.05(2)	3.01(1)
Pb-Al-La (Å)	3.29(1)	3.35(2)	4.10(1)	4.23(2)
Ti/La-O_1 (Å)	1.88(8)	1.78(7)	1.77(7)	1.75(8)
Ti/La-O_2 (Å)	2.20(5)	1.95(9)	1.88(11)	1.80(5)
$\angle Pb-Ti/La-Pb$	18.28(3)	17.68(9)	16.77(7)	16.38(8)
$\angle Pb-Ti/Al-O_1$	124.21(6)	118.14(7)	115.54(5)	113.24(5)
$\angle Pb-Ti/La-O_2$	114.75(4)	110.43(2)	109.12(5)	105.82(5)
$\angle Pb-La-Al$	105.52(1)	101.98(6)	101.78(5)	100.85(4)
$\angle La-O_2-Al$	121.41(2)	115.25(4)	111.56(4)	109.78(5)
$\angle La-O_1-Al$	104.45(1)	101.85(7)	100.81(2)	98.88(5)

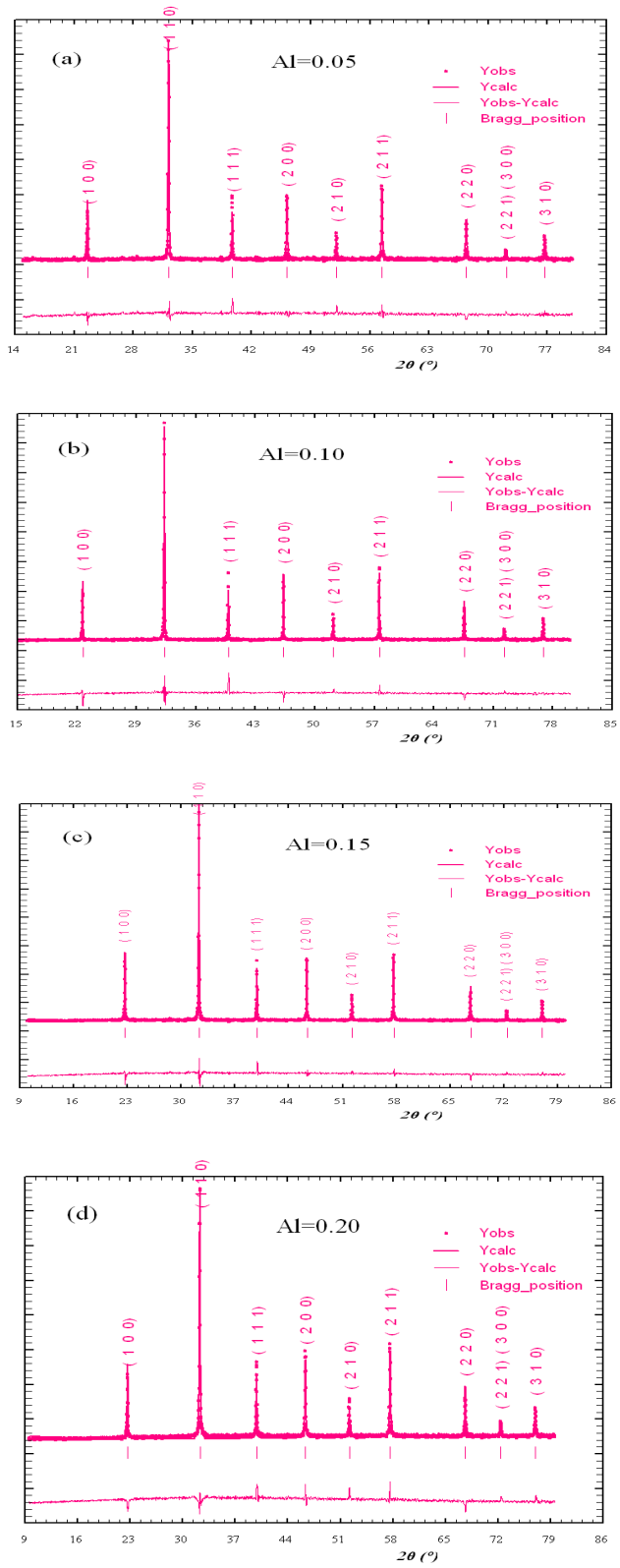

Fig. 5.17 (a-d): Refined patterns of $(Pb_{0.70}La_{0.30})(Ti_{1-x}Al_x)O_3$ for x = 0.05, 0.10, 0.15, and 0.20 samples annealed at 1100ºC for 4h. The experimental points are given as dot (**.**) and theoretical data are shown as solid lines. The difference between theoretical and experimental data is shown as a bottom line. The vertical lines represent the Bragg's allowed peaks.

Table 5.11: Parameters obtained from Rietveld analysis of $(Pb_{0.70}La_{0.30})(Ti_{1-x}Al_x)O_3$(for x = 0.0, 0.05, 0.10, 0.15, and 0.20 samples annealed at 1100ºC for 4h.

Samples → / Parameters ↓	x = 0.05	x = 0.10	x = 0.15	x = 0.20
Space group	$Pm\bar{3}m$	$Pm\bar{3}m$	$Pm\bar{3}m$	$Pm\bar{3}m$
Pb (Occup.)	0.627(3)	0.646(7)	0.660(7)	0.629(3)
La (Occup.)	0.279(3)	0.288(1)	0.263(3)	0.275(5)
Ti (Occup.)	0.957(1)	0.895(5)	0.845(7)	0.806(9)
Al (Occup.)	0.054(7)	0.107(8)	0.158(9)	0.204(1)
a=b=c(Å)	3.925(6)	3.917(3)	3.912(7)	3.913(3)
Volume ($Å^3$)	60.508(6)	60.101(4)	59.909(2)	59.906(8)
χ^2 (chi^2)	2.32	2.34	2.35	2.38
R_p	19.3	16.1	10.6	10.3
R_{wp}	22.1	24.4	17.6	17.2
R_{Bragg}	13.1	11.8	8.45	15.7
R_f	11.9	7.13	7.08	13.5
R_{exp}	8.33	8.26	7.89	8.65
Pb-Ti/La (Å)	3.56(8)	3.42(5)	3.32(5)	3.209(1)
Pb-Al-La (Å)	4.81(5)	3.98(4)	3.85(1)	3.54(1)
Ti/La-O_1 (Å)	1.89(4)	1.74(1)	1.71(2)	1.68(4)
Ti/La-O_2(Å)	2.40(4)	2.12(4)	1.94(4)	1.81(2)
$\angle Pb-Ti/La-Pb$	19.21(4)	18.67(8)	17.54(5)	16.51(4)
$\angle Pb-Ti/La-O_1$	112.29(4)	108.76(4)	105.25(5)	104.38(6)
$\angle Pb-Ti/La-O_2$	113.93(4)	111.32(9)	110.23(5)	110.16(5)
$\angle Pb-La-Al$	121.29(1)	120.56(2)	120.30(2)	119.95(6)
$\angle La-O_2-Al$	117.58(7)	114.32(4)	111.97(5)	110.84(4)
$\angle La-O_2-Al$	87.23(6)	84.52(1)	82.96(7)	80.52(7)

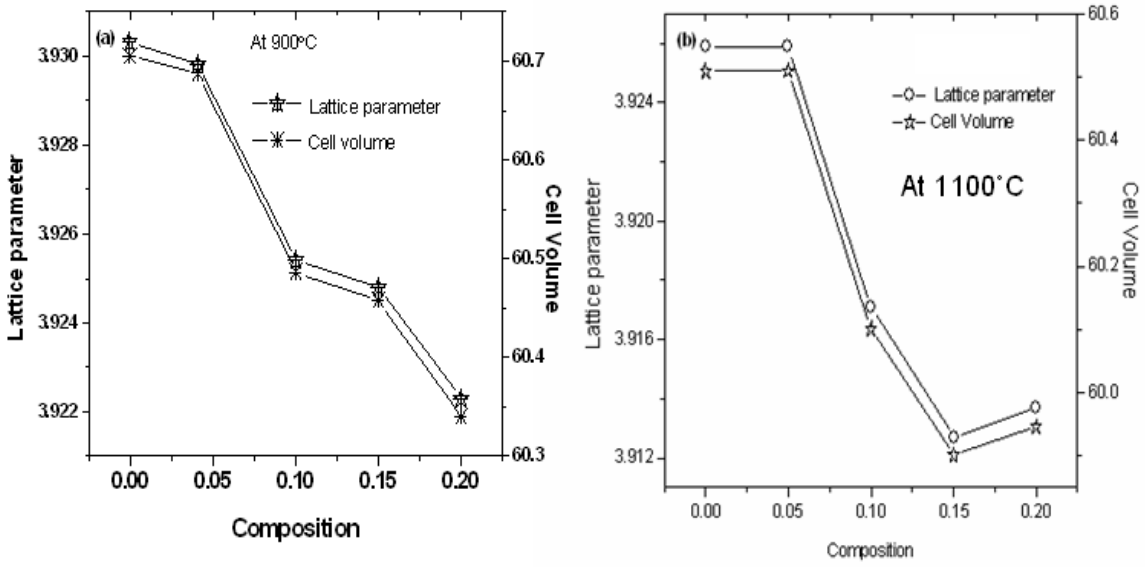

Fig. 5.18 (a, b): Lattice parameter, cell volume versus compositions of $(Pb_{0.70}La_{0.30})(Ti_{1-x}Al_x)O_3$(where x = 0.0, 0.05, 0.10, 0.15, and 0.20) samples: (a) calcined at 900ºC for 8h and (b) sintered at1100ºC for 4h.

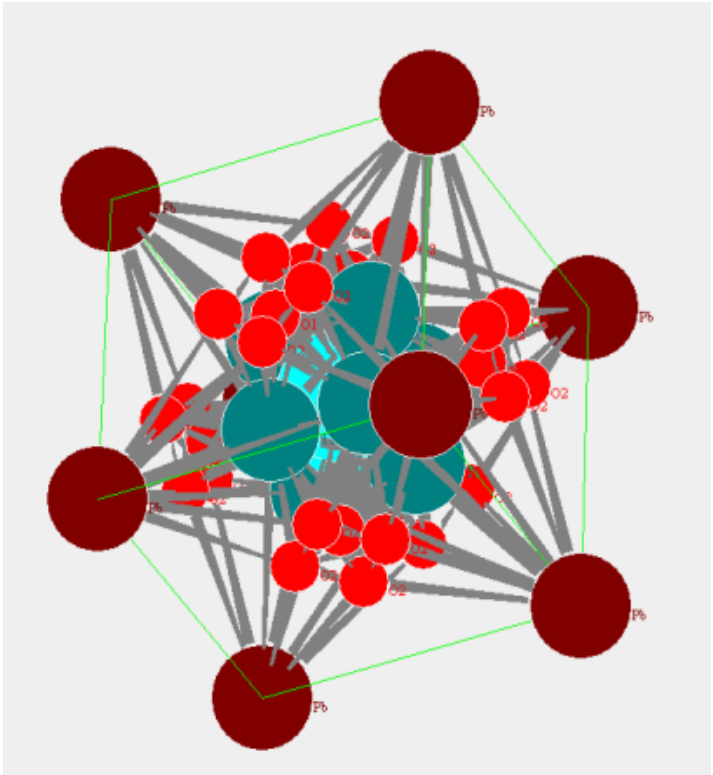

Fig. 5.19: The stable crystal structure by using the refined parameters of the typical $(Pb_{0.70}La_{0.30})(Ti_{0.85}Al_{0.15})O_3$ samples annealed at 1100ºC for 4h.

Table 5.12: The splitting of Wyckoff positions after refinement of $(Pb_{0.70}La_{0.30})$ $(Ti_{1-x}Al_x)O_3$ (for x = 0.0, 0.05, 0.10, 0.15, and 0.20 samples annealed at 1100ºC for 4h.

Sample → / Wyckoff Positions ↓	x = 0.00	x = 0.05	x = 0.10	x = 0.15	x = 0.20
Pb	1a	1a	1a	1a	1a
La	6b	6b	6b	6b	6b
Ti	8c	8c	8c	8c	8c
Al	---	8d	1d	1d	1d
O	12e	6e	6e	6e	6e

5.3.2 Microstructural and elemental analysis

Scanning electron micrographs of the sample $(Pb_{0.70}La_{0.30})(Ti_{1-x}Al_x)O_3$ for x = 0.05, 0.10, 0.15, and 0.20 annealed at 1100ºC for 4h are shown in Fig. 5.20 (a-d). The micrographs indicate the existence of uniform microstructure in the materials. The grains of equal sizes appear to be distributed homogeneously throughout the surface of the samples. It can notice the samples are uniform and the grains are in order of micron size. The average grain sizes of the samples are found to be 1.02-4.26μm. It is found that grain size decreases with increase of Al concentration. Similar behavior we have observed for crystallite size which has been discussed in the previous section (XRD analysis). The energy dispersive spectrum (EDS) analysis reveals that, all the compositions present in the samples are close to as prepared. The SEM-EDS for all the samples are shown in Fig. 5.21 (a-d). The theoretical wt% and wt% obtained from EDS analysis of different elements of various compositions of $(Pb_{0.70}La_{0.30})(Al_xTi_{1-x})O_3$ ceramics are given in Table 5.13. The theoretical wt% of the elements is almost same with the wt% calculated from the EDS spectra.

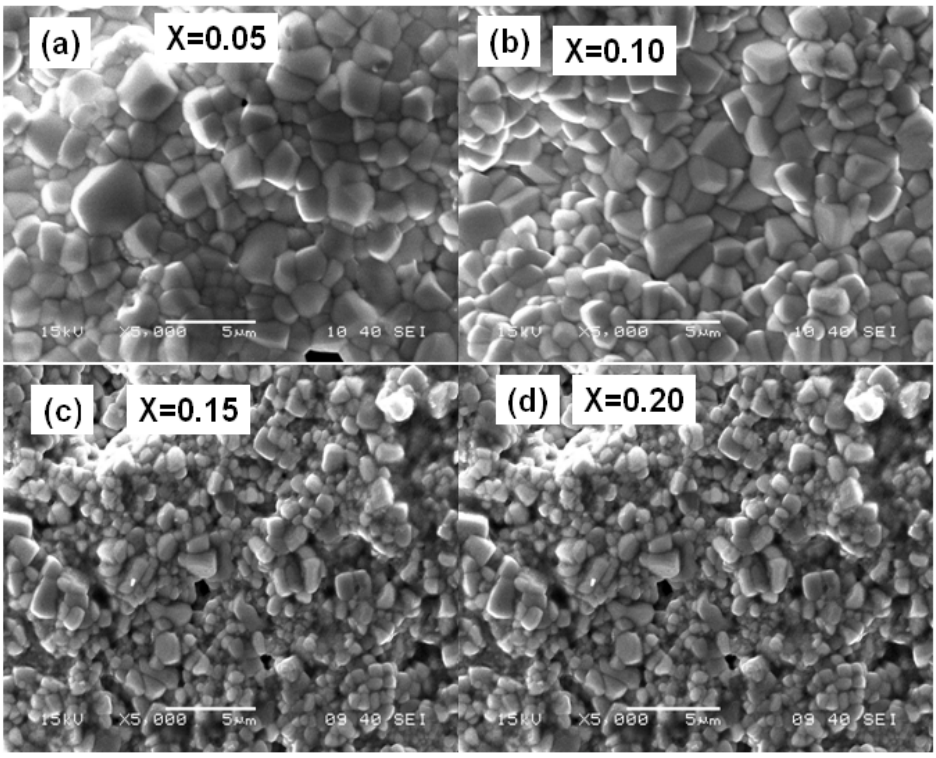

Fig. 5.20 (a-d): The scanning electron micrographs of $(Pb_{0.70}La_{0.30})(Ti_{1-x}Al_x)O_3$ for (a) x = 0.05, (b) x = 0.10, (c) x = 0.15, and x = 0.20 samples annealed at 1100ºC for 4h.

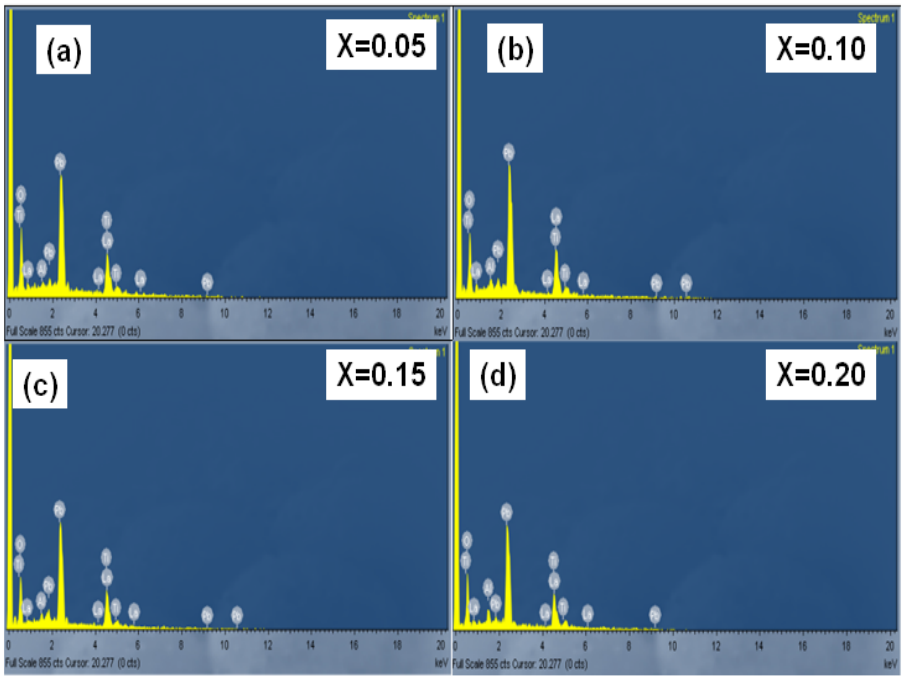

Fig. 5.21 (a-d): The energy dispersive spectrum (EDS) of $(Pb_{0.70}La_{0.30})(Ti_{1-x}Al_x)O_3$ for (a) x = 0.05, (b) x = 0.10, (c) x = 0.15, and x = 0.20 samples annealed at 1100ºC for 4h.

Table 5.13: Elemental analysis of $(Pb_{0.70}La_{0.30})$ $(Ti_{1-x}Al_x)O_3$ for x = 0.05, 0.10, 0.15, and 0.20 samples annealed at 1100ºC for 4h.

Composition	Element	EDS wt%	Theoretical wt%
x = 0.05	Pb	45.92	45.96
	La	25.74	25.75
	Ti	15.03	15.04
	O	9.50	9.53
	Al	3.81	3.71
x = 0.10	Pb	44.35	44.65
	La	24.89	25.02
	Ti	14.00	13.85
	O	10.55	9.25
	Al	7.21	7.22
x = 0.15	Pb	43.39	43.42
	La	24.65	24.32
	Ti	12.69	12.71
	O	9.05	9.01
	Al	10.22	10.53
x = 0.20	Pb	42.22	42.25
	La	23.66	23.67
	Ti	11.62	11.64
	O	8.85	8.76
	Al	13.65	13.67

5.3.3 Electrical conductivity studies

5.3.3.1 Impedance analysis

Fig. 5.22 (a) shows plot of real part of impedance (Z′) with frequency at selected temperatures (400˚C to 500˚C). The magnitude of Z′ for all the samples decreases with increase in frequency which is due to increase of AC conductivity. The Z′ values for all temperatures merge above 10 kHz which may be due to the release of space charges, as a result of reduction in the barrier properties of the material with the rise in temperature. Further, at low frequencies the Z′ values decrease with the rise in temperature which is a negative temperature coefficient of resistance (NTCR) type behavior like that of semiconductors.

Fig. 5.22 (b) shows the variation of the imaginary part of impedance (Z″) with frequency at different temperatures. The curves show that the Z″ values reach a maximum value (Z''_{max}) and, the value of Z''_{max} shifts to higher frequencies with increasing temperature. Asymmetrical peak broadening has been observed with the rise in temperature which suggests that there is a spread of relaxation times with different time constant and hence the relaxation is non-Debye type. The low frequency peak suggests that the ions can move over a long distance, whereas the high frequency peaks indicates that the confinement of the ions in the potential well. So, the temperature dependent electrical relaxation phenomenon exists in the present material. The value of maximum frequency and relaxation time of $(Pb_{0.70}La_{0.30})(Ti_{1-x}Al_x)O_3$, (x = 0.15) ceramics is listed in Table 5.14. The Arrhenius behavior of maximum frequency and temperature of a typical sample PLTA15 is shown in Fig. 5.22 (c).

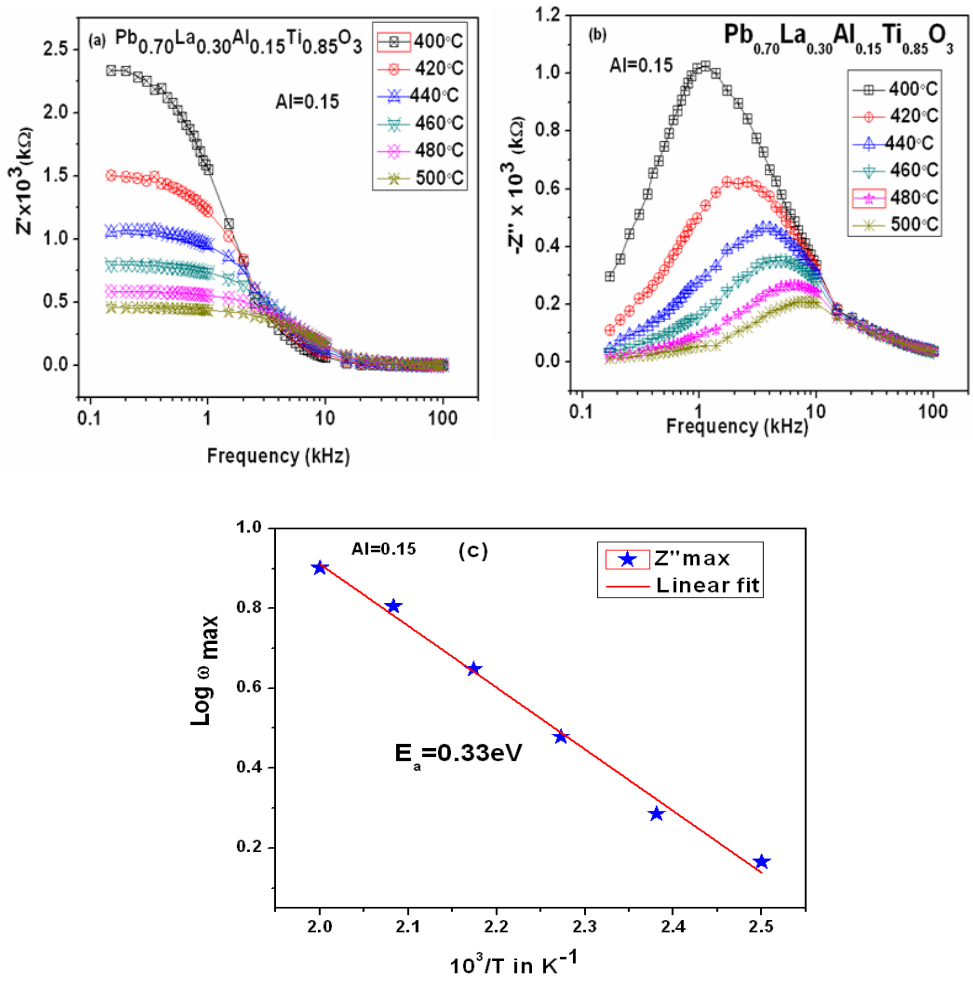

Fig. 5.22 (a-c): The typical plot of (a) real and (b) imaginary part of impedance spectra versus frequency at various temperatures and, (c) Log ω_{max} versus $10^3/T$ of $(Pb_{0.70}La_{0.30})(Ti_{1-x}Al_x)O_3$, (x = 0.15) ceramic.

Table 5.14: The value of maximum frequency and relaxation time of a typical sample $(Pb_{0.70}La_{0.30})(Ti_{1-x}Al_x)O_3$, (x = 0.15) ceramic.

Temperature	Logω_{max}	τ (rad/s)
400	0.16504	0.68385
420	0.28581	0.51784
440	0.47903	0.33187
460	0.64810	0.22486
480	0.80589	0.15664
500	0.90171	0.12543

The complex impedance spectrum (Nyquist plot) of PLTA compounds at higher temperature is shown in Fig. 5.23 (a–d). Characteristically two overlapping semicircular arcs were observed in Al free sample which has been discussed in our previous chapter (Chapter 4), whereas single semicircle was observed in the Al doped sample. The impedance result for the Al doped sample indicates that the electrical process occurs in this material only due to the bulk contribution. The electrical equivalent circuit corresponding to the sample impedance response is shown as an inset in Fig. 5.23 (a-d). The values of bulk resistance have been estimated from the intercept of the semicircular arc on the real axis. The value of bulk capacitance, bulk resistance and bulk conductivity of PLTA is cited in Table 5.15. It has been observed that sample resistance decreases with an increase in temperature, which is the conventional semiconductor behavior [92].

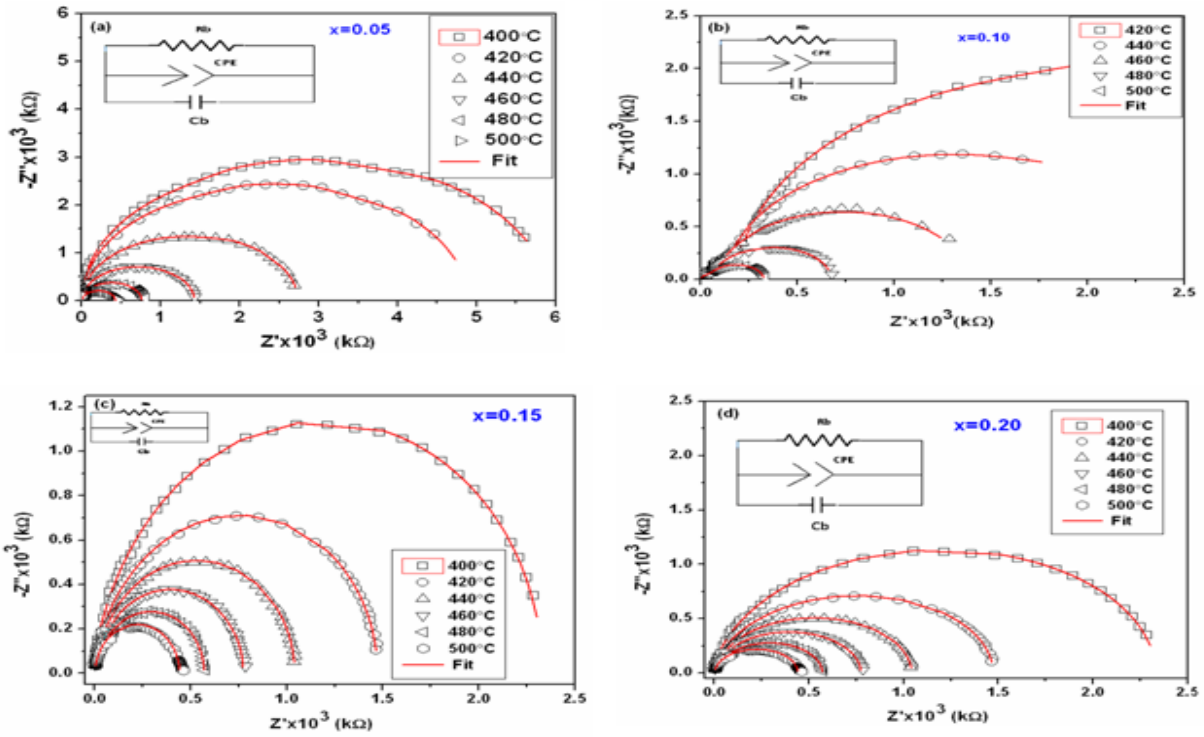

Fig. 5.23 (a–d): The complex impedance spectra of PLTA compounds at different temperatures for (a) x = 0.05, (b) x = 0.10, (c) x = 0.15, and (d) x = 0.20 samples.

Table 5.15: Grain resistance, capacitance and bulk conductivity from Nyquist plot of $Pb_{0.70}La_{0.30})(Ti_{1-x}Al_x)O_3$ for x = 0.05, 0.10, 0.15, and 0.20 ceramic.

Sample Composition	Temperature °C	CPE_g nF	R_g kΩ	$\sigma_b = t/RgA$ $(\Omega m)^{-1}$
x = 0.05	400	0.415	$5.90x10^6$	$5.02x\ 10^{-8}$
	420	0.395	$4.82x10^6$	$5.11x10^{-8}$
	440	0.385	$4.03x10^6$	$6.19x10^{-7}$
	460	0.298	$2.96x10^6$	$5.64x10^{-7}$
	480	0.253	$2.51x10^5$	$4.68x10^{-7}$
	500	0.198	$1.78x10^5$	$4.51x10^{-6}$
x = 0.10	400	0.275	$2.90x10^6$	$3.33x\ 10^{-7}$
	420	0.235	$2.82x10^6$	$3.51x10^{-7}$
	440	0.205	$2.04x10^6$	$3.87x10^{-6}$
	460	0.198	$1.91x10^5$	$3.64x10^{-6}$
	480	0.153	$1.71x10^5$	$2.68x10^{-5}$
	500	0.138	$1.40x10^5$	$2.02x10^{-4}$
x = 0.15	400	0.242	$2.41x10^5$	$3.24x\ 10^{-7}$
	420	0.222	$2.02x10^5$	$2.88x10^{-6}$
	440	0.204	$1.74x10^5$	$2.64x10^{-6}$
	460	0.184	$1.04x10^4$	$2.11x10^{-6}$
	480	0.167	$0.95x10^4$	$2.01x10^{-5}$
	500	0.124	$0.83x10^3$	$0.83x10^{-4}$
x = 0.20	400	0.214	$2.55x10^5$	$2.14x\ 10^{-6}$
	420	0.210	$2.14x10^5$	$1.79x10^{-5}$
	440	0.204	$1.01x10^5$	$1.61x10^{-5}$
	460	0.184	$0.91x10^4$	$1.13x10^{-5}$
	480	0.167	$0.71x10^4$	$1.07x10^{-4}$
	500	0.124	$0.53x10^3$	$0.77x10^{-3}$

5.3.3.2 AC and DC conductivity analysis

The log–log plots of electrical conductivity versus frequency at different temperatures are shown in Fig. 5.24 (a). To account for the high frequency dispersion, the conductivity spectra can be modeled by the form predicted by *Jonscher's* (1977) [165] universal law which is given as,

$$\sigma_{ac} = \sigma_{dc} + A\omega^n \qquad (5.3)$$

Where σ_{dc} is the frequency independent term and *n* is the dimensionless frequency exponent. The parameter *A* is frequency independent, but may be temperature and material dependent. The variation of σ_{ac} involves a power exponent, which also supports that the conduction process in the material is thermally activated. According to Jonscher, the origin of the frequency dependence of

conductivity lies in the relaxation phenomena arising due to mobile charge carriers. When a mobile charge carrier hopes to a new site from its original position, it remains in a state of displacement between two potential energy minima, which includes contributions from other mobile defects. After a sufficiently long time, the defect could relax until the two minima in the lattice potential energy coincide with the lattice site. Also, the conduction behavior of the materials obeys the power law with a slope change governed by *n* in the low temperature region,

$$\sigma_{ac} = A\omega^n \qquad (5.4)$$

The ac conductivity data are fitted to the Jonscher's equation (equ^n 5.4) and the fitting parameters A and n at various temperatures of a typical sample (PLTA15) is given in Table 5.16. The solid lines in Fig. 5.24 (a) are the fitted curves to the experimental AC conductivity data at different temperatures. The frequency exponent n is found to decrease slightly with increasing temperature. The Fig.5.24 (b) shows the DC conductivity versus the inverse of temperature. The activation energy was found to be 0.31eV for the typical sample PLTA15 ceramic. The activation energies for all the samples are given in Table 5.17.

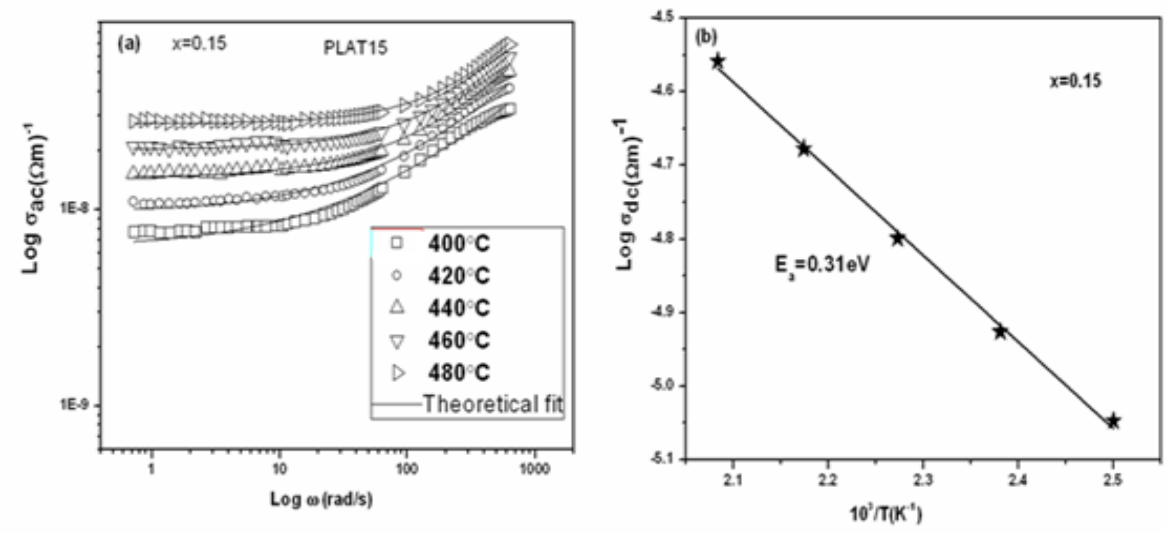

Fig. 5.24 (a, b): (a) Log of AC conductivity versus log of frequency at different temperatures and (b) log of DC conductivity versus inverse of temperature of $(Pb_{0.70}La_{0.30})(Ti_{1-x}Al_x)O_3$, (x = 0.15) ceramics.

Table 5.16: Fitting parameters of AC conductivity by Jonscher's universal law of (x = 0.05) ceramic of $(Pb_{0.70}La_{0.30})(Ti_{1-x}Al_x)O_3$, (x = 0.15) ceramic.

Temperature (˚C)	A	n
400	5.58×10^{-7}	0.14754
420	1.04×10^{-6}	0.12252
440	1.85×10^{-6}	0.11801
460	2.30×10^{-6}	0.11503
480	3.42×10^{-6}	0.11915

5.3.3.3 Modulus spectroscopy analysis

Fig. 5.25 (a) and Fig. 5.25 (b) shows the frequency (angular) dependency of $M'(\omega)$ and $M''(\omega)$ for $(Pb_{0.70}La_{0.30})(Ti_{1-x}Al_x)O_3$, (x = 0.15) ceramic as a function of temperature. A continuous dispersion with the increase in frequency of all the concentration can be seen. This may be attributed to the conduction phenomena due to short range mobility of charge carriers. It may be noted from Fig. 5.25 (b) that the position of the peak M''_{max} shifts to higher frequencies as the temperature is increased. The frequency ω_m (corresponding to M''_{max}) gives the most probable relaxation time τ_m from the condition $\omega_m\tau_m = 1$. Fig 5.25 (c) shows that the most probable relaxation time which obeys the Arrhenius relation and the corresponding activation energy E_a = 0.31eV for relaxation is found to be close to the activation energy E_a for Z''_{max} suggesting a hopping mechanism in the material. The comparison of activation energy obtained from AC conductivity, Bulk conductivity, relaxation time, Z''_{max} spectra and M'' spectra are capitalized in Table 5.17.

From Table 5.17 it is observed that activation energy decreases with an increase in Al concentration. This change in behavior indicates the participation of Al^{3+} ions in the conduction, thermally activated and relaxation process. The activation energy obtained from Z'' spectra represents the localized conduction (i.e., dielectric relaxation) where as the activation energy obtained from the M'' spectra represent non localized conduction (i.e., long range conduction). The nearly same activation energy obtained from both the spectra suggests that the nature of species is taking part in both localized and nonlocalized conductions are similar.

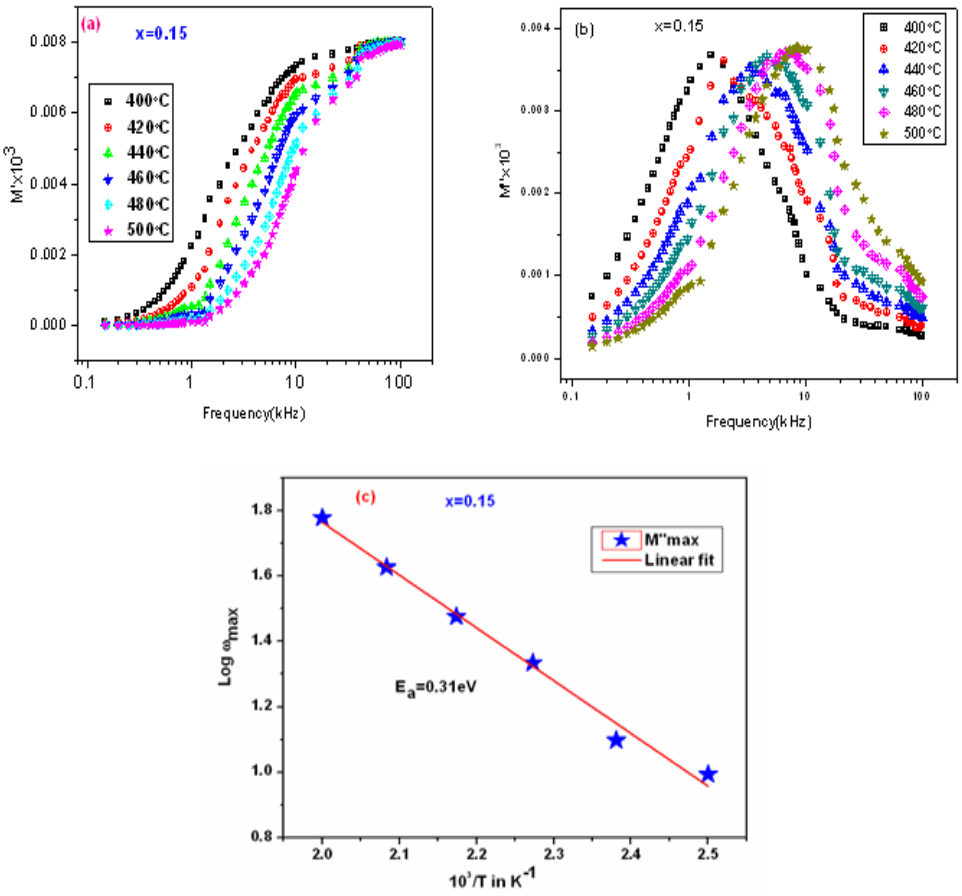

Fig. 5.25 (a-c): (a) Real part M′ and (b) imaginary part M″ versus frequency at different temperatures and, (c) Arrhenius plot of $\log\omega_{max}$ from imaginary part of modulus versus inverse of temperature of a typical sample(PLTA 15, x = 0.15) ceramic.

Table 5.17: Comparison of E_a in eV obtained from (i) apparent bulk conductivity (σ_{dc}), (ii) relaxation time (τ), (iii) grain resistance (R_g), (iv) Z''_{max} and (v) M''_{max} spectra of $Pb_{0.70}La_{0.30})(Ti_{1-x}Al_x)O_3$ for x = 0.0, 0.05, 0.10, 0.15 and 0.20 samples.

Sample	$E_a(\sigma_b)$	$E_a(\tau)$	$E_a(R_g)$	$E_a(Z'')$	$E_a(M'')$
0.00	0.31	0.35	0.47	0.41	0.43
0.05	0.29	0.31	0.37	0.39	0.42
0.10	0.29	0.30	0.35	0.36	0.37
0.15	0.27	0.22	0.30	0.33	0.31
0.20	0.24	0.22	0.28	0.29	0.27

5.3.4 Summary

The structural study was performed on Al doped $(Pb_{0.70}La_{0.30})(Ti_{1-x}Al_x)O_3$ (x = 0, 0.05, 0.10, 0.15, 0.20) compounds prepared by the conventional solid state reaction technique. The formation of the perovskite structure has been confirmed from X-ray diffraction study. The lattice parameter (which determine the positions of the reflections) and cell volume decreases with increase of Al concentration. The structure and lattice dynamics of PLTA compounds has been systematically investigated by the Rietveld XRD method. The Rietveld analysis suggests that the Goodness of fitting parameters, bond lengths and angles are useful for the development of the perovskites structure of the materials. The SEM micrographs revealed, increased grain size with the increase in sintering temperature and decreases with increase of Al concentration. From elemental analysis we confirmed that the sample is as prepared.

Impedance spectroscopy shows the existence of a non-Debye type relaxation phenomenon in materials. The reduction of grain resistances (R_g) of the materials with increase in temperature showed the negative temperature co-efficient of resistance (NTCR). So, the result indicates a typical semiconducting behavior of the materials. The nearly same activation energy obtained from both the spectra (Z'' spectra and M'' spectra) suggests that the nature of species is taking part in both localized and non-localized conductions are similar.

CHAPTER 6

STRUCTURAL ANALYSIS AND ELECTRICAL PROPERTIES OF $Pb(Zr_{0.65-x}Mn_xTi_{0.35}O_3$, $(0.0 \leq x \leq 0.15)$ CERAMICS

CHAPTER 6

STRUCTURAL ANALYSIS AND ELECTRICAL PROPERTIES OF $PbZr_{0.65-x}Mn_xTi_{0.35}O_3$, ($0.0 \leq x \leq 0.15$) CERAMICS

In this chapter crystal structure and dielectric properties of solid solutions of $Pb(Zr_{1-x}Ti_x)O_3$ for x= 1.00, 0.65 and 0.35 have been discussed. This composition is expected to be beyond the morphotropic phase boundary region (MPB). Also this chapter explains synthesis followed by dielectric and impedance studies of the Mn modified $PbZr_{0.65-x}Mn_xTi_{0.35}O_3$ samples. The detailed crystal structure has been studied by employing the Rietveld analysis with the help of FullProf program. The crystallite size has been calculated by using the Rietveld method. The detailed dielectric, conductivity and impedance properties have been discussed.

6.1 Sample preparation

At first the solid solution of the sample $Pb(Zr_{1-x}Ti_x)O_3$ for x = 1.00, 0.65,0.35 and, Mn modified sample $Pb(Zr_{0.65-x}Mn_xTi_{0.35})O_3$ (Zr/Ti=65/35) with x = 0.05, 0.10, 0.15 ceramics have been prepared by high temperature solid state reaction technique as discussed in Chapter 3. Two sets of samples were prepared for analysis. One set was prepared by annealing at the temperatures 900^{o}C for 8h and another set was prepared by sintering at 1100^{o}C for over 4h.

6.2 Structural analysis of $Pb(Zr_{1-x}Ti_x)O_3$, for x = 1.00, 0.65, 0.35 ceramic

6.2.1 X-ray diffraction study by employing the Rietveld method

The XRD patterns recorded for $Pb(Zr_{1-x}Ti_x)O_3$ samples are shown in Fig. 6.1 for x = 1.00, 0.65, and 0.35 annealed at 900˚C for 8h. Those samples are annealed at 1100˚C for 4h is shown in Fig. 6.2. It is observed that all the samples are in the single phase form. The patterns for x = 1.00 and 0.65 could be indexed to *P4mm* spacegroup in tetragonal symmetry. However, the samples for x = 0.35 could be indexed using *R3c* spacegroup in rhombohedral symmetry. We have obtained the average crystallite size by using the Rietveld method. The instrumental broadening factor has been taken

into account during the FWHM calculation. The average crystallite values obtained from the above method is listed in Table 6.1 for both 900˚C and 1100˚C annealed samples. It is found that average crystallite size increases with annealing temperature. This is due to the formation of larger crystals at high temperature.

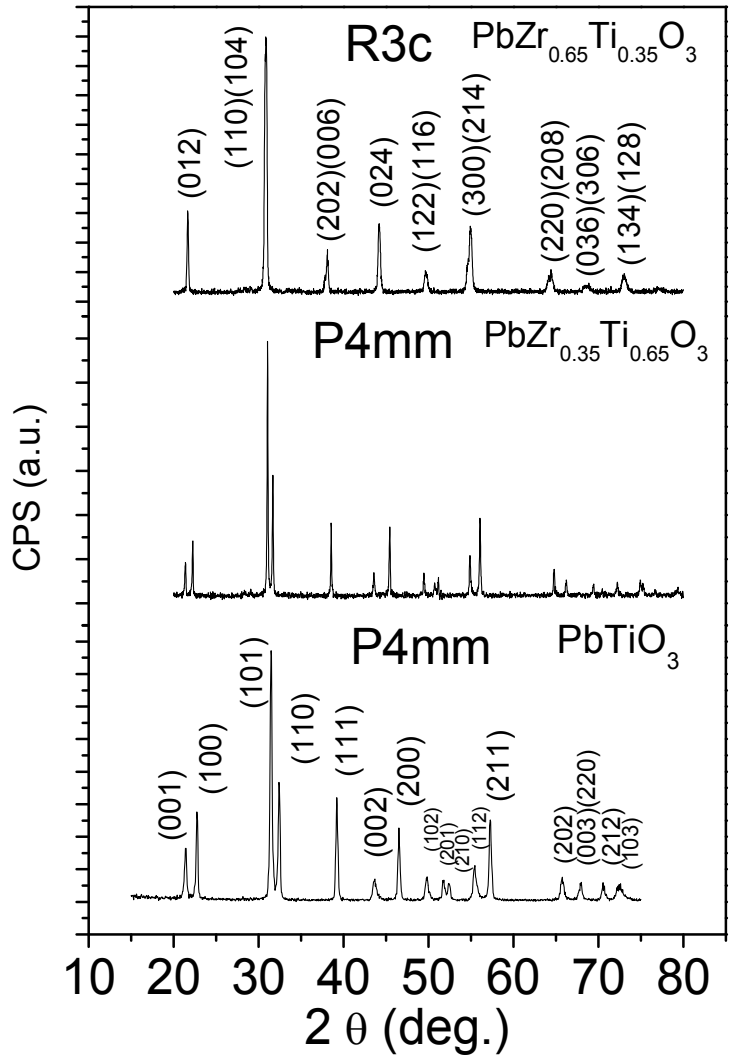

Fig. 6.1: XRD patterns for the samples $PbZr_{1-x}Ti_xO_3$ (x= 1.00, 0.65, 0.35) annealed at 900^0C for 8h.

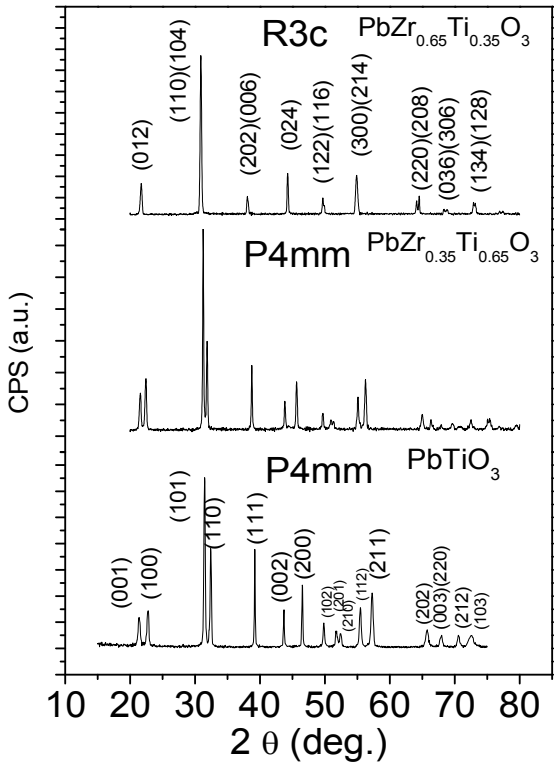

Fig. 6.2: XRD patterns for the samples $PbZr_{1-x}Ti_xO_3$ (x= 1.00, 0.65, 0.35) annealed at 1100^0C.

Table 6.1: Average crystallite size (nm) of the sample $PbZr_{1-x}Ti_xO_3$ (x = 0.65, 0.35) annealed at 900^0C and 1100^0C.

Sample	Rietveld method (crystallite size (nm))	
	900^0C	1100^0C
$PbZr_{0.35}Ti_{0.65}O_3$	13.8(5)	39.1(4)
$PbZr_{0.65}Ti_{0.35}O_3$	13.5(1)	33.0(12)

The refined XRD patterns of $PbZr_{0.35}Ti_{0.65}O_3$ and $PbZr_{0.65}Ti_{0.35}O_3$ are shown in Fig. 6.3 (a) and Fig. 6.3 (b) respectively for 1100^0C annealed sample. It is observed that all the observed peaks could be well refined. The lattice parameters, cell volume, the goodness of the fitting are listed in Table 6.2. We have obtained the fractional atomic positions Pb(0,0,0), Zr/Ti(0.5, 0.5, 0.5575), O_1(0.5, 0.5, 0.1845), O_2(0.5, 0.5, 0.5783) for x = 0.65 (*P4mm* space group) sample and Pb(0.3333, 0.6667, 0.43304), Zr/Ti (0, 0, 0.5), O(0.1733, 0.3453, 0.5843) for x = 0.35 (*R3c*) sample. The lattice parameters, occupancy, fractional atomic positions etc. were taken as the free parameter

during the fitting. The lattice parameters and unit cell volumes are found to be increased with the increase of Zr concentration which could be due to the larger ionic size of Zr to that of ionic size of Ti. The axial ratio c/a is found to be 1.0614 and 1.0395 for $PbTiO_3$ and $PbZr_{0.35}Ti_{0.65}O_3$ respectively, which is less than that of earlier reported value 1.063 for $PbTiO_3$ [191]. The low axial value shows that the material is more compact and hence structure is more stable. Bond lengths and bond angles are calculated from the refined parameters and those values are listed in Table 6.2 for all the samples.

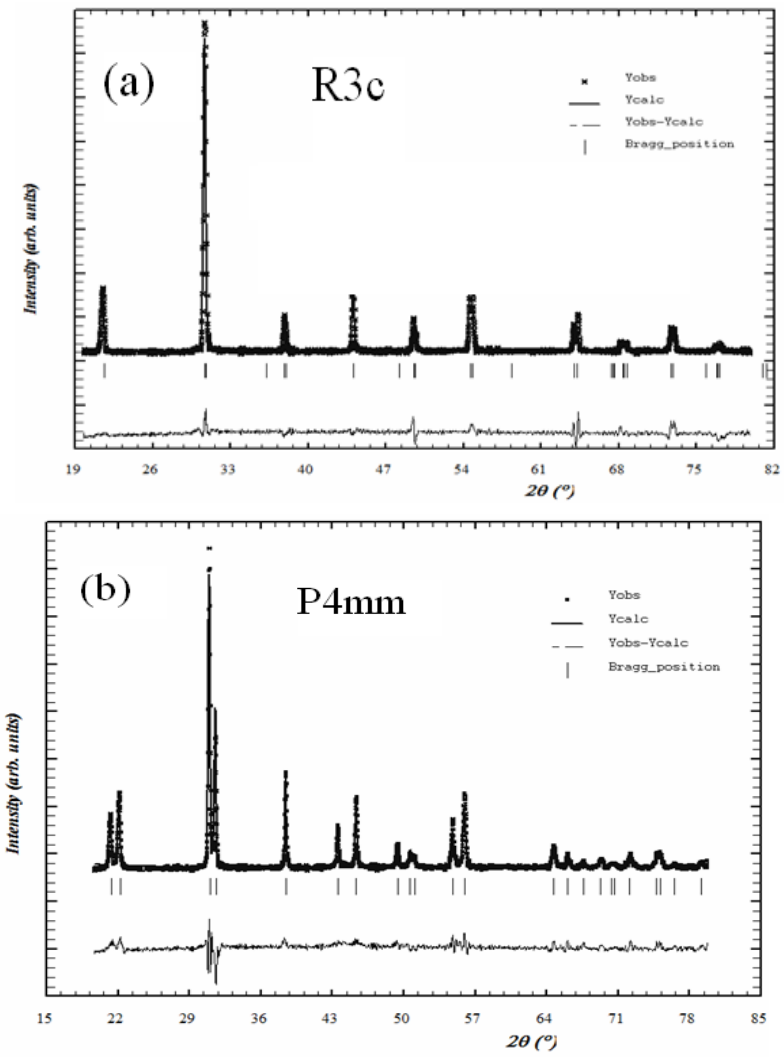

Fig. 6.3 (a, b): XRD pattern along with Rietveld refined data for the sample annealed at 1100^0C. (a) $PbZr_{0.65}Ti_{0.35}O_3$ refined using *R3c* space group and (b) $PbZr_{0.35}Ti_{0.65}O_3$ refined using *P4mm* space group. The '+' signs represent experimental points and solid line represents Rietveld refined data. The dotted lines show the difference between experimental & refined data.

Table 6.2: Parameters obtained from XRD analysis by employing the Rietveld method of $PbZr_{1-x}Ti_xO_3$ (x = 0.65, 0.35) compound annealed at 1100˚C for 4h.

Sample → / Parameters ↓	x = 0.65	x = 0.35
Space group	P4mm	*R3c*
Pb(Occup.)	0.9912(24)	0.9823(24)
Zr(Occup.)	0.3254(11)	0.3412(22)
Ti(Occup.)	0.6659(9)	0.6451(15)
a=b (Å)	3.9979(5)	5.8169(7)
c (Å)	4.1557(6)	14.1845(21)
Volume ($Å^3$)	66.42(1)	415.65(10)
χ^2 *(chi²)*	1.81	1.91
R_p	13.4	11.9
R_{wp}	16.7	16.5
R_{Bragg}	12.2	12.8
R_f	11.8	11.4
R_{exp}	12.3	12.0
Pb-Ti/Zr (Å)	3.4668(2)	3.4901(2)
Ti/Zr-O_1 (Å)	1.7506(3)	2.1111(2)/ 1.9996(11)
Ti/Zr-O_2(Å)	2.0067(4)	2.8888(10)
$\angle Pb-Ti/Zr-Pb$	109.26(3)	112.88(13)
$\angle Pb-Ti/Zr-O_1$	125.37(2)	124.51(21)
$\angle Pb-Ti/Zr-O_2$	121.58(4)	137.92(6)

6.2.2 Microstructural analysis

The scanning electron micrographs of the sample annealed at 1100˚C for 4h is shown in the Fig. 6.4(a) and Fig. 6.4(b) for the samples x = 0.35 and 0.65 respectively. It is found that the samples are uniform and the grains are in order of micron size. The average grain sizes of the samples are found to be 3-5 μm.

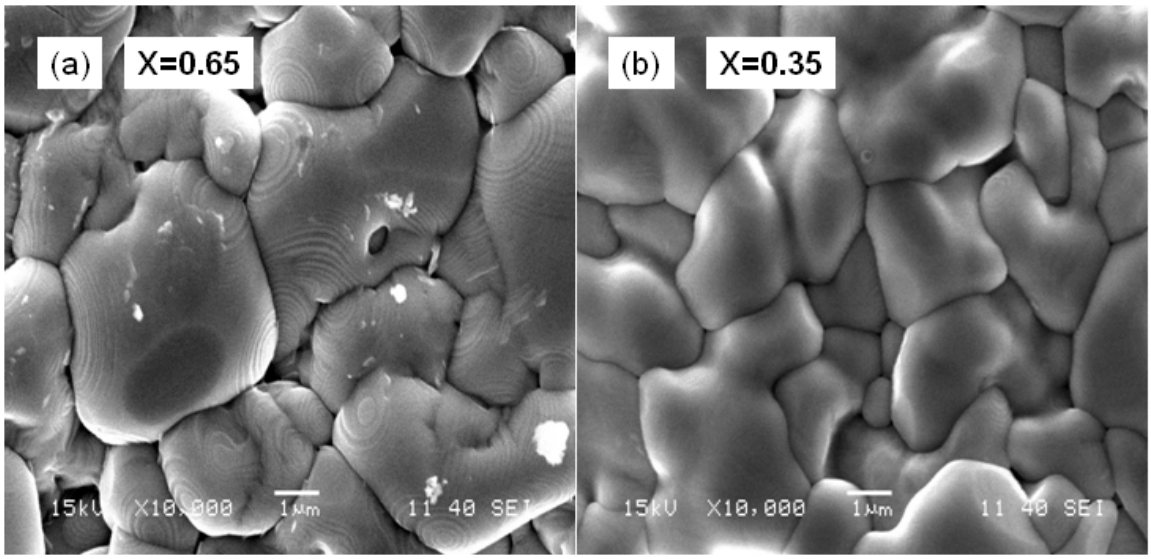

Fig. 6.4 (a, b): SEM micrographs for the sample (a) $PbZr_{0.35}Ti_{0.65}O_3$ (x = 0. 65), and (b) $PbZr_{0.65}Ti_{0.35}O_3$ (x = 0. 35) annealed at 1100˚C for 4h.

6.2.3 Dielectric analysis

The plot of temperature variation of the dielectric constant (ϵ_r) measured at 10 kHz of the samples $PbZr_{0.65}Ti_{0.35}O_3$ and $PbZr_{0.35}Ti_{0.65}O_3$ (annealed at 1100^0C) is shown in Fig. 6.5 (a). Triangles are representing the data for $PbZr_{0.35}Ti_{0.65}O_3$ and circles are representing the data for $PbZr_{0.65}Ti_{0.35}O_3$. We have observed that, both the samples exhibit ferroelectric to paraelectric transition. The dielectric constant of $PbZr_{0.65}Ti_{0.35}O_3$ sample increases gradually with increasing temperature up to the transition temperature (T_c) and thereafter it decreases. Dielectric constant increases with temperature due to interfacial polarization becoming more dominant compared to the dipolar polarization. After the Curie temperature is reached, the dielectric constant decreases due to the phase transition from ferroelectric phase to the paraelectric phase. The transition temperature (T_c) was obtained from $|d\epsilon_r/dT|$ versus temperature plot. The transition temperature (T_c) for

$PbZr_{0.35}Ti_{0.65}O_3$ is found to be 365˚C. The dielectric constant of $PbZr_{0.35}Ti_{0.65}O_3$ increases gradually with increasing temperature. The plots of dielectric constant versus frequency measured at room temperature are shown in Fig. 6.5 (b) for both the samples (annealed at 1100˚C). It has been observed that the dielectric constant decreases with the increasing in frequency. It is a typical characteristic of dielectric/ferroelectric materials. The fall in dielectric constant arises from the fact that polarization does not occur instantaneously with the application of electric field because of inertia. At low frequencies, all polarizations contribute. As frequency increases, the polarization with large relaxation times cease to respond and hence the decrease in dielectric constant. The same type of frequency-dependent dielectric behavior is found in ferroelectric ceramics [113].

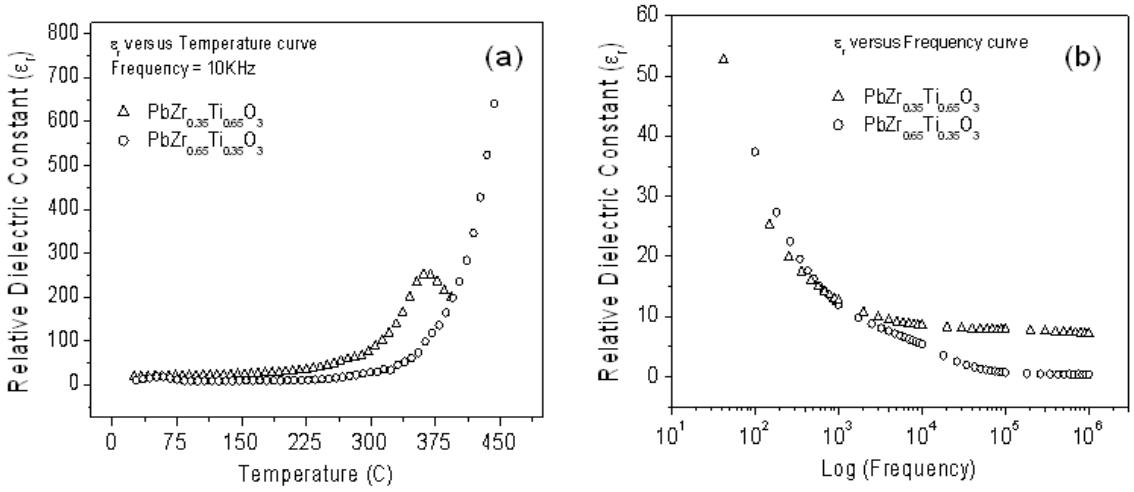

Fig. 6.5 (a, b): (a) Dielectric constant versus temperature plot for the samples $PbZr_{1-x}Ti_xO_3$ (x = 0.65 and 0.35), and (b) dielectric constant versus Log_{10} (frequency) plot for the samples $PbZr_{1-x}Ti_xO_3$ (x = 0.65 and 0.35).

6.2.4 Summary

$PbZr_{1-x}Ti_xO_3$ (x = 1.00, 0.65 and 0.35) single phase materials could be prepared by following solid state reaction method. Ti rich PZT ($PbZr_{0.35}Ti_{0.65}O_3$) sample has been successfully prepared with a low axial ratio (c/a) compare to that of $PbTiO_3$. The $PbTiO_3$ and $PbZr_{0.35}Ti_{0.65}O_3$ samples crystallize to *P4mm* spacegroup in tetragonal symmetry. However, the Zr rich PZT ($PbZr_{0.65}Ti_{0.35}O_3$) sample crystallizes to *R3c* spacegroup in rhombohedral symmetry. All the samples exhibit ferroelectric to

paraelectric transition. The ferroelectric to paraelectric transition temperature for $PbZr_{0.35}Ti_{0.65}O_3$ sample is found to be 365˚C. The dielectric constant is found to be decreased with the frequency and the ferroelectric to paraelectric transition temperature decreased with the crystallite size.

6.3 Structural analysis and impedance properties of Mn modified $Pb(Zr_{0.65}Ti_{0.35})O_3$, ($0.0 \leq x \leq 0.15$) ceramics

6.3.1 X-ray diffraction analysis by employing the Rietveld method.

XRD patterns of $Pb(Zr_{0.65-x}Mn_xTi_{0.35})O_3$, for x = 0.00, 0.05, 0.10 and 0.15 samples (high energy ball milling for 6 hours) are shown in Fig. 6.6. There are impurity peaks in the XRD pattern; hence we have annealed the samples at high temperature to grow the crystals in pure phase. The XRD patterns of the samples annealed at 900ºC for 8h and 1100ºC for 4h are shown in Fig. 6.7 and Fig. 6.8 respectively. We have observed that the samples are in the single phase form. All the observed peaks could be indexed using *R3c* space group with rhombohedral symmetry. The average crystallite values calculated by using Rietveld method are listed in Table 6.3 for both 900ºC and 1100ºC annealed samples. It is found that average crystallite size increases with annealing temperature due to the formation of larger crystals at high temperature. The XRD patterns for all the samples were analyzed with the help of Fullprof program by employing Rietveld refinement technique [152]. The refined XRD patterns of the Mn doped sample of $Pb(Zr_{0.65-x}Mn_xTi_{0.35})O_3$, for x = 0.05, 0.10 and 0.15 (annealed at 1100^0C) are shown in Fig. 6.9 (a-c) respectively. It is observed that all the peaks could be well refined to *R3c* spacegroup. Lattice parameters, occupancy, fractional atomic positions etc. were taken as the free parameter during the fitting. The lattice parameters, the goodness of the fitting are listed in Table 6.2. The fractional atomic positions are Pb (0.3333, 0.6667, 0.43304), Zr/Ti (0, 0, 0.5) and O (0.1733, 0.3453, 0.5843) for x = 0.00 (*R3c*) sample. The refined values of lattice parameters are listed in Table 6.4. The lattice parameters and unit cell volumes are found to decrease with the increase of Mn concentration, it could be due to the smaller ionic size of Mn^{3+} (0.66Å) to that of ionic size of Zr^{4+} (0.72Å). Bond lengths and angles

were calculated from the refined parameters with the help of the Powder cell program and the values are listed in Table 6.4 for all the samples.

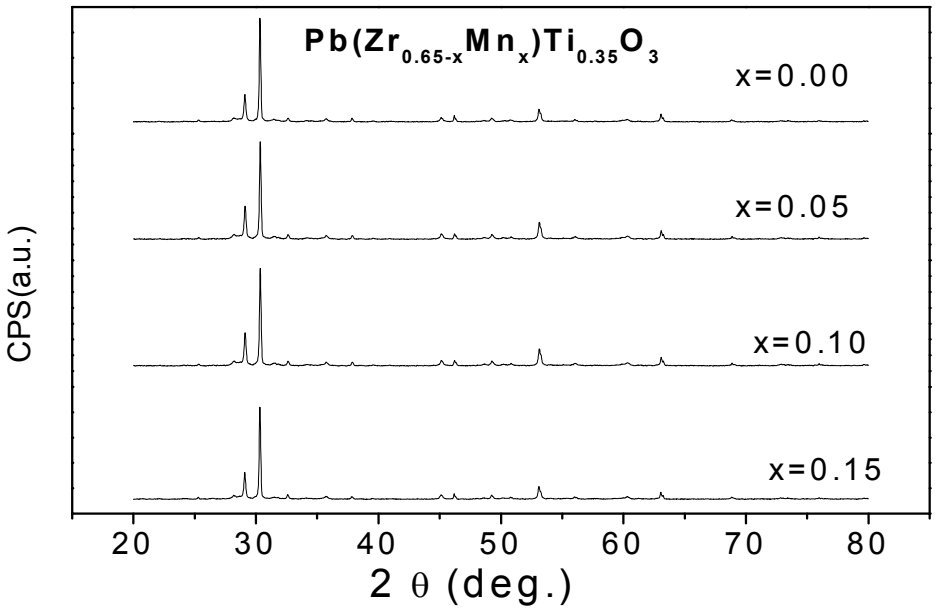

Fig. 6.6: XRD patterns of the samples Pb $(Zr_{0.65-x}Mn_xTi_{0.35})O_3$ for x = 0.00, 0.05, 0.10, and 0.15 (Ball milling 6h).

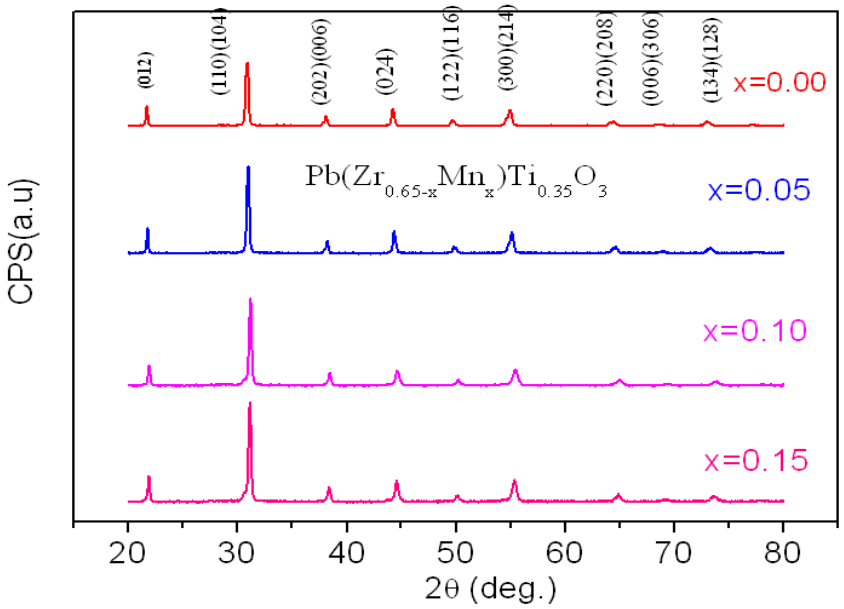

Fig. 6.7: XRD patterns of the samples Pb $(Zr_{0.65-x}Mn_xTi_{0.35})O_3$ for x = 0.00, 0.05, 0.10, and 0.15 (annealed at 900^0C for 8h).

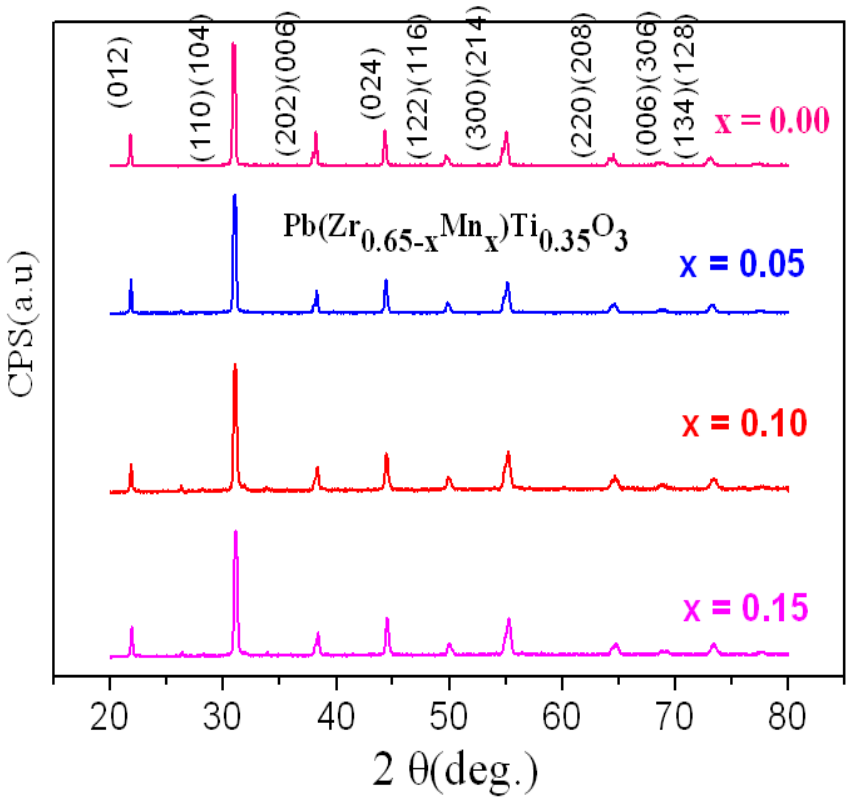

Fig. 6.8: XRD patterns of the samples Pb $(Zr_{0.65-x}Mn_xTi_{0.35})O_3$ for x = 0.00, 0.05, 0.10, and 0.15 (annealed at 1100^0C for 4h).

Table 6.3: Crystallite size of the sample $Pb(Zr_{0.65-x}Mn_xTi_{0.35})O_3$ powders for x = 0.05, 0.10, and 0.15 annealed at 900ºC for 8 h and 1100˚C for 4h.

Sample	Rietveld method (crystallite size (nm))	
	900^0C	1100^0C
$Pb(Zr_{0.60}Mn_{0.05}Ti_{0.35})O_3$	12.8(1)	30.3(1)
$Pb\ (Zr_{0.55}Mn_{0.10}Ti_{0.35})O_3$	12.5(1)	30.1(1)
$Pb\ (Zr_{0.50}Mn_{0.15}Ti_{0.35})O_3$	11.0(1)	28.0(1)

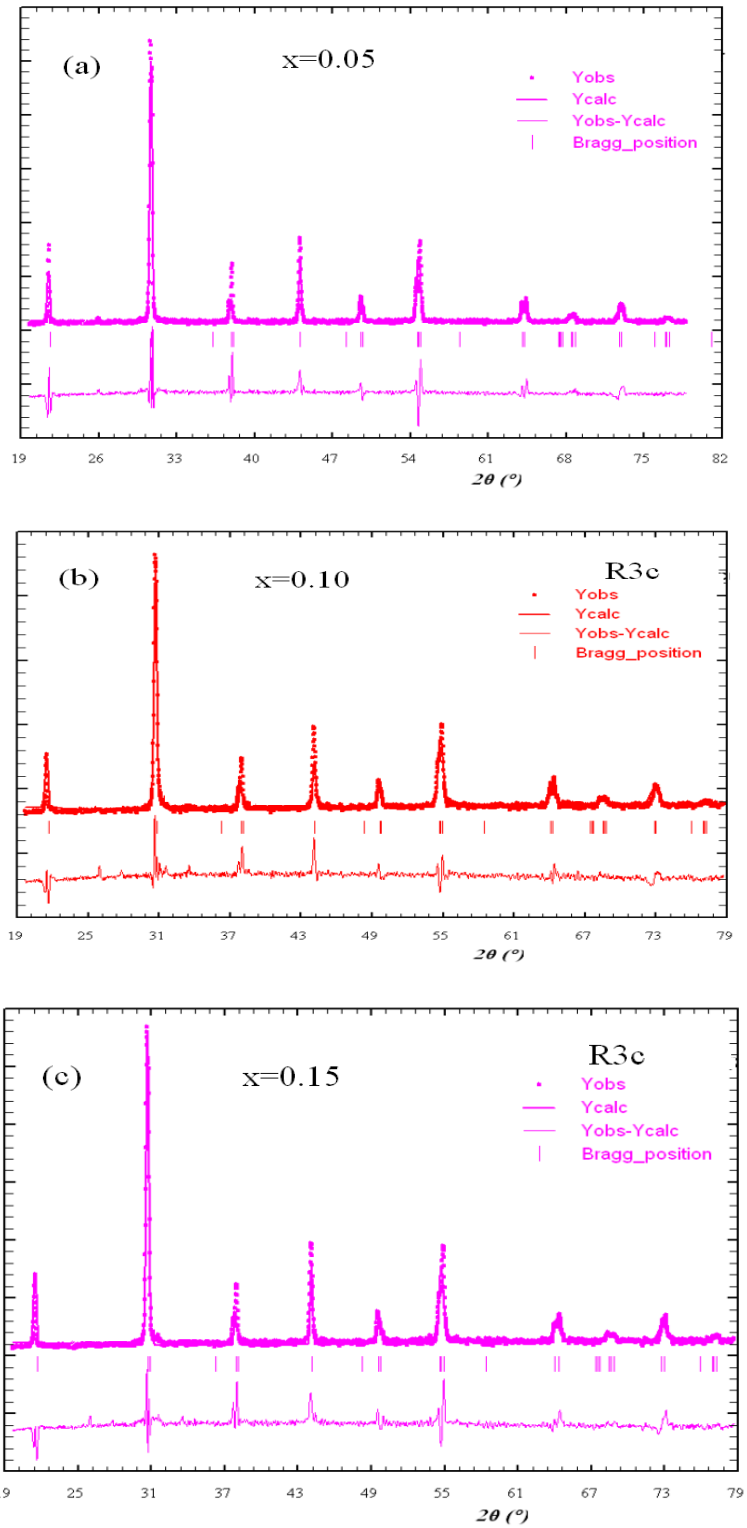

Fig. 6.9 (a-c): XRD pattern along with Rietveld refined data for the sample $Pb(Zr_{0.65-x}Mn_xTi_{0.35})O_3$ for (a) x = 0.05 (b) x = 0.10, and (c) x = 0.15 (annealed at 1100^0C for 4h). The patterns have refined using *R3c* space group. The '**.**' signs represent experimental points and solid line represents Rietveld refined data. The dotted lines show the difference between experimental and refined data.

Table 6.4: Parameters obtained from Rietveld analysis of $Pb(Zr_{0.65-x}Mn_xTi_{0.35})O_3$ powders with (x = 0.05, 0.10, and 0.15) annealed at 1100ºC for 4 h.

Sample Parameters	x = 0.05	x = 0.10	x = 0.15
Space group	*R3c*	*R3c*	*R3c*
Pb(Occup.)	0.9873(8)	0.9912(7)	0.9885(8)
Zr(Occup.)	0.6012(9)	0.5439(9)	0.5043(9)
Mn(Occup.)	0.0476(9)	0.0966(8)	0.1489(7)
Ti(Occup)	0.3424(9)	0.3482(9)	0.3464(9)
a=b(Å)	5.7863(12)	5.7797(14)	5.7789(17)
C(Å)	14.2746(32)	14.2614(38)	14.2517(49)
Volume ($Å^3$)	413.89(15)	412.18(18)	412.31(20)
$\chi 2$ (chi^2)	2.99	2.68	2.70
R_p	16.1	15.9	15.5
R_{wp}	22.1	21.3	20.9
R_{Bragg}	15.7	14.7	15.6
R_f	10.4	10.8	15.3
R_{exp}	11.5	12.1	12.7
Pb-Ti/Zr (Å)	3.3463(11)	3.28976(8)	3.2784(3)
Ti/Zr-O_1 (Å)	2.2213(24)	2.2408 (31)	2.3028 (17)
Ti/Zr-O_2 (Å)	3.2784(4)	3.2743(9)	3.2739(19)
$\angle Mn - Pb - Mn$	38.5(2)	38.4(2)	38.4(1)

6.3.2 Microstructural and elemental analysis

The scanning electron micrographs of the sample $Pb(Zr_{0.65-x}Mn_xTi_{0.35})O_3$ with (x = 0.05, 0.10, and 0.15) annealed at 1100ºC for 4 h is shown in the Fig. 6.10 (a-c). Most of the grains of the samples were found to be spherical in nature. One can notice the samples are uniform and the grains are in order of micron size. The average grain size of the sample is found to be 1.5-4.5µm. It is found that the grain size decreases with increase of Mn concentration. Similar behavior has been observed by other groups in PZT materials [137]. The SEM-EDS analysis reveals that, all the compositions present in the samples are as prepared. The SEM-EDS of the sample Pb $(Zr_{0.65-x}Mn_xTi_{0.35})O_3$ for x= 0.0, 0.05, 0.10 and 0.15 is shown in Fig. 6.11 (a-d). The theoretical EDS and experimental EDS weight% have been given in Table 6.5.

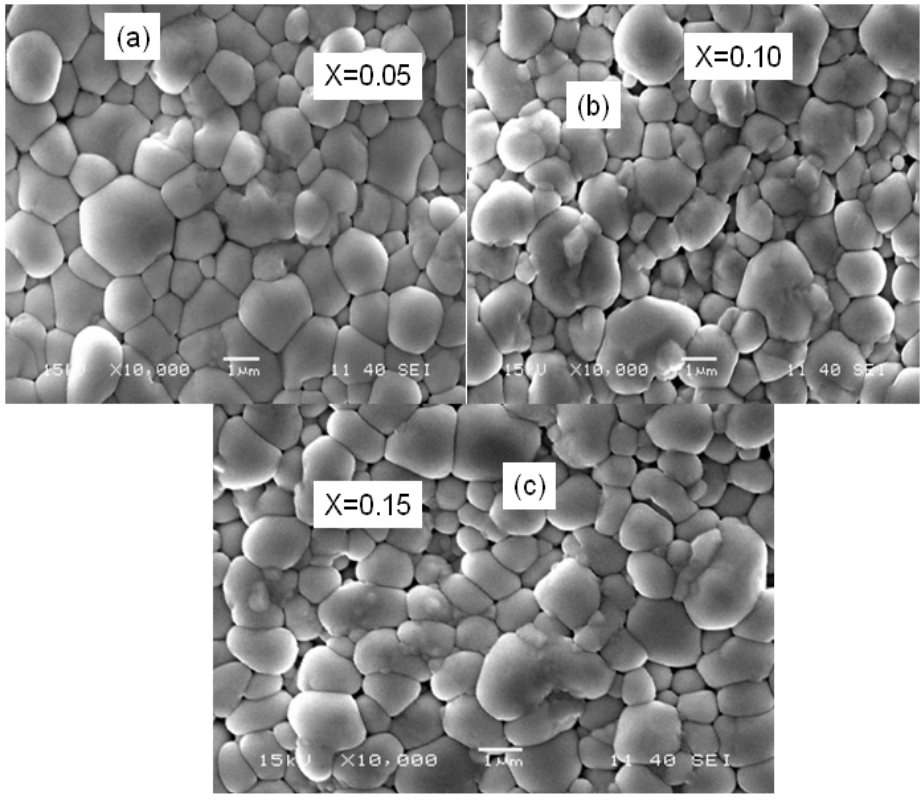

Fig. 6.10 (a-c): Micrographs of Pb $(Zr_{0.65-x}Mn_xTi_{0.35})O_3$ for (a) x = 0. 05, (b) x= 0.10, and (c) x = 0. 15 samples (sintered at 1100ºC for 4h).

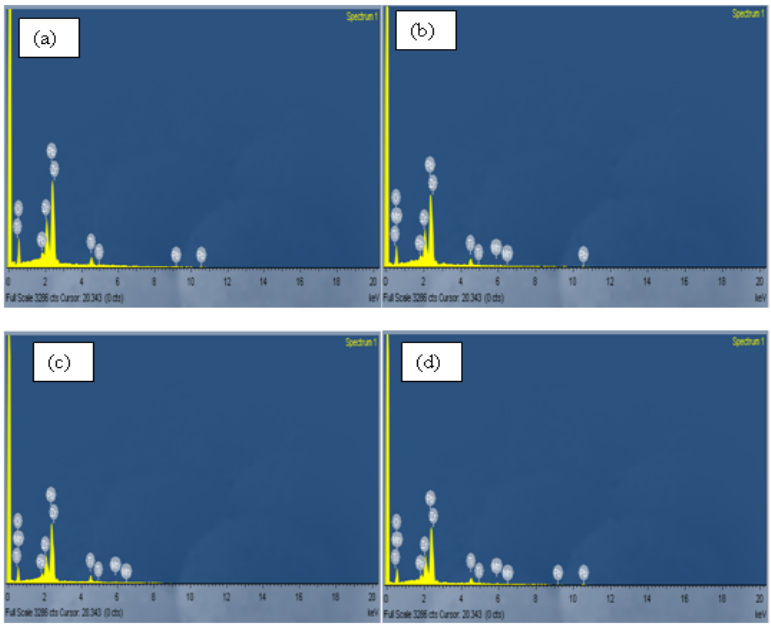

Fig. 6.11 (a-d): SEM-EDS of $Pb(Zr_{0.65-x}\ Mn_xTi_{0.35})O_3$ for (a) x = 0.00, (b) x = 0.05, (c) x = 0.10, and (d) x = 0.15 samples (sintered at 1100ºC/4h).

Table 6.5: Elemental analysis of $Pb(Zr_{0.65-x}\ Mn_xTi_{0.35})O_3$ for x = 0.00, 0.05, 0.10 and 0.15 respectively.

Composition	Element	Wt% calculated	Wt% from EDX
x = 0.00	Pb	58.85	58.83
	Zr	21.11	22.02
	Ti	7.37	7.31
	O	12.66	11.84
	Mn	0.00	0.00
x = 0.05	Pb	59.13	59.03
	Zr	19.58	19.54
	Ti	7.40	7.42
	O	12.73	12.48
	Mn	1.15	1.23
x = 0.10	Pb	59.42	59.31
	Zr	18.04	17.94
	Ti	7.44	8.01
	O	12.78	12.39
	Mn	2.31	2.35
x = 0.15	Pb	59.70	59.63
	Zr	16.48	16.91
	Ti	7.48	8.11
	O	12.85	11.82
	Mn	3.48	3.53

6.3.3 Dielectric analysis

Plots of temperature variation of the dielectric constant (ϵ_r) measured at different frequencies of the sample $Pb(Zr_{0.65-x}Mn_xTi_{0.35})\ O_3$ for x = 0.0, 0.05, 0.10 and 0.15 (annealed at 1100^0C) are shown in Fig. 6.12 (a-d) respectively. The dielectric constant of the samples increases gradually with increasing temperature up to a particular temperature and thereafter it decreases. Dielectric constant increases with temperature due to interfacial polarization becoming more dominant compared to the dipolar polarization [137]. After a certain temperature reached, the dielectric constant decreases due to the phase transition from ferroelectric to paraelectric. The transition temperature is called the Curie temperature (T_c) which was obtained from $|d\epsilon_r/dT|$ versus temperature plot and those values are given in Table 6.6. The Plots of frequency versus dielectric constant for x = 0.0, 0.05, 0.10 and 0.15 are shown in Fig. 6.13 (a-d) respectively for selected temperatures. It is observed that, the dielectric constant decreases with frequency for all the samples. This can be explained by the fact that, at low frequencies ε_r is due to the contribution of multi component of polarizability such as, deformational (electronic and ionic) and relaxation (orientational and interfacial) polarization. Electronic polarization arises from the displacement of the valence electrons relative to the positive nucleus. This type of polarization takes place up to the frequency 10^{16} Hz. Ionic type of polarization occurs due to the displacement of negative and positive ions with respect to each other. Maximum frequency of ionic polarization is 10^{13} Hz. Dipolar polarization occurs if the materials contain molecules, with permanent electric dipole moment that can change orientation in the direction of the applied electric field. The dipolar polarization takes place at frequencies up to 10^{10} Hz. Space charge polarization occurs due to impedance mobile charge carriers by interfaces. It occurs in frequency ranges from 1 to 10^3 Hz. The total polarization of the dielectric material can be explained as the sum of these 4 types of polarization [117]. When the frequency is increased, the orientational polarization decreases since it takes more time than electronic and ionic polarization. This decreases the value of relative dielectric constant ε_r reaching a constant value at higher frequency correspondingly to interfacial polarization. On the other hand the dielectric constant with

temperature can be attributed to the fact that the orientational polarization is connected with thermal motion of molecules so dipole can not orient themselves at low temperatures. When the temperature is increased the orientation of the dipole is facilitated and thus increases the orientational polarization which leads to increases of the dielectric constant with temperature. However after a certain temperature the thermal energy is very high to restrict the polarization which leads to the disordered state (paraelectric). Hence, we have observed a transition from ferroelectric to paraelectric phase with the temperature.

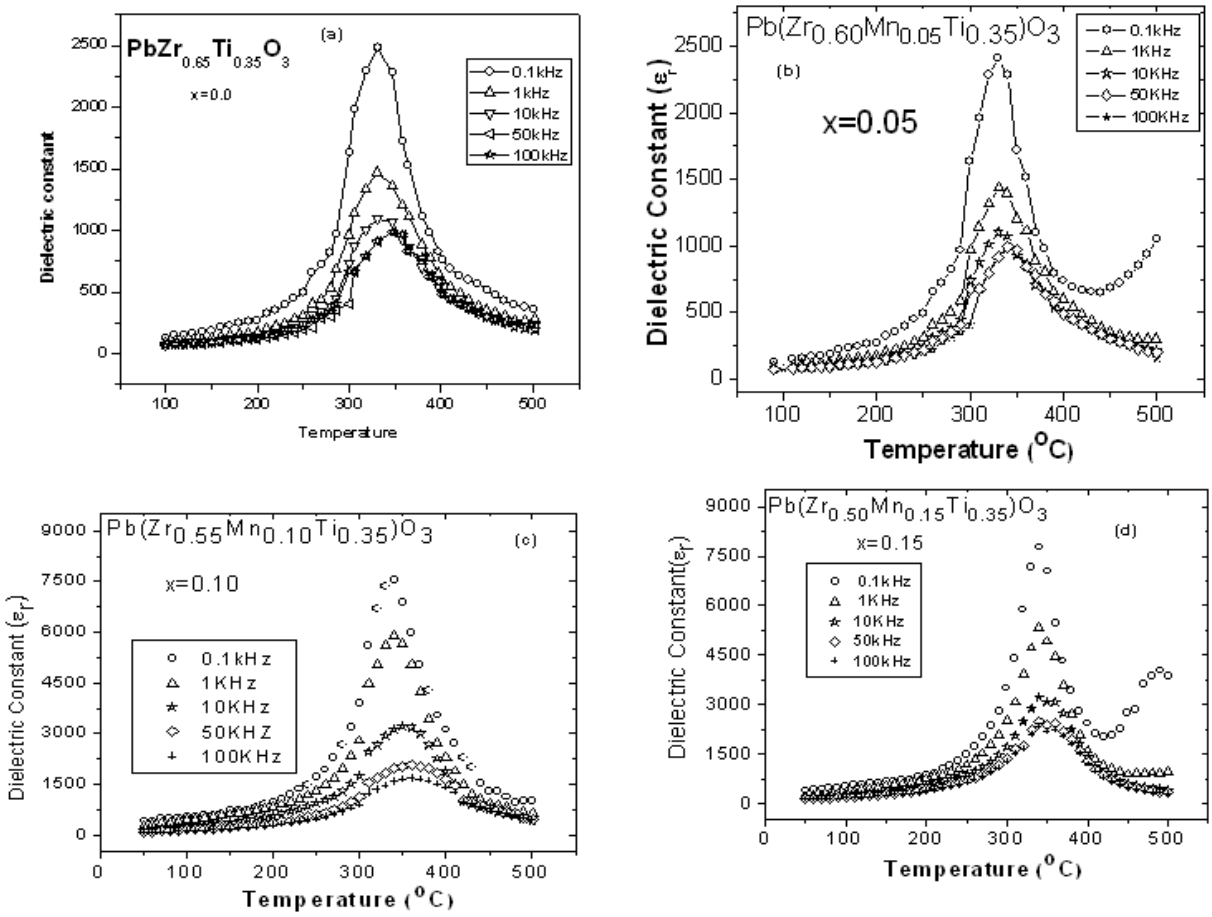

Fig. 6.12 (a-d): Variation of dielectric constant of $Pb(Zr_{0.65-x}Mn_xTi_{0.35})O_3$ for (a) x = 0.00, (b) x = 0.05, (c) x = 0.10, and (d) x = 0.15 ceramics at different frequency as a function of temperature.

Table 6.6: Dielectric constant (ε_r) and paraelectric to ferroelectric transition temperature (T_c) of the sample $Pb(Zr_{0.65-x}Mn_xTi_{0.35})O_3$ for x = 0.05, 0.10, and 0.15 at different frequencies.

Composition	Frequency (kHz)	ε_r	T_c
x = 0.00	0.1	2489	330
	1	1466	331
	10	1089	334
	50	1012	346
	100	959	352
x = 0.05	0.1	2405	329
	1	1443	331
	10	1097	332
	50	1006	340
	100	934	348
x = 0.10	0.1	7583	340
	1	5726	340
	10	3241	352
	50	2055	355
	100	1668	360
x = 0.15	0.1	7791	341
	1	5305	341
	10	3241	349
	50	2438	349
	100	2193	351

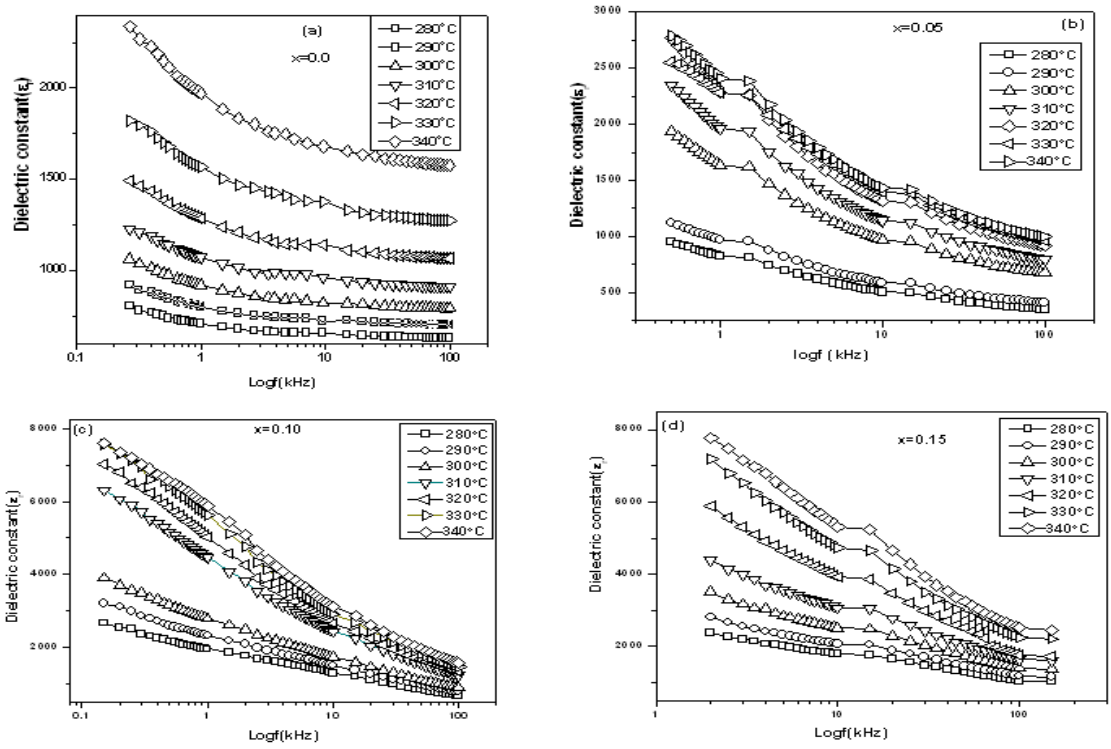

Fig. 6.13 (a-d): Variation of dielectric constant with the frequency of $Pb(Zr_{0.65-x}\ Mn_xTi_{0.35})O_3$ samples for (a) x = 0.00, (b) x = 0.05, (c) x = 0.10, and x = 0.15.

6.3.4 Polarization study

The ferroelectric hysteresis behavior was studied for $Pb(Zr_{0.65-x}\ Mn_xTi_{0.35})O_3$ samples at different fields at room temperature (30˚C) which has been shown in Fig. 6.14 (a-d). Dipoles are strongly dependent on the applied electric field. It is observed that as the applied field is increased the polarization increases and reaches to saturation at a substantially high applied field which is a typical behavior of ferroelectric material [176]. As the Mn concentration increases the remnant polarization (P_r) increases with increase in temperature which is due to increase in internal energy. The remnant polarization (P_r) and coercive field (E_c) determined from the hysteresis loops are listed in Table 6.7. Remnant polarization (P_r) was found to increase with increase in Mn substitution from which one can predict that material gets soften and can be exploited for memory applications.

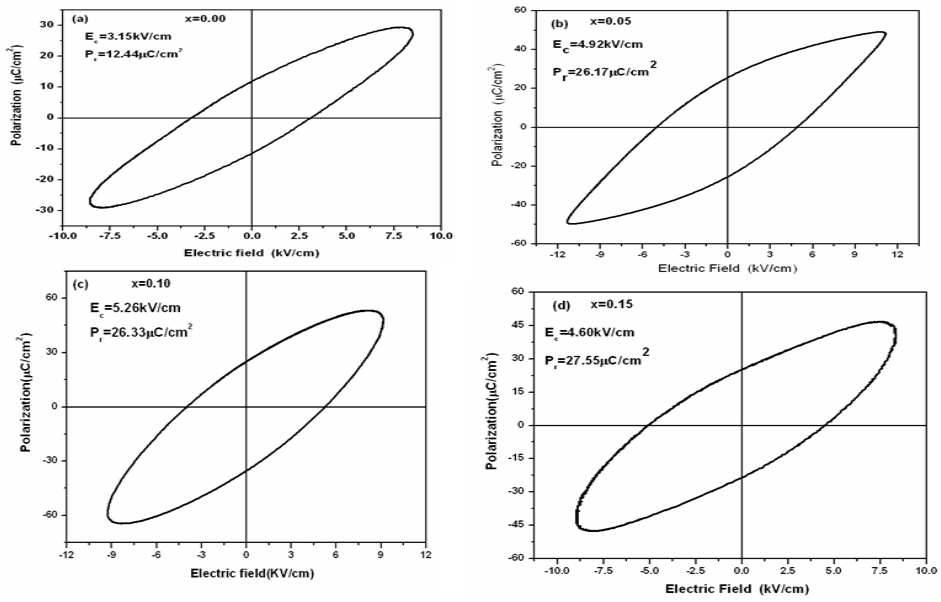

Fig. 6.14 (a-d): Polarization versus Electric field curve of $Pb(Zr_{0.65-x}Mn_xTi_{0.35})O_3$ samples for (a) x = 0.00, (b) x = 0.05, (c) x = 0.10, and x = 0.15.

Table 6.7: The observed value of P_r and E_c for PZMT samples at room temperature.

X	P_r(C/cm^2)	E_c(kV/cm)
0.00	12.44	3.15
0.05	26.17	4.92
0.10	26.33	5.26
0.15	27.55	4.60

6.3.5 Electrical conductivity studies

6.3.5.1 Impedance analysis

Fig. 6.15 (a-d) (300˚C-380˚C) and Fig. 6.16 (a-d) (400˚C-500˚C) shows the variation of the real part of impedance (Z′) with frequency at different temperatures. It has been clearly observed that Z′ has higher values at lower frequencies and it decreases monotonically with increase in frequency and attains a constant value at higher frequencies. This trend (attainment of constancy of Z′ value) appears to be shifting gradually towards the high frequency side with rise in temperature. The decrement in the real part of impedance (Z′) with a rise in the value of temperature and frequency may be due to increase in AC conductivity with a rise in temperature and frequency. The merger of the real part of impedance (Z′) for all temperatures in the high frequency domain

indicates a possibility of the release of space charge as a result of lowering in the barrier properties of the materials [166].

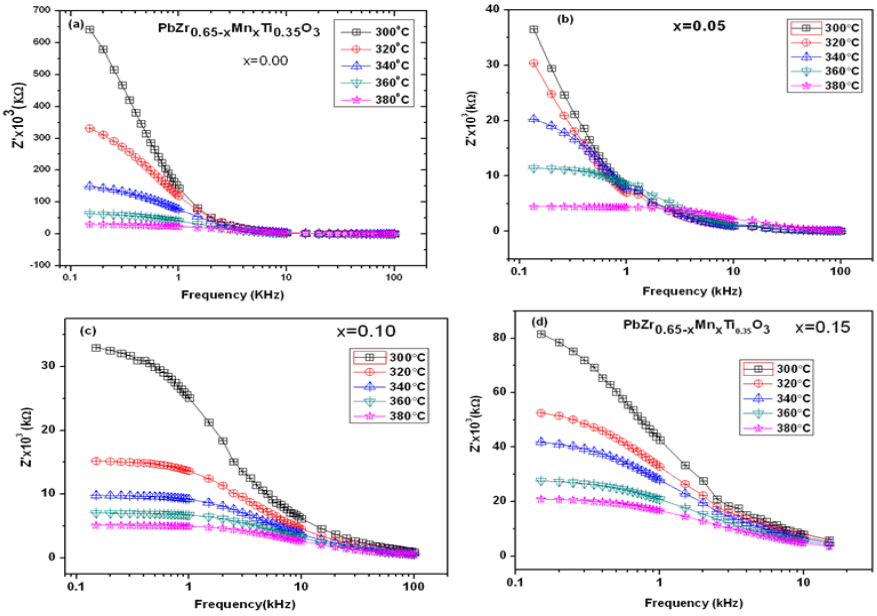

Fig. 6.15 (a–d) (300˚C-380˚C): The variation of the real part of impedance (Z') with frequency at different temperatures (300-380^{0}C). For the clarity x-axis has shown in logarithmic scale.

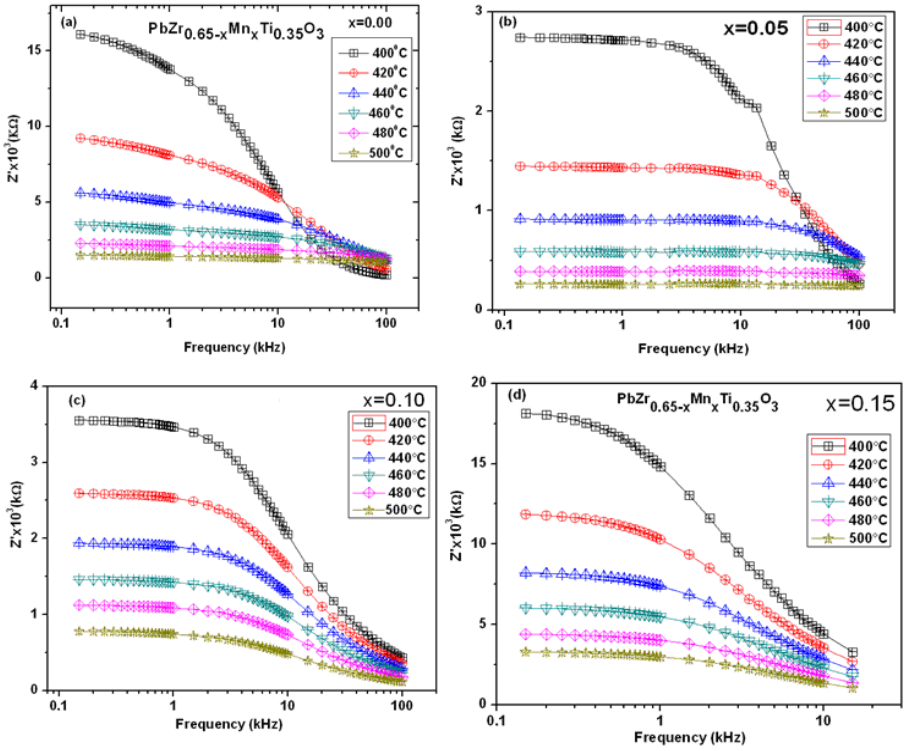

Fig. 6.16 (a-d) (400˚C-500˚C): The variation of the real part of impedance (Z') with frequency at different temperatures (400-500^{0}C). For the clarity x-axis has shown in logarithmic scale.

The variation of the imaginary part of impedance (Z″) with frequency at different temperatures of PZMT samples is presented in Fig. 6.17 (a-d) and Fig. 6.18 (a-d). This variation shows a considerable decrease in the magnitude of Z″ with a shift in the peak frequency toward the higher side with an increase in temperature. This feature becomes notable at higher temperature. The trend of variation of Z″ with a shift in the peak frequency is because of the presence of an electrical relaxation phenomenon on the material and it is a clear proof of temperature dependent relaxation. A relative lowering in the magnitude of Z″ with a shift in the peak frequency toward the higher side with the rise in temperature arises possibly due to the presence of space charge in the material. This result is in good agreement with the observation of complex impedance spectrum analysis [192]. The value $Log\omega_{max}$ and τ (rad/s) obtained from the variation of the imaginary part of impedance (Z″) with frequency at different temperatures is cited in Table 6.8. The variation of $Log\omega_{max}$ versus the inverse of temperature of PZMT samples follows Arrhenius behavior is shown in Fig. 6.19.

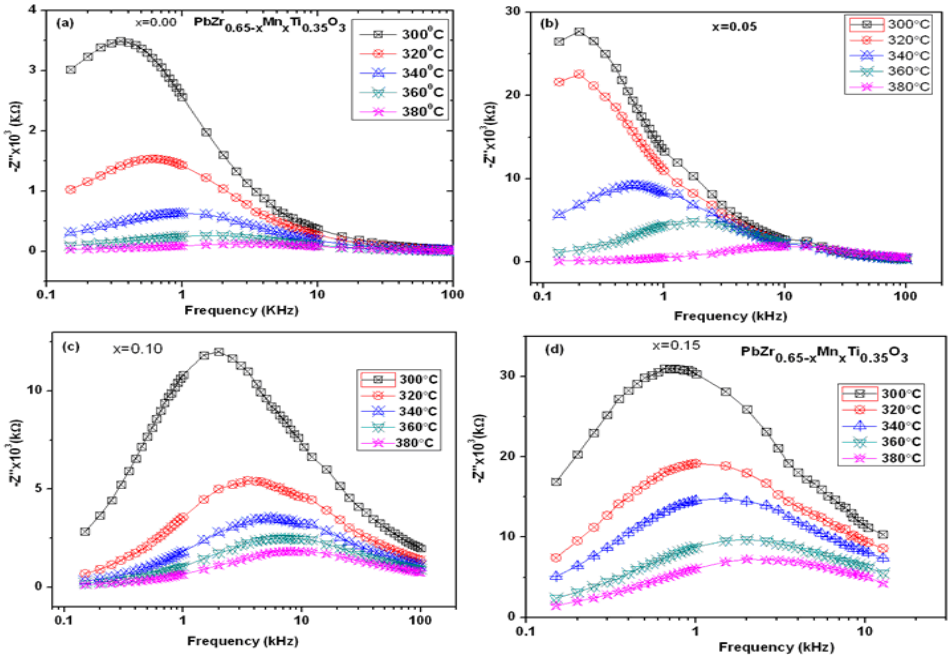

Fig. 6.17 (a–d) (300˚C-380˚C): The variation of the imaginary part of impedance (Z″) with frequency at different temperatures (300-380^{0}C) of the PZMT samples. For the clarity x-axis has shown in logarithmic scale.

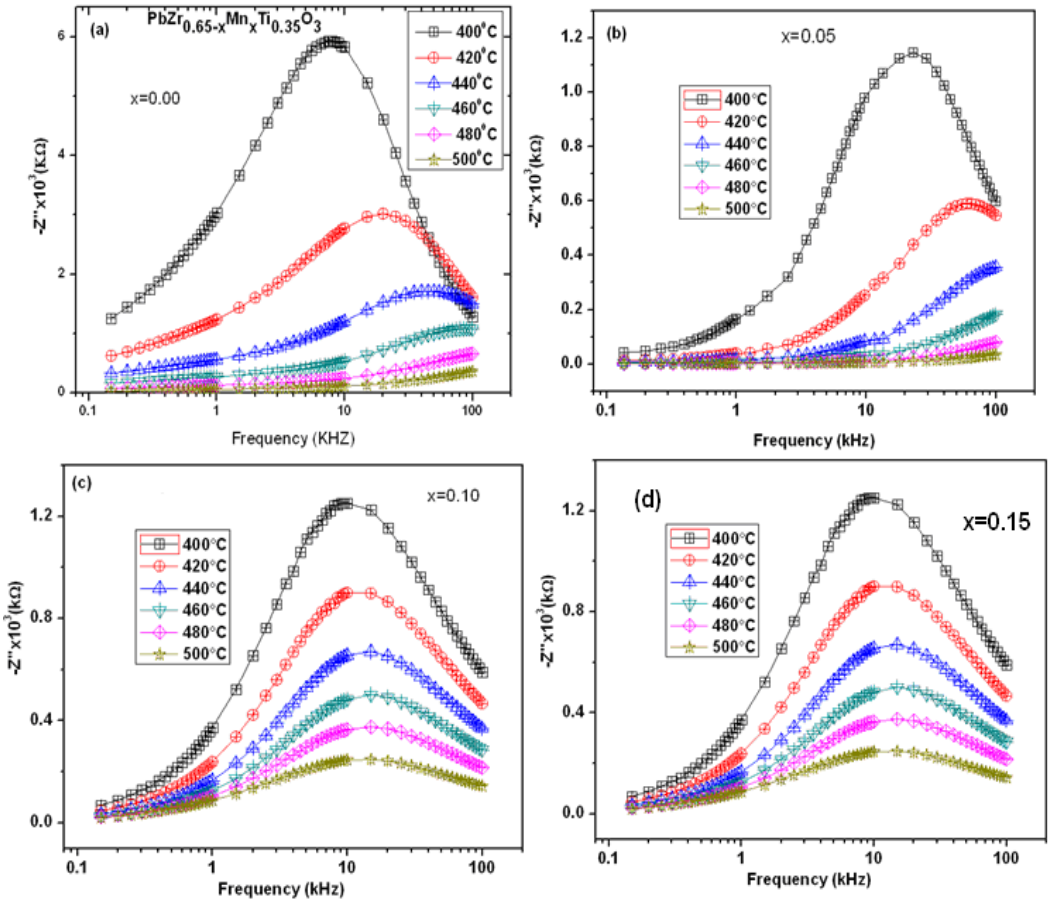

Fig. 6.18 (a-d) (400˚C-500˚C): The variation of the imaginary part of impedance (Z″) with frequency at different temperatures (400-500^{0}C) of the PZMT samples. For the clarity x-axis has shown in logarithmic scale.

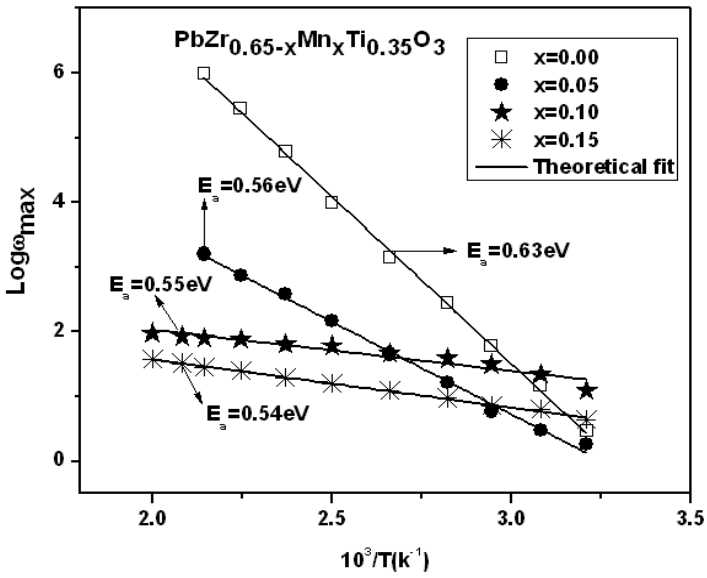

Fig. 6.19: The variation of $Log\omega_{max}$ versus inverse of temperature (obtained from Z″ spectra) of PZMT samples.

Table 6.8: The value $Log\omega_{max}$ and τ (rad/s) obtained from the variation of the imaginary part of impedance (Z'') with frequency at different temperatures of the sample of $Pb(Zr_{0.65-x}Mn_xTi_{0.35})O_3$, x = 0.0, 0.05, 0.10, and 0.15 respectively.

Sample	Temperature (˚C)	Log ω_{max}	τ (rad/s)
x = 0.00	300	0.80557	0.44684
	320	1.31498	0.26848
	340	1.79984	0.16533
	360	2.24788	0.10562
	380	2.52713	0.07989
	400	3.88612	0.02052
	420	4.79169	0.0083
	440	5.72483	0.00326
	460	6.25315	0.00192
	480	---	---
	500	---	--
x = 0.05	300	0.07142	0.81759
	320	0.09956	0.79513
	340	0.58272	0.26139
	360	1.04163	0.09086
	380	1.65602	0.02208
	400	2.1662	0.00682
	420	2.58136	0.00262
	440	2.87131	0.00162
	460	3.1123	0.00158
	480	---	----
	500	---	----------
x = 0.10	300	1.08993	0.0813
	320	1.34656	0.04502
	340	1.50054	0.03158
	360	1.58507	0.026
	380	1.67413	0.02118
	400	1.78433	0.01643
	420	1.80848	0.01554
	440	1.88094	0.01315
	460	1.90509	0.01244
	480	1.93075	0.01173
	500	1.97906	0.01049
x = 0.15	300	0.6377	0.2303
	320	0.80941	0.15509
	340	0.85781	0.13874
	360	0.97448	0.10605
	380	1.09221	0.08087
	400	1.19346	0.06405
	420	1.2815	0.0523
	440	1.39595	0.04018
	460	1.44987	0.03549
	480	1.5115	0.0308
	500	1.57313	0.02672

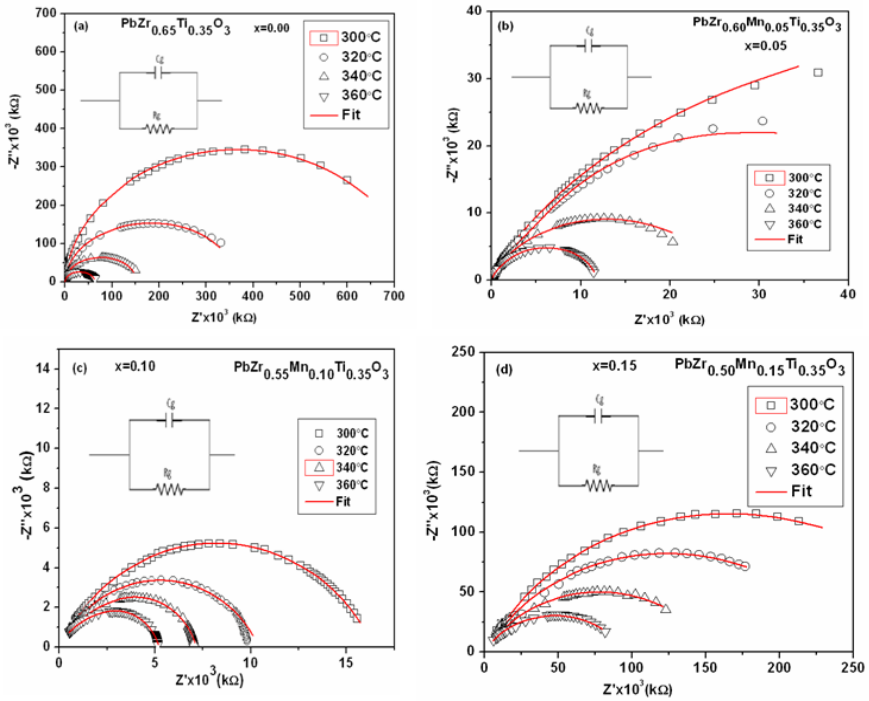

Fig. 6.20 (a–d) (300˚C-360˚C): The complex impedance spectrum (Nyquist plot) of PZMT compounds at higher temperature (300-360^{0}C).

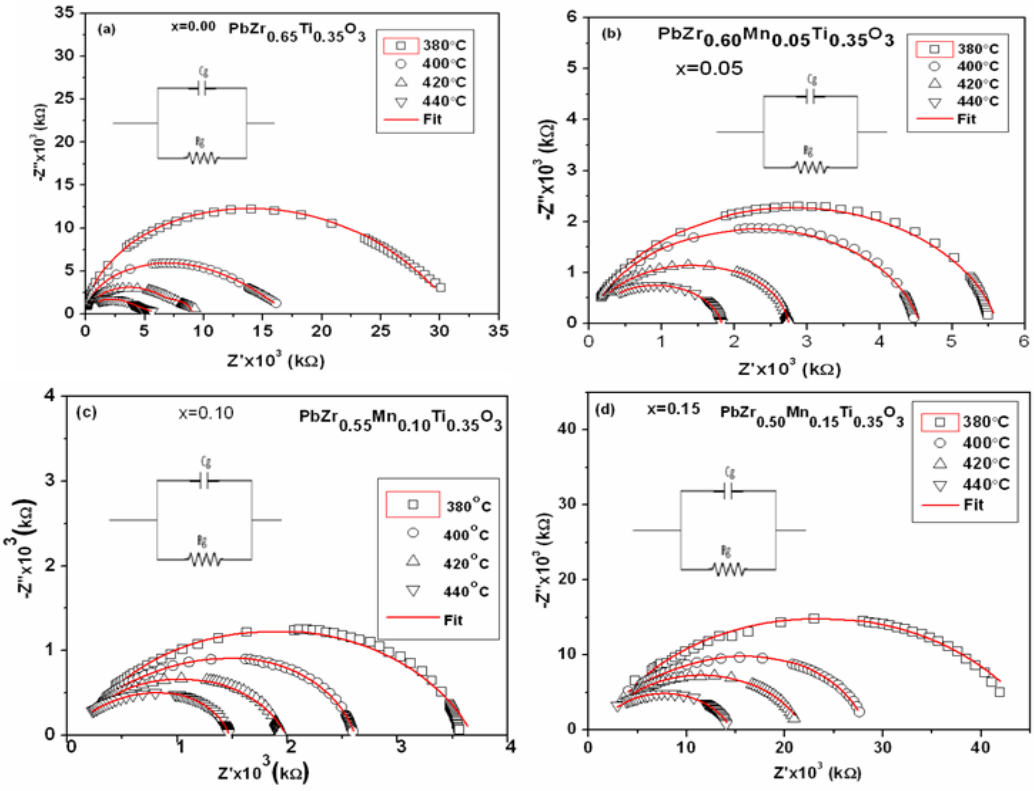

Fig. 6.21 (a-d) (380˚C-440˚C): The complex impedance spectrum (Nyquist plot) of PZMT compounds at higher temperature (380-440^{0}C).

Table 6.9: The observed value of grain capacitance (C_g), grain resistance (R_g) and apparent bulk conductivity (σ_b) of PZMT samples at different temperature.

Sample	Temperature ^oC	C_g nF	R_g kΩ	$\sigma_b = t/R_gA$ $(\Omega m)^{-1}$
x = 0.00	300	3.640	$7.36x10^5$	$2.348x10^{-7}$
	320	2.530	$2.981x10^5$	$5.80x10^{-7}$
	340	2.186	$1.263x10^5$	$1.369x10^{-6}$
	360	1.791	$5.425x10^4$	$3.188x10^{-6}$
	380	1.514	$1.694x10^4$	$1.28x10^{-5}$
	400	1.154	$1.246x10^4$	$1.021x10^{-5}$
	420	0.649	$7.346x10^3$	$2.351x10^{-5}$
	440	0.595	$1.759x10^3$	$9.841x10^{-5}$
x = 0.05	300	2.401	$1.215x10^3$	$1.50x10^{-6}$
	320	2.371	$2.146x10^4$	$8.54x10^{-6}$
	340	2.284	$4.457x10^4$	$4.11x10^{-6}$
	360	2.231	$7.251x10^3$	$2.52x10^{-5}$
	380	1.031	$5.617x10^3$	$3.26x10^{-5}$
	400	0.936	$4.548x10^3$	$4.031x10^{-5}$
	420	0.607	$2.270x10^3$	$8.071x10^{-5}$
	440	0.531	$1.805x10^3$	$1.01x10^{-4}$
x = 0.10	300	2.762	$1.63x10^4$	$1.08x10^{-5}$
	320	1.848	$1.03x10^4$	$1.71x10^{-5}$
	340	1.319	$4.82x10^3$	$3.67x10^{-5}$
	360	0.931	$3.56x10^3$	$4.97x10^{-5}$
	380	0.625	$3.58x10^3$	$4.94x10^{-5}$
	400	1.293	$1.84x10^3$	$9.62x10^{-5}$
	420	2.842	$1.91x10^2$	$9.24x10^{-5}$
	440	3.216	$1.08x10^2$	$1.63x10^{-4}$
x = 0.15	300	5.242	$9.28x10^5$	$1.94x10^{-7}$
	320	4.258	$2.44x10^5$	$7.37x10^{-7}$
	340	3.621	$1.52x10^4$	$1.18x10^{-6}$
	360	3.294	$9.50x10^3$	$1.89x10^{-6}$
	380	2.229	$4.86x10^3$	$4.02x10^{-6}$
	400	1.668	$1.95x10^2$	$9.22x10^{-6}$
	420	1.577	$2.08x10^2$	$8.64x10^{-6}$
	440	1.313	$1.35x10^2$	$1.32x10^{-5}$

The Nyquist plots of PZMT compounds at different temperatures are shown in Fig. 6.20(a–d)(300˚C-360˚C) and Fig. 6.21(a–d) (380˚C-440˚C). The high-frequency curve attributes to

the bulk properties of the material and arises due to parallel combination of the bulk resistance (R_g) and bulk capacitance (C_g), whereas the low frequency semicircles are attributed to the grain boundary effects. The arc attributed to the grain boundary contribution is equivalent electrically to the parallel combination of grain boundary resistance and capacitance. The electrical equivalent circuit corresponding to the sample impedance response is shown as an inset in Fig. 6.20 (a-d) and Fig. 6.21 (a-d). The observed values of grain capacitance (C_g), grain resistance (R_g) and apparent bulk conductivity (σ_b) of PZMT samples at different temperatures are given in Table 6.9. It has been observed that sample resistance decreases with an increase in temperature, which is an effect analogous to the negative temperature coefficient of resistance (NTCR) in the conventional semiconductors. So, the result indicates a typical semiconducting behavior of the materials.

6.3.5.2 AC Conductivity analysis

Fig. 6.22 (a-d) shows the variation of AC conductivity with frequency at room temperature of PZMT samples. All the compositions show dispersion of ac conductivity in both the low and the high frequency regions. The AC conductivity shows an increase with increase in Mn concentration at all frequencies. The existence of low frequency dispersion indicates that the charge carriers may be either ionic or electronic in nature. It can be seen that with the increase of Mn doping the value of activation energy decreases indicating an increase in conducting nature of the Mn doped PZT.

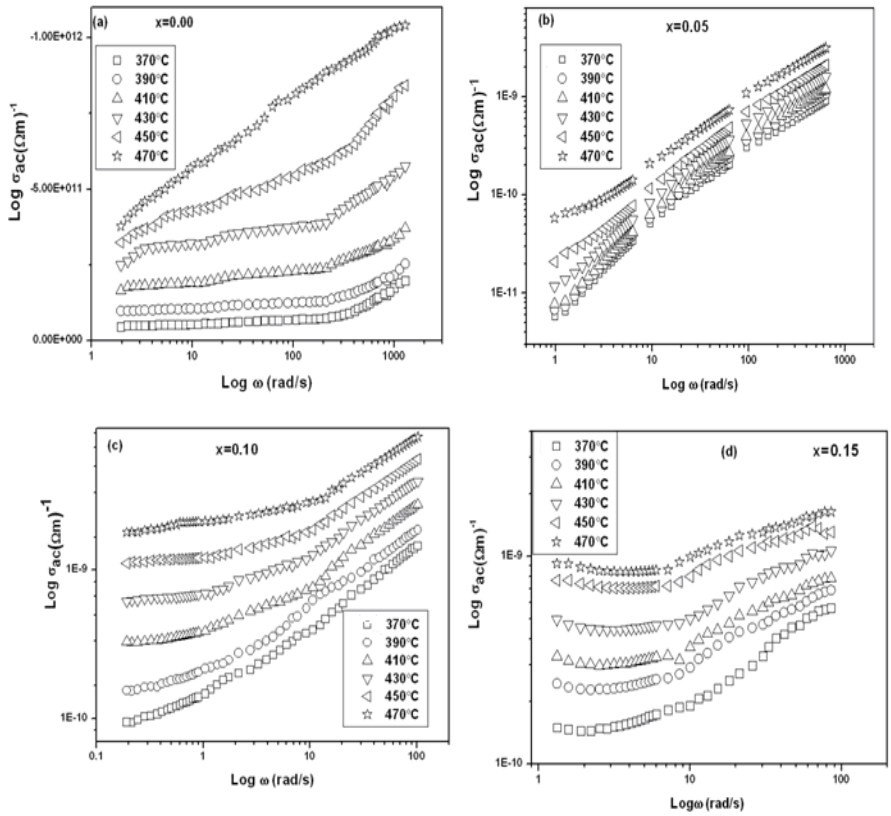

Fig. 6.22 (a-d): The variation of AC conductivity with frequency at room temperature of PZMT samples.

6.3.5.3 Complex electric modulus analysis

Fig. 6.23 (a) shows the frequency dependence of the imaginary part of the electric modulus (M″). Fig. 6.23 (b) shows Log ω_{max} versus 10^3/T, some selected temperatures of a typical sample PZMT5 ceramic. From this figure it is observed that the asymmetric modulus peaks shift towards the high frequency side, indicating a correlation between the motions of mobile ion charges [135]. The broadening of the peak also occurs with rise in temperature and it indicates the spread of relaxation with different mean time constant. The results definitely suggest non-Debye type of relaxation in the materials. The value Log ω_{max} and relaxation time have been given in Table 6.10. Also, the comparison of E_a (eV) obtained from σ_{ac}, apparent bulk conductivity (σ_{dc}), relaxation time, Z''_{max} and M''_{max} of PZMT samples are cited in Table 6.11.

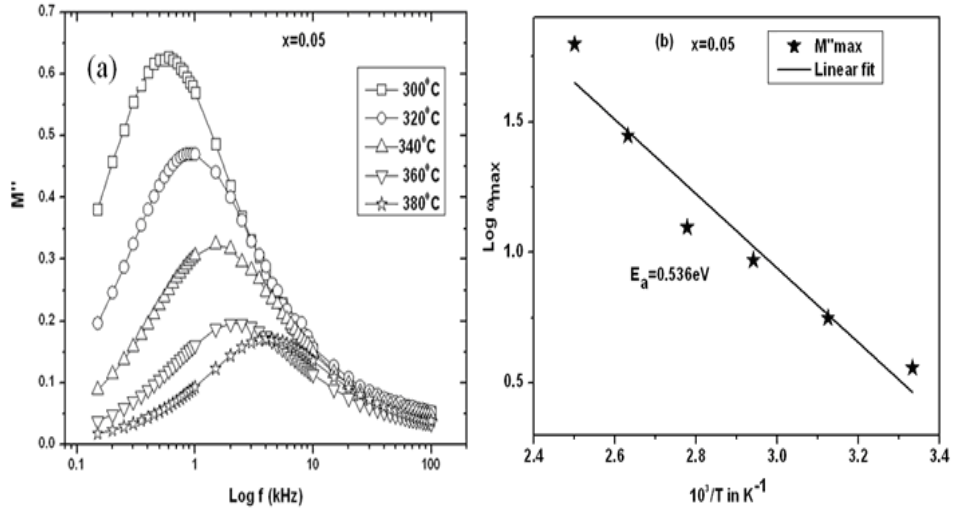

Fig. 6.23 (a, b): The imaginary part of the modulus versus frequency of a sample PZMT5 and (b) Log ω_{max} versus $10^3/T$ at different temperatures of a sample PZMT5.

Table 6.10: Observed value of Log ω_{max} and τ (rad/s) of a typical sample PZMT5 at some selected temperature.

Temperature (˚C)	Log ω_{max}	τ (rad/s)
300	0.5586	0.27631
320	0.74875	0.17834
340	0.97067	0.10699
360	1.09597	0.08017
380	1.44771	0.03567
400	1.79792	0.01593

Table 6.11: Comparison of E_a in eV obtained from (i) (σ_{ac}), (ii) apparent bulk conductivity (σ_{dc}), (iii) relaxation time (τ), (iv) Z''_{max} and (v) M''_{max} of $Pb(Zr_{0.65-x}Mn_xTi_{0.35})O_3$ for x = 0.00, 0.05, 0.10, 0.15 ceramics.

Sample	$E_a(\sigma_{ac})$	$E_a(\sigma_b)$	$E_a(\tau)$	$E_a(Z'')$	$E_a(M'')$
x = 0.00	0.87	0.83	0.85	0.63	0.61
x = 0.05	0.86	0.80	0.81	0.56	0.53
x = 0.10	0.77	0.78	0.75	0.55	0.56
x = 0.15	0.72	0.70	0.68	0.54	0.58

6.3.6 Summary

The Mn modified lead zirconate titanate has been prepared in the single phase form. The XRD patterns could be refined to *R3c* spacegroup. The lattice parameters and unit cell volumes are found to decrease with the increase of Mn concentration, it could be due to the smaller ionic size of Mn^{3+} (0.66Å) to that of ionic size of Zr^{4+} (0.72Å). All the samples exhibit ferroelectric to paraelectric transition. The dielectric constant decreases with the frequency which suggest the polarization at low frequency is due to the 4 types of polarization (deformational (electronic and ionic) and relaxation (orientational and interfacial) polarization). However, the orientational polarization decreases with frequency since it takes more time than electronic and ionic polarization. The charge carriers may be either ionic or electronic nature in the low frequency region. The AC conductivity increases with the increase in Mn concentration at all frequencies. Activation energy decreases with an increase in Mn concentration. This change in behavior indicates the participation of Mn ions in the relaxation, thermally activated and conductivity process. From impedance analysis of PZMT compounds confirms the presence of a non-Debye type of single relaxation in the material. The modulus analysis provides wider information related to charge transport processes.

CHAPTER 7

STRUCTURAL ANALYSIS AND ELECTRICAL PROPERTIES OF Fe^{3+} ION MODIFIED $Pb(Zr_{0.65}Ti_{0.35})O_3$ CERAMICS

CHAPTER 7

STRUCTURAL ANALYSIS AND ELECTRICAL PROPERTIES OF Fe^{3+} ION MODIFIED $Pb(Zr_{0.65}Ti_{0.35})O_3$ CERAMICS

This chapter explains the synthesis of Fe^{3+} ion modified $Pb(Zr_{0.65}Ti_{0.35})O_3$ samples by the solid state reaction route followed by structural analysis by employing the Rietveld method. The doping of Fe^{3+} ion creates a vacancy in B-site of ABO_3 perovskite structure of PZT which leads to create free space charge in the materials. The dielectric, AC conductivity, impedance and modulus analysis have been discussed.

7.1 Sample preparation

Perovskite $Pb(Zr_{0.65-x}Fe_xTi_{0.35})O_3$ with x = 0.00, 0.05, 0.10 and 0.15 ceramics have been prepared by solid state method which has been discussed in Chapter 3. Stoichiometric ratios of PbO, ZrO_2, Fe_2O_3 and TiO_2 with 99.9% purity were weighed by using a high precision electronic balance. The above materials were mixed thoroughly with the help of agate mortar and pestle. The grinding was carried out under acetone till the acetone evaporates from the mortar. The mixture was ball milled for 8h to make homogeneous mixture and presintered at different temperatures with intermediate grindings. The presintered samples were fired at 900^oC for 8h. The fine calcined powders of the above samples were pressed into cylindrical pellets of 6mm diameter and 1mm thickness under a uni-axial pressure of 6 tons using a hydraulic press. Finally the pellets were sintered at 1100^oC for over 4h.

7.2 Results and discussion

7.2.1 Structural analysis by employing the Rietveld method

Fig. 7.1 shows the X-ray diffraction (XRD) patterns of $Pb(Zr_{0.65-x}Fe_xTi_{0.35})O_3$ (PZFT) for x = 0.00, 0.05, 0.10 and 0.15 annealed at 900^0C. The XRD patterns indicate that the samples are in mixed phase. Hence, we have sintered the samples at 1100ºC for 4h and the corresponding XRD patterns

are shown in Fig. 7.2. The peaks in the XRD patterns were found to be very sharp which indicates good homogeneity and crystallization of the samples. We have not observed structural change in Pb $(Zr_{0.65-x}Fe_xTi_{0.35})O_3$ with the substitution of Fe^{3+} ions at Zr-site. It reveals that Fe^{3+} ions diffuse into PZT lattice to form a single-phase compound. All the diffraction peaks were indexed to the cubic, tetragonal and rhombohedral symmetry. The rhombohedral unit cell was selected as per the best agreement between observed (obs) and calculated (cal) interplaner spacing *d* (i.e., $\Sigma\Delta d = \Sigma(d_{obs} - d_{cal})$ = minimum. We have obtained the average crystallite size by using Rietveld method (The detailed discussed in Chapter 3) and these values are listed in Table 7.1 for all the samples. The unit cell parameters of the rhombohedral system were refined by employing the Rietveld refinement technique with the help of Fullprof program. The patterns could be refined using *R3c* space group in rhombohedral symmetry of $Pb(Zr_{0.65-x}Fe_xTi_{0.35})O_3$ for x = 0.05, 0.10 and 0.15. The refined XRD patterns of Pb $(Zr_{0.65-x}Fe_xTi_{0.35})O_3$ powders for x = 0.05, 0.10, and 0.15 samples annealed at 1100^0C are shown in Fig. 7.3 (a-c) respectively. We have observed that, all the observed peaks could be well refined. The lattice parameters, the goodness of the fitting are listed in Table 7.2. Lattice parameters, occupancy, fractional atomic positions etc. were taken as the free parameter during the fitting. The lattice parameters and unit cell volumes are found to be decreased with the Fe^{3+} ion concentration, it could be due to the smaller ionic size of Fe^{3+} (0.65Å) to that of ionic size of Zr^{4+} (0.73Å). Similar behavior has been observed by other groups [193,194]. Bond lengths and bond angles were calculated from the refined parameters and the values are listed in Table 7.2 for all the samples sintered at 1100ºC temperatures.

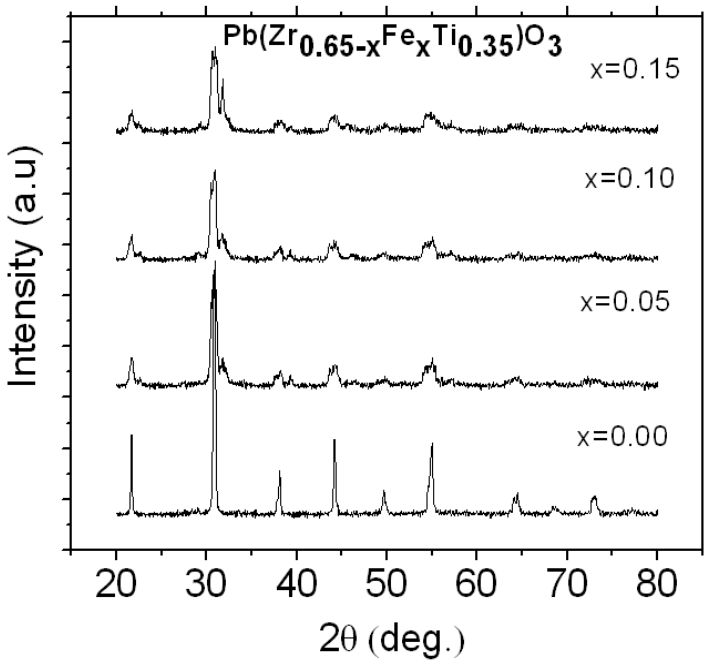

Fig 7.1: XRD patterns of Pb $(Zr_{0.65-x}Fe_xTi_{0.35})O_3$ with x = 0.00, 0.05, 0.10, and 0.15 annealed at 900^0C for 8h.

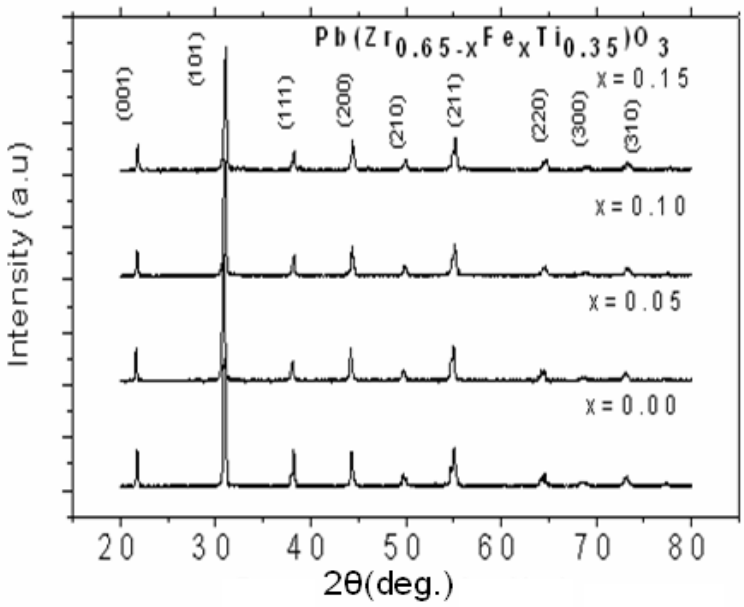

Fig. 7.2: XRD patterns of Pb $(Zr_{0.65-x}Fe_xTi_{0.35})O_3$ for x = 0.00, 0.05, 0.10, and 0.15 annealed at 1100^0C for 4h.

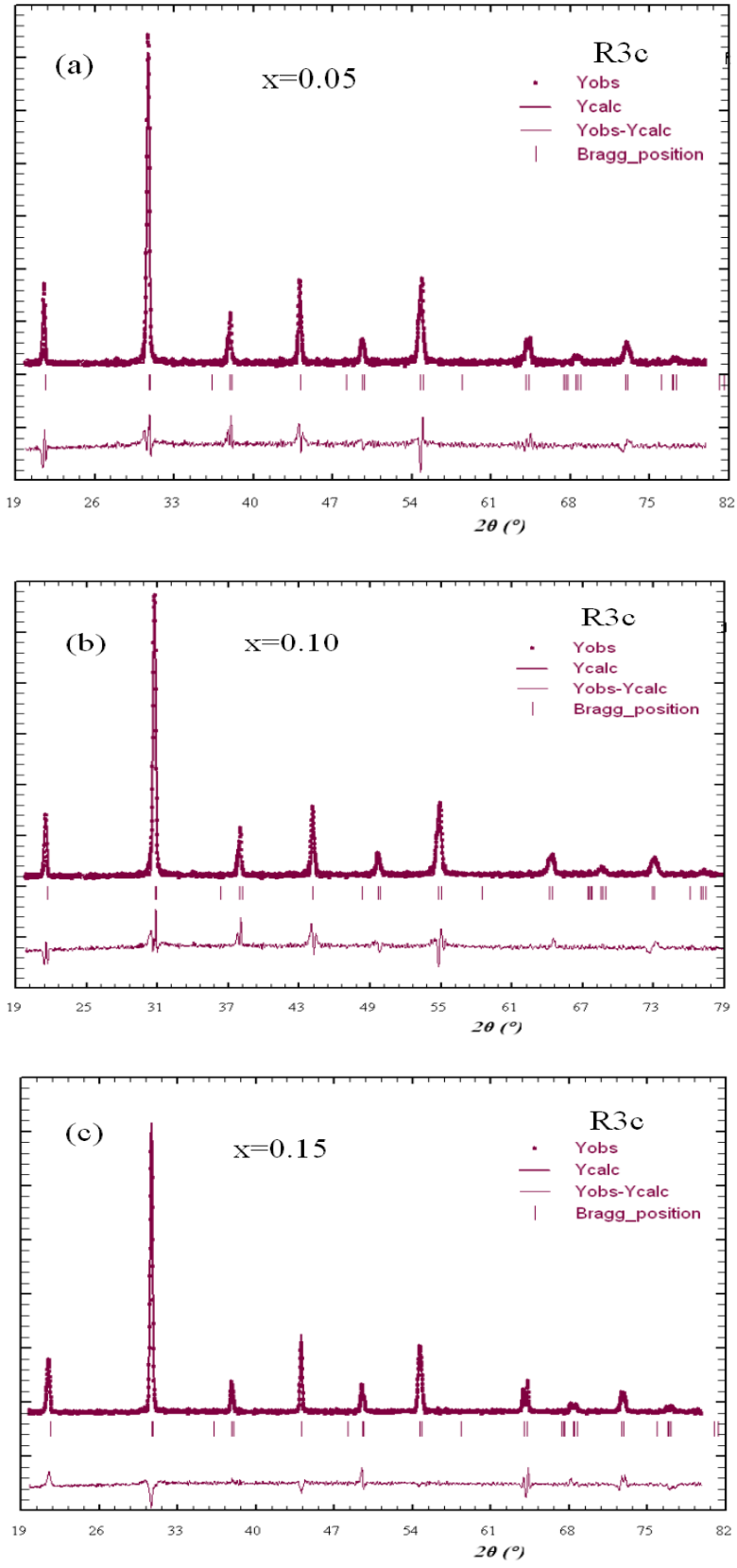

Fig. 7.3 (a-c): XRD patterns along with Rietveld refined data for the sample $Pb(Zr_{0.65-x}Fe_xTi_{0.35})O_3$ for x = 0.05, 0.10, and 0.15 annealed at 1100^0C for 4h.

Table 7.1: Crystallite size of the sample $Pb(Zr_{0.65-x}Fe_xTi_{0.35})O_3$ for x = 0.05, 0.10, and 0.15 annealed at 1100°C for 4h.

Sample	Rietveld method (crystallite size (nm))
	1100^0C
$Pb(Zr_{0.60}Fe_{0.05}Ti_{0.35})O_3$	32.1(10)
$Pb(Zr_{0.55}Fe_{0.10}Ti_{0.35})O_3$	31.5(14)
$Pb(Zr_{0.50}Fe_{0.15}Ti_{0.35})O_3$	29.0(10)

Table 7.2: Parameters obtained from Rietveld analysis of $Pb(Zr_{0.65-x}Fe_xTi_{0.35})O_3$ powders for x = 0.05, 0.10, and 0.15 annealed at 1100ºC for 4h.

Sample→ / Parameters ↓	x = 0.05	x = 0.10	x = 0.15
Space group	*R3c*	*R3c*	*R3c*
Pb(Occup.)	0.97365(5)	0.95497(5)	0.96553(6)
Zr(Occup.)	0.60135(7)	0.54355(8)	0.51447(10)
Ti(Occup.)	0.35000	0.35000	0.35000
a=b (Å)	5.8089(5)	5.8018(2)	5.8016(3)
c (Å)	14.1518(7)	14.1395(16)	14.1344(19)
Volume ($Å^3$)	413.5501(9)	412.1796(14)	412.0097(7)
χ^2 (chi^2)	1.15	1.127	1.101
R_p	14.2	14.4	14.8
R_{wp}	13.3	14.4	14.6
R_{Bragg}	15.7	19.4	19.4
R_f	14.3	14.4	16.9
R_{exp}	12.3	13.0	11.8
Pb-Ti/Zr (Å)	3.2731(6)	3.2691(6)	3.2690(5)
Ti/Zr-O_1 (Å)	1.9983/ 1.7382	1.87690/ 1.58761	1.7784/ 1.3423
Ti/Zr-O_2 (Å)	3.2731/1.5891	3.2691/1.3995	3.2690/1.7890
$\angle Pb-Ti/Zr-Pb$	110.32(2)	110.17(8)	110.17(1)
$\angle Pb-Ti/Zr-O_1$	120.87(7)	120.21(5)	120.21(5)
$\angle Pb-Ti/Zr-O_2$	106.5481(5)	86.9645(6)	94.5397(5)
$\angle Fe-Pb-Fe$	38.3983(9)	58.3862(3)	69.3973(4)
$\angle Zr-O_2-Zr$	101.3501(2)	110.7800(3)	114.5411(4)

7.2.2 Microstructural and elemental analysis

The SEM micrographs of 10000 magnifications are shown in Fig. 7.4 (a-c) for the samples x = 0.05, 0.10, and 0.15 respectively. Only Fe doped samples micrographs have shown because the parent sample has been already discussed in Chapter 6. It was found that the grains of different sizes are uniformly distributed in the samples. The SEM micrographs reveal that the grain size decreases with increase of Fe^{3+} ion concentration. The decrease of both the crystallites and the grain sizes could be due to the size mismatch of Fe^{3+} and Zr^{4+} ions which creates a strain in the lattice.

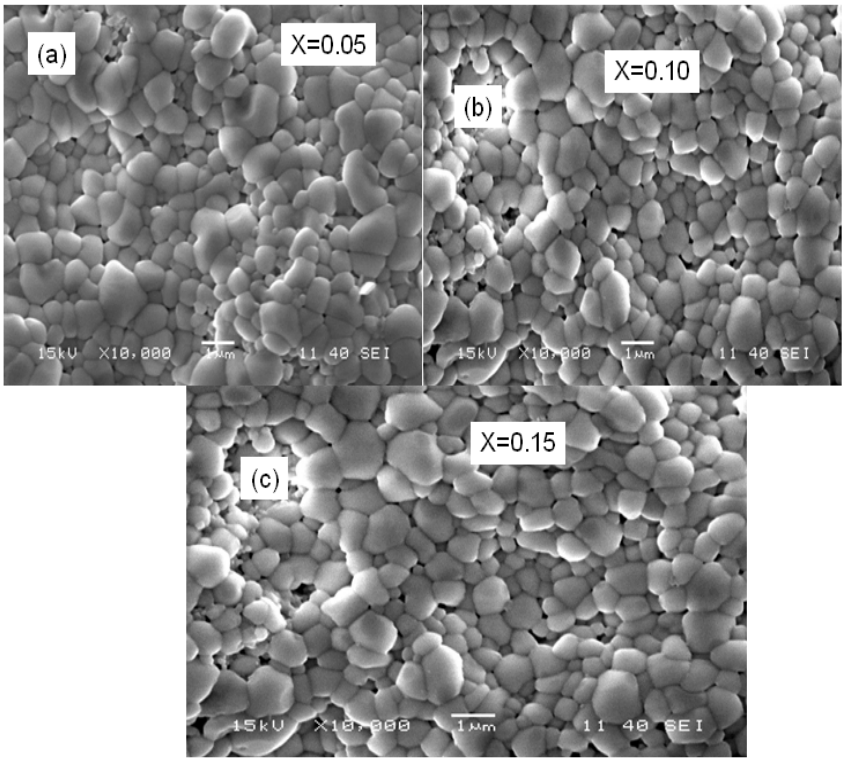

Fig. 7.4 (a-c): Micrographs at 10000 magnifications of $Pb(Zr_{0.65-x}\,Fe_xTi_{0.35})O_3$, for (a) x = 0.05, (b) x = 0.10 and (c) x = 0.15 samples sintered at 1100ºC.

Fig. 7.5 (a-c) shows the energy dispersive X-ray spectroscopy (EDS) for all the samples. The compositions present in the sample areas prepared. Generally Pb evaporates during the high temperature annealing. However, we have taken by adding 5% extra PbO during sintering which is already reported in this type of materials. The experimental EDS weight % and theoretical EDS wt% have been calculated and cited in Table 7.3 for the Fe doped samples.

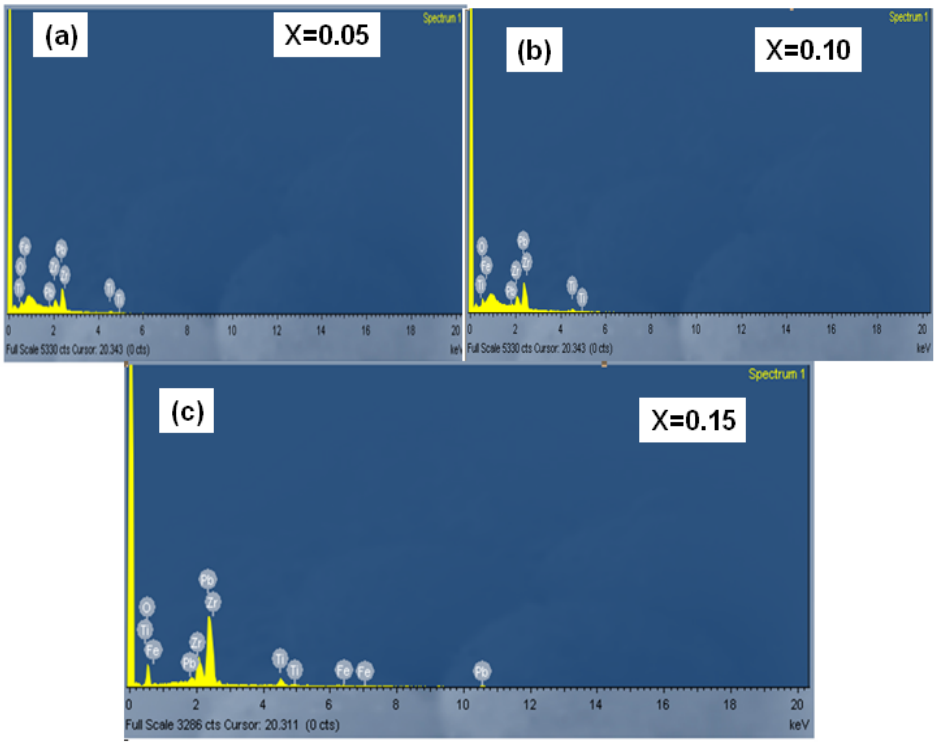

Fig. 7.5 (a-c): EDS of $Pb(Zr_{0.65-x}\ Fe_xTi_{0.35})O_3$ for (a) x = 0.05, (b) x = 0.10, and (d) x = 0.15 samples sintered at 1100ºC.

Table 7.3: Elemental analysis of $Pb(Zr_{0.65-x}\ Fe_xTi_{0.35})O_3$ (PZFT, for x = 0.05, 0.10, and 0.15) ceramic.

Composition	Element	Wt% calculated	Wt% from EDS
x = 0.05	Pb	58.65	58.63
	Zr	19.48	18.99
	Ti	7.34	7.30
	O	12.64	13.15
	Fe	1.88	1.93
x = 0.10	Pb	59.49	59.92
	Zr	18.12	18.38
	Ti	7.45	7.84
	O	12.81	11.70
	Fe	2.12	2.16
x = 0.15	Pb	59.84	59.86
	Zr	16.57	17.04
	Ti	7.49	7.46
	O	12.88	12.37
	Fe	3.21	3.27

7.2.3 Dielectric analysis

Fig. 7.6 (a) shows the variation of dielectric constants with the temperature at 10 kHz for the sample $Pb(Zr_{0.65-x}Fe_xTi_{0.35})O_3$,(x = 0.00, 0.05, 0.10 and 0.15). The dielectric constant increases with temperature to its maximum value and then decreases, which reveals that a phase transition from ferroelectric to paraelectric phase occurs in a particular temperature which is the Curie temperature (T_c). The transition temperature (T_c) and the dielectric constant (ε_{max}) at T_c of the samples are given in Table 7.4. The ε_{max} increases with the Fe^{3+} ion concentration. Fig. 7.6 (b) shows temperature variation of dielectric loss for all the samples. It is observed that the dielectric loss is almost invariant with temperature up to 350ºC and then rises sharply up to 500ºC. The increasing trend in dielectric loss at high temperature may be due to the presence of space charge polarization. Similar behavior has been observed by other research groups in PZT materials [92,135,195,196].

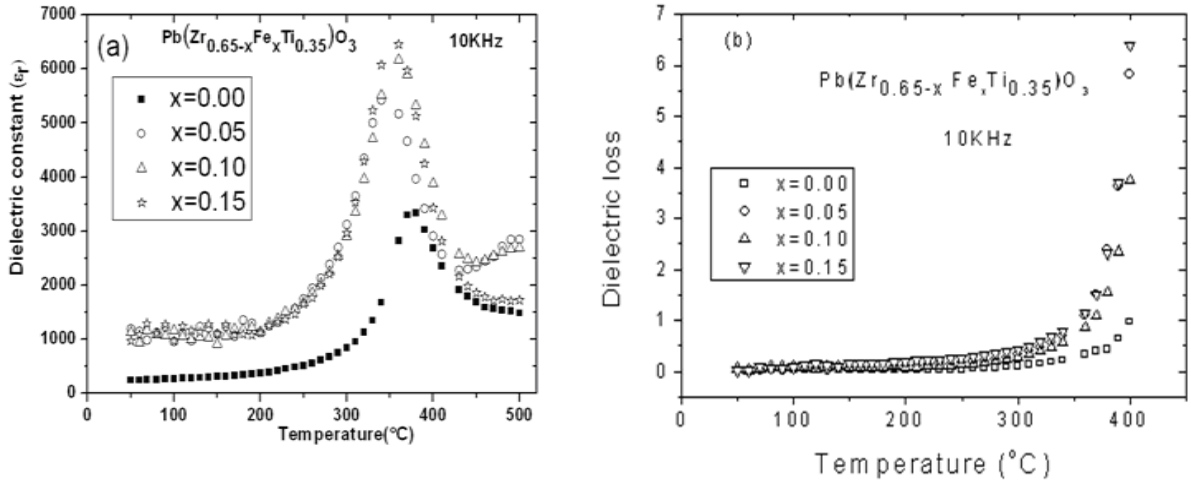

Fig. 7.6 (a, b): Plot of (a) dielectric constant and (b) dielectric loss versus temperature of Pb $(Zr_{0.65-x}Fe_xTi_{0.35})O_3$, (x = 0.00, 0.05, 0.10, and 0.15) ceramics at 10 kHz.

Table 7.4: Dielectric constant (ε_{max}), Curie temperature (T_c) and activation energy (E_a) of $Pb(Zr_{0.65-x}Fe_xTi_{0.35})O_3$, (x = 0.00, 0.05, 0.10, and 0.15) at 10 kHz.

Compositions(x)	ε_{max}	T_c(°C)	E_a(eV)
x = 0.00	3340	376	0.870
x = 0.05	5348	343	0.646
x = 0.10	6127	361	0.421
x = 0.15	6360	357	0.373

The plots of frequency verses dielectric constant and dielectric loss tangent are shown in Fig.7.7 (a) and Fig.7.7 (b) respectively for Pb ($Zr_{0.\ 65-x}$ $Fe_xTi_{0.35}$) O_3, (x = 0. 00, 0.05, 0.10 & 0.15) ceramics. We have observed that the both dielectric constant and loss decreases with the increase in frequency. Similar behavior has been observed by other research groups in PZT ceramics [197]. All types of polarization due to the interfacial, ionic, electronic and space charge are contributed at low frequency. Hence we have observed the high dielectric constant at low frequency. At higher frequencies, the main contribution to dielectric constant comes from electronic polarization, as some of the polarizations become ineffective and thus, the value of dielectric constant decreases. We have observed that, both dielectric constant and dielectric loss increase with increase of Fe^{3+} ions in PZFT compound.

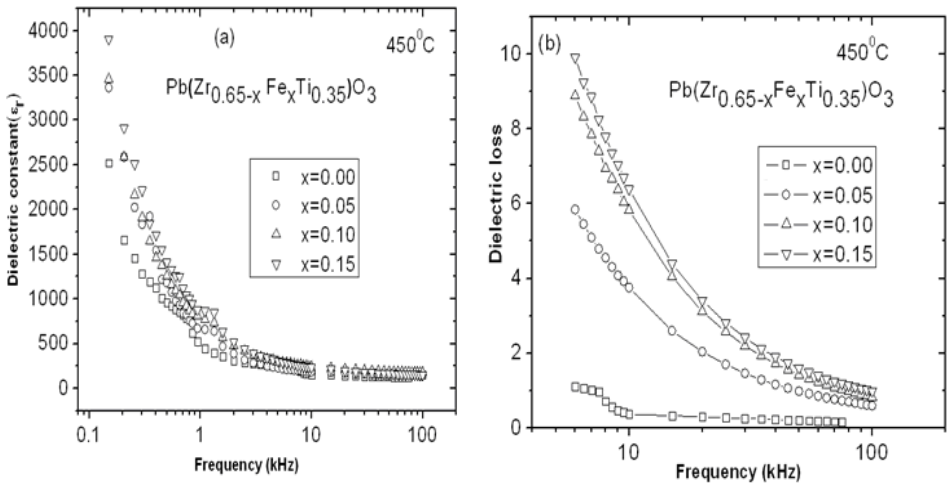

Fig. 7.7 (a, b): Plot of (a) dielectric constant and (b) dielectric loss versus frequency for $Pb(Zr_{0.65-x}$ $Fe_xTi_{0.35})O_3$,(x=0.00, 0.05, 0.10 & 0.15) ceramics at the temperature 450ºC. For the clarity x-axis is shown in logarithmic scale.

7.2.4 Polarization study

Fig. 7.8 (a-c) shows P-E hysteresis loops of Fe^{3+} ion doped PZT ceramic of (a) x = 0.05 (b) x = 0.10 and (c) x = 0.15 at 1100˚C for 4h. The observed values of remnant polarization and coercive field have been cited in Table 7.5. It is found that remnant polarization increases with increase of Fe^{3+} ion concentrations. It could be due to increase of internal polarizability, strain, electromechanical coupling and electro optic activity with increase of Fe^{3+} ions in the material. We

have observed from structural and microstructural analysis crystallite size and grain size decreases with increase of Fe^{3+} ion concentration which causes the increase of coercive field. Hence, it can be concluded that higher the coercive field means lower is the grain size [136].

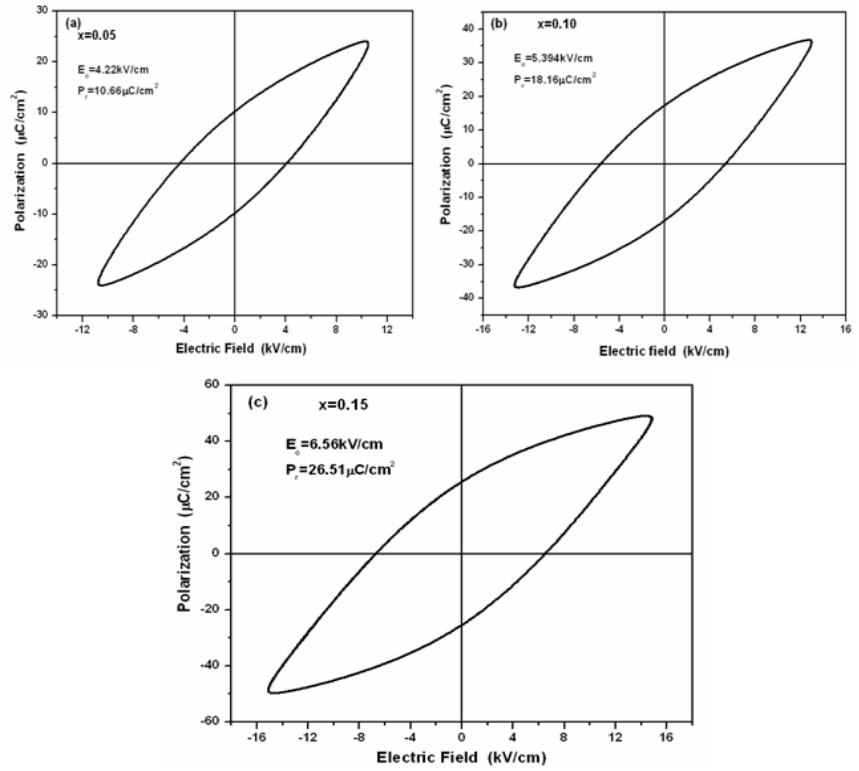

Fig. 7.8 (a-c): P-E hysteresis loops for $Pb(Zr_{0.65-x}\ Fe_xTi_{0.35})O_3$ samples of (a) x = 0.05, (b) x = 0.10, and (c) x = 0.15 at 1100˚C for 4h.

Table 7.5: The estimated values of P_r(C/cm^2) and E_c(kV/cm) of $Pb(Zr_{0.65-x}\ Fe_xTi_{0.35})O_3$ for x= 0.05, 0.10, and 0.15ceramics.

Sample	P_r(C/cm^2)	E_c(kV/cm)
x = 0.05	10.66	4.22
x = 0.10	18.16	5.39
x = 0.15	26.51	6.56

7.2.5 Electrical conductivity studies

7.2.5.1 Impedance analysis

Fig. 7.9 (a-c) and Fig.7.10 (a-c) shows the variation of the real part of impedance (Z′) with frequency at different temperatures (300-500^{0}C) of Fe doped PZT ceramics. It indicates that the real part of impedance (i.e., resistance) decreases with rise in frequency. A decrease in Z′ with rise in frequency indicates a possibility of increase in the ac conductivity with frequency. The merger of the real part of impedance (Z′) in the higher-frequency domain suggests a possible release of space charge and a consequent lowering of the barrier properties of the materials [93].

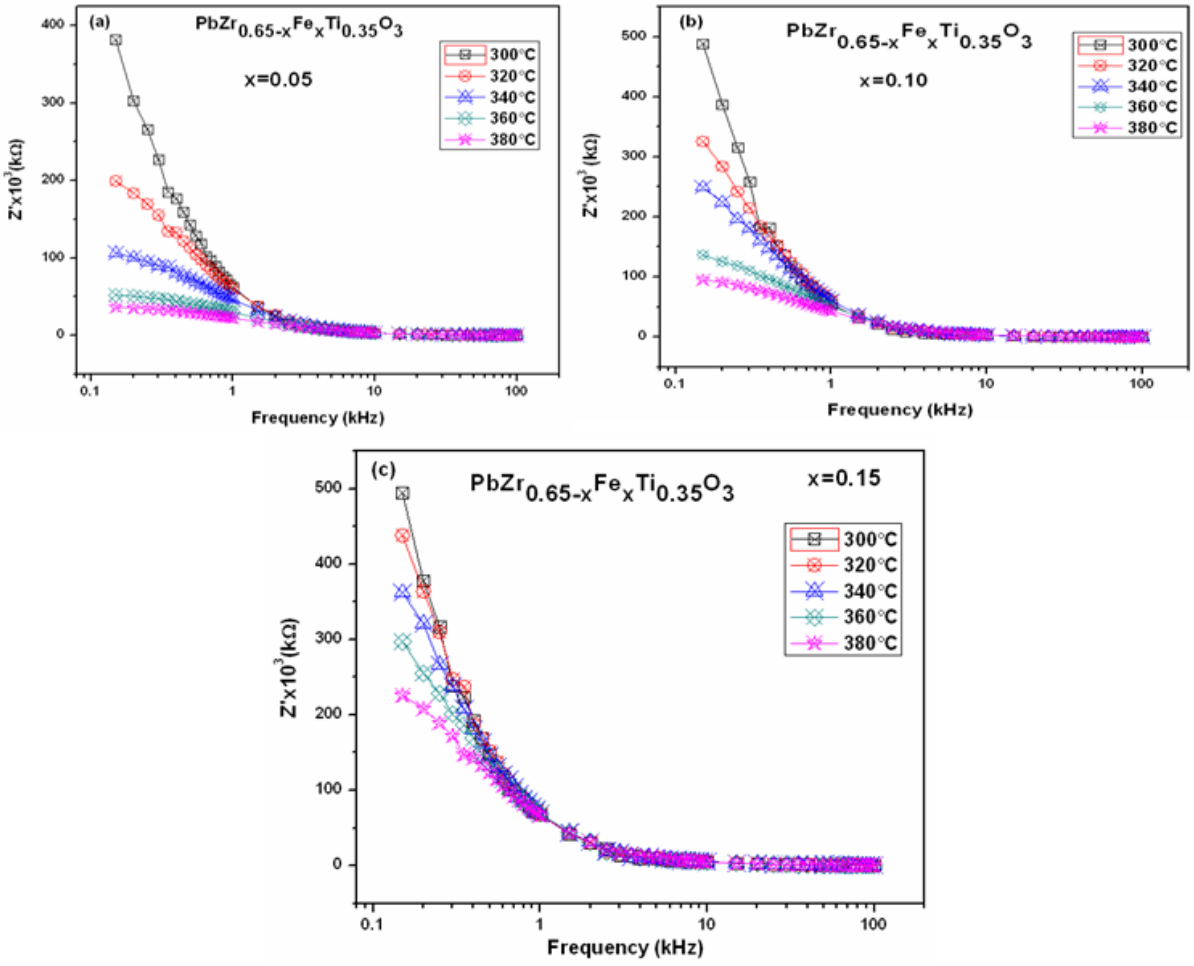

Fig. 7.9 (a-c): Variation of real (Z′) part of impedance with frequency of $Pb(Zr_{0.65-x}Fe_xTi_{0.35})O_3$ for x = 0.05, 0.10, and 0.15 at the temperature range 300˚C-380˚C. For the clarity x-axis has shown in logarithmic scale.

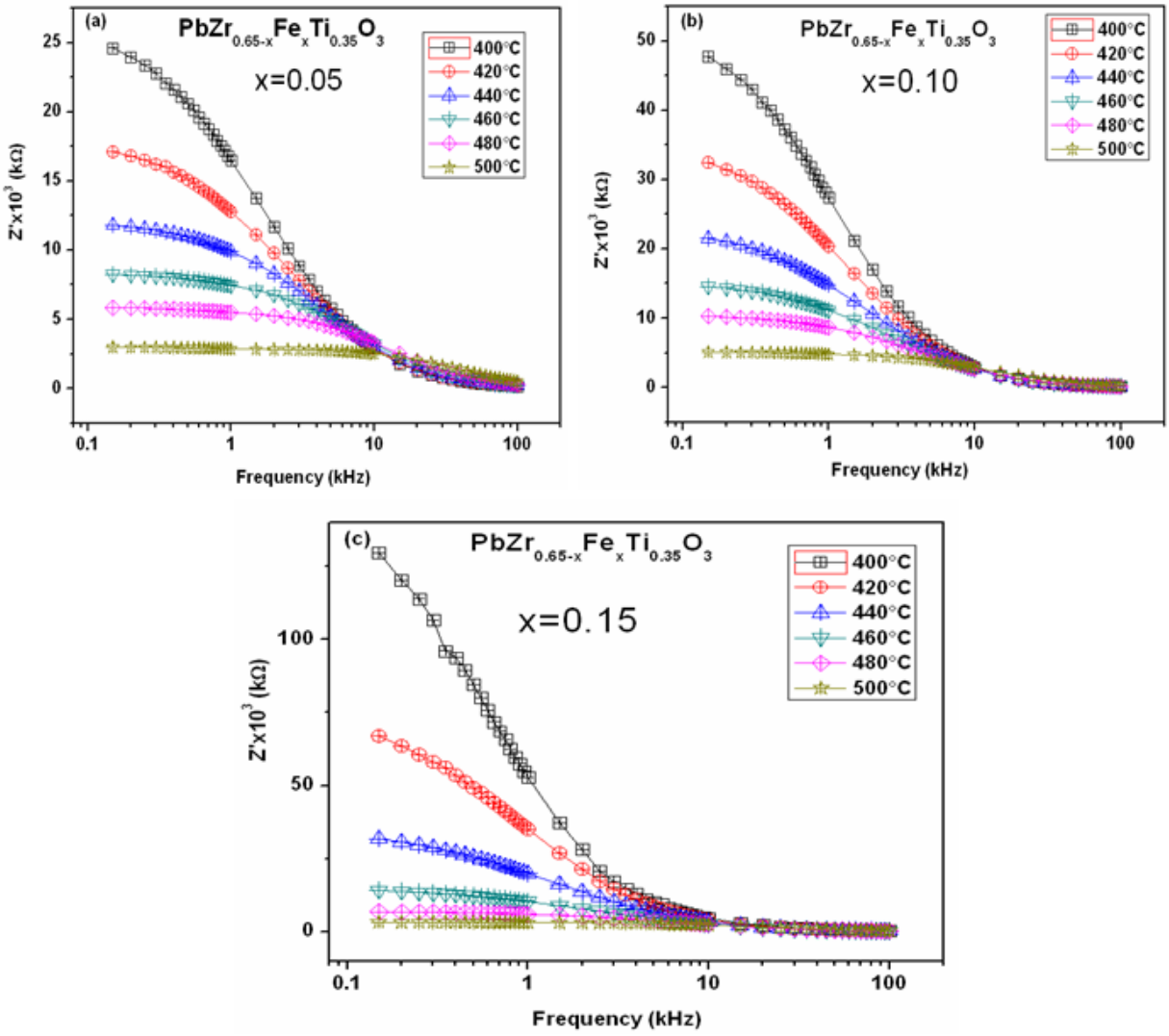

Fig. 7.10 (a-c): Variation of real (Z′) part of impedance with frequency of $Pb(Zr_{0.65-x}\ Fe_xTi_{0.35})O_3$ for x= 0.05, 0.10, and 0.15 at the temperature range 400˚C-500˚C. For the clarity x-axis has shown in logarithmic scale.

Plots of the imaginary part of impedance (Z″) versus frequency are shown in Fig. 7.11 (a-c) and Fig. 7.12 (a-c) at different temperatures. These plots give insight into the electrical processes having the largest resistance in accordance with the equations (3.42) and (3.43) which is discussed in Chapter 3. The nature of variation of Z″ with frequency is characterized by the (i) appearance of peaks at a particular frequency for the Fe^{3+} ion free sample (discussed in chapter 6) and Fe-modified PZT, (ii) a decrease in the height of the peaks with an increase in Fe^{3+} ion concentration of PZFT, (iii) significant broadening of the peaks with an increase in Fe^{3+} ion concentration, (iv) marked asymmetry in the peak pattern and (v) merger of the spectrum at

higher frequencies irrespective of concentration. Broadening of the peaks with change in concentration suggests the presence of concentration dependent relaxation process in the material. Since these observations are made at higher temperatures some relaxation species, such as defects, may be responsible for electrical conduction in the material by hopping of electrons/oxygen ion vacancy/defects among the available localized sites [98]. Further, the magnitude of Z'' decreases and a shift in the peak frequency towards the high frequency side has been observed to increase in Fe^{3+} ion concentration. This type of impedance spectra arises probably due to the presence of space charge in PZFT material. It gives an indication that the electrical process occurring in the material is slowed down initially on Fe substitution due to accumulation of space charge. The observed value of $Log\omega_{max}$ and relaxation (τ) time obtained from the imaginary part of impedance analysis of Fe^{3+} ion doped samples have been capitalized in Table 7.6. The variation of $Log\omega_{max}$ versus inverse of the temperature is presented in Fig. 7.13 (a-d).

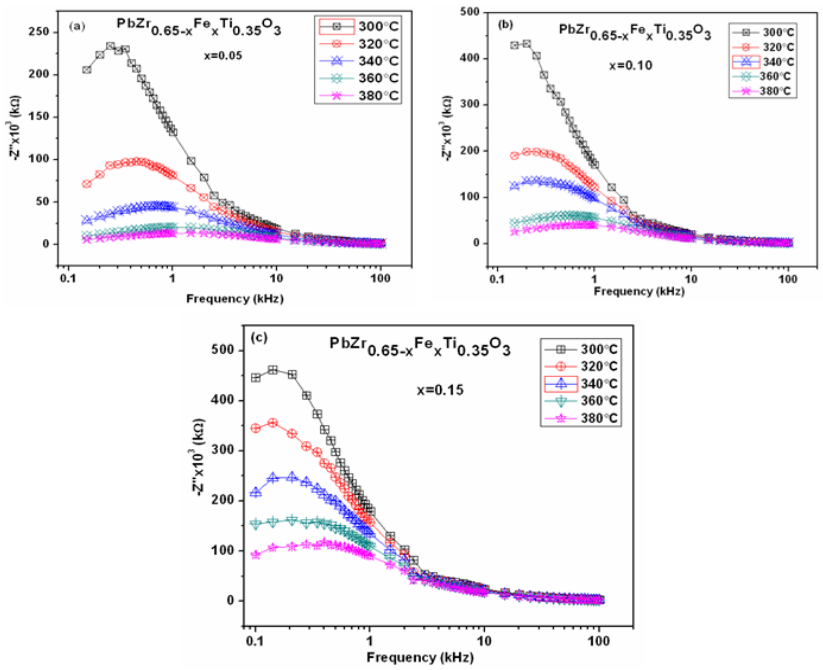

Fig. 7.11 (a-c): Variation of imaginary (Z'') part of impedance with frequency of $Pb(Zr_{0.65-x}Fe_xTi_{0.35})O_3$ for x = 0.05, 0.10 & 0.15 at the temperature range 300°C-380°C. For the clarity x-axis has shown in logarithmic scale.

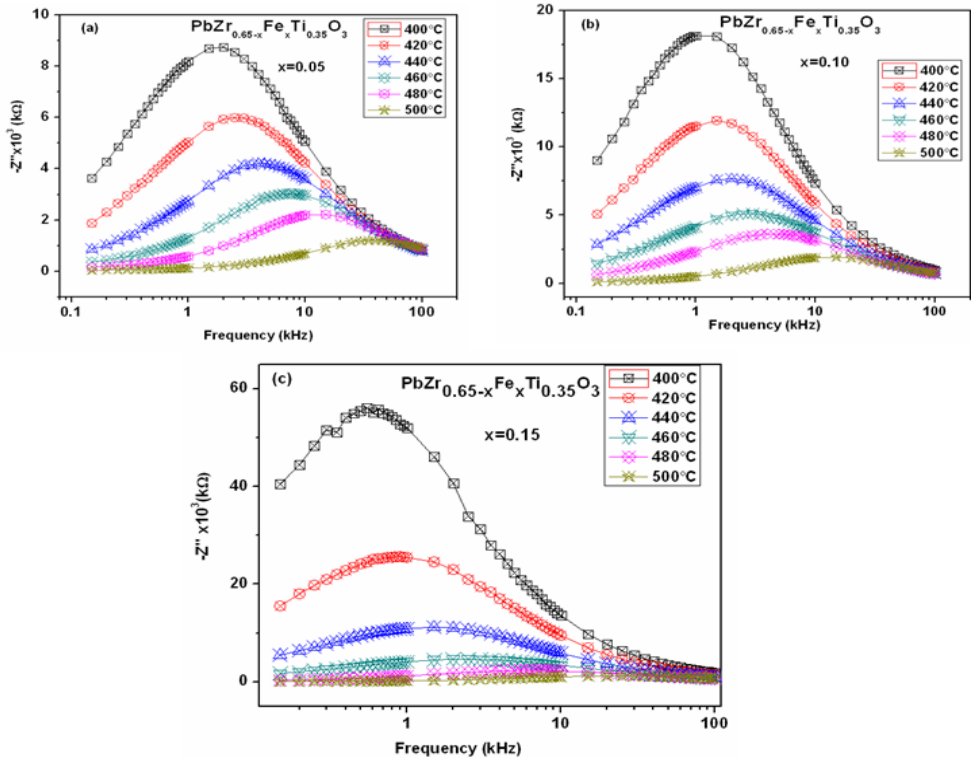

Fig. 7.12 (a-c): Variation of imaginary (Z″) part of impedance with frequency of $Pb(Zr_{0.65-x}Fe_xTi_{0.35})O_3$ for x = 0.05, 0.10 & 0.15 at the temperature range 400˚C-500˚C. For the clarity x-axis has shown in logarithmic scale.

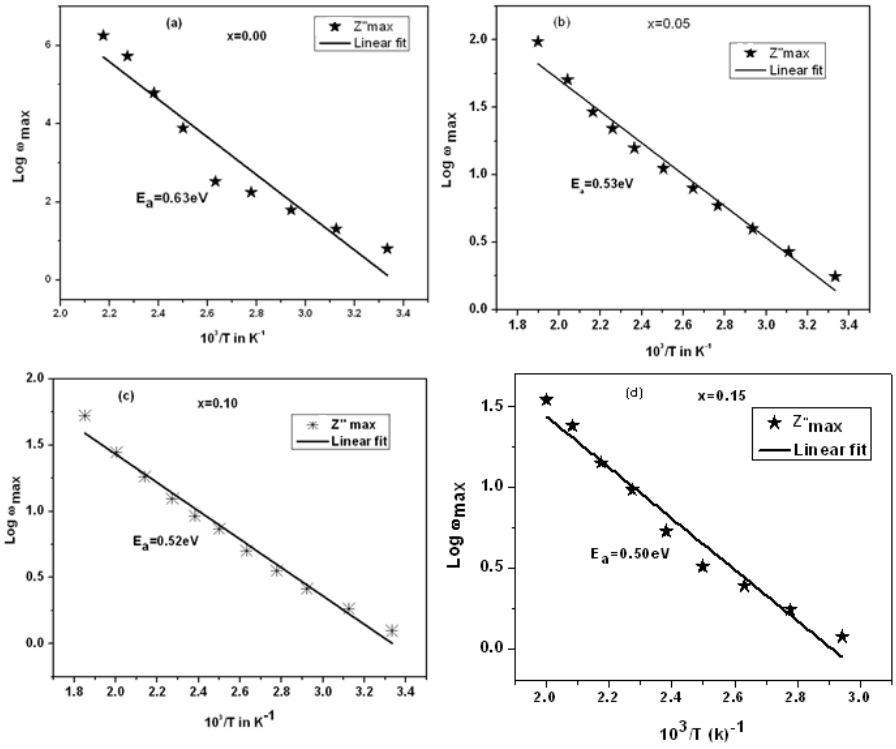

Fig. 7.13: $Log\omega_{max}$ versus the inverse of temperature (obtained from Z″spectra) of $Pb(Zr_{0.65-x}Fe_xTi_{0.35})O_3$ for (a) x = 0. 0, (b) x = 0. 05, (c) x = 0. 10 and (d) x = 0. 15 ceramics.

Table 7.6: The value $Log\omega_{max}$ and τ (rad/s) obtained from the imaginary part of impedance (Z'') with frequency at different temperature measurement of the sample $Pb(Zr_{0.65-x}Fe_xTi_{0.35})O_3$ for x = 0.05, 0.10 and 0.15.

Sample	Temperature (˚C)	Log ω_{max}	τ (rad/s)
x = 0.05	300	0.24758	0.56549
	320	0.43033	0.34278
	340	0.59836	0.23713
	360	0.77049	0.16751
	380	0.90027	0.14376
	400	1.04645	0.08476
	420	1.19809	0.05743
	440	1.3429	0.03784
	460	1.46721	0.02494
	480	1.70492	0.01512
	500	1.98634	0.00602
x = 0.10	300	0.09651	0.80073
	320	0.26571	0.54237
	340	0.41516	0.46545
	360	0.54953	0.28214
	380	0.70048	0.19931
	400	0.86651	0.13599
	420	0.96313	0.10886
	440	1.09597	0.08017
	460	1.26107	0.06599
	480	1.44549	0.03386
	500	1.72213	0.01079
x = 0.15	300	0.16366	1.07557
	320	0.06918	1.04658
	340	0.0741	0.80641
	360	0.2423	0.45901
	380	0.38973	0.41792
	400	0.50913	0.40269
	420	0.72716	0.1937
	440	0.98153	0.09505
	460	1.14973	0.06298
	480	-----	-----
	500	-----	-----

Fig. 7.14 (a-c) and Fig. 7.15 (a-c) shows the Nyquist plot of Fe doped PZT ceramics at higher temperature. From these figures, it has been observed that the high-frequency semicircles depicting the bulk effects. This bulk effect arises due to the parallel combination of bulk resistance (R_g) and bulk capacitance (C_g). The value of R_g (bulk resistance) of the materials was obtained from the intercept of the semicircular arc on the real axis (Z′). In order to analyze the experimental data, it is essential to have a model equivalent circuit that provides a realistic representation of the electrical properties. The equivalent electrical circuits for the materials are shown as inset in Fig. 7.14 (a-c) and Fig. 7.15 (a-c). It is found that the sample does not show any grain boundary and/or ceramic electrolyte electrode interface effect for any Fe concentration in the said experimental conditions. On the basis of the above observations, we can conclude that the equivalent electrical circuits of the materials are parallel combination of R_g (bulk or grain resistance) and C_g (bulk or grain capacitance). Also, it is observed that all the semicircles exhibit some degree of depression, indicating that the center of these semicircles lies below the abscissa axis showing the presence of a non-Debye type of relaxation phenomenon in the material. The calculated grain capacitance (C_g), grain resistance (R_g) and apparent bulk conductivity (σ_b) are listed in Table 7.7.

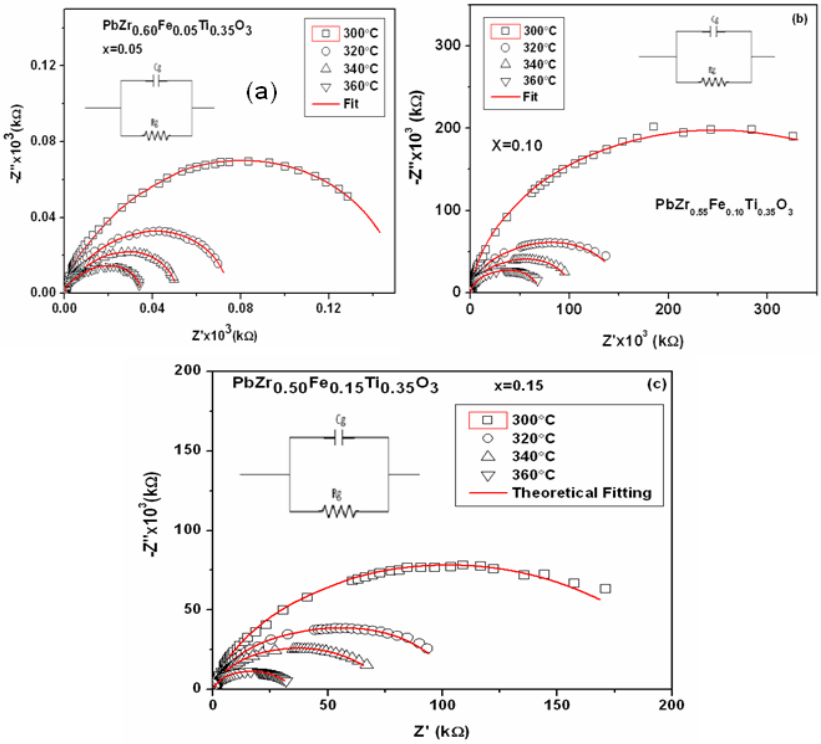

Fig. 7.14 (a–c) (300˚C-360˚C): Nyquist plot of PZFT compounds at different temperature (300-360^{0}C).

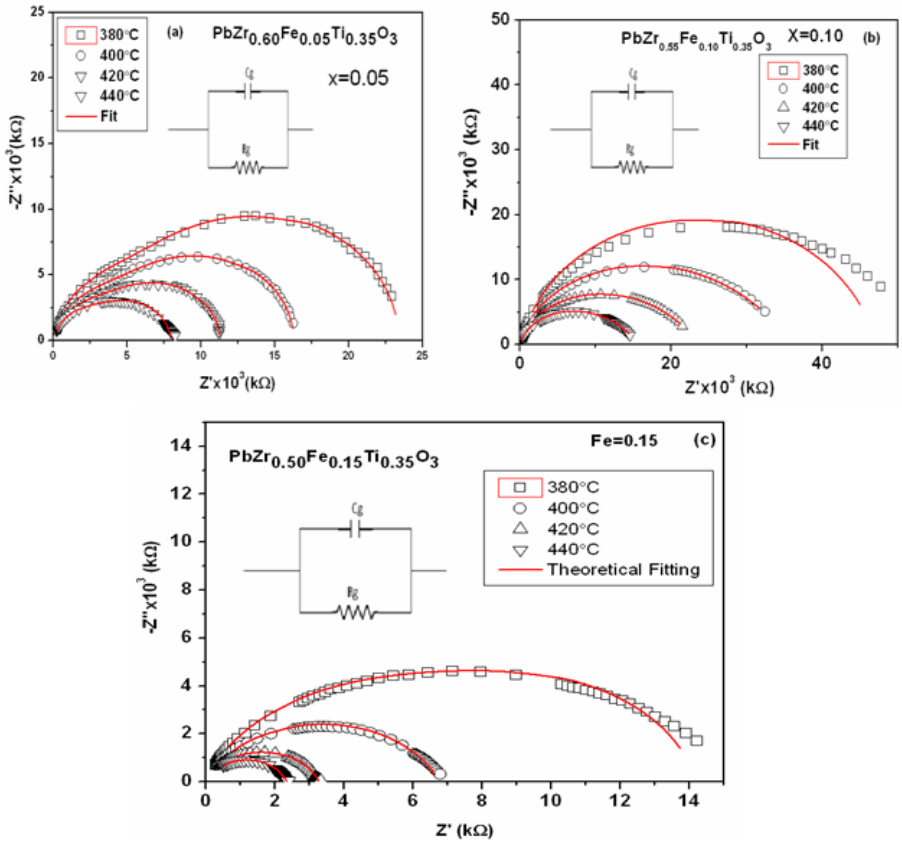

Fig. 7.15 (a-c) (380˚C-440˚C): Nyquist plot of PZFT compounds at different temperature (380-440^{0}C).

Table 7.7: Grain capacitance (C_g), grain resistance (R_g) and apparent bulk conductivity (σ_b) of PZFT samples at different temperatures.

Sample	Temperature ^oC	C_g nF	R_g kΩ	$\sigma_b = t/R_gA$ $(\Omega m)^{-1}$
x = 0.05	300	1.446	$6.05x10^5$	$3.09x10^{-7}$
	320	1.349	$3.34x10^4$	$5.584x10^{-6}$
	340	1.261	$2.35x10^4$	$7.94x10^{-6}$
	360	1.210	$1.61x10^4$	$1.15x10^{-5}$
	380	0.666	$1.57x10^4$	$1.06x10^{-5}$
	400	0.664	$1.16x10^4$	$1.60x10^{-5}$
	420	0.583	$7.59x10^3$	$2.45x10^{-5}$
	440	0.554	$3.01x10^3$	$6.20x10^{-5}$
x = 0.10	300	1.170	$3.86x10^5$	$4.86x10^{-7}$
	320	2.137	$1.37x10^5$	$1.52x10^{-6}$
	340	2.361	$1.34x10^5$	$1.36x10^{-4}$
	360	3.360	$5.50x10^4$	$0.92x10^{-4}$
	380	4.202	$3.71x10^4$	$5.05x10^{-4}$
	400	5.391	$2.42x10^4$	$7.73x10^{-3}$
	420	6.154	$4.86x10^3$	$3.86x10^{-2}$
	440	8.354	$9.89x10^2$	$1.86x10^{-2}$
x = 0.15	300	1.592	$1.60x10^5$	$0.11x10^{-5}$
	320	1.814	$1.16x10^4$	$0.16x10^{-4}$
	340	1.985	$1.00x10^4$	$0.18x10^{-4}$
	360	2.510	$6.36x10^3$	$0.29x10^{-3}$
	380	3.031	$3.68x10^3$	$0.50x10^{-3}$
	400	5.391	$3.16x10^3$	$0.32x10^{-2}$
	420	2.135	$1.49x10^3$	$0.12x10^{-2}$
	440	3.324	$2.85x10^2$	$0.65x10^{-2}$

7.2.5.2 AC and DC conductivity analysis

Fig. 7.16 shows the frequency variation of the AC conductivity of a typical sample PZFT5 (x = 0.05). The AC conductivity data are fitted to the Jonscher's equation [165] and the fitting parameters *A* and *n* at various temperatures of a typical sample (PZFT5) (x = 0.05) is given in Table 7.8. The frequency exponent n is found to decrease with increase in temperature. The Fig. 7.17 shows the DC conductivity versus inverse of the temperature of $Pb(Zr_{0.65-x}Fe_xTi_{0.35})O_3$ for x = 0.0, 0.05, 0.10 and 0.15 which obeys Arrhenius behavior. The activation energy was found to be

decreased with increase of Fe concentration. Electrical conduction in dielectrics is due to the ordered motion of loosely bound charge particles due to the influence of an electric field. The bulk conductivity of the compounds at higher temperature can be evaluated from impedance data using the relation; $\sigma_{dc} = t/R_bA$, where R_b is the bulk resistance, t is the thickness and A is the area of the electrode deposited on the sample. The value of bulk resistance (R_b) is obtained from the low- frequency intercept of the semicircle on the real axis (Z′) in the complex impedance plot. This shows that the above compounds have a negative temperature coefficient of resistance at higher temperatures which matches well with the Cole–Cole plot.

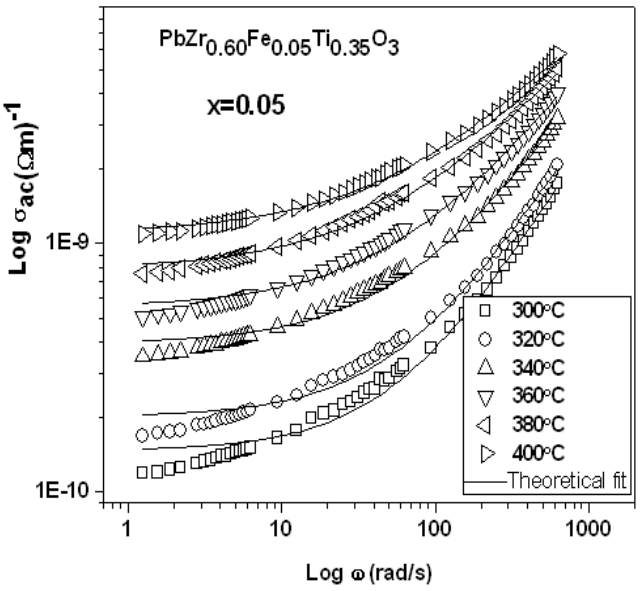

Fig. 7.16: Variation of AC conductivity of the sample $Pb(Zr_{0.65-x}Fe_xTi_{0.35})O_3$ (x = 0.05) with frequency at different temperatures.

Table 7.8: Fitting parameters of AC conductivity from Jonscher's universal law of $Pb(Zr_{0.65-x}Fe_xTi_{0.35})O_3$ (x = 0.05) ceramic.

Temperature(˚C)	A	n
300	1.46×10^{-7}	0.997
320	2.04×10^{-7}	0.988
340	3.95×10^{-7}	0.890
360	5.54×10^{-7}	0.820
380	7.84×10^{-7}	0.743
400	1.09×10^{-6}	0.703

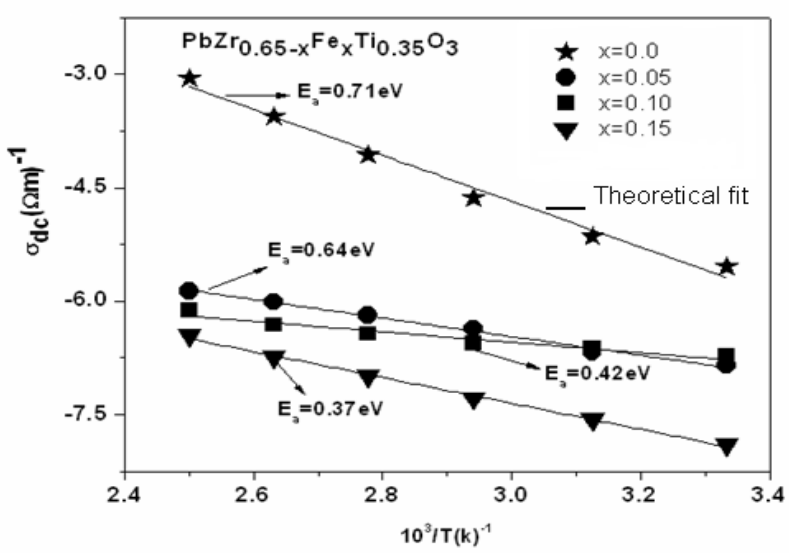

Fig. 7.17: Variation of DC conductivity with inverse of temperature of $Pb(Zr_{0.65-x}Fe_xTi_{0.35})O_3$ for x = 0.0, 0.05, 0.10, 0.15 compounds.

7.2.5.3 Modulus spectroscopy analysis

Fig.7.18 (a-d) shows the variation of M″ with frequency over a wide range of temperature. The appearance of peak in the spectrum and changes its position with temperature confirms the presence of temperature dependent relaxation is in good agreement with the complex impedance spectroscopy (CIS) results. However, the relaxation peak vanishes at elevated temperatures on Fe substitution. The peaks undergo a systematic shift towards higher frequency with increase in temperature. The results definitely suggest non-Debye type of relaxation in the materials. It is known that at the maxima the equation $\tau = \frac{1}{\omega_{max}} = \frac{1}{2\pi f_r}$ holds well [181]. The variation log ω_{max} with the inverse of the temperature is presented in Fig. 7.19. The value Logω_{max} and τ (rad/s) obtained from the variation of the imaginary part of the modulus (M″) with frequency at different temperatures of the sample of Pb $(Zr_{0.65-x}Fe_xTi_{0.35})O_3$, x = 0. 0, 0.05, 0.10 and 0.15 is cited in Table 7.9. The activation energy evaluated from the slope of log ω_{max} versus $10^3/T$ (from Fig. 7.19) using the Arrhenius equation as discussed in previous chapters and the corresponding values are given in Table 7.10. The value of activation energy found to be comparable to those evaluated from the impedance data.

The complex electric modulus spectrum (M′ vs. M″ which is well known Cole-Cole plot) of the samples is shown in Fig. 7.20 (a–d). The modulus spectrum has a typical semicircular pattern with their center lying below the real axis (unlike the ideal Debye type response). This is evident from the shape of the deformed arcs with their centers positioned below the x-axis. Asymmetrical semicircular arc indicates that the non-Debye type relaxation phenomenon exist in the material. The comparison of activation energy obtained from conductivity, relaxation time, the imaginary part of impedance and modulus are enlisted in Table 7.10.

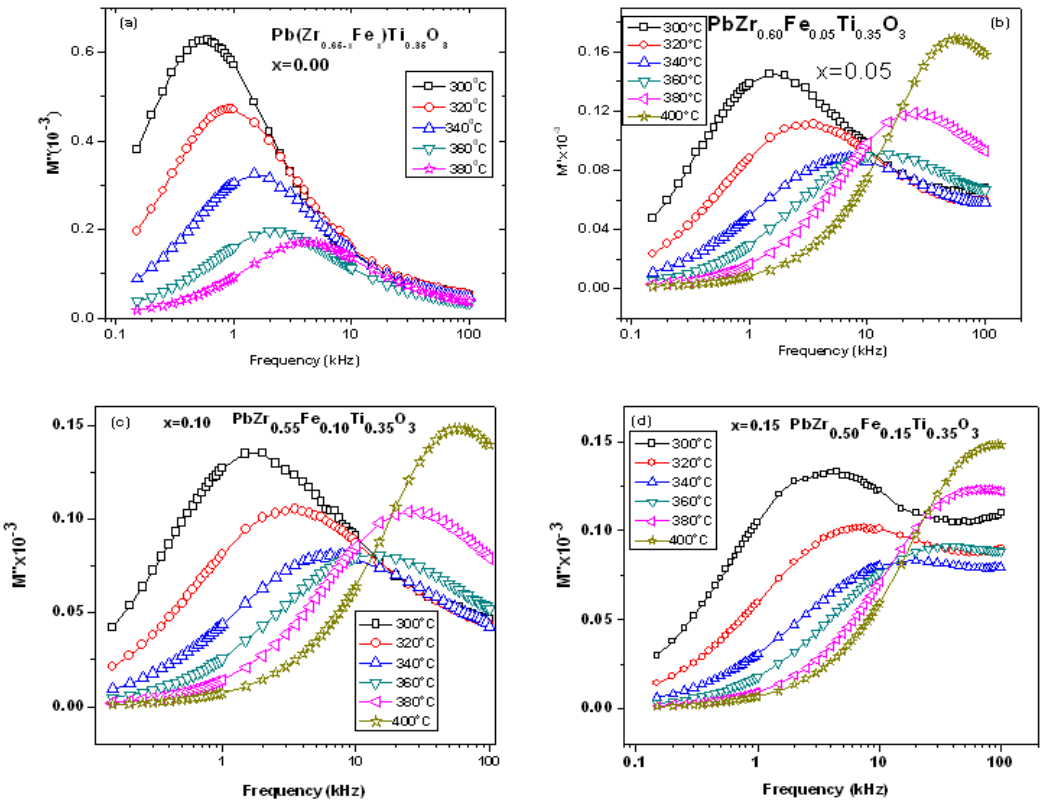

Fig.7.18 (a-d): Variation of imaginary (M″) part of modulus with frequency of Pb ($Zr_{0.\ 65-x}$ $Fe_xTi_{0.35}$) O_3 for x = 0. 0, 0.05, 0.10 & 0.15 at the temperature range 300˚C-400˚C.

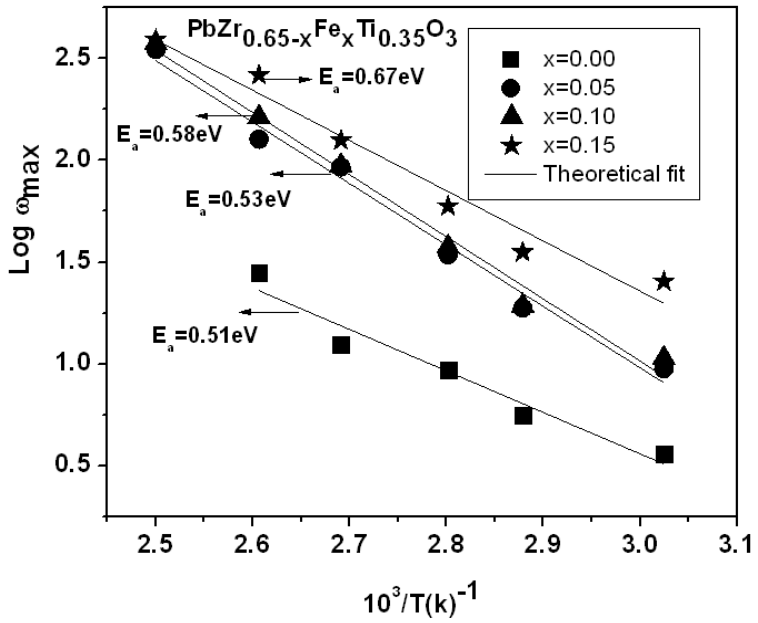

Fig. 7.19: Variation of Log ω_{max} (obtained from M''_{max} spectra) versus inverse of temperature of $Pb(Zr_{0.65-x}Fe_xTi_{0.35})O_3$ for x = 0.0, 0.05, 0.10, 0.15 samples.

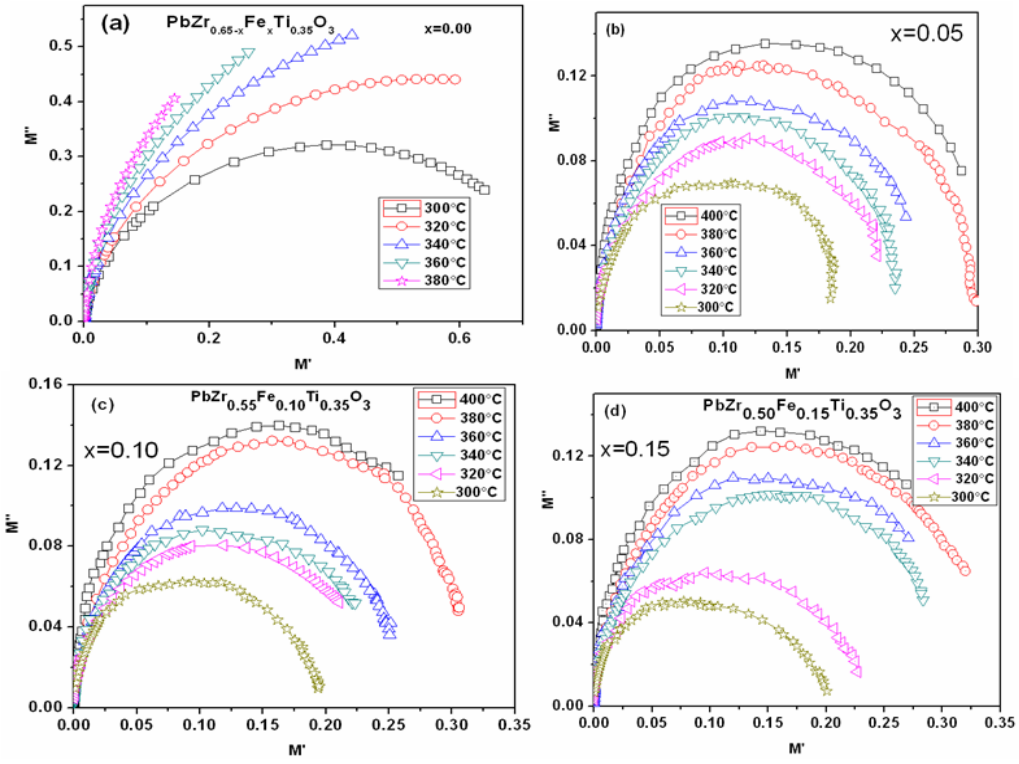

Fig.7.20 (a-d): Variation of real and imaginary part of modulus spectrum with temperature of $Pb(Zr_{0.65-x}Fe_xTi_{0.35})O_3$ for x = 0.0, 0.05, 0.10, 0.15 samples.

Table 7.9: The value $Log\omega_{max}$ and τ (rad/s) obtained from the variation of the imaginary part of the modulus (M'') with frequency at different temperatures of the sample of $Pb(Zr_{0.65-x}Fe_xTi_{0.35})O_3$ for x = 0. 0, 0.05, 0.10, and 0.15.

Sample	Temperature (˚C)	Log ω_{max}	τ (rad/s)
x = 0.00	300	0.5586	0.27631
	320	0.7487	0.17834
	340	0.9706	0.10699
	360	1.0959	0.08017
	380	1.4477	0.03567
	400	----	-----
x = 0.05	300	0.97673	0.1055
	320	1.2741	0.0532
	340	1.53677	0.02906
	360	1.96698	0.01079
	380	2.10435	0.00786
	400	2.54513	0.00285
x = 0.10	300	1.02829	0.09369
	320	1.28685	0.05166
	340	1.57605	0.02654
	360	1.97587	0.01057
	380	2.2131	0.00612
	400	2.57694	0.00265
x = 0.15	300	1.40543	0.03932
	320	1.54885	0.02826
	340	1.77527	0.01678
	360	2.09831	0.00797
	380	2.41984	0.0038
	400	2.59344	0.00255

Table 7.10: Comparison of E_a in eV obtained from (i) σ_{dc}, (ii) relaxation time (τ), (iii) Z''_{max} and (iv) M''_{max} of PZFT ceramic.

Sample	$E_a(\sigma_{dc})$	$E_a(\tau)$	$E_a(Z'')$	$E_a(M'')$
x = 0.00	0.71	0.69	0.63	0.67
x = 0.05	0.64	0.61	0.53	0.52
x = 0.10	0.42	0.47	0.52	0.53
x = 0.15	0.37	0.39	0.51	0.51

7.3 Summary

Fe^{3+} ion modified $PbZr_{0.65}Ti_{0.35}O_3$ compounds have been prepared by using the solid state reaction method. The dielectric constant increases with temperature to its maximum value and then decreases, which reveals that a phase transition from ferroelectric to paraelectric phase occurs in a particular temperature which is the Curie temperature (T_c). It is found that remnant polarization increases with increase of Fe^{3+} ion concentration which is an indication to the high internal polarizability, strain, electromechanical coupling and electro optic activity in the material. The structure remains unchanged with the substitution of Fe^{3+} ion at the Zr site of PZT samples. Activation energy decreases with the Fe^{3+} ion concentration which causes the increase of conductivity. The activation energies calculated from the temperature dependence of conductivity pattern and the relaxation time variation pattern is almost same. This indicates that the conductivity and relaxation species are identical and thermally activated process. The increase in AC conductivity with frequency exhibits an existence of the inhomogeneities in the materials, and hence a simple hopping model provides a qualitative picture of the conduction process. Impedance studies indicate a negative temperature coefficient of resistance and temperature dependence of relaxation phenomena in the materials. The modulus analysis indicates the possibility of hopping mechanism for electrical transport processes in the PZFT ceramics.

CHAPTER 8

CONCLUSIONS AND FUTURE WORK

CHAPTER 8

CONCLUSIONS AND FUTURE WORK

The present thesis work mainly deals with structural, dielectric and electrical studies of lead titanate and lead zirconate titanate with different substitutions. For the present study all the samples were prepared in single phase by solid - state reaction technique. Different experiments were carried out and the results were careful analyzed to monitor the changes in the structure and electrical properties of the influence of different substitutions in the lead titanate and lead zirconate titanate on both A and B-site respectively. This chapter presents conclusions and future work based on the results and discussions presented in the previous chapters on lead titanate and lead zirconate titanate based electroceramics.

8.1 Conclusions

The significant findings of this work are as follows:

The composition $Pb_{1-x}La_xTiO_3$ (x = 0.0, 0.10, 0.25, 0.30, 0.50) ceramics was prepared in the single phase form. The X-ray diffraction pattern reveals that the materials crystallize to pure perovskite phase. The Rietveld refinement of XRD data confirms that La goes into the lattice site. A structural phase transition (tetragonal to cubic) has been observed with the doping of La concentration on A-site of the compound. Crystallite size decrease and grain size increases with increase of La concentration. It is observed that at low temperature ferroelectric to high temperature paraelectric phase transition has been occurring in the materials. Ferroelectric property diffuses with high La concentrations. Remnant polarization increases with the increase of La concentration, which reveals that the material becomes softer. The composition of La 30% and 50% shows highest remnant polarization (27.50μC/cm^2, 35.56μC/cm^2) and lowest coercive field (1.87 kV/cm, 1.81 kV/cm) which can be exploited for memory applications. The conductivity (both AC and bulk) increases and activation energy decreases with increase of La concentration. In spite of this relaxation time is also found to decrease with increase of La concentration. It is confirmed that the conduction is

temperature dependent and thermally activated process which is existing in the material. It is found that a non-Debye type of relaxation behavior is studied in the material. From the Nyquist plot analysis the grain resistance decreases with an increase in temperature which shows negative temperature coefficient of resistance (NTCR) of the material. The comparison of activation energy reveals that the conduction La modified PT is mainly due to the single ionized oxygen defects. Finally La^{3+} ion can take part in conduction, thermally activated and relaxation process.

The compound has a general formula $Pb_{0.70}La_{0.30}Ti_{1-x}A_xO_3$ (A = Al & Mn) (x = 0.0, 0.05, 0.10, 0.15, 0.20) could synthesize in single phase form by ceramic route. No structural change has been found for both the substitution of B-site of the materials. The detailed crystal structure was analyzed by employing Rietveld refinement method and it is observed that lattice parameters and cell volume decreases with an increase of Mn/Al concentrations. The structure and lattice dynamics of PLMT/PLAT compounds were systematically investigated by the Rietveld XRD method. Grain size decreases with an increase of Mn/Al concentrations. From electrical studies it is found that the non-Debye type relaxation phenomenon exists and has been used to establish a relation between microstructure and electrical properties of both the substitution of the materials. For Mn substitutions both grain and grain boundary effects have been observed. However, in Al substitution only grain properties have been observed. The reduction of grain and grain boundary resistances (Rg and Rgb) of the materials with increase in temperature shows the negative temperature co-efficient of resistance (NTCR) which is the property of a conventional semiconductor. So, the result indicates a typical semiconducting behavior of the materials. The nearly same activation energy obtained from both the spectra (Z″ spectra and M″ spectra) for both the substitutions suggest that the nature of species is taking part in both localized and non-localized conduction is similar. Activation energy decreases with an increase in Mn/Al concentration. This change in behavior indicates the participation of Mn/Al ions in the conduction, thermally activated and relaxation process.

The compositions of $Pb(Zr_{0.65-x}A_xTi_{0.35})O_3$, (A= Mn & Fe and x = 0.00, 0.05, 0.10, 0.15) have been prepared in the single phase form by solid state reaction route at high temperature. The X-ray diffraction patterns have been analyzed by employing the Rietveld refinement method with *R3c* symmetry. Lattice parameters, cell volume and grain size have decreased with increase of Mn/Fe concentration of the materials. By using the lattice parameter, space group and atomic number of the atoms in the Powder cell program, bond lengths, bond angles and Wyckoff position of the atom was determined. Using the refined parameters a stable crystal structure is suggested for the materials. Low temperature ferroelectric to high temperature paraelectric phase transition has been observed for the present materials. It is found that remnant polarization increases with increase of Mn/Fe concentration which is an indication to the high internal polarizability, strain, electromechanical coupling and electro optic activity in the material. The material becomes softened and fit for memory application in electronic industry. The activation energies calculated from the temperature dependence of conductive pattern and the relaxation time variation pattern is almost same. This indicates that the conductivity and relaxation species are identical. The increase in AC conductivity with frequency exhibits an existence of the inhomogeneities in the materials, and hence a simple hopping model provides a qualitative picture of the conduction process. The AC conductivity obeys Jonscher's universal power low. Impedance studies indicate a negative temperature coefficient of resistance and temperature dependence of relaxation phenomena (non-Debye type) in the materials. Modulus analysis indicates the possibility of hopping mechanism for electrical transport processes in the PZMT/PZFT compounds. In PZFT material, due to the existence of different oxidation states of Fe^{3+} ions, there may be occurrences of the large number of oxygen ion vacancies in the sample, which is responsible for dipole moment and possibly contribute to DC conduction. The plot of DC conductivity and inverse of temperature obey Arrhenius behavior.

8.2 Scope of the future work

The scopes of the future works are proposed as:

1. To provide further, an in depth analysis of the structure and microstructure of the compounds. The temperature variation of X-ray diffraction study to observe the changes in the crystal structure, transmission electron microscopy (TEM) study to understand the domain wall motion and High Resolution (HRTEM) to observe the degree of order, X-ray Photoelectron Spectroscopy (XPS) for compositional analysis.

2. For the application point of view, piezoelectric and pyroelectric measurements should be carried out. Research can be further extended to enhance the piezoelectricity in the system by suitable cation substitution.

4. Thin film and single crystal can be prepared to explore the technological applications of the present thesis materials.

5. With the advent of nanotechnology, a tremendous surge in research on miniaturization and high efficiency electronic devices is on rise. These modern devices exclusively need soft ferroelectric materials doping with magnetic materials are extensively used in multiferroic applications in electronic industry which form a basic requirement in high technology areas. So, one can prepare these materials in nanostructure to study its crystal structure and physical properties.

6. Simulation work can be carried out to understand the experimental findings in the present thesis works.

References

[1] J. Valasek, "Piezoelectric and allied phenomena in Rochelle salt", *Phys. Rev*.**17** (1921) 475.

[2] G. H. Haertling, *J. Am. Ceram. Soc*. **82** (1999) 797.

[3] M. Deri, Ferroelectric Ceramics (Gordon and Breach, New York, 1969).

[4] M. E. Lines and A. M. Glass, Principles and Applications of Ferroelectric and Related Materials (Clarendon Press, Oxford, 1977).

[5] H. D. Megaw, Ferroelectricity in Crystals (Methuen, London, 1957).

[6] Y. Xu, Ferroelectric Materials and their Applications (North Holland, Amsterdam, 1991).

[7] G. Shirane, R. Pepinsky, B. Frazer, *Acta Cryst*. **9** (1956) 131.

[8] K.K. Deb, *Ferroelectrics,* **82** (1998) 45.

[9] K.S. Knight, *Solid. Stat. Ion*, **74** (1994)109.

[10] J. H. Yang, W. K .Choo, J. H. Lee, C. H. Lee, Acta *Cryst. B*, **55** (1999) 348.

[11] A. Okazaki, Y. Suemune, *J. Phys. Soc. Jpn,* **16** (1961) 176.

[12] D. L. Corker, A. M. Glazer, J. Dec, K. Roleder, R. W. Whatmore, *Acta Cryst. B*, **53** (1997) 135.

[13] A. M.Glazer, *Acta Cryst. B*, **28** (1972) 3384.

[14] A.J. Moulson, J. M.Herbert, "Electroceramics", Chapman and Hall Ltd, (1990) London.

[15] K. Ishikawa, T. Uemori, *Phys. Rev. B*, **60** (1999) 11841.

[16] R. E. Nettleton, *Ferroelectrics*, 1, 3, 87, 93, 111, 121,127, 207, 221 (1970)

[17] R. E. Nettleton, *Ferroelectrics*, 2, 5, 77, 93 (1971)

[18] S. Neirman, *J. of Mater. Sci*, **23** (1988) 3973.

[19] D. Hennings, A. Schnell, G. Simon, *J. Am. Ceram. Soc*. **65** (1982) 539.

[20] W. Kanzig, "Ferroelectrics and Antiferroelectrics", Academic Press, (1957) New York.

[21] R. Ramesh, D. G. Schlom, *Science* **296** (2002) 1975.

[22] V. S. Tiwari, D. Pandey, *J.Am Ceram. Soc.II*, **77** (1994) 1819.

[23] V. V. Kirillov, V. A. Isupov, "*Ferroelectrics*, **5** (1973) 3.

[24] K. M. Rittenmyer, R. Y. Ting, *Ferroelectrics*, **171** (1990)110.

[25] J. F. Scott, L. Kammerdiner, M. Paris, S. Traynor, V. Ottenbacher, A. Shawabkeh, W. F. Oliver, *J. Appl. Phys*, **64** (1988) 787.

[26] A. von. Hippel*, Rev. Modern Phys*, **22** (1950) 221.

[27] S. G. Porter, *Ferroelectrics*, **33** (1981) 193.

[28] R. C. Buchanan, ed, *Ceramic Materials for Electronics - Processing, Properties and Applications* (Marcel Dekker, New York, 1986).

[29] J. M. Herbert, *Ferroelectric Transducers and Sensors* (Gordon and Breach, London, 1982).

[30] A. Ya. Dantsiger, O.N. Razumovskaya, L. A. Rezni- chenko, et al, *in High-Efficiency Piezoceramic Materials*: A Reference Book (Kniga, Rostov-on-Don, 1994).

[31] J. Fritesberg, "Proc. 4th Int. Meeting on Ferroelectricity", Leningrad (1977).

[32] G.H. Haertling, C.E. Land, *J. Am. Ceram. Soc*. **54** (1) (1971) 1.

[33] C.E. Land, P.P. Thacher, Proc. IEEE **57** (1969) 751.

[34] J. S. Wright, L. F. Francis, *J. Maker. Res.* **8** (1993) 1712.

[35] T. Ohno, D. Suzuki, K. Ishikawa, H. Suzuki, Adv. Powd. Tech, **18** (2007) 579.

[36] K. Iijima, Y. Tomita, R. Takayama, I. Veda, *J. Appl. Phys*. **60** (1986) 361.

[37] D. Bersani, P. P. Lottici, A. Montenero, S. Pigoni, *Mater. Sci*. **31** (1996) 3153.

[38] J. F. Scott, C. A. Araujo, *Science* **246** (1989) 1400.

[39] S. K. Dey, R. Zuleeg, *Ferroelectrics,* **112** (1990) 309.

[40] R. Takayama, Y. Tomita, K. Iijima, I. Ueda, *J. Appl. Phys*. **63** (1988) 5868.

[41] W.P. Robbins, *Integr. Ferroelectrics,* **11** (1995) 179.

[42] S. J. Lee, K.Y. Kang, S. K. Han, M. S. Jang, B. G. Chae, Y. S. Yang, S. H. Kim, *Appl. Phys. Lett.* **72** (1998) 299.

[43] M. Ishida, H. Matsurami, T. Tanaka, *Appl. Phys. Lett*. **31** (1977) 433.

[44] C. H. Ahn, J. M. Triscone, J. Mannhart, *Nature* **424** (2003) 1015.

[45] K. Dorr, *J. Phys. D Appl. Phys*. (Berlin) **39** (2006) R125.

[46] H. Adachi, T. Mitsuyo, O. Yanazaki, K. Wasa, *J. Appl. Phys*. **60** (1986) 736.

[47] H. Mike, Y. Ohji, Jpn. *J. Appl. Phys*. **33** (1994) 5143.

[48] H. Bakashima, S. Hazumi, T. Kamiya, K. Tominaga, M. Okada, *Jpn. J. Appl. Phys*. **33** (1994) 5139.

[49] X. Daj, Z. Xu, D. Viehland, *J. Appl. Phys*. **79** (1996) 1025.

[50] W. Ren, Y. Liu, J. Qin, L. Zhang, X. Yao, *Ferroelectrics,***152** (1994) 201.

[51] S. Bhaskar, R.S. Katiyar, J. Appl. Phys. **89** (10) (2001) 5637.

[52] K.Okazaki, K. Nagata. *Am Ceram Soc.* **52** (1973) 85.

[53] H.T. Martirena, J. C. Burfest, *J Phys. C.* **7** (1974) 3182.

[54] S. S.Chandratreya, R. M. Fulrath, J. A. Pask, *J. Am. Ceram. Soc.* **64** (1981) 422.

[55] B. V. Hiremath, A. I Kingon, J.V. Biggers, *J. Am. Ceram. Soc*. **66** (1983) 790.

[56] A. K. C. Patil, S. S. Manoharan, D. Gajpathy, *"Preparation of high density ferrites,"* in Handbook of Ceramics and Composites, New York: Marcel Decker, **1** (1990) 469.

[57] M. N. Rahaman, "Ceramic Processing and Sintering", Marcel Dekker, New York, 20 Edit, **483** (1995) 103.

[58] M. N. Rahaman, "Sintering of Ceramics", CRC Press/Taylor and Francis Group, Boca Raton, **55** (2008).

[59] S. J. L. Kang, "Sintering-Densification", Grain Growth and Microstructure, Amsterdam: Elsevier, 10 Edit. **39** (2005).

[60] N. Ichinose, M. Kimura, *Jpn. J. Appl. Phys.* **30**(1991) 2220.

[61] A. P. Barranco, Y.G. Abreu, *Solid State Commun*. **149** (2009) 2082.

[62] Z. Zhang, Wu. Ping, Lu. Li, Shu. Chang, *Appl. Phys. Lett*. **92** (2008) 112909.

[63] K. Ramam, K. Chandramouli, *Mater. Sci. Eng. B* **145** (2007) 41.

[64] T. Yong Kim, H. M. Jang, *Appl. Phys. Lett*. **77** (2000) 3824.

[65] H. Ihrig, *J. Am.Ceram. Soc*. **64** (1981) 617.

[66] G. Smolensky, *Ferroelectricity*, **53** (1984)129.

[67] K. Keizer, G. J. Lansink, A. J. Burggraaf, *J. Phys. Chem. Solids*. **39** (1978) 59.

[68] X. Dai, Z. Xu, D.Viehland, *J. Appl. Phys*. **51** (1996) 4356.

[69] D. Hennings, *Mater. Res. Bull*. **6** (1971) 329.

[70] K. Keizer, J.Bouwama, A Burgraaf, *J. Phys. Status Solid*. **281** (1976) A35.

[71] M. Kuwabara, K. Goda, K. Oshima, *Phys. ReV. B* **42** (1990)10012.

[72] R. D. Shannon, Acta Crystallogr. **751** (1976) A32.

[73] E. C. S. Tavares, P. S.Pizani, J. A. Eiras, *Appl. Phys. Lett*. **72** (1998) 897.

[74] Gurvinderjit Singh, V. S.Tiwari, *J.Appl.Phys*.**106** (2009)124104.

[75] K. Wójcik, *Ferroelectrics,* **99** (1989) 5.

[76] X. Y. Lang, Q. Jiang, J. Nanopart. Res. **9** (2007) 595.

[77] M. Kuwabara, K. Goda, K. Oshima, *Phys. ReV. B* **42** (1990)10012.

[78] G. Shirane, R. Pepinsky, B. C. Frazer, *Phys. ReV*. **97** (1955)1179.

[79] G.Shirane, R.Pepinsky, B. C. Frazer, Acta Crystallogr. **9** (1956)131.

[80] A. M.Glazer, S. A. Mabud, *Acta Crystallogr,* **34** (1978) 1065.

[81] S.Teslic, T. Egami, D. Viehland. *J. Phys. Chem. Solids.* **57** (1996) 1537.

[82] T. Egami, S.Teslic, W. Dmowski, D.Viehland, S.Vakhrushev. Ferroelectrics, **199** (1997)103.

[83] P. P. Neves, A. C. Doriguetto, V. R. Mastelaro, L. P. Lopes, Y. P. Mascarenhas, A. Michalowicz, J. A. Eiras, *J. Phys. Chem. B* **108** (2004) 14840.

[84] M. Kellati, S. Sayouri, N. El Moudden, M. Elaatmani, A. Kaal A, M. Taibi, *Mater. Res.Bull.* **39** (2004) 867.

[85] W. Ren, Y. Liu, J. Qin, L. Zhang, X. Yao, *Ferroelectrics,* **152** (1994) 201.

[86] X. Yao, Z. Chen, L. S. Cross, *J. Appl. Phys*. **54** (1983) 3399.

[87] P. Venkateswarlu, Apurba Laha, S.B. Krupanidhi, *Thin Solid Films* **474** (2005) 1.

[88] Emerson R. Camargo, Cristiano M. Barrado, Caue Ribeiro, Elson Longo, Edson R. Leite, *J. Alloys and Comp*. **475** (2009) 817.

[89] L. Zivkovic, V. Paunovic, M. Miljkovic, M.M. Ristic, *Mater. Sci. Forum* **518** (2008) 229.

[90] Y. Ito, K. Nagatsuma, H. Takeuchi, S. Jyomura, *J. Appl. Phys*. **52** (1981) 4479.

[91] Z. Zhang, P. Wu, L. Lu, C. Shu, *Phys. Rev. B* **76** (2007) 125102/1.

[92] A. Shukla, R.N.P. Choudhary, *Physica B* **405** (2010) 2508.

[93] M. Savinov, V. A Trepakov, P. P Syrnikov, V. Zelezny, J. Pokorny, A. Dejneka, L. Jastrabk, P. Galinetto, *J. Phys.: Condens. Matter* **20** (2008) 095221 (6pp).

[94] J. R. Macdonald, Impedance Spectroscopy: Emphasizing Solid State Materials and Systems, Wiley, New York, 1987 (Chapters 2 and 4).

[95] S. B. Majumder, B. Roy, S. B. Krupanidhi, R. S. Katiyar, *Appl.Phys. Lett*.**79** (2001) 239.

[96] K. Prabakar, S. P. Mallikarjun Rao, *J. Alloys Compd*. **437** (2007) 302.

[97] S. Bhattacharyya, S. S. N. Bharadwaja, S. B. Krupanidhi, *J. Appl. Phys*. **88** (2000) 4294.

[98] D. K. Pradhan, R. N. P. Choudhary, C. Rinaldi, R. S. Katiyar, *J. Appl. Phys*. **106** (2009) 024102.

[99] C. Sun, J. G. Wang, P. H. Hu, Moon J. Kim, X. R. Xing, *Dalton Trans*, **39** (2010) 5183.

[100] G. V. Lewis. R. A. Catlow, *J. Phys. Chem. Solids*, **47** (1986) 89.

[101] T. Iijima, S. Kudo, N. Sanada, *Jpn. J. Appl. Phys*, **36** (1997) 5829.

[102] T. Iijima, H. Nafe, F. Aldinger, *Integr. Ferroelectr,* **30** (2000) 9.

[103] M. Dawber, K. M. Rabe, J. F. Scott, *Rev. Mod. Phys*, **77** (2005) 1083.

[104] G. Shirane, S. Hoshino, K. Suzuki, *Phys. Rev*, **80** (1950) 1105.

[105] X. R. Xing, J. X. Deng, J. Chen, G. R. Liu, *Rare Metals*, **22** (2003) 294.

[106] J. Frantti, S. Ivanov, S. Eriksson, H. Rundl, V. Lantto, J. Lappalainenand, M. Kakihana, *Phys. Rev. B*, **66** (2002) 064108.

[107] B. Noheda, D. E. Cox, G. Shirane, J. A. Gonzalo, L. E. Cross, S. E. Park, *Appl. Phys. Lett.* **74** (1999) 2059.

[108] L. Bellaiche, A. Garcia, and D. Vanderbilt, *Phys. Rev. Lett*. **84** (2000) 5427.

[109] Y. M. Jin, Y. U. Wang, A. G. Khachaturyan, J. F. Li, and D. Viehland, *J. Appl. Phys.* **94** (2003) 3629.

[110] T. Ikeda, T. Okano, *Jpn. J. Appl. Phys.* **3** (1964) 263.

[111] P. Roychoudhary, S.B. Deshpande, *IJPA* **22** (1984) 708.

[112] S. L. Fu, S.Y. Cheng, C.C. Wei, *Ferroelectrics,* **67** (1986) 93.

[113] R. Lal, S. C. Sharma, R. Dayal, *Ferroelectrics*. **100** (1989) 43.

[114] W. Jackson, W. Reddish, Nature **156** (1945) 717.

[115] T. B. Weston, A. H. Webster, V. M. McNamara, *J. Am. Ceram. Soc.* **52** (1969) 253.

[116] B. Jaffe, W. R. Cook, H. Jaffe, Piezoelectric Ceramics, Academic Press, New York, (1971), p. 148.

[117] Edson R. Leite, *J.Am. Ceram. Soc.* **79** (19960) 1563.

[118] J. Joseph, T. M Vimala, V. Sivasubramanian, V. R. K. Murthy, *J. Mater. Sci.* **35** (2000) 1571.

[119) M. Pereira, A. G. Peixoto, M. J. M. Gomes, *Eu Ceram Soc*. (2001) 1353.

[120] Chandraprakash, O. P. Thakur, *Mater Lett*. **57** (2003) 231.

[121] G. Shirane, R. Pepinsky, B. Frazer, *Acta Cryst*. **9** (1956) 131.

[122] X. Yao, Z. L. Chen, L. E. Cross, *J. Appl. Phys*. **54** (1984) 3399.

[123] K. Uchino, S. Nomura, *Ferroelectric Lett. Sect*. **44** (1982) 55.

[124] T. Takenaka, *J. Ceram. Soc. Jpn*. **110** (2002) 215.

[125] I. Ueda, *Jpn. J. Appl. Phys*. **11**(1972) 450.

[126] G. A. Smolenskii, *J. Phys. Soc. Jpn.* **28** (1970) 26.

[127] P. Goel, K.L. Yadav, A. R. James, *J. Phys. D: Appl. Phys*.**37** (2004) 3174.

[128] Q. Zhang, *J. Phys. D: Appl. Phys*. **37** (2004) 98.

[129] T. Haccart, D. Remiens, E. Cattan, *Thin Solid Films*. **423** (2003) 235.

[130] F. Kulcsar, J. Am. Ceram. Soc, **48** (1965) 54.

[131] B. Guiffard, E. Boucher, L. Lebrun, D. Guyomar, *Mater. Sci. Eng.B* **137** (2007) 272.

[132] V. V. Klimov, N. I. Selikova, A. N. Bronnikov, *Inorganic Mat*. **42** (2006) 573.

[133] B. Cherdhirunkorn, D. A. Hall, *Integ. Ferroelectrics* **62** (2004) 61.

[134] J. H. Park, B. K. Kim, K. H. Song, S. J. Park, *J. Mater.Sci.: Mater. Elect*. **6** (1995) (2) 97.

[135] B. Tiwari, R. N. P. Choudhary, *Sol. Stat. Sci.***11** (2009) 219.

[136] S. K. Pandey, O. P. Thakur, D. K. Bhattacharya, Chandra Prakash, Ratnamala Chatterjee, *J. Alloys and Comp*. **468** (2009) 356.

[137] B. Tiwari, R. N. P. Choudhary, *J. Phys. Chem. Solid*. **69** (2008) 2852.

[138] R. Ranjan, R. Kumar, B. Behera, R. N. P. Choudhary, *Mater. Chem. Phys.***115** (2009) 473.

[139] S. R. Shannigrahi, R. N. P. Choudhary, H. N. Acharya, *Mater. Sci. Engg*. B **56** (1999) 31.

[140] C. H. Park, D. J. Chadi, *Phys. Rev. B* **57** (1998) R13961.

[141] L. X. Zhang, X. B. Ren, *Phys. Rev. B* **73** (2006) 094121.

[142] M. I. Morozov, D. Damjanovic, *J. Appl. Phys*.**104** (2008) 034107.

[143] K. Carl, K. H. Härdtl, *Ferroelectrics,* **17** (1978) 473.

[144] R. A. Eichel, *J. Electroceramic*. **19** (2007) 11.

[145] U. Robels, G. Arlt, *J. Appl. Phys*. **73** (1993) 3454.

[146] L. X. Zhang, X. B. Ren, *Phys. Rev. B* **71** (2005)174108.

[147] C. Moure, M. Villegas, J.F. Fermandez, P. Duran, *Ferroelectrics,* **127** (1992) 113.

[148] D. M. Smyth, M. P. Harmer, P. Peng, *J. Am. Ceram. Soc*. **72** (1989) 2276.

[149] E. S.Choo, J. Kim, S. L. Kang, *Jap. J. Appl. Phys*.**36** (1997) 5562.

[150] A. I. Kingon, B. Clark, *J. Am. Ceram. Soc*. **66** (1982) 253.

[151] H. M. Rietveld, J. Appl. Crystallogr. **2** (1969) 65.

[152] R. A. Young, "The Rietveld Method" International Union of Crystallography, (New York, Oxford University Press 1996).

[153] L. W. Finger, D. E. Cox, A.P.Jephcoat, *J. Appl. Crystallogr*. **27** (1994) 892.

[154] P. W. Stephens, *J. Appl. Crystallogr*. **32** (1999) 281.

[155] A. Taylor, X – ray Metallography (Wiley, New York, 1961).

[156] P. Scherrer, *Math Phys K*, **1** (1918) 98.

[157] B. D. Cullity, 'Elements of X-ray diffraction', 2nd Ed, Addision-Wesley. INC (1978).

[158] A. J. C. Wilson, X-ray Optics (Methuen, London), 1949.

[159] G. K. Williamson, W.H. Hall, *Acta Met*. **1** (1953) 22.

[160] S. Upadhyay, O. Parkash, D. Kumar, *J. All. Compd*. **432** (2007) 258.

[161] A. Guinier, W. H. Freeman, X-ray diffraction, SanFrancisco (1963).

[162] C. Kittel, Introduction to Solid State Physics, John Wiley and Sons, New York, (1995).

[163] C. Kittel, Introduction to solid state physics, John Wiley and Sons, Singapore, 2006.

[164] H. P. Klung, L. B. Alexander, X-ray Diffraction Procedures, Wiley, New York, 1974 p. 687.

[165] A. K. Jonscher, The 'universal' dielectric response, *Nature 276* (1977) 673.

[166] J. R. Macdonald, "Impedance Spectroscopy Emphasizing Solid materials and Systems", John Wiley and Sons, New York (1987).

[167] J. R. Carvajal, FULLPROF, A Rietveld Refinement and Pattern matching Analysis Program, Laboratorie Leon Brillouin (CEA-CNRS) France.

[168] S. Bhattacharyya, A. Laha and S. B. Krupanidhi, *J. Appl. Phys*. **91** (2002) 4543.

[169] D. K. Mahato, R. K. Choudhary, S. C. Srivastava, *J. Appl. Sci*. **6** (2006) 716.

[170] G. Burns, F. Dacol, *Phys. Rev. B* **28** (1983) 2527.

[171] J. J. Shyu, K. L. Mo, Jpn. *J. Appl. Phys*. **34** (1995) 5683.

[172] B. Vodopivec, C. Filipic, A. Levstik, J. Holc, Z. Kutnjak, H. Beige, *Phys. Rev.B* **69** (2004), p. 224208.

[173] E. A. Stern and Y. Yacoby, *J. Phys. Chem. Solids* **57** (1996)1449.

[174] M. H. Lente, E. N. Moreira, D. Garcia, J. A. Eiras, P. P. Neves, A. C.Doriguetto, V. R. Mastelaro, and Y. P. Mascarenhas, *Phys. Rev. B* **73** (2006) 054106.

[175] V. R. Mastelaro, P. P. Neves, A. Michalowicz, J. A. Eiras *AIP Conf. Proc*. **882** (2007) 496.

[176] S. Singh, O. P. Thakur, C. Prakash, *Def. Sci. Jour*. **55** (2005) 349.

[177] A. Mansingh, *Ferroelectrics,* **102** (1990) 69.

[178] M. A. L. Nobre, S. Langfredi, *J. Phys. Chem. Solids* **62** (2001) 1999.

[179] A. R. James, Chandra Prakash, G. Prasad, *J. Phys.D: Appl. Phys*. **39** (2006) 1635.

[180] A. Mansingh, A. Dhar, *J. Phys. D: Appl. Phys*. **18** (1985) 2059.

[181] S. Dutta, R. N. P. Choudhary, *Appl. Phys. A* **90** (2008) 323.

[182] I. M. Hodge, M. D. Ingram, A. R, West. J. Electroanal. Chem, **74** (1976)125.

[183] K. C. Sobha, K. Rao, J. *Solid State Ionics* **81**(1995)145.

[184] M. Ganguli, M. H, Bhat. K. Rao, J. *Phys. Chem. Glasses*, **40** (1999) 297.

[185] S. Lanfredi, P. Saia, R. S. Lebullenger. A. C Hernandes, *Solid State Ionics* **146** (2002) 329.

[186] S. Ghosh, A. Ghosh, *Solid State Ionics* **149** (2002) 67.

[187] R. Ranjan, A. Dviwedi, *Solid State Comm.* **135** (2005) 394.

[188] P. Jha, A. K. Ganguli, *Proc. Ind. Acad. Sci. (Chem. Sci.)* **115** (2003) 431.

[189] D. Viehland, S. J. Jang, L. E. Cross, M. Wuttig, *Phys. Rev. B* **46** (1992) 8003.

[190] Y. Hosono, K. Harada, Y.Yamashita, Jpn. *J. Appl.Phys*. **40** (2001) 5722.

[191] S. Sen, S. K. Mishra, S. K. Das, A. Tarafdar, *J. Alloy. Comp*. **453** (2008) 395.

[192] F. Jona and G. Shirane, *Ferroelectric crystals*, Dover publications, Inc, New York, (1993).

[193] R. Rai, S. Sharma, R. N. P. Choudhary, *Mat. Let.* **59** (2005) 3921.

[194] J. E. Garcia, R. Perez, A. Albareda, J. A. Eiras, *J. Eu Ceram. Soc*. **27** (2007) 4029.

[195] M. Kumar, K.L. Yadav, *J. Phys: Cond. Matter.* **19** (2007) 242.

[196] A.Yang, C. A. Wang, R. Guo, Y.Huang, C. W. Nan, *Ceram. Int*. **36** (2010) 549.

[197] G. H. Heartling In: R. C. Buchanan., *Ceram. Mat. Elect.* (1991) (Chapter3).

LIST OF PUBLICATIONS

Papers Published/Communicated in Journals:

[1] Fundamental understanding and modeling of spin coating process: A review

Niranjan Sahu, B. Parija and S. Panigrahi *Indian J. Phys.* **83** (4) 493-502 (2009).

[2] Rietveld Refinement, Microstructure and Electrical Properties of $PbTiO_3$ Ceramic Materials.

Niranjan Sahu, Manoranjan Kar and S. Panigrahi, *J. Arch. Phys. Res*, **1**(2010) (1)75-87.

[3] Rietveld Refinement of a Nanocrystalline $Pb_{0.5}Zr_{0.5}TiO_3$ Ceramic.

Niranjan Sahu, Manoranjan Kar, S.Panigrahi, *Int. J. phys.*, **3**(2010) (2)157-164.

[4] Structural study of Zr doped $PbTiO_3$ materials by employing Rietveld method.

Niranjan Sahu, S.Panigrahi, Manoranjan Kar, *J.Adv.Powd.Tech.* **22**(2011)689-694.

[5] Mathematical aspects of Rietveld refinement and Rietveld Crystallographic investigation of a single phase $PbTiO_3$ Ceramics.

Niranjan Sahu , S. Panigrahi. Bull. Mater. Sci., Vol. 34, No. 7, December 2011, pp. 1–6.

[6] Rietveld Analysis of La^{3+}/Al^{3+} Modified $PbTiO_3$ Ceramics.

NiranjanSahu, S. Panigrahi, Ceramics International 38 (2012) 1085–1092.

[7] Structural investigation and dielectric properties of Mn Substituted $Pb(Zr_{0.65}Ti_{0.35})O_3$ Perovskite.

Niranjan Sahu, S. Panigrahi and Manoranjan Kar**,** Ceramics International 38 (2012) 1549–1556.

[8] Rietveld structural investigation, dielectric and impedance properties of $Pb(Zr_{0.65}Ti_{0.35})O_3$ Perovskite.

Niranjan Sahu, M.Kar and S.Panigrahi (Communicated)

[9] Structural change and diffusion of ferroelectric in $Pb_{1-x}La_xTiO_3$ Perovskite.

Niranjan Sahu, S.Panigrahi and Manoranjan Kar, (Communicated).

[10] Rietveld Analysis of La^{3+}/Mn^{4+} Modified $PbTiO_3$ Ceramics.

Niranjan Sahu, S. Panigrahi (Communicated).

[11] Rietveld Analysis, dielectric and impedance behavior of Mn^{4+}/Fe^{3+} ion modified $Pb(Zr_{0.65}Ti_{0.35})O_3$ Perovskite, (Communicated).

Papers Published in Refereed Conference Proceedings:

[12] Rietveld analysis of a single phase $PbTiO_3$.

Niranjan Sahu, Manoranjan Kar & S.Panigrahi, Presented a paper on **National Conference** on Mechanism Science and Technology: from Theory to Application, November 13-14, 2008 National Institute of Technology, Hamirpur (H.P.) India -177005.

[13] Structural Transition and Rietveld Refinement on a Single Phase Nanocrystalline $Pb_{0.5}Zr_{0.5}TiO_3$ Ceramics.

Niranjan Sahu, Manoranjan Kar & S.Panigrahi, presented a paper on **CONDENSED MATTER DAYS-2009** *(*Symposium on condensed Matter Physics*), 26-28th August 2009*, Jadavpur University, Kolkata.

[14] Structural change of Zr Doped $PbTiO_3$ Ceramics.

Niranjan Sahu, S. Panigrahi and Manoranjan Kar, Presented a paper at the **International conference** of electro ceramics, Dec13-17, **2009 Delhi University.**

[15] Rietveld structural study, microstructure, dielectric and impedance properties of Fe^{3+} ion modified on $Pb(Zr_{0.65}Ti_{0.35})O_3$ Perovskite Ceramics.

Niranjan Sahu, Manoranjan Kar, and S.Panigrahi, **National seminar** on physics and technology of Novel materials (PTNM-2010), Sambalpur University

[16] Enhancement of Conductivity in Fe^{3+} and Mn^{3+} modified $Pb(Zr_{0.65-x}Fe_xTi_{0.35})O_3$ ceramics

S. Panigrahi, **Niranjan Sahu** and Manoranjan kar, ***accepted for oral presentation*** in ICE-2011, **Sydney, Australia.**